UNIVERSITÉ DU LUXEMBOURG

PhD-FSTM-2022-105
The Faculty of Science, Technology and Medicine

DISSERTATION

Defence held on 07/09/2022 in Luxembourg

to obtain the degree of

DOCTEUR DE L'UNIVERSITÉ DU LUXEMBOURG

EN BIOLOGIE

by

Kristopher John SCHMIT

Born on 19 October 1986 in Esch-sur-Alzette, (Luxembourg)

TRIGGERS OF PARKINSON'S DISEASE PATHOGENESIS: INTERACTION OF EXOGENOUS AND ENDOGENOUS FACTORS CONTRIBUTING TO DIFFERENT DISEASE PATHOLOGIES

Dissertation defence committee

Dr Michel MITTELBRONN, dissertation supervisor
Professor, Université du Luxembourg

Dr Evan WILLIAMS, Chairman
Associate Professor, Université du Luxembourg

Dr Manuel BUTTINI, Vice Chairman
Research Scientist, Université du Luxembourg

Dr Sylvie CLAEYSEN
Senior Researcher, Université Montpellier

Dr Ygoesh SINGH
Research Scientist, Universitätsklinikum Tübingen

TRIGGERS OF PARKINSON'S DISEASE PATHOGENESIS: INTERACTION OF EXOGENOUS AND ENDOGENOUS FACTORS CONTRIBUTING TO DIFFERENT DISEASE PATHOLOGIES

Dissertation by

Kristopher John SCHMIT

DOCTOR OF PHILOSOPHY

University of Luxembourg

Doctoral School in Science and Engineering (DSSE)
Doctoral Programme in Systems and Molecular Biomedicine

Luxembourg 2018-2022

Thesis committee:

Chair
Prof. Dr. Evan Williams
University of Luxembourg

Vice-Chair
Dr. Manuel Buttini
University of Luxembourg

Co-Supervisor
Prof. Dr. med. Michel Mittelbronn
University of Luxembourg

External Jury
Dr. Sylvie Claeysen
Université Montpellier

Dr. Yogesh Singh
Universitätsklinikum Tübingen

Expert:

Co-Supvervisor
Prof. Dr. Paul Wilmes
University of Luxembourg

Funding partners

Affidavit

I hereby confirm that the PhD thesis entitled "Triggers of Parkinson's disease pathogenesis: exogenous and endogenous factors contributing to different disease pathologies" has been written independently and without any other sources than cited. All necessary ethical approvals have been obtained in accordance with the "Règlement grand-ducal du 11 janvier 2013 relatif à la protection des animaux utilisés à des fins scientifiques" adapted from and in line with the European Directive 2010/63/EU.

Luxembourg, 7th September 2022

Kristopher John SCHMIT

Acknowledgments

The different studies presented in this PhD thesis have been supported by various institutions, which are listed in each publication. I would like to particularly thank the University of Luxembourg, the Luxembourg National Research Fund (FNR) and the NCER-PD Consortium for their support over the entire course of my thesis. My work would have especially not been possible without the FNR PhD AFR Individual Fellowship Grant (Project Code: 12515776).

More importantly I want to thank all the people that supported and trusted me along this journey:

My colleagues and dear friends from the *Luxembourg Center of Neuropathology*. Thank you for what all you have done with and for me. The discussions and motivations that I received from each and everyone of you helped me on my way and led me to where I am now. Special thanks to Pierre Garcia, Alessia Sciortino, Mélanie Thomas, Beatriz Pardo, Irati Bastero Acha, Jean-Jacques Gérardy , Camille Cialini and Tony Heurtaux. Not only did you help me in my projects, but I learned so much professionally and personally from you. I am eternally grateful to have shared this time with you.

My dear colleagues and friends from the Systems Ecology team. Coming from Neuropathology, I ventured into a completely unknown field. You made it possible for me overcome various hurdles. Thank you Janine Habier, former colleague Beatrice Peisl, Camille Martin-Gallausieux, Susheel Bhanu Busi for the technical help and suggestions that helped me shape my experiments. Thank you Rashi Halder and Paula Cristina Lupu from the omics platform. Special thanks to the 2-HP crew, Velma Aho and former colleague Jean-Pierre Trezzi.

I would also like to mention some former colleagues: Oihane Uriarte Huarte and Amer Ashrafi. In the very early days of my scientific career, you were my first to-go-to people. I really appreciated you and our time together.

To my supervisors, Dr. Prof. Michel Mittelbronn and Prof. Paul Wilmes, thank you for believing in me. Your trust in my abilities was certainly challenged at times, but you never ceased to do so.

Special thanks to Sylvie Claeysen and Yogesh Singh to have agreed to be part of my jury and to Prof. Evan Williams to have accepted to take over the role of committee chair.

This last person needs to be mentioned separately. Manuel Buttini, what can I say more than THANK YOU from the bottom of my heart. I would certainly not have managed the entire time without your support, nagging, figurative butt-kicking, but most importantly mentoring. Thank you very much.

My family and friends, you kept me sane. I cannot start naming you all, but each and everyone were and are so important to me.

The most important two people during my entire studies are without a doubt though my parents. I did not always tell you, but I could have never made it without you. With all the setbacks, you always had my back and supported me in every possible way. Mom and Dad I love you and thank you for it all.

Again, thanks to everyone.

Contents

Table of Figures

Table of Tables

Abbreviations

αSyn	alpha-synuclein/a-synuclein
ΔEC	isogenic Curli-KO E. coli strain
E. coli	Escherichia coli
EC	Curli expressing E. coli
FD	Fibre-deprived diet
FR	Fibre-rich diet/normal chow
iRBD	idiopathic Rapid eye movement sleep disorder
LC	Locus coeruleus
M. smithii	Methanobrevibacter smithii
pan-αSyn	total α-synuclein
PD	Parkinson's disease
PPN	Pedunculopontine nucleus
pS129-αSyn	phosphorylated S129 alpha-synuclein
RBD	Rapid eye movement sleep disorder
S. thyphimurium	Salmonella thyphimurium
SN	Substantia nigra
SNpc	Substantia nigra pars compacta
SCFA	short-chain fatty acids
GIT	gastrointestinal tract
CNS	central nervous system
ENS	enteric nervous system
PNS	peripheral nervous system
2-HP	2-hyroxypyridine

TRIGGERS OF PARKINSON'S DISEASE PATHOGENESIS:

INTERACTION OF EXOGENOUS AND ENDOGENOUS FACTORS CONTRIBUTING TO DIFFERENT DISEASE PATHOLOGIES

by

Kristopher John SCHMIT

Abstract

Parkinson's disease (PD) is the most common movement disorder. Empiric observations brought forth that clinical and pathogenesis do not progress the same in all patients. This is most likely due to the multi-factorial nature of PD. Different endogenous, e.g. genetic predispositions, and exogenous factors such as pesticides and diet, independently or together, can be at the origin of the disease or accelerate and alter disease progression. One particular "organ" is most exposed to such factors: the gut and its residing microbiota. Findings of aggregated α-synuclein (αSyn) in the enteric nervous system (ENS) and altered gut microbiomes in PD patients suggest that gut-brain axis is a potential route for corrupted αSyn to spread to the central nervous system (CNS). Additionally, the impact of various environmental (exogenous) factors on the gut microbiome in the context of disease progression has been brought to the limelight. Resulting dysbiosis can lead to different physiological reactions such as "leaky gut" and inflammation (systemic and neuroinflammation). Subsequent interactions with other exogenous or endogenous toxins can act as triggers or accelerators in the disease process. Understanding the underlying mechanisms of such factors could give new insights into differing disease progressions, help to venture into novel therapeutic approaches and mitigate disease progress. Thus, we used different sophisticated in vivo approaches to investigate these complex interactions and mechanisms.

First, we exposed a transgenic human wild-type α-synuclein (αSyn) overexpressing mouse model (Thy1-Syn14) to a fibre deprived diet and the bacterial Curli protein. We aimed to understand how these factors exacerbate, individually or in combination, the disease-related phenotype in the enteric (ENS) and central nervous (CNS) systems. Using 16S rRNA amplicon sequencing, various histopathology approaches and motor behaviour tests, we uncovered that the combination of fiber deprivation and microbiome-born insults can be a trigger in PD progression along the

gut-brain axis. It provides a model for the heterogeneity observed in and entails implications for lifestyle management of PD patients.

Next, we investigated the effect of a newly isolated archaeal compound, 2-hydroxypyridine (2-HP), which was found to be increased in stool samples of PD and idiopathic REM sleep behaviour disorder (iRBD) patients. 2-HP showed a positive correlation with *Methanobrevibacter smithii*, which belongs to the most abundant archaeal genus *Methanobrevibacter*. Initial *in vitro* data suggested that 2-HP is seeding αSyn aggregation in an αSyn-overexpressing yeast model and a human iPSC-derived ENS model. When we injected 2-HP into the right striatum of Thy1-Syn14 mice we observed motor behaviour changes, αSyn aggregation in the prefrontal cortex and TH-fiber loss in the striatum. To our knowledge, we are the first to show a connection of an archaeal molecule in PD.

Finally, we studied the mechanisms after intrastriatal injection of fibrillary αSyn forms. We performed quantitative analyses of αSyn inclusion formation, neurodegeneration and neuroinflammation/microgliosis. Our most important observation was that neurodegeneration and microgliosis, or only microgliosis, could be observed in the absence of αSyn inclusions. The longitudinal gene expression study revealed a dominant inflammatory profile early after injury, which precedes neurodegeneration. Our findings suggest a crucial role of microgliosis which be induced by environmentally induced changes in the gut microbiota, in the induction of PD pathologies.

PART I

General Introduction

1 Parkinson's disease

1.1 Short historic summary

It's been more than 200 years that James Parkinson published his "Essay on the shaking palsy" (Parkinson, 1817). Here, the main milestones in Parkinson's disease (PD) research will briefly be summarized (**Figure 1**). He further described this disease to be accompanied by "Involuntary tremulous…" motions, in which the muscular power and posture worsens over time, whilst "…the senses and intellects being uninjured." In his manuscript, he details the etiopathology of six subjects, in between whom he observed many common symptoms such as worsening tremors and muscle weakness. The subjects had more and more difficulties to write, read, walk or even sleep. Further, their posture and gait were affected to a level where they had to walk on the tip of their feet to avoid falling over. Motor symptoms continued to worsen, including digestive agitations, another common symptom in the etiopathology.

Previous works and James Parkinson's manifesto, described merely symptoms of the disease. With advancements in anatomical pathology around the turn of the 20th century, PD pathology was proposed to be mainly located in the Substantia nigra (SN). Frederick Lewy, almost 100 years after Parkinson, described aggregated bodies in the SN, which were later termed Lewy bodies by Konstantin Tretiakoff. Following advances were made in disease stage scaling (Hoehn-Yahr scale) and treatment optimisations such as novel combinatorial medication treatment, cell therapies and deep brain stimulation approaches. One pivotal milestones was the molecular decomposition of Lewy bodies in 1997 and the identification of αSyn as main component (Spillantini et al.,

1997). The following years and the progress in molecular biology led to the identification of more than 20 different genes involved in the development of PD. This allowed to develop novel models helping researchers around the world to study in greater detail the complexity of PD.

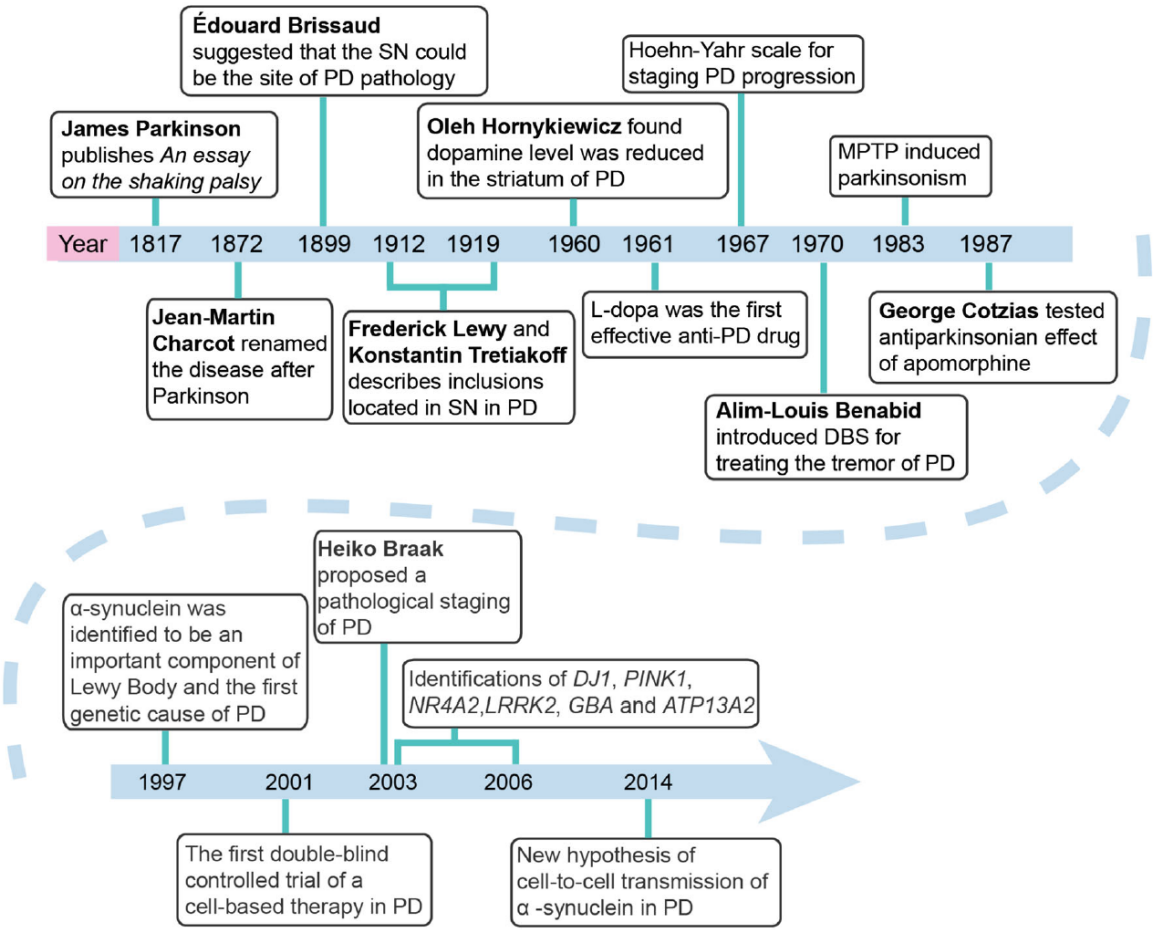

Figure 1 | Milestones since James Parkinson's "An essay on the shaking palsy" (Fig. 2 from Lie and Le, 2017)

1.2 Prevalence, clinical features, diagnosis and treatment

There are about 10 million PD patients worldwide. With an ever-aging population, this number is estimated to almost double by 2030. The majority of cases are sporadic (90-95%) and diagnosed in people older than 60 years of age. Beyond 80 years of age, roughly 3% of the world population suffers from PD and, in most populations, there is a higher prevalence in men.

Diagnostic criteria are a set of motor symptoms and other criteria defined by the *International Parkinson and Movement disorder Society-Unified Parkinson's disease rating scale* (MDS-UPDRS)(Goetz et al., 2008), adapted from the *UK Parkinson's disease society Brain Bank Clinical Diagnostic* criteria (**Table 1**) (Hughes et al., 1992). The cardinal motor symptoms are bradykinesia, the progressive slowness of movement initiation, and at least one amongst muscular rigidity, postural instability, and resting tremor (**Table 1**, **Figure 2**). Motor deficits differ in PD patients. Two major subtypes have been distilled from empiric observations: tremor-dominant and non-tremor dominant PD. The non-tremor dominant subtype has a stronger postural instability phenotype. Further, this subtype and later age of onset PD have been reported to progress faster and show a generally more severe motor phenotype (Jankovic et al., 1990).

As the disease progresses, other motor symptoms appear such as dyskinesia. However, PD is marked by several non-motor symptoms. These manifest themselves already prior motor symptoms. This so called pre-clinical or prodromal phase can precede the onset of motor deficits 10-20 years. This will be further elucidated below.

To date there is no cure for PD. Current approved therapies focus on reducing clinical symptoms to relief the patients (Ellis and Fell, 2017). The common mode of action of current treatments is the elevation of dopamine in the striatum (see below for details on pathogenesis). Unfortunately, the efficacy declines over time since the degenerative process is still ongoing. The most common prescribed drug is Levodopa (L-DOPA), a dopamine agonists, which is often given in combination with other drugs (Ellis and Fell, 2017). Alternative, once medication loses efficacy, is deep brain stimulation. Current studies focus on stopping or at least slowing down disease progression. Ongoing clinical trials mainly focus on direct and indirect dopamine modulators, to find more stable approaches (Ellis and Fell, 2017).

Table 1 | UK PD Society Brain Bank clinical diagnostic criteria (adapted Panel 1 from Lang, 2015)

Step 1 **diagnosis of parkinsonian syndrome**	**Step 2** **exclusion criteria for Parkinson's disease**	**Step 3** **supportive prospective positive criteria for Parkinson's disease**
Bradykinesia (ie, slowness of initiation of voluntary movement with progressive reduction in speed and amplitude of repetitive actions) plus one or more of the following features:	One or more of the following features suggest an alternate diagnosis:	Three or more of the following features are required for diagnosis of definite Parkinson's disease:
• Muscular rigidity • 4–6 Hz rest tremor • Postural instability not caused by primary visual, vestibular, cerebellar, or proprioceptive dysfunction	• History of repeated strokes with stepwise progression of parkinsonian features • History of repeated head injury • History of definite encephalitis • Neuroleptic treatment at onset of symptoms • 1-methyl-4-phenyl-1,2,3,6-tetrahydropyridine (MPTP) exposure • Negative response to large doses of levodopa (if malabsorption excluded) • More than one affected relative* • Sustained remission • Strictly unilateral features after 3 years • Early severe autonomic involvement • Early severe dementia with disturbances of memory, language, and praxis • Oculogyric crises • Supranuclear gaze palsy • Babinski sign • Cerebellar signs • Presence of a cerebral tumour or communicating hydrocephalus on CT scan or MRI	• Unilateral onset • Rest tremor present • Progressive disorder • Persistent asymmetry affecting the side of onset most • Excellent response (70–100%) to levodopa • Severe levodopa-induced chorea • Levodopa response for 5 years or more • Clinical course of 10 years or more

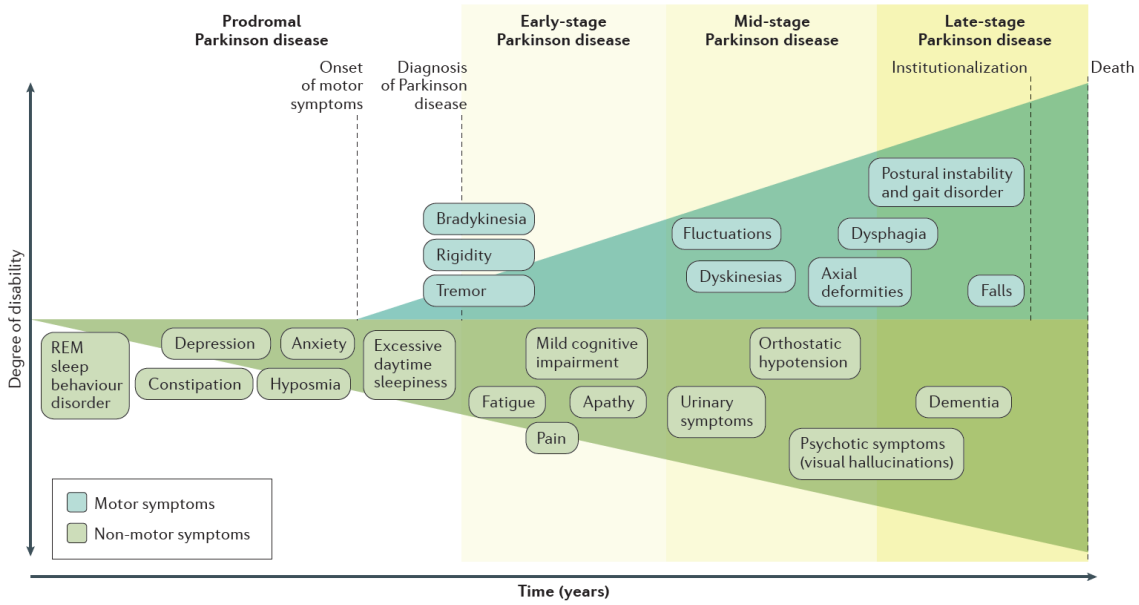

Figure 2 | Progression of clinical features in PD (Figure 5 from Poewe, 2017)

1.3 Pre-clinical/Prodromal PD and non-motor symptoms

PD is mainly defined by its motor deficits. However, PD has a long list of pre-clinical/prodromal and accompanying progressive non-motor symptoms (**Table 2**).

Table 2 | Non-motor features of PD (adapted from Poewe, 2008)

Neuropsychiatric dysfunction	Sleep disorders	Autonomic dysfunction	Sensory symptoms and pain
Mood disorders	Sleep fragmentation and insomnia	Orthostatic hypotension	Olfactory dysfunction
Apathy and anhedonia	RBD	Urogenital dysfunction	Abnormal sensations
Frontal executive dysfunction	PLMS/RLS	Constipation	Pain
Dementia and psychosis	Excessive daytime somnolence		

RBD, rapid eye movement sleep behaviour disorder; PLMS, periodic limb movement in sleep; RLS, restless legs syndrome (Poewe, 2008)

The most common non-motor symptoms are hyposmia, constipation and REM sleep behaviour disorder (RBD). Regions relating to these symptoms are often affected in PD patients. For instance, the locus coeruleus is involved sleep-wake cycling/RBD (Van Egroo et al., 2022) and the myenteric plexus is responsible for the peristaltic movement of the gut (Shahrestani and Das, 2021). Current therapies, however, are mainly focusing on dopamine replacement in the nigrostriatal pathway.

Some non-motor symptoms (e.g. RBD and constipation) are indicative of a potential risk to develop PD (Poewe, 2008). Such so called pre-clinical or prodromal PD symptoms appear up to 20 years prior PD motor deficits (**Figure 2**) (Poewe et al., 2017) and could serve as markers for early diagnosis.

1.5 Neuropathology

1.5.1 Neurodegeneration

Even though the accuracy of clinical diagnosis has improved over the last decades (Marsili et al., 2018), only post-mortem autopsy provides a definitive diagnosis for PD. The pathological hallmarks of PD are neuronal loss of dopaminergic neurons and Lewy pathology in the substantia nigra. Individually, these pathologies are not exclusive to PD. Only when found together, a definitive diagnosis for PD can be made.

Neurodegeneration in PD is required but not limited to the substantia nigra. Other regions showing neuronal loss in PD are amongst others the ventral tegmental area, nucleus basalis of Meynert, cortex, amygdala, dorsal motor nucleus of the vagus, locus coeruleus and pedunculopontine nucleus (Giguère et al., 2018; Kalia and Lang, 2015). The in-depth description of all regions is beyond the scope of this work. Here, the focus will remain on the substantia nigra, pedunculopontine nucleus (PPN) and locus coeruleus.

The substantia nigra, first described in 1786 by French anatomist Félix Vicq d'Azyr (Parent and Parent, 2010), is located in the ventral midbrain and comprises two functionally and morphologically distinct regions (Sonne et al., 2022). The neuromelanin pigmented dopaminergic neurons, which are lost in PD, are located in the dorsolateral

pars compacta (SNpc) region of the substantia nigra (Sonne et al., 2022). The ventrolateral tier of that neuron population is the most affected (Kalia and Lang, 2015) and projects to the dorsal striatum (or caudate putamen), which is mainly involved in conscious motor control (Young et al., 2021). Estimates of striatal dopamine terminal loss at disease onset vary between studies, ranging mostly from 50%-70% (Bernheimer et al., 1973; Cheng et al., 2010; Fearnley and Lees, 1991; Greffard et al., 2006). The neurodegenerative process is suggested to be a "dying-back process" starting in the striatum (Ehringer and Hornykiewicz, 1960; Hornykiewicz, 1998), preceding and exceeding the loss of dopaminergic neurons in the SNpc. At disease onset loss of dopaminergic neurons in the SNpc is estimated to be around 30% (Cheng et al., 2010; Fearnley and Lees, 1991), rising to about 68% at end stage (Giguère et al., 2018).

The SNpc receives glutamatergic and cholinergic inputs from the PPN, which is located in the upper pons (French and Muthusamy, 2018). As the substantia nigra, the PPN can be subdivided into two subregions, the pars compacta (PPNc) and the pars dissipates (PPNd) (French and Muthusamy, 2018). The PPNc presents the more prominent region of the PPN and almost exclusively comprises large cholinergic neurons (Pahapill and Lozano, 2000; Winn, 2008). In PD, neuronal (mainly cholinergic neurons) loss in the PPNc reaches almost 60% at end stage (Hirsch et al., 1987; Jellinger, 1988) and the degree of loss is associated with disease severity (Chambers et al., 2020). It remains, however, unclear if the neuronal loss in the PPN precedes or is consequence of nigrostriatal degeneration (Bensaid et al., 2016; MacLaren et al., 2018). There is evidence for both processes, which would provide an explanation for the heterogeneity of PD (Chambers et al., 2020).

Another key CNS nuclei in PD is the locus coeruleus (LC). It is, identical to the PPN, located in the upper pons. It is mainly composed of noradrenergic neurons, which have widespread projections throughout almost the entire brain including the substantia nigra (Bari et al., 2020). In PD, up to 93% of neurons from the LC are lost (Giguère et al., 2018; Oertel et al., 2019). In PD patients with REM behaviour disorder (RBD), changes to the autonomic system and LC precede changes of the nigrostriatal system (Borghammer and Van Den Berge, 2019).

Interestingly, both the PPN and the LC are involved in rapid-eye-movement (REM) sleep control and consequently RBD, which is a prominent prodromal PD non-motor symptom (Chambers et al., 2020; Van Egroo et al., 2022) as described before.

1.5.2 Alpha-synuclein and Lewy pathology

There are three different synuclein proteins of which only αSyn and β-synuclein can be found in the brain, and only αSyn has been implicated in PD (George, 2002). Alpha-synuclein is a 140 amino acid long and 14.4kDa heavy protein mainly located in pre-synaptic terminals (Emamzadeh, 2016). Its primary structure consists of three functionally distinct domains: the lipid interacting N-terminus, the central amyloid binding domain or NAC, and the acidic C-terminal tail (Emamzadeh, 2016). The NAC sequence is essential for aggregation of αSyn typical to PD and other synucleinopathies (Lashuel et al., 2013).

The overall physiological function of αSyn remains unknown. On the cellular level it occurs mainly in the cytosol, and to a more limited extend in the nucleus and mitochondria (Lashuel et al., 2013). However, along its high prevalence in pre-synapses it has been shown to be involved in synaptic vesicle recycling and neurotransmitter release (Bendor et al., 2013; Lashuel et al., 2013).

While the knowledge about the normal function of αSyn is still scarce, there is a great body of evidence on its role in neurodegenerative diseases. Especially synucleinopathies[1] are characterized by the presence of abnormal forms of αSyn. There is evidence for different αSyn conformations. The most prominent forms and at the same time the second diagnostic hallmarks in PD are Lewy bodies (LB) or Lewy neurites (LN). Electron microscopy analysis revealed that LBs and LNs consist of unbranched αSyn filaments with lengths ranging from 200-600nm and widths varying between 5-10nm

[1] "The synucleinopathies refer to a group of disorders characterized by abnormally misfolded α-synuclein aggregates in the peripheral and central nervous systems. Differences in the cellular location and pattern of α-synuclein deposition lead to clinically distinct entities of synucleinopathies: pure autonomic failure, multiple system atrophy (MSA), dementia with Lewy bodies (DLB), and Parkinson disease." (Coon and Singer, 2020)

(Goedert et al., 2013; Spillantini et al., 1998). The core of the filaments are stacked β-sheets (Vilar et al., 2008) and the majority of its αSyn is hyperphosphorylated at serine 129 (Anderson et al., 2006). LBs, one or multiple, occupy the intracellular space, whereas LNs can be found in axons and dendrites of affected neurons.

In PD, αSyn structures can be found throughout the brain at different disease stages. Braak and colleagues (Braak et al., 2003a) proposed a pathological staging for the sporadic form of the disease based on the distribution pattern of αSyn structures. They subdivided the disease associated pathologies into 6 stages (**Table 3**, **Figure 3**). Briefly, prior to any clinical symptoms, the first regions presenting αSyn positive structures are the dorsal motor nucleus of the vagus and to a lesser degree the olfactory bulb (Stage 1). The pathology subsequently progresses in a caudorostral manner reaching the midbrain structures (Stages 3-4) such as the SNpc and finally the neocortex at end stages (Stages 5-6).

Table 3 | Braak stages (adapted Table 1 from Braak et al., 2003a)

Stage 1	
Medulla oblongata	Lesions in the dorsal IX/X motor nucleus and/or intermediate reticular zone
Stage 2	
Medulla oblongata and pontine tegmentum	Pathology of stage 1 plus lesions in caudal raphe nuclei, gigantocellular reticular nucleus, and coeruleus–subcoeruleus complex
Stage 3	
Midbrain	Pathology of stage 2 plus midbrain lesions, in particular in the pars compacta of the substantia nigra
Stage 4	
Basal prosencephalon and mesocortex	Pathology of stage 3 plus prosencephalic lesions. Cortical involvement is confined to the temporal mesocortex (transentorhinal region) and allocortex (CA2-plexus). The neocortex is unaffected
Stage 5	
Neocortex	Pathology of stage 4 plus lesions in high order sensory association areas of the neocortex and prefrontal neocortex
Stage 6	
Neocortex	Pathology of stage 5 plus lesions in first order sensory association areas of the neocortex and premotor areas, occasionally mild changes in primary sensory areas and the primary motor field

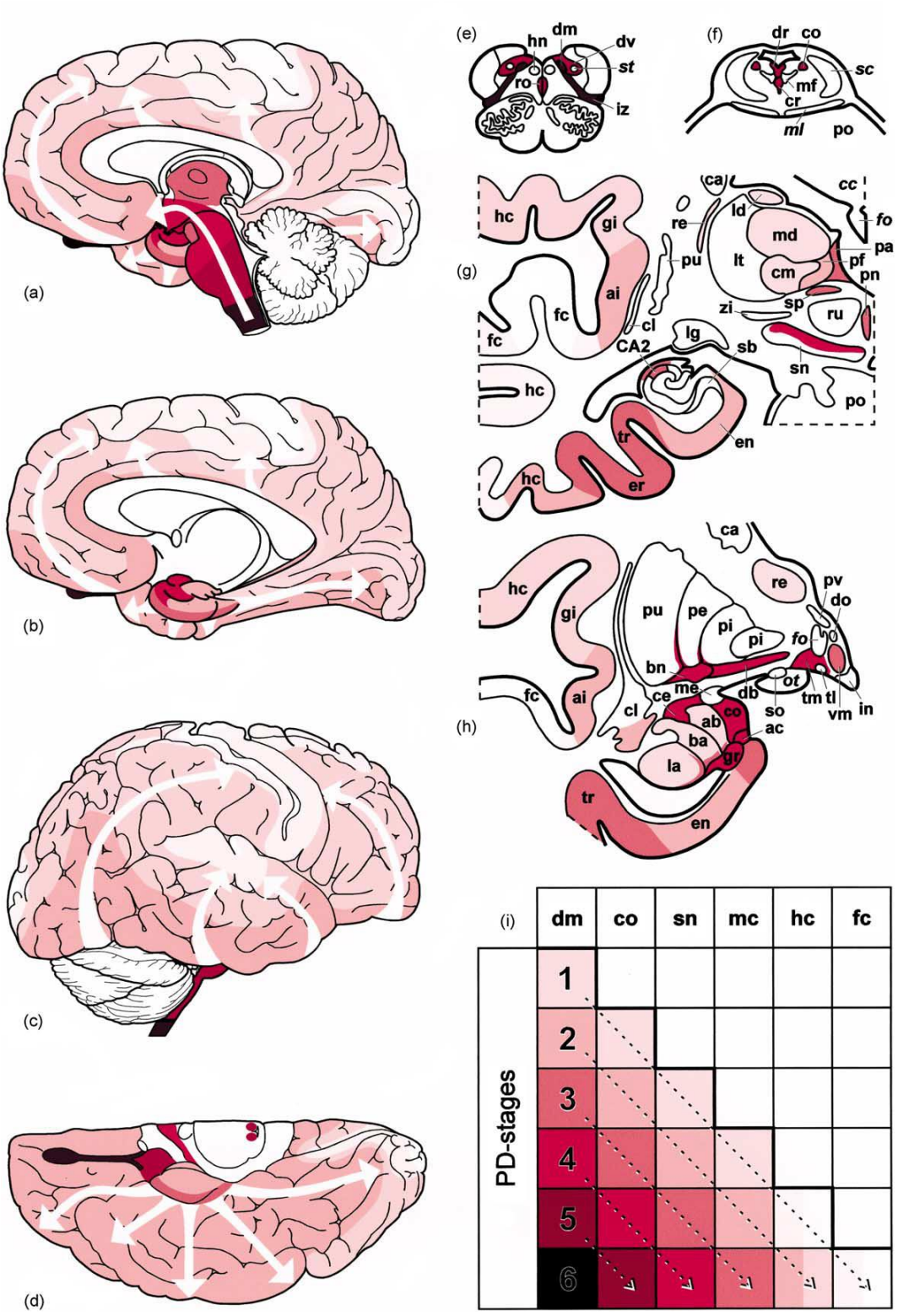

from Braak et al., 2003

Figure 3 | "Progression of PD-related intraneuronal pathology"

"The pathological process targets specific subcortical and cortical induction sites (a–i).(a and e) Lesions initially occur in the dorsal IX/X motor nucleus and frequently (a and d) in the anterior olfactory nucleus as well. Thereafter, less susceptible brain structures gradually become involved (see white arrows). The pathology in the anterior olfactory nucleus expands less readily into related areas than that evolving in the brain stem. The brain stem pathology takes an upward course (see white arrows). (a–d, g–h) Cortical involvementfollows, commencing with the anteromedial temporal mesocortex (tr and er in g and h). From there, the neocortex succumbs, beginning with high order sensory association and prefrontal areas. First order sensory association/premotor areas and, thereafter, primary sensory and motor fields follow suit. In(a–h), the gradual decrease in shading intensity is intended to represent the topographical expansion of the lesions during the course of the disease. Simplified diagram (i) showing the topographic expansion of the lesions (from left to right: dm to fc) and, simultaneously, the growing severity on the part of the overall pathology (from top to bottom: stages 1–6). With the addition of further predilection sites, the pathology in the previously involved regions increases. List of abbreviations: ab, accessory basal nucleus of the amygdala; ac, accessory cortical nucleus of the amygdala; ai, agranular and dysgranular insular cortex; ba, basal nucleus of the amygdala; bn, basal nucleus of Meynert; ca, caudate nucleus; CA1, first sector of the Ammon'shorn; CA2, second sector of the Ammon's horn; cc, corpus callosum; ce, central nucleus of the amygdala; cl, claustrum; cm, centromedian nucleus of the thalamus; co, coeruleus–subcoeruleus complex; cr, nucleus raphes centralis; db, interstitial nucleus of the diagonal band; dm, dorsal motor nucleus of the glossopharyngeal and vagal nerves; do, dorsomedial nucleus of the hypothalamus; dr, nucleus raphes dorsalis; dv, dorsal nuclear complex of the glossopharyngeal and vagal nerves containing melanized projection neurons; en, entorhinal region; er, ectorhinal region (mesocortex); fo, fornix; fc, first order sensory association areas, premotor areas, as well as primary sensory and motor fields; gi, granular insular cortex; gr, granular nucleus of the amygdala; hc, high order sensory association areas and prefrontal fields; hn, motor nucleus of the hypoglossal nerve; in, infundibular nucleus of the hypothalamus; iz, intermediate reticular zone; la, lateral nucleus of the amygdala; ld, laterodorsal nucleus of the thalamus; lg, lateral geniculate body of the thalamus; lt, lateral nuclei of the thalamus; me, medial nucleus of the amygdala; ml, medial lemniscus; mf, medial longitudinal fascicle; mc, anteromedial temporal mesocortex; ot, optic tract; pa, paraventricular nucleus of the thalamus; pe, pallidum, external segment; pf, parafascicular nucleus of thalamus; pi, pallidum, internal segment; pn, parabrachial pigmented nucleus; po, pontine nuclei; pu, putamen; pv, paraventricular nucleus of the hypothalamus; re, reticular nucleus of the thalamus; ru, red nucleus; ro, nucleus raphes obscurus; sb, subiculum; sc, superior cerebellar peduncle; sn, substantia nigra; so, supraoptic nucleus; sp, subparafascicular nucleus; st, solitary tract; tl, lateral tuberal nucleus of the hypothalamus; tm, tuberomamillary nucleus of thehypothalamus; tr, transentorhinal region (mesocortex); vm, ventromedial nucleus of the hypothalamus; zi, zona incerta."

from Braak et al., 2003

1.6 Disease mechanisms/pathogenesis

1.6.1 Overview

Determining the cause for PD has been a longstanding challenge for researchers around the world. In the past, the disease was thought to be of complete idiopathic nature with age being the strongest feature. While age still is the most crucial risk factor of PD today, many factors have been shown to increase the risk for PD onset and progression. Today, it is known that the majority of cases (90-95%) and often heterogeneous clinical profiles are due to a highly complex, multi-factorial interplay of genetic and environmental factors. Even tough rare (5-10%), the discovery of genetic familial forms of the disease and thereby genetic mutations, researchers were able to unravel some aspect of the disease pathogenesis. Since familial and idiopathic/sporadic PD cases, have a very similar behavioural phenotype, one can deduce that the underlying mechanisms, leading up to the various symptoms, are the same or at least closely related with intersecting common pathways (Hirsch et al., 2013). These mechanisms can be split into cell-autonomous and non-cell-autonomous processes (Hirsch et al., 2013). Cell-autonomous processes contributing to PD are impairment of proteostasis and degradation systems, mitochondrial dysfunction, and oxidative stress. The non-cell-autonomous processes, which will be discussed in more detail below, are prion-like spreading of αSyn and neuroinflammation.

αSyn aggregation is seen in all PD patients. The imbalance in αSyn levels or misfolding and oligomerization of αSyn due to different mutations in or multiplications of the αSyn gene *SNCA* have been associated with increased PD risk. To restore proteostasis, the cellular degradation systems, ubiquitin-proteasome system and lysosomal autophagy system, are crucial. In PD, these systems are impaired. Thus, the cell is not properly cleared, αSyn can aggregate, and form LBs and LNs.

Aggregation can have a direct impact on mitochondrial function, and vice versa, entering a vicious cycle. In PD patients, the mitochondrial complex I activity is reduced. Underlying causes leading to this deficit are accumulation of αSyn or different genetic mutations. It has been proposed that the subsequent energy deficit leads to

dysfunctional and degenerate axon terminals in the striatum before culminating in neuronal death in the SNpc.

A direct consequence of mitochondrial dysfunction is cellular oxidative stress. Especially, dopaminergic neurons are highly susceptible to oxidative stress due to their long, unmyelinated processes and their high energy demand because of their pacemaking activity. Further, the synthesis of dopamine and other metabolites can cause additional oxidative stress. Together, mitochondrial dysfunction and oxidative stress can further lead to impairments in the lysosomal autophagy system.

1.6.2 Prion-like spreading

In recent years, the concept of αSyn spreading in a cell-to-cell manner and acting as a seed for corrupting endogenous αSyn has gained momentum. The propagation mechanism is referred to as "prion-like" (Brundin et al., 2010). Prion proteins are infectious agents originating from misfolded cellular protein with the ability to jump from an infected cell to a healthy one seeding the misfolded conformation (Prusiner, 1991). Such behaviour has been suggested to for other mammalian proteins carrying prion-like domains (Jucker and Walker, 2018).

The spreading of αSyn was first proposed in Braak's pathology staging, as described above, and later post mortem LB findings in patients who received foetal mesencephalic dopaminergic neurons supported this hypothesis (Kordower et al., 2008; Li et al., 2008). It is proposed that under pathological conditions, toxic αSyn moieties (various oligomeric or fibrillar forms) are evacuated from neurons via exocytosis (Lee et al., 2008), exosomal release (Danzer et al., 2011; Emmanouilidou et al., 2010) or penetration (Jao et al., 2008) into the extracellular domain. It has been shown that such extracellular αSyn forms can enter neighbouring cells via simple endocytosis (Kordower et al., 1998) or penetration (Tang et al., 2012), trans-synaptic dissemination (Danzer et al., 2011) and membrane-receptor-mediated uptake (Lee et al., 2008).

In vitro and *in vivo* model systems have demonstrated the prion-like spreading properties of αSyn (Chu et al., 2019; Luk et al., 2012; Luna and Luk, 2015; Rey et al., 2016; Ulusoy et al., 2013). One of the most prominent *in vivo* models investigating

spreading of αSyn was established by Luk and colleagues. They injected pre-formed fibrils of recombinant αSyn intrastriatally into C57Bl/6j mice (Luk et al., 2012). They could show that after injection, there was αSyn deposits (LBs and LNs) formed in the nigrostriatal pathway, led to selective dopaminergic neurodegeneration in the SNpc and drove the appearance of motor deficits (Luk et al., 2012).

1.6.3 Neuroinflammation

Neuroinflammation is by definition the immune reaction upon an insult of the CNS (Streit et al., 2004). The involved cell types are microglia, astrocytes, oligodendrocytes, and oligodendrocyte precursor cells. The CNS was considered to be an immune-privileged site due to the blood brain barrier, however, even though delayed, the adaptive immune system does also play its part (Wraith and Nicholson, 2012). Nevertheless, microglia are the key effector cells of neuroinflammation (Ransohoff et al., 2015). They are the first responders to brain injuries and insults and phagocytic properties (Bilbo and Stevens, 2017).

McGeer and colleauges were the first to describe reactive microglia and infiltrating lymphocytes in the SN of PD patients (McGeer et al., 1988). Increased expression of various microglia associated markers, and cytokines, have since been described in the midbrain (Boka et al., 1994; Croisier et al., 2005; Hunot et al., 1999; Imamura et al., 2003; McGeer et al., 1988), and in plasma, serum and cerebrospinal fluid, respectively, in PD patients (Brodacki et al., 2008; Lindqvist et al., 2013; Mogi et al., 1994).

The exact mode of action of the neuroinflammatory response in PD is not fully understood. Since microgliosis has been described in iRBD patients, which suggests that the response precedes PD motor symptoms and is involved in the disease progression early on (Tansey and Romero-Ramos, 2019). While different environmental factors have been proposed to be at the origin of neuroinflammation (Tansey and Goldberg, 2010), the main culprit are toxic forms of αSyn. The molecular structure is key concerning which receptor it binds. Oligomeric αSyn is exclusively recognized by the toll-like receptor 2 (TLR2) (Kim et al., 2013), while fibrillar forms are recognized by TLR4 (Fellner et al.,

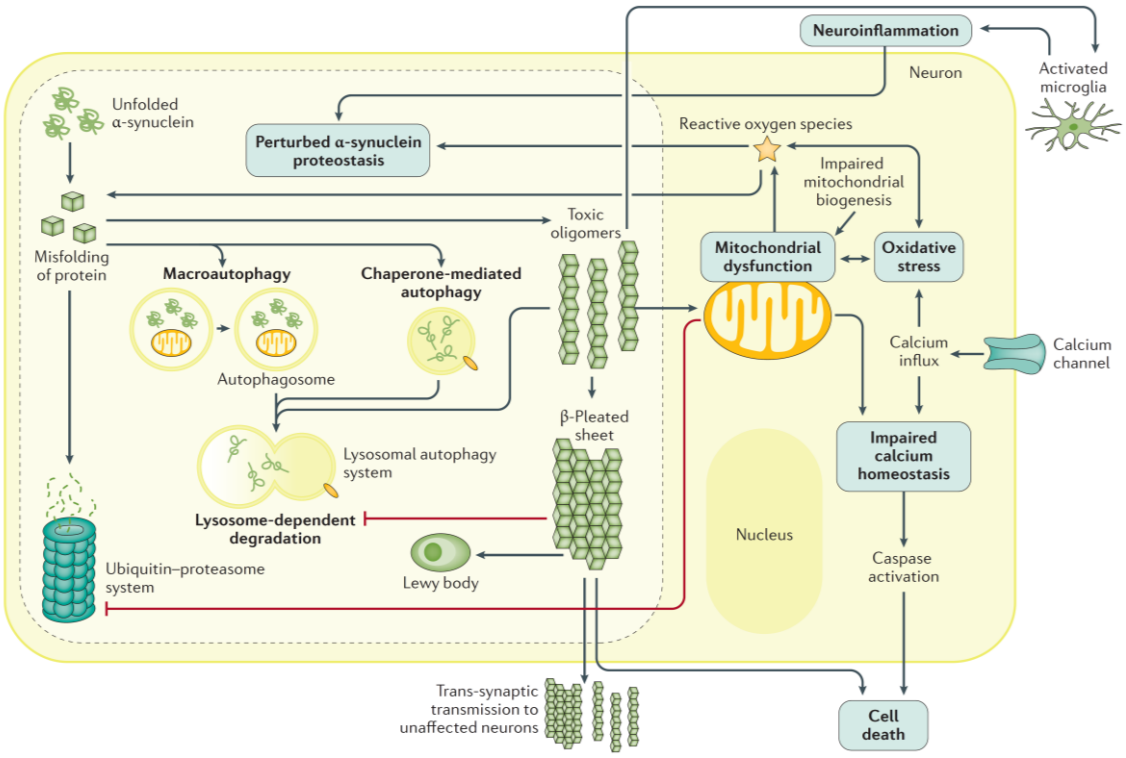

Figure 4 | Different pathogenic mechanisms of PD (from Poewe, 2017)

2013). Using transgenic models overexpressing αSyn, microglia was activated early on (1-month) and remained reactive until 14 months of age (Watson et al., 2012). Other models confirmed that αSyn led to microglia activation (Wilms et al., 2009) and preceded neurodegeneration (Duffy et al., 2018; Whitton, 2007; Wu et al., 2002). Thus, there is mounting evidence that microglia response is directly implicated in the pathogenesis of PD.

1.7 PD in the periphery

1.7.1 Body-first vs Brain-first hypothesis

In recent years, the hypothesis that PD originates in the periphery has gained momentum, supported by pathological αSyn in sympathetic, parasympathetic ganglia and ENS (Hilton et al., 2014; Shannon et al., 2012; Stokholm et al., 2016; Van Den Berge et al., 2019). However, neuropathologically not all patients fit those criteria as some do not, for instance, show pathological changes in the dorsal motor nucleus of the vagus (Borghammer and Van Den Berge, 2019; Kalaitzakis et al., 2008). The debate on body-

first versus brain-first is controversial and discussions often take on a dichotomous format. Similar to what is observed clinically, one should though consider that there are different disease scenarios depending on the site of onset and progression (Borghammer and Van Den Berge, 2019).

The brain-first scenario, appears to be restricted to mainly familial rare forms of the disease with the exception of PD patients carrying *GBA* mutations or *SNCA* multiplications (Borghammer and Van Den Berge, 2019). In a body-first scenario, there are measurable damages in the peripheral nervous system (PNS) preceding those in the CNS (**Figure 5**). It has to be noted that this type of scenario is especially associated with RBD. Different *in vivo* imaging studies showed that in RBD-positive cases the nigrostriatal pathway is in most cases still intact, while there is autonomic denervation (Bauckneht et al., 2018; Knudsen et al., 2018). Changes in the LC are increased in PD patients with RBD, while dopamine levels are only reduced 20-25% as compared to 50% in H&Y I-II stage PD patients (Bauckneht et al., 2018; Knudsen et al., 2018).

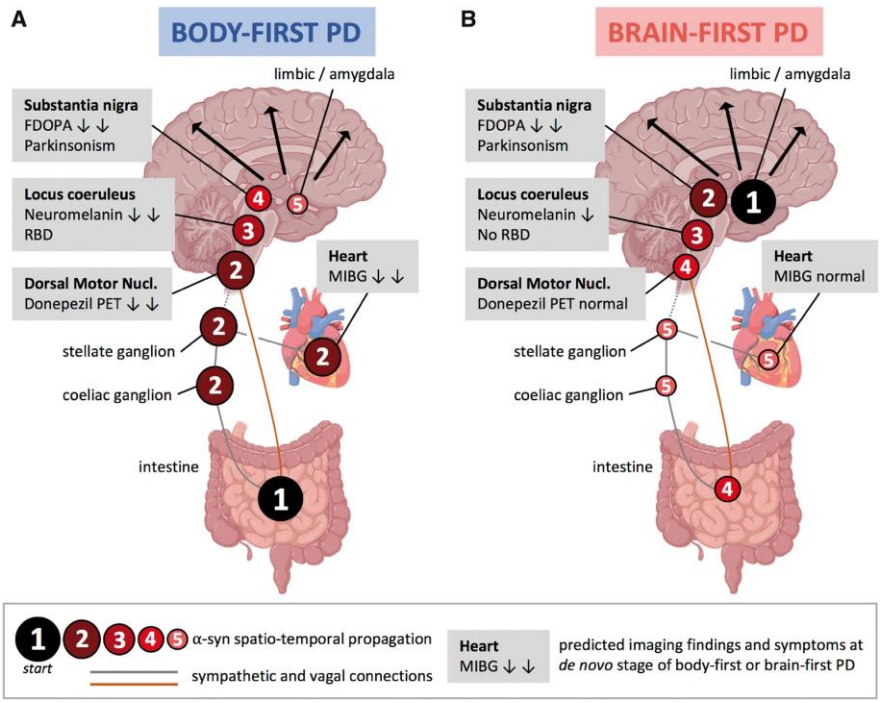

Figure 5 | Body-first versus Brain-first hypothesis depicting two contrasting spreading routes

(Figure 1 from Horsager et al., 2020)

There is unfortunately only a limited number of studies (Leclair-Visonneau et al., 2017; Sprenger et al., 2015; Vilas et al., 2016) that investigated αSyn pathology between RBD positive and RBD negative PD patients in the periphery. Nevertheless, αSyn pathology in the colon (ENS) and the submandibular glands is more frequent in RBD positive PD patients (Borghammer and Van Den Berge, 2019).

In summary, there is a difference between RBD-positive and RBD-negative PD patients. The body-first scenario is especially seen in RBD-positive idiopathic PD patients, where the gut is potentially the site of onset (**Figure 5**) (Lionnet et al., 2018).

1.7.2 The gut-brain axis in the pathogenesis of PD

Even though the involvement of the gut and the propagation via the preganglionic fibers of the vagus nerve (**Figure 6**) to lower brainstem regions of the CNS is still debated (Lionnet et al., 2018), there is mounting evidence that at least a subset of PD cases originate in the gut.

Constipation is a progressive non-motor symptom observed in at least 30% up to 80% of PD cases (inter-study variations). It was considered to be a symptom of progressed PD, but today it is known that it is also a pre-clinical/prodromal symptom. Further, constipation and early enteric Lewy pathology coincide (Abbott et al., 2007).

The myenteric and submucosal plexuses of the gut are greatly innervated by the vagus nerve (Hopkins et al., 1996). Therefore, Braak and colleagues proposed that based on their αSyn aggregation findings in the DMV, αSyn potentially spreads from the ENS to the brain via the preganglionic fibres of the vagus nerve. Lewy pathology in the ENS has been described in post mortem studies (Braak et al., 2006; Wakabayashi et al., 1988, 1990), which also led to a degree of criticism regarding the dynamics of Braak's hypothesis. Multiple studies (Hilton et al., 2014; Shannon et al., 2012; Stokholm et al., 2016) were able to show that Lewy pathology can be detected in the ENS years prior to the first motor symptoms. Epidemiological studies also showed that the risk to develop PD was reduced in people whom have undergone a truncal vagotomy (Liu et al., 2017; Svensson et al., 2015), supporting the gut-brain axis scenario in PD.

Truncal vagotomy but also hemivagotomy in mice has also been shown to prevent αSyn from spreading to the DMV (Kim et al., 2019; Pan-Montojo et al., 2012). Without the vagotomy, both models, exhibited αSyn aggregation in the SNpc after 3 months (Kim et al., 2019; Pan-Montojo et al., 2010). While, Kim and colleagues used a model based on intramuscular injection of preformed αSyn fibril into the gut wall, Pan-Montojo showed that chronic low-grade exposure to the environmental toxin rotenone causes αSyn to aggregate and the subsequent spreading to the CNS. Interestingly, it was shown that a product from commensal *E. coli*, the amyloidogenic protein Curli, can also reproduce these observations (Chen et al., 2016; Sampson et al., 2020).

The gut represents a gateway to the environment. Changes in the gut and its microbiome in PD have been documented (Boertien et al., 2019; Keshavarzian et al., 2020; Romano et al., 2021). The interaction of environmental factors and the gut microbiome are a potential risk factor in PD. This provides potentially novel therapeutic targets to mitigate PD progression.

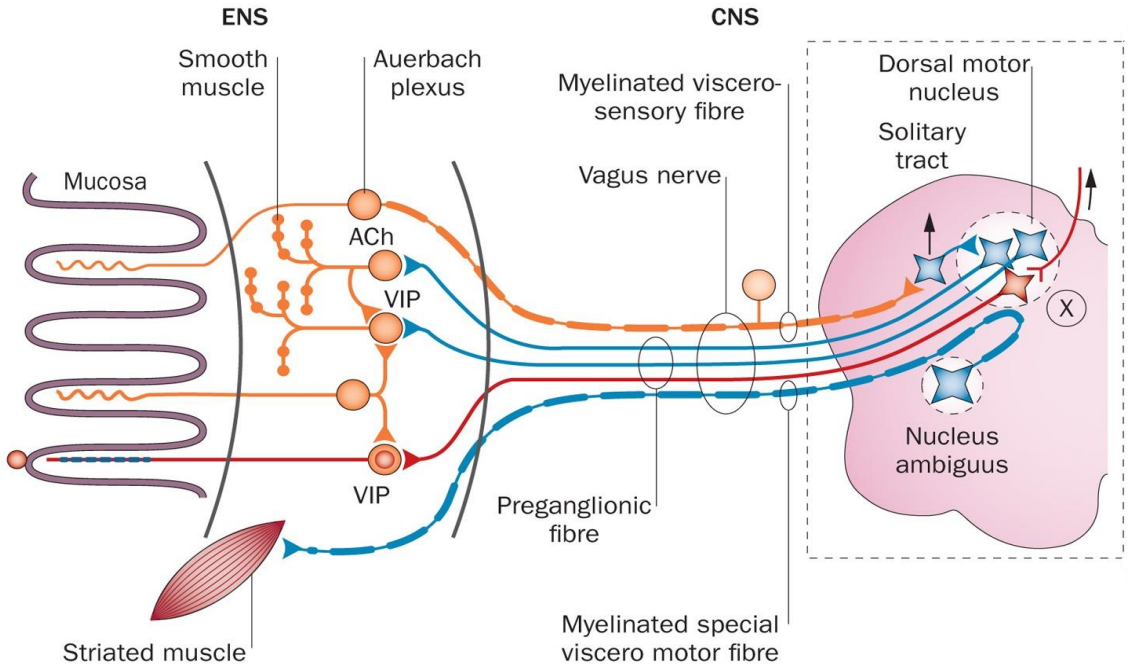

Figure 6 | Representative vagal route of the gut-brain axis

(adapted Figure 1 from Klingelhoefer and Reichmann, 2015)

2 The gut microbiome and PD

2.1 From Leeuwenhoek to multi-omics: defining the microbiome

"*I then most always saw, with great wonder, that in the said matter there were many very little living animalcules, very prettily a-moving.*"

Antonie van Leeuwenhoek

The microbiome research as it is known today, started with the first handcrafted microscope by Leeuwenhoek at the end of the 17th century (**Figure 7**). In his letter to the royal society in 1683, he described what he called animalcules, known today as microbes, from his and others' saliva. He went on to compare oral and fecal microbiota and observed body site differences as well as differences between healthy and diseased subjects. He also discovered biofilm formations. The first indication of complex interactions within the microbial world. Fast forwarding to 1853, Joseph Leidy published the book what many consider the origin of microbiota research: A flora and fauna within living animals. This was followed by works of Pasteur, Escherich and Metchnikoff. They all believed that understanding the endogenous microbiota and its interaction with the host were essential in health and disease. At the end of the 19th century Koch postulated the causative relationship between microorganisms and diseases (Berman, 2019). This led researchers to focus on single disease-related microorganisms and their eradication. However, environmental microbiology at the time introduced a paradigm shift and

presented the concept of beneficial host-microbe interactions. More than 50 years later, the concept of beneficial interactions was translated to humans. Ben Eiseman and colleagues treated four patients suffering from a *C.difficile* infection using the fecal microbiota transplant (FMT) approach. Later it was shown that normal physiology lacking in germ free mice could be reconstituted after FMT. It was not until the development of novel cultivation and molecular biology techniques though that the field saw its next big leap. Today, researchers perform complex high-throughput sequencing to understand the crucial roles that microbial communities have in health and disease.

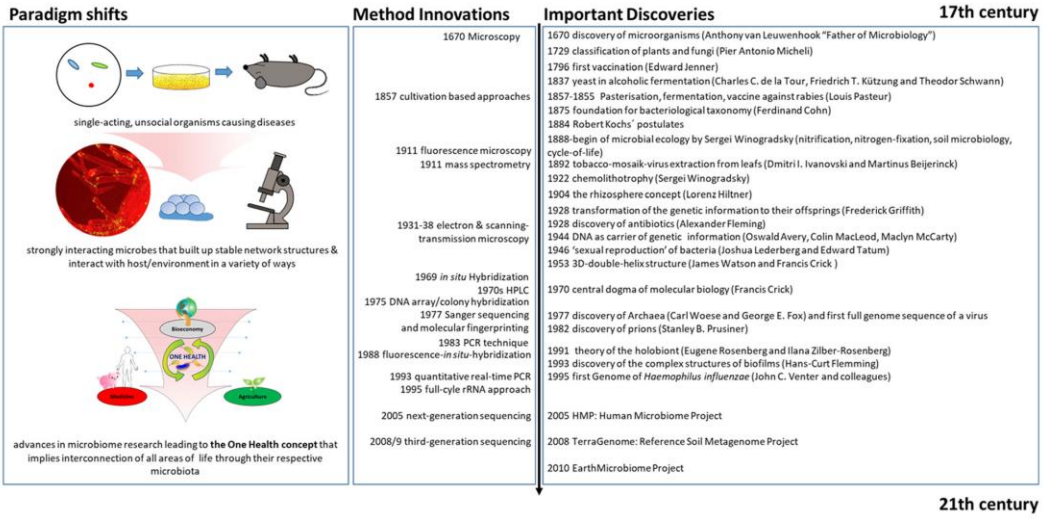

Figure 7 | The history of microbiome research (Fig. 1 from Berg et al., 2020)

Microbial communities were defined as a collection of microorganisms occupying a specific niche. The term microbiome was first introduced in 1988 by Whopps and colleagues. It is the combination of "micro", defining a characteristic microbial community, and "biome", a well-defined habitat with distinct physio-chemical properties. Many different definitions followed. The most cited today is by Lederberg describing microbiomes as communities of commensal, symbiotic, and pathogenic microorganisms within a body or other environment (Berg et al., 2020). Its members are bacteria, archaea, fungi, algae and small protists. The status of phages, virus or other mobile non-living particles is controversial. Some researchers therefore differentiate between microbiome and microbiota. For the latter usually only living microorganisms such as bacteria and archaea are considered. The microbiome encompasses all genomes of both living and non-living organisms. Non-living organisms, such as phages and

viruses, are considered to be part the “theatre of activity” including the whole spectrum of molecules produced by the microbiota.

2.2 The gut microbiome in health and disease

Microbiomes in mammals are present in and on different body sites. In humans functionally relevant microbiota/microbiomes are found on skin, in different mucosal passages, in the lung and, the most prominent, in the gut. Under healthy conditions, microbiomes are large communities of different microbes, both symbiotic/commensal and pathogenic, occupying these different sites, forming stable communities which are resistant to external pathogens. Here, the focus will be kept on the gut microbiome, and its implications in health and disease mechanisms.

On a cellular level the microbiome is estimated to encompass 100 trillion microbes, exceeding 10 times the count for cells in the human body. This number is made of approximately 500-1000 different microbial species. The species are however not common to every person. A study, investigating the collective human gut microbiota make up, suggests that there are more than 35,000 different species (Frank et al., 2007). On the phylum level, the gut microbiome is very much conserved between people containing 6 different phyla: *Firmicutes*, *Bacteroidetes*, *Actinobacteria*, *Proteobacteria*, *Fusobacteria*, and *Verrucomicrobia*. The most common phyla *Firmicutes* and *Bacteroidetes* and their shifting ratios used to serve as a disease indicator. Most disease relevant changes are seen in the colon, which makes up about 70% of the entire human microbiome.

The microbiome has essential functions contributing to the host physiology. The gut microbiome is involved in the development and maturation of both the mucosal and systemic immune system. The mucosal immune system requires to function in two seemingly uncoupled ways: on one hand it needs to tolerate the mucus resident microbiota, while keeping them from overgrowing and entering systemic sites. Besides that, the gut microbiota does pose a physical barrier to competitive exogenous pathogens. The commensal microbes have therefore developed different strategies such as production of various bacteriocins, bacteriophage deployment or abortive

infection (Hou et al., 2022). Another crucial role of the indigenous microbiome is the structural and functional development and maturation of the intestinal peristalsis, surface and barrier, and the regenerative capacity (Sekirov et al., 2010). The microbiome also influences drug metabolism and lastly, specialized microbes aid the host in digesting foods, such as the fermentation of non-digestible substrates e.g. dietary fibres (Sekirov et al., 2010). Latter promotes the growth of specialized microbial species synthesizing short-chain fatty acids (SCFA), which are involved in glucose and energy homeostasis, gluconeogenesis, cholesterol metabolism and can regulate inflammatory responses (Jovel et al., 2018; Valdes et al., 2018). Even though the microbiome is involved and crucial for drug (e.g. antibiotics) and diet metabolisms, they and others (e.g. heavy metals and pesticides) are strong modulators of the microbiome and can cause it to shift. Such a shift is referred to as dysbiosis and is observed in various disorders/diseases. Additionally, dysbiosis can also be a result of enteric bacterial or viral infections (Sekirov et al., 2010). These compositional and consequently functional changes have been associated with cardiovascular diseases, chronic liver and kidney diseases, diabetes, inflammatory bowel diseases, respiratory diseases, cancer and brain disorders such as PD (Sekirov et al., 2010).

2.3 Microbial changes in PD

Braak postulated that toxins or pathogens could trigger idiopathic PD in the gut (Braak et al., 2003b). The interaction of external toxins/pathogens with αSyn in the ENS ultimately leads to misfolded oligomeric toxic forms of the protein, which would subsequently propagate to the CNS via the vagus nerve (Braak and Del Tredici, 2017; Braak et al., 2003b). Otherwise such factors could also lead to physiological changes in the gastrointestinal tract (GIT). The GIT harbours the most complex “organ” of the human body contributing to crucial physiological functions. Changes to its composition can have disease altering consequences, such as inflammation and increased gut barrier permeability allowing toxins and pathogens to access the ENS more easily (**Figure 8**).

In many studies from the USA, Northern, Western and Eastern Europe, and Asia (see Table 3 in Keshavarzian et al., 2020) the gut microbial composition in PD patients has been shown to be significantly altered compared to healthy controls. Even though

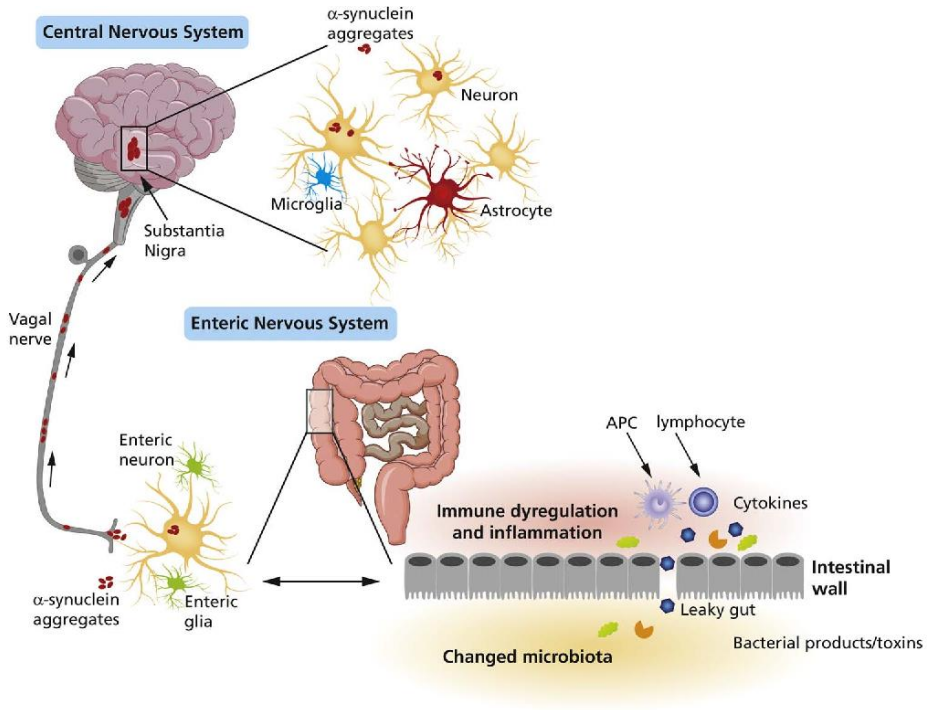

Figure 8 | Proposed gut to brain spreading of aSyn after environmental impact and dysbiosis

(Figure 1 from Perez-Pardo et al., 2017)

the studies show differences between each other for certain taxa, a core set of taxa has emerged whose abundance differs significantly between healthy controls and PD patients (Boertien et al., 2019; Keshavarzian et al., 2020)(**Table 4**). Observed α-diversity changes can be explained by a significant decrease of the most abundant taxa in healthy conditions and an increase of usually low abundant species (Romano et al., 2021).

Many of the decreased taxa, such as *Prevotella*, *Faecalibacterium* or the *Lachnospiraceae* family, in PD patients are SCFA-producing bacteria. As mentioned before, SCFAs are involved in various homeostatic functions. Consequently, reduced SCFA levels have been associated with constipation, leaky gut and increased enteric and systemic inflammation (Keshavarzian et al., 2020). Sampson and colleagues (Sampson et al., 2016) showed that in germ-free mice overexpressing human αSyn colonized with a PD microbiota low in SCFA-producing bacteria would exacerbate motor impairments. (Sampson et al., 2016).

Genera increased across most PD microbiome studies are *Lactobacillus*, *Bifidobacterium* and *Akkermansia* (Boertien et al., 2019; Romano et al., 2021)(**Table 4**). Interestingly, *Lactobacillus* and *Bifidobacterium* are considered beneficial for human

health. While, the enzymatic interaction with Levodopa provides a potential explanation for the vast increase in *Lactobacillus* (van Kessel et al., 2019; Maini Rekdal et al., 2019), the role in PD for both species needs to be further elucidated.

Table 4 | Most common microbial changes in PD patients (Boertien et al., 2019)

Phylum	Family	Genus	Number of citations (statistically significant)	Increased abundance (statistically significant)	Decreased abundance (statistically significant)
Verrucumicrobia	**Verrucomicrobiaceae**		9 (6)	9 (6)	0 (0)
Bacteroidetes	**Prevotellaceae**		8 (3)	0 (0)	8 (3)
Firmicutes	**Lactobacillaceae**		7 (6)	5 (4)	2 (2)
Verrucomicrobia	Verrucomicrobiaceae[1]	*Akkermansia*	6 (6)	6 (6)	0 (0)
Actinobacteria	Bifidobacteriaceae	*Bifidobacterium*	6 (4)	5 (4)	1 (0)
Firmicutes	**Lachnospiraceae**		6 (5)	1 (1)	5 (4)
Verrucomicrobia			5 (4)	5 (4)	0 (0)
Firmicutes	Clostridiaceae	*Faecalibacterium*	5 (3)	0 (0)	5 (3)
Bacteroidetes	Prevotellaceae	*Prevotella*	5 (1)	0 (0)	5 (1)
Proteobacteria	**Enterobacteriaceae**		5 (4)	4 (4)	1 (0)
Firmicutes	Lactobacillaceae	*Lactobacillus*	5 (5)	4 (4)	1 (1)
Actinobacteria	**Bifidobacteriaceae**		5 (3)	4 (3)	1 (0)
Firmicutes	Lachnospiraceae	*Roseburia*	4 (4)	0 (0)	4 (4)
Firmicutes	**Enterococcaceae**		4 (4)	3 (3)	1 (1)
Firmicutes			4 (3)	1 (1)	3 (2)
Bacteroidetes			4 (3)	2 (1)	2 (2)
Firmicutes	**Erysipelotrichaceae**		4 (3)	2 (2)	2 (1)
Firmicutes	**Ruminococcaceae**		4 (1)	2 (1)	2 (0)

Akkermansia, consistently increased in PD patients, has also been associated with human health. However, under neurodegenerative conditions, concerns have been raised to use *A. muciniphila* as therapeutic probiotic (Hazards (BIOHAZ) et al., 2020). Based on animal studies, enteric dysbiosis with increased abundance of the mucin degrading *A. muciniphila*, due to e.g. fibre deprivation, has been shown to cause significant colonic mucus erosion, drier stools, reduced numbers of goblet cells, and gut barrier integrity loss (Romano et al., 2021). Intriguingly, such conditions are seen in patients with constipation, one of the most common non-motor symptoms of PD. The methanogenic archaeon *Methanobrevibacter*, is also found in people with constipation. Two recent studies (Li et al., 2019; Romano et al., 2021) have reported increased *Methanobrevibacter* in PD patients, suggesting that methane production is increased leading to greater intestinal transit times due to methane-induced decreased peristaltic movements (Triantafyllou et al., 2014; Vandeputte et al., 2016).

It is yet to be answered if microbial changes are involved in the onset or if they are a consequence of the disease. Evidence suggests (Keshavarzian et al., 2020) that changes to the microbiome do at least contribute to the disease. For example, specialized Gram-negative and Gram-positive bacteria can produce and secrete amyloid proteins. These proteins have similar molecular tertiary structure as seen in Tau, PrP^{Sc}, β-amyloid or αSyn. Under physiological conditions, the gut microbiota makes use of these amyloids to enhance bacterial adhesion, colonization and biofilm formation. Additionally, as shown for e.g. β-amyloid or αSyn, bacterial amyloids have cross-seeding abilities of other amyloid protein. The best described amyloidogenic bacterial protein is Curli. It is predominantly expressed in *Escherichia coli* (*E. coli*) and *Salmonella typhimurium*, and it is implicated in the bacterial colonization and biofilm formation (Chapman et al., 2002). Both E. coli and S. typhimurium belong to the Enterobacteriaceae family, which is associated with faster progression and a more severe, non-tremor-dominant, motor phenotype (Klingelhoefer and Reichmann, 2015). Such a phenotype is additionally associated with higher loads of αSyn aggregates in the ENS (Klingelhoefer and Reichmann, 2015). This is potentially due to seeding ability of Curli, which has been shown *in vitro* and *in vivo* to promote αSyn aggregation (Chen et al., 2016; Johansson et al., 2011; Sampson et al., 2020).

2.4 Diet and PD

Diet is a strong modulator of gut microbiota composition. As previously elaborated, such changes could have direct implications on the onset or progression of PD. Various studies (reviewed in Agim and Cannon, 2015; Erro et al., 2018; Seidl et al., 2014) investigated the direct link to different nutrients such as vitamins and fats. While a few associations between individual nutrients have been confirmed, the research interests are shifting towards the disease relevant impact of complex dietary patterns.

Higher intake of complex carbohydrates or dietary fibre from plant-based diets has been associated with a decreased risk for disease overall (O'Keefe, 2019a, 2019b). Therefore, in PD, a Mediterranean diet richer in vegetables, fruits, nuts, whole grain, and healthy fats has been proposed as a therapeutic strategy to mitigate disease

progression (Alcalay et al., 2012). Functional comparative metagenomics analysis of rural “hunter-gatherer” compared to “westernized” urban gut microbiomes has shown significant gene expression differences for carbohydrate to SCFA fermentation related genes (Rampelli et al., 2015). A “western style” diet, with low amounts of fibre and high amounts of saturated fats and simple carbohydrates, has been associated with generally altered gut microbiomes and many different diseases, such as constipation (Cotillard et al., 2013; Sonnenburg et al., 2016). These changes are consequently leading to low grade inflammation and gut barrier integrity loss (Keshavarzian et al., 2020). In different mouse models a low to no fibre intake was shown to alter the gut microbiome leading to lower abundance of fibre fermenting bacteria (Schroeder et al., 2018) and higher abundance of mucus foraging species like *A. muciniphila* (Desai et al., 2016) as also seen in PD. Hence, susceptibility to exogenous pathogens (Desai et al., 2016) and potentially endogenous bacterial toxins, e.g. Curli, increases.

PART II

Thesis Aims

PD is a complex multi-factorial disease. Over the past decade many different factors have been described that could potentially contribute to the disease. Since 1997, about 20 PD-related genes have been described with only a few responsible for hereditary PD cases. The majority of PD cases are of idiopathic origin where age is the dominant risk factor. Aside from latter, exposure to various environmental and lifestyle factors such as diet for instance in the onset and progression of the disease has gained momentum in recent years. Especially the impact on the gut microbiome consequently interacting with the host is of great interest. A lot more studies will be needed to understand the interactions of the different, and occasionally interacting, factors with the host in the disease development. Current observations indicate that under dysbiotic conditions, mucosal vulnerability and inflammation is increased. This allows various pathogens to invade the ENS and peripheral systems, corrupting physiological states, potentially triggering, and contributing to disease mechanisms.

Additonally, there has been a paradigm shift regarding pathogenic PD mechanisms in recent years. The αSyn centrist point of view has been challenged as sole driver of PD pathogenesis. Neurodegeneration was observed in the absence of αSyn inclusions, evoking additional mechanisms in the pathogenesis of PD. Neuroinflammation was evoked as potential contributor to PD pathogenesis. Especially early changes are believed to be microglia/neuroinflammation-driven.

Aim 1 | Does fibre deprivation in combination with the bacterial protein Curli increase αSyn pathology in the ENS?

The gut is a potential route of entry for different pathogens. Impacted by environmental or lifestyle factors such as diet, the microbiome shifts and the resulting dysbiosis would lead to physiological enteric and microbial changes allowing pathogens or commensal bacterial toxins to penetrate more easily into the mucosa and the ENS.

Our first aim was to characterize microbial changes due to a fibre poor diet, the related impact on mucosal barrier integrity and αSyn changes in the ENS upon exposure to the amyloidogenic bacterial protein Curli in genetically predisposed PD mouse model.

Therefore, we combined 16S rRNA amplicon sequencing and histology approaches to identify the combined effect of fibre deprivation and Curli exposure to investigate the potential αSyn aggregation in the ENS.

Aim 2 | Does fibre deprivation accelerate PD CNS pathologies in bacterial protein Curli exposed animals? Are already presenting motor deficits exacerbated?

It has already been shown that Curli interacts with αSyn (Chen et al., 2016; Sampson et al., 2020), leading to PD different PD pathologies *in vivo*. We were interested in the additional impact of a fiber-deprived diet.

As for our first aim, where we expected to see increased αSyn aggregation in the ENS, we wanted to investigate pathological changes of the nigrostriatal pathway after fibre deprivation and Curli exposure.

Using different immunofluorescent approaches we looked into changes of αSyn and dopaminergic neurons.

Aim 3 | Are other regions affected besides the nigrostriatal pathway after fiber deprivation and Curli exposure?

Braak's hypothesis states that αSyn propagates from the ENS to the lower regions on the CNS brainstem and then propagates in caudorostral manner throughout the brain (Braak et al., 2003b). Amongst the most reported and vulnerable nuclei in the lower regions are the DMV, LC and PPN. Extensive LB pathology and cell loss have been reported in the LC and PPN (Giguère et al., 2018; Hirsch et al., 1987; Jellinger, 1988; Oertel et al., 2019). Additionally, both regions innervate directly the SNpc (Bari et al., 2020; French and Muthusamy, 2018).

Hence, we expected to observe similar or greater changes in the LC and PPN as compared to the SNpc and the dorsal striatum. To analyse neuronal changes we stained for noradrenergic neurons in the LC using the tyrosine hydroxylase marker and for cholinergic neurons in the PPN using the choline acetyltransferase marker. Additonally, we looked into αSyn changes in both regions.

Aim 4 | Do intrastriatal injections of the archaeal compound 2-hydroxypyridine lead to PD-like pathologies?

Interaction mechanisms between host and microbes are, still today, elusive. Multi-omics approaches hold great promise in helping to decipher at least in parts this complex machinery. Our team developed a multi-omics pipeline where fecal samples from PD, iRBD and healthy controls patients were analysed on the DNA, RNA, protein and metabolite levels. Metabolomics results revealed a yet unknown metabolite, which was identified as 2-hydroxypyridine (2-HP).

Not much was known about that metabolite. Further analysis revealed a significant positive correlation with *Methanobrevibacter smithii.* The genus *Methanobrevibacter* is the most abundant archaeal taxa in the human gut microbiome (Tyakht et al., 2013) and was recently shown to be elevated in PD patients (Romano et al., 2021).

Further in-house in vitro models showed that 2-HP can lead to αSyn aggregation and increased cytotoxicity. Previously, a ring-fused 2-pyridone (tautomer of 2-HP) molecule (FN075) showed in vitro to interact with αSyn and to lead to different PD pathologies in vivo (Chermenina et al., 2015; Horvath et al., 2012; Kelly et al., 2021).

Our goal was to test whether 2-HP itself can lead to PD pathologies and confirm our in vitro findings. Therefore, we used a human αSyn overexpressing mouse model and injected 2-HP intrastriatally. We performed behaviour tests, and analysed αSyn and neuronal changes in different PD-relevant brain regions.

Aim 5 | Does neuroinflammation contribute to the neurodegenerative process?

Changes to the microbiome, especially regarding SCFA-producing bacteria and the resulting altered SCFA levels have been associated with neuroinflammation in PD models. Neuroinflammation, where microglia is the most important representative, has been proposed to actively participate in PD pathogenesis, since αSyn pathology does not always correlate with neuronal loss or clinical progression (Jellinger, 2009). Additionally, microglia have been shown to bind and even phagocytose abnormal forms of αSyn (Fellner et al., 2013; Janda et al., 2018; Kim et al., 2013).

To investigate this question, we used a seeding/spreading model, where preformed fibrils (PFF) are injected into the right striatum of wild-type mice. Previously, this model showed αSyn inclusions in dopaminergic neurons the SNpc 90 days post injection (dpi). So we set an early (13dpi) and a late timepoint (90dpi), since we hypothesized that microglia activity is an early event. We analysed different brain regions by immunohistochemistry using neuronal, αSyn and microglia associated antibodies.

Aim 6 | What is the molecular profile in the ventral midbrain and what is the translational relevance?

Immunohistochemistry analysis is very informative regarding regional morphological changes, but does miss dynamic and functional changes. Especially early changes preceding notable morphological differences are not visible using classical histological approaches. Especially microglia has been described to be a highly diverse and dynamic population with regional differences (Uriarte Huarte et al., 2021).

Hence, we used a microarray system to elucidate transcriptional changes in our seeding/spreading model, performed comparative analysis using meta-analysis data from literature and conducted a translational relevance assessment using the LCSB curated PD map.

PART III

Results & Publications

3 Pathogenic effects of fiber deprivation and Curli in Parkinson's disease

Kristopher J Schmit, Alessia Sciortino, Velma TE Aho, Pierre Garcia, Beatriz Pardo Rodriguez, Mélanie H Thomas, Jean-Jacques Gérardy, Irati Bastero Acha, Rashi Halder, Camille Cialini, Tony Heurtaux, Michel Mittelbronn, Manuel Buttini and Paul Wilmes

Submitted to Cell Press Community Review

Pre-print on bioRxiv (Different title: Dietary fibre deprivation and bacterial curli exposure shift gut microbiome and exacerbate Parkinson's disease-like pathologies in an alpha-synuclein-overexpressing mouse)

3.1 Preface

There is a long list of risk factors involved in the progression or even the onset of Parkinson's disease. The "body first" hypothesis has gained momentum in recent years, in which amongst others a dysbiotic gut microbiome and the role of the microbiome-gut-brain axis was proposed as a potential key modulator of disease progression. An adapted diet is crucial for the maintenance of a balanced, well-functioning gut microbiome. Hence, a diet altering gut microbial diversity and abundance could increase disease risk by facilitating host-pathogen interactions.

To investigate such disease promoting events, we developed a multi-step protocol:

a. A fibre deprived diet causing a microbial shift leading to colonic mucus erosion and decreased barrier function
b. Exposure to the bacterial amyloid protein Curli, which can act as seed for alpha-synuclein aggregation
c. An alpha-synuclein overexpressing mouse model

The following manuscript is currently in preparation to be submitted to the community review service in Cell Press and figures already as pre-print on bioRxiv. The pre-print version is slightly different to the current version, due to the Cell Press formatting guidelines.

The results presented in this manuscript are part of the main project of my doctoral thesis work entitled "CoMiMePa –A combinatorial microbiome-driven mechanism for the pathogenesis of Parkinson's disease" for which I received the AFR Individual PhD grant (Application ID: 12515776) from the national funding agency FNR.

I was involved in all and even led most aspects of the study, starting from the study design, the animal ethics protocol, the experiments, the analyses (except for the 16S rRNA gene amplicon sequencing), generation of figures and tables, and interpretations of the results. Further, I wrote the manuscript and together with my co-supervisor Paul Wilmes I am corresponding author for this publication.

Supplementary figures and table, and additional information not included in the published manuscript can be found in **Appendix A**.

3.2 Graphical abstract

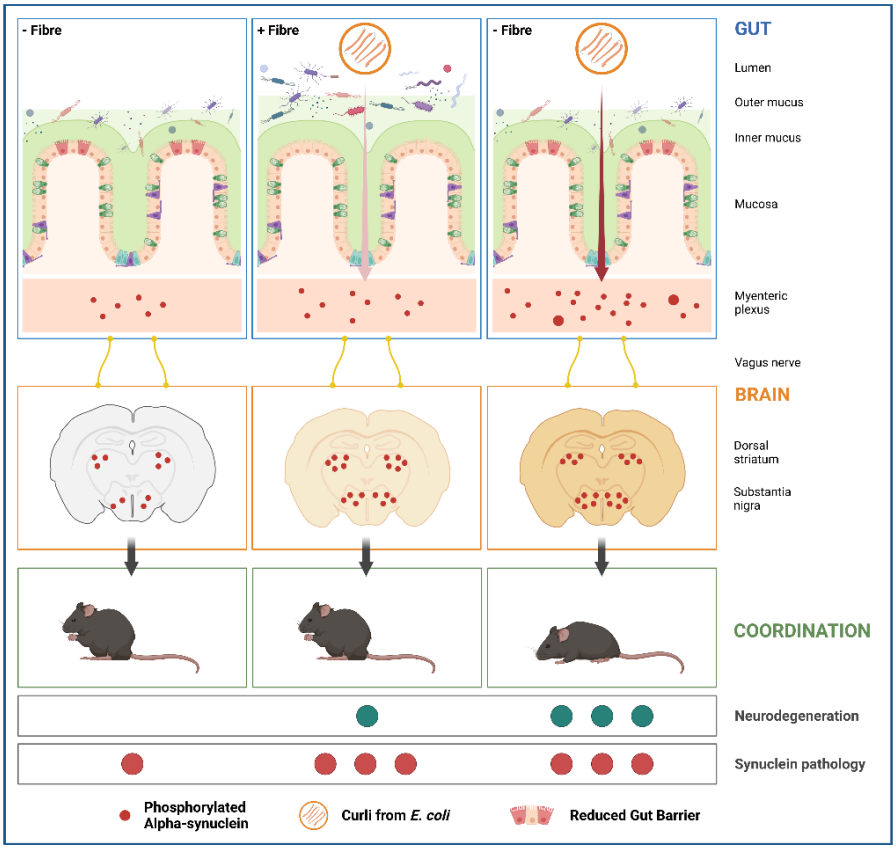

3.3 Publication

Title

Pathogenic effects of fiber deprivation and Curli in Parkinson's disease

Authors/affiliations

Kristopher J Schmit[1,2]*, Alessia Sciortino[1,2]†, Velma TE Aho[1]†, Pierre Garcia[1,2], Beatriz Pardo Rodriguez[1,2], Mélanie H Thomas[1,2], Jean-Jacques Gérardy[2,3], Irati Bastero Acha[1,2], Rashi Halder[1], Camille Cialini[2,4], Tony Heurtaux[2,5], Irina Ostahi[3], Eric C Martens[6], Michel Mittelbronn[1,2,3,4,6,7], Manuel Buttini[1,2]* and Paul Wilmes[1,7]

1. Luxembourg Centre for Systems Biomedicine, University of Luxembourg, Esch-sur-Alzette, 4362, Luxembourg
2. Luxembourg Center of Neuropathology, Dudelange, 3555, Luxembourg
3. National Center of Pathology, Laboratoire National de Santé, Dudelange, 3555, Luxembourg
4. Department of Cancer Research, Luxembourg Institute of Health, Luxembourg, 1526, Luxembourg
5. Department of Life Sciences and Medicine, University of Luxembourg, Esch-sur-Alzette, 4362, Luxembourg
6. Department of Microbiology & Immunology, University of Michigan Medical School, Ann Arbor, Michigan, 48109, USA
7. Faculty of Science, Technology and Medicine, University of Luxembourg, Esch-sur-Alzette, 4365, Luxembourg

Contact info

Correspondence: Kristopher J Schmit, kristopher.schmit@hotmail.com

Paul Wilmes, paul.wilmes@uni.lu

Summary

The microbiome-gut-brain axis has been proposed as a pathogenic route in Parkinson's disease (PD). Diet-driven dysbiosis and reduced gut barrier function may increase exposure of the enteric nervous system to toxic compounds thereby triggering PD. Amyloid bacterial proteins such as Curli can act as seed to stimulate enteric α-synuclein aggregation. Misfolded α-synuclein can subsequently propagate to and throughout the brain. Here, we studied if a combination of fiber deprivation and exposition to the amyloidogenic protein Curli could, individually or together, exacerbate the disease-related phenotype in both the enteric and central nervous system in a transgenic mouse model overexpressing wild-type human α-synuclein. We analysed the gut microbiome, motor behaviour, gastrointestinal and brain pathologies in these mice. Our findings show that both dietary and microbiome-derived factors can exacerbate PD-like pathologies in mice. Our results shed important insights on how combinations of diet and microbiome-born insults may trigger key disease processes along the gut-brain axis entailing implications for lifestyle management of PD.

Keywords

Parkinson's disease, lifestyle, fiber deprivation, dysbiosis, Curli, microbiome-gut-brain axis, α-synuclein

Introduction

Lifestyle and environmental factors contribute to a variety of chronic, degenerative diseases burdening socio-economic structures in an expanding and ever-ageing population (Council (US) et al., 2013; Nations). The incidence of Parkinson's disease (PD), the second most common neurodegenerative disease, has consistently increased over the last three decades (Dorsey et al., 2018) and is predicted to increase further (Yang et al., 2020). Of all current cases, only 5-10% can be attributed to heritable genetic factors alone (Poewe et al., 2017). For most cases, PD is a complex multi-factorial disease with genetic and environmental/lifestyle risk factors contributing to its onset and progression (Gorell et al., 2004). Environmental and lifestyle factors modulating PD risk and progression are exposure to different chemicals (e.g. pesticides), head trauma, physical activity, stress, smoking, and diet (Marras et al., 2019). Except for smoking and caffeine consumption, all other factors have been associated with increased risk of PD (Marras et al., 2019). In recent years, a growing body of evidence has put forward the importance of diet and its implications in PD progression. It has been proposed that a Mediterranean diet rich in fresh unprocessed foods, especially vegetables, reduces the risk for PD (Maraki et al., 2019). On the other hand, a "western" diet with low amounts of fiber, high amounts of saturated fats, and simple carbohydrates has been shown to increase risk for a variety of diseases, including PD (Hirschberg et al., 2019; Martínez Leo and Segura Campos, 2020) and is a strong modulator of the gut microbiome.

The contribution of dietary habits to the disease is only beginning to be understood (Nag and Jelinek, 2019). Functional comparative metagenomic analysis has shown that such a diet is associated with reduced gene expression related to complex carbohydrate fermentation (Rampelli et al., 2015). In different mouse models, low to fiber-free diets led to lower abundance of fiber fermenting bacteria (Schroeder et al., 2018) and higher abundance of mucus foraging species like Akkermansia muciniphila (Desai et al., 2016). Increased levels of Akkermansia muciniphila are consistently found in PD patients (Rosario et al., 2021) and they lead to mucus erosion in humans (Rosario et al., 2021) and mice (Desai et al., 2016). Consequently, mucus thinning has been linked to increased pathogen susceptibility (Desai et al., 2016).

While such pathogens typically originate from infectious agents (Nerius et al., 2020), there is evidence that they can also originate from commensal bacteria of the resident gut microbiome, and contribute to disease (Miller et al., 2021). Commensal bacteria occupy the outer mucus layer of the colon and can form biofilms (Johansson et al., 2011, 2013). Even though there is no consensus on biofilm formation in the healthy gut (Tytgat et al., 2019; de Vos, 2015), it has been observed in a variety of gastrointestinal disease scenarios. One biofilm forming microbial family, Enterobacteriaceae, has been associated with severity of a specific subtype of PD (Scheperjans et al., 2015). Amongst the most prominent biofilm forming species are Escherichia coli (E. coli) and Salmonella, which both express Curli, a major biofilm component (Miller et al., 2021). Curli is an amyloidogenic protein, which has structural and physiological similarities to β-amyloid and α-synuclein (αSyn) (Barnhart and Chapman, 2006; Chapman et al., 2002), and it has been shown to act as a seed for αSyn aggregation in vitro and in vivo (Chen et al., 2016; Sampson et al., 2020). Alpha-synuclein aggregations in the gut have been observed in many PD patients (Qualman et al., 1984; Wakabayashi et al., 1988, 1990, 1993). Braak and colleagues proposed that αSyn aggregations in the enteric nervous system (ENS) precede those in the lower brainstem regions of the central nervous system (CNS), and that, subsequently, αSyn propagates retrogradely in a "prion-like" manner, via the vagus nerve, to and throughout the brain (Braak et al., 2006).

Because PD is a multifactorial disease and because environmental factors modulating disease act in combination, we wanted to investigate the effect of dietary fiber deprivation and bacterial Curli exposure, individually or combined, on a human Syn overexpressing transgenic mouse. Our treatment protocol was to first prime the naïve untreated microbiome with a "westernized" fiber deprived diet (Desai et al., 2016), followed by exposure to Curli producing bacteria (Chen et al., 2016). We analysed the mice at gut microbial, behavioural, gastrointestinal, and neuropathological levels. Overall, transgenic, but not wild-type mice, were susceptible to the different challenges. In transgenic mice, our findings suggest that even though αSyn overexpression was largely responsible for the observed behavioural impairments, the fiber deprivation caused dysbiosis, with increased levels of *Akkermansia* spp. and *Bacteroides* spp.,

sparked mucus erosion, and favoured enteric pathogen accessibility. This resulted in exacerbated PD-like pathologies, such as αSyn aggregation in the ENS, nigro-striatal degeneration, and αSyn aggregation in the CNS, which further exacerbated impaired coordinative skills of our transgenic mice. We believe that our study sheds light on how a combination of internal and external pathogenic factors can differentially contribute to PD-like pathologies in the CNS and ENS. Therefore, our findings may have important implications for lifestyle adjustments that could mitigate PD.

Results

Thy1-Syn14 overexpress αSyn in brain and gut with regional differences

The mouse model used in this study was created by Kahle et al., 2001. It overexpresses human wild-type αSyn under the transcriptional control of the neuron-specific Thy1 promotor, and carries 13 copies of the transgene (Kahle et al., 2001). The model has so far not been fully described in the literature, and only protein levels in bulk brain tissue have been reported (Kahle et al., 2001). Thus, determining baseline expression and protein levels of αSyn in different CNS regions and in the gut was crucial for the subsequent interpretation of data generated in our study.

In the CNS, we focused on ventral midbrain and dorsal striatal structures using RT-qPCR for gene expression, and Western blot for protein level quantifications. We focused on both the differences between genotypes and the PD-relevant brain regions (dorsal striatum and ventral midbrain). First, we saw that gene expression levels for the murine αSyn (Snca) gene (Figure 1A, left panel) did not change between genotypes, but were significantly different ($p < 0.0001$) between the ventral midbrain and dorsal striatum. On the other hand, for the human transgene of αSyn (SNCA), (Figure 1A, right panel), we were only able to detect a signal in transgenic (TG) mice and those levels did not differ significantly between regions. In particular, we saw similar protein profile changes for total αSyn protein levels. To measure total αSyn protein levels, we used a pan-αSyn antibody that detects both murine and human αSyn. We observed significant differences between genotypes in the dorsal striatum and the midbrain. For transgenic mice, we measured a 2.91-fold increase ($p = 6.67E-4$) in the dorsal striatum and a 6.67-fold increase ($p = 6.67E-4$) in the ventral midbrain compared to their wild-type littermates (Figure 1B). However, αSyn protein levels were significantly higher in the dorsal striatum compared to the ventral midbrain (WT: $p = 1.52E-2$; TG: $p = 1.55E-4$; Figure 1B).

Next, we checked the αSyn expression profile in the colon. We split the colon into proximal and distal parts, and measured both Snca and SNCA expression levels via RT-qPCR. We observed that the levels for Snca and SNCA were much lower compared to those in the CNS (Figure 1C). This is most likely due to the much lower density of neurons in whole colon compared to e.g. ventral midbrain tissue. In the colon, only about 1% of

all cells are neurons (Drokhlyansky et al., 2020), whereas ventral structures of the midbrain (e.g. Substantia Nigra and Ventral Tegmental Area), comprising several populations of dopaminergic neurons, have a roughly estimated proportion of 15-20% neurons (Keller et al., 2018; Murakami et al., 2018; Zhang et al., 2007, 2012). Nevertheless, we observed that SNCA was only expressed in transgenic mice, and Snca was expressed at significantly different levels between proximal and distal colonic regions but not between genotypes (Figure 1C). Additionally, we stained for human αSyn and total αSyn (Figure 1D). The latter was expressed in both genotypes, while only the transgenic mice expressed human αSyn (Figure 1D, left bottom panel).

Based on our detailed analysis, the Thy1-Syn14 model presents an appropriate system to investigate the effect of environmental challenges directed toward the gut in the context of αSyn overexpression.

Thy1-Syn14 mice exhibit progressive motor deficits

PD-like motor deficits have been reported in a variety of mouse models of the disease (reviewed in Barber Janer et al., 2021). Here we assessed grip strength, hindlimb reflexes and coordination/movement which represent key phenotypic features associated with PD.

To assess grip strength, which is indicative of striatal dysfunction and neurotransmitter loss (Tillerson et al., 2002a), we used a simplified version of the inverted grid test (Tillerson and Miller, 2003; Tillerson et al., 2002b). We only measured the hanging time and, hence, assessed the simultaneous 4-limb grip strength. Grip strength gradually decreased as the TG mice aged (3M: 16.2 ± 9.88s, p = 3E-4; 6M: 11 ± 9.39s, p = 3E-4; 13M: 0.17 ± 0.41s, p = 4.86E-7; Figure 1E). Grip strength in wild-type littermates remained unchanged.

The hindlimb clasping or reflex test, an additional test assessing striatal dysfunction (Fernagut et al., 2004; Lieu et al., 2013), confirmed that the performance of TG mice decreased with age (3M: p = 9.33E-3; 6M: p = 5.7E-2; 9M: p < 0.0001; 13M: p = 4E-3; Figure 1F), while, in contrast, we did not observe an age-dependent motor impairment in the wild-type littermates.

Finally, we tested mice for coordination and fine motor skills with the adhesive removal test. Deficits in time for removal have been associated with loss of dopaminergic neurons (Fleming et al., 2013). We did not observe relevant motor deficits in young mice (3M and 6M; Figure 1G). At 9 and 13 months, we saw that both sensitivity (Time at touch, left panel), as well as coordination (Time at removal, right panel), were significantly delayed in TG mice (Time at touch – 9M: p = 7.57E-7, 13M: p = 0.057; Time at Removal – 3M: p= 0.016, 9M: p = 1.12E-6, 13M: p = 0.016).

Taken together, these data indicate that overexpression of human wild-type Syn drives progressive motor dysfunction in the Thy1-Syn14 mice.

Fiber deprivation induces PD-related microbiome changes

Onset and progression of PD, especially idiopathic PD, have been linked to various environmental factors (Chen and Ritz, 2018; Di Monte et al., 2002; Dick et al., 2007; Warner and Schapira, 2003), of which some, e.g. diet, impact the gut microbiome (Bernardo-Cravo et al., 2020; Singh et al., 2019). Changes in gut microbial composition in PD have been described extensively in humans (Boertien et al., 2019; Gerhardt and Mohajeri, 2018; Heintz-Buschart et al., 2018; Keshavarzian et al., 2015; Scheperjans et al., 2015; Shen et al., 2021; Unger et al., 2016), but also in different animal models (Gorecki et al., 2019; Sampson et al., 2016; Yan et al., 2021). Using 16S rRNA gene amplicon sequencing, our goal was to understand how the different exogenous challenges affected, independently or in combination, the gut microbiome in our mice. The exogenous challenges were:

- Diet; a normal fiber-rich (FR) or a fiber-deprived (FD) diet
- Gavages; PBS, Curli knock-out isogenic E. coli (ΔEC) or Curli producing E. coli (EC)

First, we looked on a large scale how the challenges affected microbial diversity. Overall, we saw that the fiber deprived (FD) diet and TG challenges both reduce inner-group diversity (alpha diversity), while we saw no changes due to the gavage challenges (Figure S1A). Alpha diversity was lowest at weeks 2 (WT: p = 0.045; TG: p = 6.1E-4) and 9 (TG: p = 9.7E-3) in FD challenged and more prominently so in TG mice (Figure 2A). We

made similar observations for beta diversity, where the diet challenge was the main driver (adonis p = 0.001) of dissimilarities between groups (Figure S1B, middle panel). However, in contrast to alpha diversity, the gavage challenges (adonis p = 0.001) appeared to contribute to microbial community structural shifts as well (Figure S1B, right panel). This observation might however be due to the PBS gavaged mice having all been FD challenged. Hence, solely the FD challenge drove the observed rapid shift in microbiome structure (Figure 2B). Already at week 2, the FD and fiber rich (FR) challenged groups, independent of the other challenges, formed two homogeneous clusters until the end of the experimental in-life phase. Such a shift is indicative of dysbiosis, an imbalance in the microbiome. Changes in the Firmicutes to Bacteroidetes ratio, the two most abundant phyla in the gut, can indicate an overall microbial and functional imbalance (Magne et al., 2020; Mariat et al., 2009). Our data particularly showed significant increases in the Firmicutes to Bacteroidetes ratio in FD challenged mice (Figure S2).

Next, we focused our analysis on taxa abundance changes at the genus level. We first subdivided the taxa according to their abundance into three separate groups (high, mid, and low; Figure S3). Analogous to what we had seen before, the diet challenge was the main driver of microbial abundance changes (Figure S3). Next, we focused our analysis on the most relevant genera in our data, which were *Alistipes, Faecalibaculum, Bacteroides, Lachnospiraceae NK4A136 group, Lactobacillus, Intestinimonas, Odoribacter, Colidextribacter, Lachnoclostridium, Lachnospiraceae UCG 006, Rikenellaceae RC9 gut group* and *Akkermansia* (Figure 2C). FD challenged mice had increasing or constantly higher levels in *Faecalibaculum, Intestinimonas, Odoribacter, Colidextribacter, Rikenellaceae RC9 gut group* and *Akkermansia*, and decreasing levels in *Lachnospiraceae NK4A136 group* and *Lactobacillus* over time (Figure 2C, Figure S3). *Alistipes, Bacteroides, Lachnoclostridium* and *Lachnospiraceae UCG_006* on the other hand saw fluctuations over time. They first increased in abundance before dropping back down to initial levels in FD challenged mice.

Additionally, when compared to data from PD patients (Table 3 in Boertien et al., 2019), FD challenged mice showed similar changes in *Akkermansia* (and its corresponding family and phylum), *Lachnospiraceae, Roseburia* and *Prevotellaceae*, while *Lactobacillaceae* and its genus *Lactobacillus* were inversely altered (Table S1).

Other taxa that are often reported to be dysregulated in human PD stool samples were not detected, e.g. *Bifidobactericaceae, Faecalibacterium* (*Clostridiaceae*) or *Enterobacteriaceae* (Table S1). When we checked for the relative abundance of *Escherichia coli*, the *Enterobacteriaceae* species that we gavaged with, it was barely detected in our 16S rRNA gene amplicon sequencing data (not shown).

In summary, the FD challenge caused reduced gut microbial diversity and similar shifts as seen in PD patients. To note are reduced levels of *Lactobacillus*, a genus with many known probiotic species (Heeney et al., 2018; Martín et al., 2013) and possible neuroprotective effects (Wang et al., 2021) as well as associated with gut barrier integrity (Blackwood et al., 2017), and *Lachnospiraceae NK4A136 group*, which inversely correlates with risk for PD or dementia (Stadlbauer et al., 2020). Additionally, *Lachnospiraceae NK4A136 group* and *Roseburia* are important butyrate producers, thus associated with gut barrier function (Plöger et al., 2012). Consequently, even though plasma endotoxin levels were not significantly increased in FD challenged mice (not shown), it is reasonable to assume that FD challenged mice had reduced gut barrier function. Despite pronounced inner group variability, Western blot analysis for ZO-1 indicated a loss in tight junctions for WT FR EC and TG FD EC mice, implying a further involvement of Curli in barrier integrity loss (Figure S4). Nevertheless, together with higher levels of the known mucin-foraging genera *Akkermansia* and *Bacteroides* (Desai et al., 2016; Tailford et al., 2015), the susceptibility for pathogenic agents were therefore most likely increased.

Microbiome-driven mucus erosion of the colon in fiber deprived mice

The mucus layers of the colon have two basic functions: the inner layer acts as physical barrier to prevent pathogens from reaching the gut epithelium, and the outer layer harbours commensal bacteria interacting with the host (Johansson et al., 2013). Increasing levels of mucin degrading bacteria, such as *Akkermansia muciniphila* and certain *Bacteroides* spp. (Desai et al., 2016), have been shown to cause mucus thinning and consequently enabling epithelial access for potential pathogens.

In our animals, we did not detect changes of the inner mucus layer (Figure S5A, B). This is most likely due to the extended treatment period triggering adaptational host

processes (Schroeder et al., 2018). Therefore, we focused on the outer mucus layer here. Our results clearly showed that the FD challenge caused significant ($p = 1.15E-12$) thinning of the outer mucus layer (Figure 3A). The layer thickness decreased extensively by 49.1 to 92.9% in the FD diet group (Figure 3B). Hence, the habitat for gut bacteria was reduced, which we expected to have direct consequences on microbial diversity. Therefore, we compared alpha diversity and mucus thickness using the Spearman's rank test (Figure S5C). We were specifically interested in dietary or transgene driven associations. While we only saw moderate dietary driven correlations (FR: $r=-0.47$, $p=0.051$; FD: $r=0.38$, $p=0.087$; Figure S5D, E), there was a significant positive correlation between alpha diversity and mucus thickness in TG mice (Figure 3C). This puts forth a potential higher risk under specific endogenous-exogenous interactions.

Bacterial Curli drives alpha-synuclein aggregation in the colonic myenteric plexus in fiber-deprived Thy1-Syn14 mice

αSyn aggregation in the gut has been observed in a substantial number of PD patients (Braak et al., 2006; Del Tredici and Braak, 2012; Del Tredici and Duda, 2011). To test for αSyn aggregation in the gut of our mice, we used an antibody directed against phosphorylated Ser129 αSyn (pS129-αSyn). This type of antibody is commonly used to detect αSyn aggregation in both the murine and human CNS (Vaikath et al., 2019) and ENS (Shannon et al., 2012; Stokholm et al., 2016). We quantified the pS129-αSyn positive deposits in protein gene product 9.5 (PGP9.5), a neuronal cytoplasmic marker (Sidebotham et al., 2001), positive ganglions of the myenteric (or Auerbach) plexus. Other pS129-αSyn positive deposits in the submucosal plexus and submucosa were irregular and mainly detected in TG mice. This did however not differ between the different treatment groups, and we could not determine the cell types involved using our approach.

First, the staining showed that both WT and TG mice had pS129-αSyn positive signals in ganglions of the myenteric plexus (not shown). The quantification of the area occupied showed that only TG mice exposed to the combined challenges of fiber deprivation and Curli-expressing E. coli (FD EC) had increased levels of pS129-αSyn in PGP9.5 positive ganglions (vs TG FD PBS: $p = 0.019$; vs WT FR EC: $p = 0.019$; vs TG FR EC:

p = 0.008; vs WT FD EC: p = 0.019; Figure 4). Besides having a greater area occupied, the average particle size of the αSyn aggregations appeared increased in TG FD EC challenged mice (representative images Figure 4).

We can sum up that even though, as seen above, the FD challenge in general led to an increased pathogen/pathobiont susceptibility, only TG EC challenged mice showed significantly higher levels of pS129-αSyn positive aggregates in the myenteric plexus of the colon.

Combination of bacterial Curli protein and dietary fiber deprivation challenges further exacerbate motor deficits in already impaired Thy1-Syn14 mice

The exposure to Curli, herein as well as in previous studies (Chen et al., 2016; Sampson et al., 2020), has been shown to lead to increased accumulation of abnormal αSyn in the gut. The subsequent spreading to and within the brain has been associated with the progression of motor impairment, as hypothesized by Braak and colleagues (Braak et al., 2003, 2006). In our aged TG mice, we did already observe motor performance deficits compared to their WT littermates. Therefore, we turned our interest to the exacerbation of motor performance deficits after the challenges, individually or in combination.

Three different tests were chosen to assess motor performance: hindlimb clasping, grip strength and adhesive removal. Hindlimb clasping and grip strength are basic or gross motor function tests and were used to monitor motor performance changes along the in-life phase of the study. Already at baseline, our aged mice differed significantly in their clasping and grip strength phenotype (Figure S6A,B). Over the course of the experiments only TG mice showed changes for both features (Figure S6A,B). The behavioural changes in TG mice were, however, neither linked to the diet, nor the gavage challenges. Hence, the progressive impairment of these features was driven by the overexpression of αSyn.

The adhesive removal test was used to assess changes in fine motor function. The test consists of measuring the latencies of touch and removal, which at baseline were significantly ($p < 0.0001$) greater in TG mice compared to their WT littermates (Figure 1G, 9M). This was still the case at the end of the 9-week long experimental phase ($p < 0.0001$; Figure 5A, Figure S6C). Hence, αSyn overexpression was again key in driving

motor impairment. For the external challenges, particularly TG EC challenged mice, independent of diet, showed increased timespans of touch and removal compared to the WT littermates (Figure 5A, Figure S6C). Further, we saw a much greater increase in both measures for a subset of TG FD EC challenged mice. This raised additional questions: How did the performance change over time for these TG mice? And what is the interval between the time of touch and time of removal? To answer these questions, we 1) subtracted the time of touch from the time of removal and then 2) compared "Baseline" to "Endpoint" results. We found that for the TG FD EC group 3 out of 6 mice had reduced coordinative ability to remove the adhesive tape compared to their initial performance (Figure 5B). While we did not observe statistically significant differences, the combination of the diet and Curli challenges did appear to further exacerbate the motor phenotype in aged TG mice.

Bacterial Curli mediates aggregation of αSyn in the nigrostriatal pathway

All neuropathological analyses were limited to TG mice, since they have shown to be more susceptible to the challenges. In a first step, we wanted to determine abnormal αSyn aggregates by immunofluorescence staining in the nigrostriatal pathway. Therefore, we used again the pSy129-αSyn antibody and quantified pS129-αSyn positive aggregates in the dorsal striatum and the substantia nigra pars compacta (SNpc). Overall, we observed that the EC challenge was the main driver of pS129-αSyn aggregation in both regions of interest (Figure 6).

In the dorsal striatum, the FR EC challenged TG mice had the highest levels of pS129-αSyn positive aggregates, with even a significant difference to the FR ΔEC ($p = 0.018$) group (Figure 6A, top panel), as seen in the representative microscopy images (Figure 6A, lower panels). In the SNpc, we saw that the impact of the FD challenge was greater than in the dorsal striatum (Figure 6A). Both pS129-αSyn positive cell body counts and all "other" pS129-αSyn positive aggregates were especially increased in FD EC challenged mice ("Cell Body", vs FR ΔEC: $p = 0.127$; "Other", vs FD PBS: $p = 0.109$, vs FR ΔEC: $p = 0.019$, vs FR EC: $p = 0.072$, vs FD ΔEC: $p = 0.13$, Figure 6B, top panel). Qualitatively, the pS129-αSyn positive aggregates that we observed in cell bodies were usually diffused when in the cytoplasm but, in contrast, more compact in the nuclei

(Figure 6B, bottom panel, white arrowhead). However, in FD EC challenged mice we also found dense pS129-αSyn positive deposits in cell bodies (Figure 6B, bottom panel, blue arrowheads). All other pS129-αSyn positive aggregates, not limited to cell bodies, appeared generally more intensively immunopositive. We observed three different forms of aggregates:

1. bead like varicosities (Figure 6B, bottom panel, white arrow), similar to what has been observed in other in vivo (Lauwers et al., 2003) and in vitro (Kouroupi et al., 2017) models, and human post-mortem brains (Del Tredici et al., 2002).
2. spheroid shaped aggregates (Figure 6B, bottom panel, open arrow).
3. corkscrew-like spheroid aggregates (Figure 6B, bottom panel, blue arrow). This form of aggregates, however, was rare and only observed in FD EC challenged mice.

In summary, the EC challenge drove increased pS129-αSyn positive aggregate formation, a process that was further exacerbated in FD challenged TG mice.

Combination of bacterial Curli protein and dietary fiber deprivation challenges drive neurodegeneration in Thy1-Syn14 mice

The loss of neurons in the SNpc and their projections to the dorsal striatum is amongst the main pathological hallmarks of PD (Poewe et al., 2017). To detect neurodegeneration in our TG mice, we stained against tyrosine hydroxylase (TH), an enzyme involved in dopamine synthesis and a marker for dopaminergic neurons and their projections, in both the SNpc and dorsal striatum. Additionally, in the dorsal striatum, we stained for the dopamine transporter (DAT), a marker for dopamine-cycling synapses.

In the dorsal striatum, the combination of FD and EC challenges in TG mice resulted in a significantly reduced area occupied by TH positive projections when compared to the FR EC ($p = 0.029$) and FR EC ($p = 0.04$) groups (Figure 6C, top panel). For DAT, we observed almost the exact same pattern (Figure 6D, top panel). The FD EC challenged TG mice showed significantly reduced levels in DAT area occupied when compared to FD EC ($p = 0.05$) and strong trends compared to the FD PBS and FR EC groups (Figure 6D, top panel).

Tyrosine hydroxylase positive fibers in the dorsal striatum are the projections from dopaminergic neurons located in the SNpc. Quantitation of the area occupied by TH positive neurons (Figure 6E, top panel) showed that the exposure to Curli caused significant neuronal loss (EC-PBS: FDR = 0.041; EC-ΔEC: FDR = 1.68E-4). Fiber-deprived mice showed an exacerbation of this loss. The difference between the FR EC and FD EC groups does show a strong (p = 0.054) trend. Hence, this indicates that the FD challenge leads to an increased susceptibility to a Curli-driven neurodegenerative process.

The combination of fiber deprivation and bacterial Curli exacerbates PD-like pathologies in Thy1-Syn14 mice

To obtain an integrated view that parsed out the contribution of each disease challenge to PD pathologies' progression in our mice, we generated a radar plot summarising the collection of our findings. We simplified the output by classifying the results of the different treatment groups (FD PBS, FR ΔEC, FR EC, FD ΔEC, FD EC) from lowest (centre of plot, Figure 7A) to highest (plot outline, Figure 7A). We further split our findings over two categories (brain and gut) and 8 sub-categories (gut: alpha diversity decrease, mucus foraging genera, lower gut barrier integrity, mucus erosion and αSyn aggregation (ENS); brain: motor impairment, neurodegeneration and αSyn aggregation (CNS); Figure 7A).

Especially in TG mice, fiber deprivation was the underlying cause for changes in the gut microbiome and barrier, while bacterial Curli drove αSyn aggregation in both ENS and CNS (Figure 7A). However, overall the combination of the different challenges (TG FD EC) had the greatest effect on all PD relevant pathologies (Figure 7A).

Based on our results, we propose a sequence of events (Figure 7B) whereby chronic dietary fiber deprivation leads to changes in microbial populations (enrichments in mucus-foraging taxa including Akkermansia spp.) and enteric physiology. These changes cumulate in an increase of gut permeability. The linked higher exposure to the bacterial protein Curli caused increased αSyn aggregation in the ENS and in the CNS accompanied by neurodegeneration in the nigrostriatal pathway. These changes finally resulted in the further exacerbation of already strong motor deficits in these TG mice.

Discussion

Most PD cases have a complex multi-factorial risk and progression profile. Not much is known about how various factors affect or exacerbate PD initiation and progression (Nag and Jelinek, 2019). In our study, we investigated how genetically predisposed aged mice were affected by a fiber-deprived diet and exposure to Curli-producing E. coli, individually or combined. Based on these findings we propose a possible sequence of events, starting with diet induced dysbiosis, leading to reduced barrier integrity, culminating in the exacerbation of PD pathologies.

There is a great body of evidence on the impact of diet on microbial gut health. In vivo studies in which rodents were fed a fiber-deprived diet reported rapid shifts in microbial gut populations (Desai et al., 2016; Neumann et al., 2021; Riva et al., 2019; Schroeder et al., 2018). Accordingly, our data showed decreased diversity, increased Firmicutes/Bacteroidetes ratios and altered abundances of many PD-associated taxa when mice were fed a fiber-deprived diet. The lack of dietary fiber was shown to make specialized taxa, such as Akkermansia spp. and Bacteroides spp., switch to host glycans as energy resource, which results in increased mucus erosion and susceptibility to pathogens (Desai et al., 2016; Martens et al., 2008). Longer-term lack of dietary fiber is thought to trigger a compensatory mechanism, increasing mucin production, and re-establishing at least the inner mucus thickness (Schroeder et al., 2018). In our study, however, the outer mucus layer does not show such a compensatory mechanism. In the present work, the thin outer mucus layer was associated with reduced bacterial diversity and therefore it can be assumed that there are changes in host-microbe interactions. Recent studies showed the impact of microbial metabolite changes on gut barrier integrity. The metabolite butyrate for instance is essential in regulating energy metabolism, proliferation, and differentiation of gut epithelial cells, has anti-inflammatory properties, stimulates mucin production, and most importantly is involved in gut barrier protection by stimulating expression of ZO-1, ZO-2, cingulin and occludin (Plöger et al., 2012; Rivière et al., 2016). We observed reduced abundances of the butyrate producing genera *Lachnospiraceaea NK4A136* and *Roseburia*. Additionally, Lactobacillus, which was also reduced in our fiber deprived fed mice, has been proposed to stimulate butyrate production of such bacteria (Lin et al., 2020). There is still

conflicting evidence on the effect of short-chain fatty acids, in particular butyrate, in PD (Silva et al., 2020). Most animal studies however report beneficial effects (Paiva et al., 2017; Sharma et al., 2015; St. Laurent et al., 2013). Taken together, our observations of reduced outer mucus thickness, higher levels of mucus foraging taxa and reduced gut health relevant taxa under fiber deprived conditions let us to conclude that these mice's gut barrier integrity was affected, and that they were more susceptible to potential pathogenic factors such as Curli.

Curli is a bacterial protein produced by Enterobacteriaceae. This bacterial family has been reported to be increased in PD patients and is associated with disease severity (Barichella et al., 2019; Li et al., 2017). The Curli protein has amyloidogenic properties and has been shown to act as a seed for αSyn aggregation in vitro (Sampson et al., 2020). In physiological conditions, either gavaged (Chen et al., 2016) or supplemented in a human faecal microbiota transplant (Sampson et al., 2020), Curli presence induced or aggravated different PD pathologies in gut and brain. Chen and colleagues observed increased αSyn aggregation in the gut of exposed Fischer 344 rats (Chen et al., 2016). Similarly, we found increased pS129-αSyn positive aggregation in the gut, more specifically in the myenteric plexus. A separate study by Sampson and colleagues (Sampson et al., 2020) did not investigate αSyn in the ENS, but they did, similar to our findings, show increased pS129-αSyn positive levels in the brain in transgenic mice exposed to Curli-producing E. coli.

PD initiation and progression can be modulated by a number of external factors, for which an important entry point may be the gut from where abnormal forms of αSyn could spread in a prion-like manner via the vagus nerve to the brain (Braak et al., 2003, 2006). One of the most obvious factors is diet, and a "western" diet poor in fibers worsens PD progression, whereas a fiber-rich diet delays it (Mischley et al., 2017). The gut is inhabited by the microbiome, which has been reported dysregulated in PD in numerous studies (Boertien et al., 2019). In this study, using an αSyn transgenic animal model, we show how these factors work together in worsening PD progression. Fiber deprivation shifts the composition of the microbiome toward bacteria that harm gut barrier integrity. Dysbiosis in PD is also thought to enhance bacteria that produce amyloidogenic peptides and induce an inflammatory response (Albani et al., 2020). We

show that oral administration of E.coli to αSyn mice exacerbates PD-like pathologies, in particular αSyn aggregation, a process more pronounced in mice fed a fiber deprived diet. We show that this effect was most likely due to the production of the amyloidogenic peptide Curli by E. coli. Thus, our study indicates that, in the context of initial PD-like disease induced by abnormal αSyn production, PD pathologies can be significantly precipitated by environmental factors action through the gut and its microbiome. Our study provides insights on why PD progresses with different degrees of severity among patients. Whether similar mechanisms also play a role in modulating PD initiation remains to be studied, and will be the subject of future studies.

To our knowledge, we are the first to propose a combinatorial mechanism of interdependent exogenous and endogenous factors contributing to PD progression. We further underline the importance of a balanced healthy diet and its implications in PD progression. Hence, our results point to a translational PD-relevant sequence of events exacerbating disease progression and putting forth the idea for lifestyle adaptations to mitigate the disease.

Data Availability

16S rRNA gene amplicon sequencing raw data can be retrieved from https://www.ebi.ac.uk/ena/browser/home under the accession number PRJEB51988. All other original datasets are available upon reasonable request to the corresponding author (kristopher.schmit@hotmail.com).

Acknowledgments

Kristopher J. Schmit was recipient of a pre-doctoral fellowship (FNR AFR 12515776) from the Luxembourg National Research Fond. Alessia Sciortino is part of PARK-QC DTU funded by the Luxembourg National Research Fund (PRIDE17/12244779/PARK-QC). Michel Mittelbronn thanks the Luxembourg National Research Fond for support (FNR PEARL P16/BM/11192868). The authors thank Wagner Zago (Prothena Biosciences) for providing the 11A5 antibody and Matt Chapman (University of Michigan) for providing the two E. coli strains used in this study. The authors would like to thank the Animal Facility of the University of Luxembourg for their support throughout the animal experiments.

Authors contributions

K.J.S., M.B., E.C.M. and P.W. designed the study. K.J.S, A.S., B.P.R., P.G., M.H.T., J.J.G., I.B.A., C.C., and T.H. did the experiments (gavages, behavioural tests, tissue processing, stainings, imaging, DNA, RNA and protein extractions, and Western blots). R.H. performed the 16S rRNA amplicon sequencing. V.T.E.A. analysed the 16S rRNA gene amplicon sequencing data. K.J.S., A.S., V.T.E.A., P.G., I.O., M.M., M.B., and P.W. analysed and interpreted the data. K.J.S. drafted the paper. All authors read and approved the final manuscript.

Declaration of interests

The authors declare no competing interests.

Material and Methods

Animals and experimental design

Ethical Approval

All animal experiments were approved by the Animal Experimentation Ethics Committee of the University of Luxembourg and the appropriate Luxembourg governmental agencies (Ministry of Health and Ministry of Agriculture) and registered under LUPA 2020/25. Additionally, all experiments were planned and executed following the 3R guidelines (https://www.nc3rs.org.uk/the-3rs) and the European Union directive 2010/63/EU.

Mice

The transgenic line B6.D2-Tg(Thy1-SNCA)14Pjk (Kahle et al., 2000, 2001) was used, referred to as Thy1-Syn14 or TG from here on forth. This line overexpresses wild-type human αSyn under the transcriptional regulation of the neuron specific Thy1 promoter. As control animals, wild-type (WT) littermates were used. All mice used were male. For the characterization of the line, different cohorts were used. For the experimental challenge cohort, 72 male animals, 36 TG and 36 WT littermates, were used. They were singly-caged to avoid coprophagy, had access ad libitum to food and water and were exposed to a regular 12h-day-night cycle. Animals were monitored twice a week. According to welfare guidelines, humane endpoints were set based on different physical parameters, e.g. weight loss/gain, body temperature and coat condition. At the end of the in-life phase, the mice were anesthetized with a mix of 150mg/kg ketamine + 1mg/kg medetomidine and subsequently transcardially flush-perfused with 1X PBS. Prior to perfusion, blood was collected from the right atrium.

During the in-life phase of the study, 10 mice were either found dead in their home cage or reached a humane endpoint (Figure S7A). This measure agrees with the animal welfare guidelines.

Experimental Design

For the challenge study, mice were randomly assigned to 10 different treatment and respective control groups (Figure S7A) and treated for a total of 9 weeks; 1-week dietary priming of the colon and additional 8 weeks combined diet and bacterial challenges (Figure S7B). Food was replaced every other week and the mice were gavaged with the

respective bacteria or sham solution weekly. Body weight and overall health was checked twice a week. Stool samples for microbiome analysis and monitoring of basis gross motor functions via hindlimb clasping and grip strength was also performed weekly (Figure S7B). After euthanasia, blood, brains and colons for molecular biology and histology were collected.

Bacterial solution preparation and gavage

The E. coli strains used for treatment were C600 (EC) and its isogenic Curli-operon knock-out (ΔEC) (Chapman et al., 2002; Chen et al., 2016). Both strains were a kind gift from Matthew Chapman, University of Michigan. Expression/absence of Curli operon was tested via PCR using the following primer pairs: csgA_F-5'-GCG-TGA-CAC-AAC-GTT-AAT-TTC-CA-3', csgA_R-5'-CAT-ATT-CTT-CTC-CCG-AAA-AAA-AAC-AG-3'; csgB_F-5'-CCA-TCG-GAT-TGA-TTT-AAA-AGT-CGA-AT-3', csgB_R-5'-AAT-TTC-TTA-AAT-GTA-CGA-CCA-GGT-CC-3'. Additionally, Curli protein expression was confirmed by Congo red staining (not shown). Both strains were grown in Lennox broth under aerobic (5% CO2) conditions at 37°C agitating at 300rpm. Bacteria were resuspended in sterile PBS for oral administration at 1010CFUs/mL.

They were gavaged 100µL of bacterial solution, or PBS for the gavage control groups, at a total bacterial load of 109CFUs. Reusable stainless steel 20G feeding needles (Fine Science Tools, 18060-20) were used. Prior and in-between gavages, the feeding needle was washed with filtered 70% ethanol and rinsed with sterile PBS. One group of feeding needles per treatment was used to avoid cross-contamination. Importantly, the mice were not pre-treated with an antibiotic mix because 1) antibiotics have been shown to prevent αSyn aggregation and to be neuroprotective (Yadav et al., 2021), and 2) measuring the impact of the fiber deprivation on a native microbiome was an essential readout.

Tissue collection and preparation

Prior to the transcardial perfusion, up to 400µL of venous blood from the right atrium were collected in EDTA K3 coated collection tubes (41.1504.005, Sarstedt), for blood-endotoxin measurements. The tubes were gently inverted and then kept on ice. Plasma

was collected after centrifugation at 2000 x g for 10 mins, transferred to RNase-free tubes and stored at -80°C.

After perfusion, the brain was placed on ice, and split along the longitudinal fissure into two hemibrains. For molecular biology analyses, one hemibrain was dissected into different regions of interest (striatum and ventral midbrain). The dissected regions were then put on dry ice and stored at -80°C. The other hemibrains were fixed for immunohistochemistry in 4% PBS-buffered paraformaldehyde (PFA) for 48h at 4°C and then stored in PBS-azide (0.02%) at 4°C. Subsequently, they were cut to generate 50µm thick free-floating sections using the Leica vibratome VT1000 (Wetzlar, Germany), and sections were stored in a 1% (w/v) PVPP + 1:1 (v/v) PBS/ethylene glycol anti-freeze mix at -20°C until staining.

Colon samples for mucus measurements and histopathology were fixed in methacarn (60% absolute methanol: 30% chloroform: 10% glacial acetic acid) solution for 2-4 hours, then transferred to 90% ethanol and kept at 4°C. Next, whole colon samples were first transversally cut by hand with a microtome blade into 4-5mm long sections. Those pre-cut sections were then put into a histology cassette while respecting the proximal to distal order. They were held in place in an ethanol-soaked perforated sponge. After 24h post-fixation in 10% formalin, the samples were processed in a vacuum infiltration processor. Finally, all samples were embedded in paraffin, and cut at 3µm on a microtome. If not processed immediately, the slides were stored at 4°C before being stained.

RNA extraction and RT-qPCR

RNA from dissected colon and different brain regions was extracted using the Qiagen RNeasy Plus Universal Mini Kit (Qiagen, 73404). Briefly, 900µL QIAzol lysis buffer (Qiagen, 79306) and three cold 5mm steel balls were added to each sample (previously stored at -80°C). In ice cooled racks, samples were homogenized at 20Hz for 2mins using the Retsch Mixer Mill MM400. Homogenates were transferred to new RNase clean 2mL tubes and left to rest for 5mins at room temperature (RT). 100µL gDNA eliminator solution was added and the tubes were shaken vigorously for 15 seconds. Then 180µL of chloroform was added and another strong shake was applied for 15 seconds. Homogenates were left to incubate for 3mins at RT. Samples were then centrifuged at

12000 x g for 15 mins at 4°C. Five hundred µL of the upper aqueous phase was collected and transferred to new 2mL RNase free tubes. Five hundred µL of ethanol was added to the supernatant and mixed by inverting the tubes back and forth. RNeasy mini spin columns were then loaded with 500µL of the mix, centrifuged at 8000 x g for 30s at RT, followed by discarding the flow-through from the collection tube. This step was repeated once more. The spin columns were then washed with two different buffers in three steps: one time with 700µL of RWT buffer and twice with 500µL of RPE buffer. At each washing step, the columns were centrifuged at 8000 x g for 30s at RT, and the flow-through was discarded. Columns were then transferred to new collection tubes and spun at maximum speed for 1min. Finally, columns were transferred to an RNase free 1.5mL Eppendorf tubes. Fifty µL of RNase-free water was added to the columns to elute total RNA. RNA purity and quantity were checked by spectrophotometry using the NanoDrop™ 2000 (ThermoFisher Scientific) and the Agilent 2100 Bioanalyzer, respectively. Finally, RNA samples were stored at -80°C.

The model used in this study, Thy1-Syn14, carries a transgene for wild-type human αSyn (SNCA). To determine the levels of transcript expression in comparison to endogenous murine αSyn (Snca), quantitative RT-PCR was performed on a separate untreated age-matched male cohort (N=15), using the following primer pairs: Snca F 5'-GAT-CCT-GGC-AGT-GAG-GCT-TA-3', R 5'-CT-TCA-GGC-TCA-TAG-TCT-TGG-3', SNCA F 5'-AAG-AGG-GTG-TTC-TCT-ATG-TAG-GC-3', R 5'-GCT-CCT-CCA-ACA-TTT-GTC-ACT-T-3' and reference gene Gapdh F 5'-TGC-GAC-TTC-AAC-AGC-AAC-TC-3', R 5'-CTT-GCT-CAG-TGT-CCT-TGC-TG-3'. For the reverse transcription of RNA to cDNA the SuperScript™ III RT reverse transcriptase from Invitrogen was used. Briefly, 1µL of oligo (dT) 20 (50µM) and 1µL of 10mM dNTP mix was added to 1µg of total RNA. If needed, nuclease free water was added to obtain the final reaction volume of 13µL. The mixture was briefly centrifuged for 2-3s, heated at 65°C for 5 minutes, and again chilled on ice for at least 1 minute. Another mixture of 4µL 5× first strand buffer, 1µL RNaseOUT (RNase inhibitor), 1µL of 0.1M DTT, and 1µL of Superscript reverse transcriptase (200 U/µl), was added. The final mixture was briefly centrifuged and incubated at 50°C for 1h followed by 15mins at 70°C for enzyme deactivation. 80µL of RNase free water were added to the reaction mixture. The obtained cDNA was then placed on ice for immediate use, or stored at -20°C for future use.

The qPCR reaction mix contained 2µL of cDNA, 10µM forward and reverse primers, 1X iQTM SYBR® Green Supermix (Bio-Rad) and PCR grade water up to a volume of 20µL. Each qPCR reaction was run in duplicates on a LightCycler ® 480 II (Roche). The thermo cycling profile included an initial denaturation of 3 minutes at 95°C, followed by 40 cycles at 95°C for 30 seconds, 62°C (annealing) for 30 seconds and 72°C (elongation) for 30 seconds, with fluorescent data collection during the annealing step. Data acquisition was performed by LightCycler® 480 Software (version 1.5.0.39).

Protein extraction and Western blot

For the mouse line characterisation, total protein was extracted as described before (Garcia et al., 2010; Keller et al., 1997) with minor adaptations. Briefly, fresh frozen (stored at -80°C) dissected dorsal striatal and midbrain tissue was homogenized in a lysis buffer solution using a dounce homogenizer. The lysis buffer volumes were adapted based on sample size (midbrain: 400µL; dorsal striatum: 800µL). Protein concentrations were determined by Bradford assay.

Samples at 20µg of total protein were run on an SDS-PAGE gel. For total αSyn, the polyclonal rabbit anti-pan-αSyn antibody (S3062, Sigma-Aldrich, 1:1000) was used, and, as internal reference, a monoclonal mouse anti-β-tubulin antibody (clone [DM1A], ab7291, Abcam, 1:1000), followed by LI-COR IRDyeR 700 CW donkey anti-rabbit (1:10000) and IRDyeR 800 CW donkey anti-mouse (1:10000) incubated for 1 hour at RT incubation. Images were captured using the LI-COR Bioscience C-Digit Chemoluminescence scanner.

Microbial DNA extraction and 16S rRNA gene amplicon sequencing

For microbial DNA extraction from single faecal pellets, an adapted version of the IHMS protocol H (Dore et al., 2015) was used. Faecal samples were preserved in 200µL of a glycerol (20%) in PBS solution, and stored at -80°C. Prior to the extraction, the samples were slightly thawn and added 250µL guanidine thiocyanate and 40µL N-lauryl sarcosine (10%). The samples were then left at RT to fully thaw. Then, 500µL N-lauryl sarcosine (5%) were added before the faecal pellet was scattered and vortexed to homogeneity. Samples were then shortly spun down and incubated at 70°C for 1h. Seven hundred fifty µL pasteurized zirconium beads were added to the tubes, then put in pre-cooled racks

and horizontally shaken for 7.5mins at 25Hz in a Retsch mixer mill MM400. Fifteen mg polyvinylpyrrolidone (PVPP) was added and vortexed until dissolved. Then the samples were centrifuged at 20814 x g for 3mins. The supernatants were transferred to new 2mL tubes and kept on ice. The pellet was washed with 500µLTENP (Tris, EDTA, NaCl and PVPP) and centrifuged at 20814 x g for 3mins. This step was repeated three times in total, and each supernatant was added to the previously new 2mL tube. To minimize carryover, the tubes were centrifuged again at 20814 x g for 5mins, and the supernatant was split equally in two new 2mL tubes. One mL isopropanol (Merck) was added to each tube, and mixed in by inverting the tubes. After a 10min incubation at RT, the samples were centrifuged at 20814 x g for 15mins. The supernatant was discarded, and the remaining pellet air dried under the fume hood for 10mins. The pellet was then resuspended in 450µL phosphate buffer and 50µL potassium acetate by pipetting up and down, before the duplicates were pooled and incubated on ice for 90mins. Then, the sample was centrifuged (20814 x g) at 4°C for 35mins, the supernatant transferred into a new tube. Next, 2µL of RNase (10mg/ml) were added. Then, the tube was vortexed, briefly centrifuged, and finally incubated at 37°C for 30mins. Then, 50µL of sodium acetate, and 1mL of ice cold 100% ethanol (Merck) were added, and mixed in by inverting the tube several times. The sample was again incubated at RT for 5mins, and centrifuged at 20814 x g for 7.5min. The supernatant was discarded, and the newly formed pellet was subsequently washed three times with 70% ethanol (Merck), and centrifuged at 20814 x g for 5mins. The supernatant was discarded each time. Finally, the clean pellet was dried at 37 °C for 15 min, then resuspended in 100µl TE Buffer, and homogenized by pipetting. After incubation at 4°C overnight, DNA quality and quantity were checked by Nanodrop ™ 2000/2000c and Qubit 2.0 fluorometer (Thermo Fischer Scientific). Samples were stored at -80°C until sequencing.

Five ng of isolated gDNA was used for PCR amplification using primers (515F (GTGBCAGCMGCCGCGGTAA) and 805R (GACTACHVGGGTATCTAATCC)) specific to the V4 region of the 16S rRNA gene. For the first round of PCR, samples were amplified for 15 cycles to avoid over-amplification. Six additional PCR amplification cycles were performed in the second round to introduce sample specific barcode information. All samples were pooled in equimolar concentration for sequencing. Sample preparation

and sequencing were performed at LCSB Sequencing platform using v3 2x300 nucleotide paired end sequencing kit for MiSeq.

16S rRNA gene amplicon sequence analysis

Sequence analysis Amplicon Sequence Variants (ASVs) were inferred from 16S rRNA gene amplicon reads using the dada2 package (Callahan et al., 2016) following the paired-end big data workflow (https://benjjneb.github.io/dada2/bigdata_paired.html, accessed: September, 2020), with the following parameters: truncLen = 280 for forward, 250 for reverse reads, maxEE = 3, truncQ = 7, and trimLeft = 23 for forward, 21 for reverse reads. The reference used for taxonomic assignment was version 138 of the SILVA database (https://www.arb-silva.de)(Quast et al., 2013).

Microbial diversity and related statistics Microbiome count data was managed using the phyloseq R package (McMurdie and Holmes, 2013). This package was also used to calculate the Shannon index for alpha diversity and the Bray-Curtis dissimilarity based non-metric multidimensional scaling (NMDS) ordination for beta diversity. Statistical significances of alpha diversity differences were evaluated with the Kruskal-Wallis test (overall comparison between all groups) and the Wilcoxon Rank Sum Test with false discovery rate correction for multiple comparisons (pairwise contrasts). For beta diversity comparisons, the adonis PERMANOVA test from the R package vegan (Oksanen et al., 2020) was used. All diversity comparisons were performed using ASV count data rarefied to the lowest number of sequences in a sample. Taxon-specific plots (genus and family level) were made using relative abundances (% of taxa out of total).

Endotoxin plasma level measurement by ELISA

Plasma samples were diluted 1:10 in 1X PBS. To measure the endotoxin plasma, the EndoLISA® kit from BioVendor was used, based on supplier's protocol. Briefly, a serial dilution for the standard for the non-linear regression model was prepared. In duplicates, 100µL of well mixed standard and samples were applied on the supplied 96-well plate. Then, 20µL of 6X binding buffer were added to each well, and the plate was sealed with a cover foil. The plate was incubated at 37°C for 90mins on a shaker at 450rpm. The reaction buffer was removed by quickly inverting the plate. The excess buffer was removed as best as possible by tapping the plate gently on a paper towel.

The wells were then washed twice with 150µL of wash buffer. Again, the plate was inverted quickly, and the excess buffer was removed by tapping the plate gently on a paper towel. Finally, 120µL of detection buffer were added and measurements were taken in a 37°C pre-heated plate reader at 15 mins intervals, form T=0min to T=90mins.

Alcian blue staining and outer mucus thickness measurements

The Alcian blue stainings were performed at the National Center of Pathology (NCP) of the Laboratoire National de Santé in Dudelange (Luxembourg). The sections were stained for Alcian blue (Artisan Link Pro Special Staining System, Dako, Glostrup, Denmark) according to manufacturer's instructions.

Five-10 images per section at 20x magnification were collected for each mouse. This resulted in up to 24 images per animal. The criterion for the correct images was that the sections were cut at the correct plane level. This was determined by the orientation and definition of the colonic crypts, which had to be fully visible pointing towards the colonic lumen. Only the outer mucus areas which could clearly be distinguished from the inner mucus layer and the colonic content were measured. In Image J, the scale of each image was adapted using the imprinted scale bar as reference and an average of 6 measure points, spanning the outer mucus layer, per image were taken.

Immunofluorescent staining of colon sections

Sections were deparaffinised in xylene 3 x 5mins. Before proceeding to rehydration, the slides were checked for paraffin residues. If not, the sections were treated another round with xylene. A three-step rehydration with 100%, 70% and 50% ethanol each twice for 10 mins followed deparaffinization. After washing with dH2O, slides were treated with a citrate buffer (0.1M, pH6.0, + 0.1% Tween 20) for antigen retrieval at 80°C for 30-35mins. After letting the sections cool down for 20mins, the slides were again washed with dH2O 2 x 5mins. Next, endogenous peroxidase activity was quenched by incubating the slides in a 3% H2O2 methanol solution for 15 mins, followed by tissue permeabilization in PBS + 0.4% Triton X100 (PBS-T) + 1% BSA (2 x 10mins). Finally, unspecific antigen binding was blocked by incubation with PBS-T + 5% BSA for 30-45 mins. After washing again with dH2O, the tissue was circled with a hydrophobic Dako pen (S2002, DAKO), and the primary antibodies were added. They were incubated at

room temperature (RT) for 2 hours (hrs), and then transferred to 4°C for overnight incubation in a humidified chamber. The following day, slides were washed briefly with dH2O, then washed with 1% BSA + PBS-T 2 x 5mins, and finally rinsed with dH2O. Tissues were circled again with the hydrophobic pen and secondary antibodies were added. Slides were then incubated for 2 hrs at RT in the humidified chamber. Finally, they were washed 3 x 5mins with PBS-T, and rinsed with dH2O. Excess water was removed by gentle tapping, and slides were coverslipped with DAPI Fluoromount-G® (0100-20, SouthernBiotech).

To detect phosphorylated αSyn in the ENS, double staining using the following antibodies: polyclonal chicken anti-PGP9.5 (ab72910, Abcam; 1:1000), monoclonal rabbit anti-pS129-αSyn (ab51253, Abcam; 1:500) was used.

For the localisation of total and human αSyn in the colon, primary antibodies used were a polyclonal rabbit anti-pan-αSyn (S3062 Sigma-Aldrich, 1:1000) and a monoclonal mouse anti-human-αSyn (clone 211, S5566, Sigma-Aldrich, 1:1000). The protocol was the same except for the revelation steps. Briefly, after primary antibody incubation, slides were incubated with the appropriate secondary biotinylated antibody for 2 hours. Next, they were incubated with an avidin-biotin-complex mix for 1 hour. After washing 2x10mins in PBS-T, the revelation was done using 3,3'-diaminobenzidine (DAB) and H2O2 for 3mins. The slides were finally washed in twice ddH2O for 2mins each and again once in dH2O for 2mins. As counterstain, the slides were emersed 2 times in haematoxylin for 20s and washed in dH2O. A final rinse under tap water was done to intensify the colorization. All slides were again dehydrated (70% EtOH, 95% EtOH and Xylene) and coverslipped using Merck's Neo-Mount®.

Behaviour

Hindlimb clasping

The method was adapted from Guyenet et al., 2010. In brief, animals were taken by the tail near the base and suspended for 10 seconds. If both hindlimbs stayed stretched and did not touch the abdomen for more than 50% of the suspension time, the mouse was scored 0. A score of 1 or 2 was given if one respectively both hindlimbs were retracted for more than 50% of the suspension time. If they were retracted and touched the abdomen for the entire suspension time, a score of 3 was given. In the most severe

cases, the animals twisted around the vertical body axis or even rolled up to a so-called bat position. These cases were given a score of 4. This test was repeated weekly.

Grip strength

The grip strength test (Mao et al., 2016) was performed using Bioseb's grip strength meter (Vitrolles, France). Animals were gently placed on a grid, allowed to grab onto it with all four paws, and then gently pulled off in a continuous backwards motion by their tail. Technical triplicates were taken for each mouse. Values were normalized to the weight of the respective mouse. The test was repeated weekly.

Adhesive removal

The test was adapted from Bouet and colleagues (Bouet et al., 2009). Briefly, animals were placed in a round transparent arena for one minute as habituation. A piece of rectangular tape (3x5mm) was placed on each forepaw. The time was taken once the animals touched the bottom of the arena. Then, the time of first touch and first removal was taken. The test was performed in duplicates, and performed at baseline as well as at the end of the in-life phase.

Immunofluorescent staining on free-floating brain sections

Immunofluorescent stainings on free-floating sections were performed following a standard protocol (Ashrafi et al., 2017) with minor adaptations. Briefly, sections were washed in PBS + 0.1% Triton X100 (TX100) to rinse off the anti-freeze solution. Then, they were treated with a permeabilization/peroxidase inactivation solution (PBS + 1.5% TX100 + 3% H2O2) for 30mins, followed by 2x5mins washing. To prevent unspecific antibody binding, the sections were incubated in 5% BSA + 0.02% TX100 for 1 hour. After a short washing step, sections were incubated with primary antibody(ies) diluted in antibody solution (PBS + 2% BSA) over night at room temperature (RT) on an orbital shaker. The next day, sections were washed with PBS + 0.1% TX100 to remove all excess first antibody. Sections were then incubated with secondary antibody (+ antibody solution) for 2hrs at RT on an orbital shaker under a light trap. Finally, sections were washed with simple PBS (at least three times for 10mins) and then mounted on Superfrost™ (ThermoFisher Scientific) slides, left to dry for up to 12hrs, and cover-slipped using the Fluoromount-G® (Invitrogen) mounting solution.

The following antibodies were used: monoclonal rabbit anti-pS129-αSyn (Abcam, ab51253; 1:1000), monoclonal mouse anti-pS129-αSyn (Prothena Biosciences Inc., 11A5; 1:1000), polyclonal chicken anti-tyrosine hydroxylase (Abcam, ab76442; 1:1000), polyclonal rabbit anti-tyrosine hydroxylase (Merck (Sigma-Aldrich), AB152; 1:1000), polyclonal rat anti-dopamine transporter (MAB369, Merck (Sigma-Aldrich); 1:1000), polyclonal rabbit pan-αSyn (S3062, Sigma-Aldrich, 1:1000), monoclonal mouse human αSyn 211 clone (S5566, Sigma-Aldrich, 1:1000), monoclonal rabbit murine specific αSyn D37A6 clone (4179S, Cell Signalling, 1:1000).

Quantitative neuropathology

Sections were imaged using a Zeiss AxioImager Z1 upright microscope, equipped with a PRIOR motorized slide stage and coupled a "Colibri" LED system to generate fluorescence light of defined wavelengths, and a Zeiss Mrm3digital camera for image capture. The complete imaging system was controlled by Zeiss' Blue Vision software. All histological analyses were performed blinded.

The quantification of TH-positive fibers and DAT-positive synaptic terminals was done as described before in Garcia et al., 2022. Briefly, two doubly labelled (rabbit anti-TH and rat anti-DAT) sections were used. A total of 6 (3/section) 40x (223.8 × 167.7 µm2) pictures of the dorsal striatum were acquired using the optical sectioning system Apotome.2 (Zeiss). The percent area occupied of TH and DAT by intensity thresholding was determined using Image J software and averaged for each mouse.

The quantification of TH-positive neurons in the SNpc has been described and the obtained results were shown to correlate with stereological cell counts (see supplementary information in Ashrafi et al., 2017). Briefly, to estimate TH-positive neurons in the SNpc, anatomically distinguishable levels were identified and applied to 7-12 fifty-micron sections/mouse. Then, 2x2 tiled pictures/section were taken at 10X objective and converted into single Tiff files for image analysis. Next, the region-of-interest (ROI) of the area occupied only by TH-positive neurons was outlined. After thresholding, the ROI occupied (in pixels) by TH-positive neurons was measured. For each anatomical levels of the SN, up to 2 sections/level were measured. Single and/or averaged values/level were finally summed up to one single representative value, the "cumulative SN surface" and converted to mm2.

To quantify pS129-αSyn in the dorsal striatum (Double label: area reference marker polyclonal rabbit anti-TH; pS129-αSyn marker monoclonal mouse 11A5), 40x images were converted to 8-bit and the threshold was automatically set to "MaxEntropy". Next, the images were appropriately scaled from pixel to µm. Greater non-synaptic particles were excluded by selecting them using the "Analyze Particles" tool (Size (µm2): 30.00-Infinity; Circularity: 0.25-1) and adding them to the ROI Manager. Before measuring the area occupied by pS129-αSyn+ synapses, all images were again manually curated for wrongly selected areas. Finally, the ROIs to be excluded were selected using the "XOR" tool from the ROI manager. This resulted in a final curated ROI for quantification of the percent area occupied by pS129-αSyn+ synaptic areas.

To estimate pS129-αSyn positive aggregates in the SNpc (monoclonal rabbit anti-pS129-αSyn), the same ROIs as chosen for TH quantification were used. In Image J, a virtual grid with a square area of 2500µm2 was overlaid. Pictures were then manually analysed for pS129-αSyn positive accumulations. Based on morphology, pS129-αSyn positive cell bodies (1 count = 1 cell body) and other pS129-αSyn positive particles (number of particles per square) of non-cell shapes were counted seperately. Finally, counts were normalized per square (area of ROI/area of square) and summed up for all 4 zones (see TH quantification).

Statistics

For the statistics of the 16S rRNA gene amplicon sequencing data see above. For all other measurements of the challenged mouse cohort, the non-parametric Mann-Whitney U test was performed. False discovery rate (FDR) was used to correct for multiple comparison. However, in many cases the uncorrected p-values were used to illustrate noteworthy differences. This is specified in the figure legends.

References

Albani, G., Albani, S., and Keshavarzian, A. (2020). Editorial: Role of Diet, Physical Activity and Immune System in Parkinson's Disease. Front Neurol 11, 611349. https://doi.org/10.3389/fneur.2020.611349.

Ashrafi, A., Garcia, P., Kollmus, H., Schughart, K., Del Sol, A., Buttini, M., and Glaab, E. (2017). Absence of regulator of G-protein signaling 4 does not protect against dopamine neuron dysfunction and injury in the mouse 6-hydroxydopamine lesion model of Parkinson's disease. Neurobiology of Aging 58, 30–33. https://doi.org/10.1016/j.neurobiolaging.2017.06.008.

Barber Janer, A., Vonck, E., and Baekelandt, V. (2021). Chapter Two - Modeling synucleinopathies in rodents. In International Review of Movement Disorders, B. Dehay, and E. Bezard, eds. (Academic Press), pp. 65–154.

Barichella, M., Severgnini, M., Cilia, R., Cassani, E., Bolliri, C., Caronni, S., Ferri, V., Cancello, R., Ceccarani, C., Faierman, S., et al. (2019). Unraveling gut microbiota in Parkinson's disease and atypical parkinsonism. Movement Disorders 34, 396–405. https://doi.org/10.1002/mds.27581.

Barnhart, M.M., and Chapman, M.R. (2006). Curli biogenesis and function. Annu Rev Microbiol 60, 131–147. https://doi.org/10.1146/annurev.micro.60.080805.142106.

Bernardo-Cravo, A.P., Schmeller, D.S., Chatzinotas, A., Vredenburg, V.T., and Loyau, A. (2020). Environmental Factors and Host Microbiomes Shape Host–Pathogen Dynamics. Trends in Parasitology 36, 616–633. https://doi.org/10.1016/j.pt.2020.04.010.

Blackwood, B.P., Yuan, C.Y., Wood, D.R., Nicolas, J.D., Grothaus, J.S., and Hunter, C.J. (2017). Probiotic Lactobacillus Species Strengthen Intestinal Barrier Function and Tight Junction Integrity in Experimental Necrotizing Enterocolitis. J Probiotics Health 5, 159. https://doi.org/10.4172/2329-8901.1000159.

Boertien, J.M., Pereira, P.A.B., Aho, V.T.E., and Scheperjans, F. (2019). Increasing Comparability and Utility of Gut Microbiome Studies in Parkinson's Disease: A

Systematic Review. Journal of Parkinson's Disease 9, S297–S312. https://doi.org/10.3233/JPD-191711.

Bouet, V., Boulouard, M., Toutain, J., Divoux, D., Bernaudin, M., Schumann-Bard, P., and Freret, T. (2009). The adhesive removal test: a sensitive method to assess sensorimotor deficits in mice. Nat Protoc 4, 1560–1564. https://doi.org/10.1038/nprot.2009.125.

Braak, H., Tredici, K.D., Rüb, U., de Vos, R.A.I., Jansen Steur, E.N.H., and Braak, E. (2003). Staging of brain pathology related to sporadic Parkinson's disease. Neurobiology of Aging 24, 197–211. https://doi.org/10.1016/S0197-4580(02)00065-9.

Braak, H., de Vos, R.A.I., Bohl, J., and Del Tredici, K. (2006). Gastric alpha-synuclein immunoreactive inclusions in Meissner's and Auerbach's plexuses in cases staged for Parkinson's disease-related brain pathology. Neurosci. Lett. 396, 67–72. https://doi.org/10.1016/j.neulet.2005.11.012.

Callahan, B.J., McMurdie, P.J., Rosen, M.J., Han, A.W., Johnson, A.J.A., and Holmes, S.P. (2016). DADA2: High-resolution sample inference from Illumina amplicon data. Nat Methods 13, 581–583. https://doi.org/10.1038/nmeth.3869.

Chapman, M.R., Robinson, L.S., Pinkner, J.S., Roth, R., Heuser, J., Hammar, M., Normark, S., and Hultgren, S.J. (2002). Role of Escherichia coli curli operons in directing amyloid fiber formation. Science 295, 851–855. https://doi.org/10.1126/science.1067484.

Chen, H., and Ritz, B. (2018). The Search for Environmental Causes of Parkinson's Disease: Moving Forward. J Parkinsons Dis 8, S9–S17. https://doi.org/10.3233/JPD-181493.

Chen, S.G., Stribinskis, V., Rane, M.J., Demuth, D.R., Gozal, E., Roberts, A.M., Jagadapillai, R., Liu, R., Choe, K., Shivakumar, B., et al. (2016). Exposure to the Functional Bacterial Amyloid Protein Curli Enhances Alpha-Synuclein Aggregation in Aged Fischer 344 Rats and Caenorhabditis elegans. Sci Rep 6, 1–10. https://doi.org/10.1038/srep34477.

Council (US), N.R., Medicine (US), I. of, Woolf, S.H., and Aron, L. (2013). Physical and Social Environmental Factors (National Academies Press (US)).

Del Tredici, K., and Braak, H. (2012). Lewy pathology and neurodegeneration in premotor Parkinson's disease. Movement Disorders 27, 597–607. https://doi.org/10.1002/mds.24921.

Del Tredici, K., and Duda, J.E. (2011). Peripheral Lewy body pathology in Parkinson's disease and incidental Lewy body disease: Four cases. Journal of the Neurological Sciences 310, 100–106. https://doi.org/10.1016/j.jns.2011.06.003.

Del Tredici, K., Rüb, U., de Vos, R.A.I., Bohl, J.R.E., and Braak, H. (2002). Where Does Parkinson Disease Pathology Begin in the Brain? Journal of Neuropathology & Experimental Neurology 61, 413–426. https://doi.org/10.1093/jnen/61.5.413.

Desai, M.S., Seekatz, A.M., Koropatkin, N.M., Kamada, N., Hickey, C.A., Wolter, M., Pudlo, N.A., Kitamoto, S., Terrapon, N., Muller, A., et al. (2016). A dietary fiber-deprived gut microbiota degrades the colonic mucus barrier and enhances pathogen susceptibility. Cell 167, 1339-1353.e21. https://doi.org/10.1016/j.cell.2016.10.043.

Di Monte, D.A., Lavasani, M., and Manning-Bog, A.B. (2002). Environmental Factors in Parkinson's Disease. NeuroToxicology 23, 487–502. https://doi.org/10.1016/S0161-813X(02)00099-2.

Dick, F.D., De Palma, G., Ahmadi, A., Scott, N.W., Prescott, G.J., Bennett, J., Semple, S., Dick, S., Counsell, C., Mozzoni, P., et al. (2007). Environmental risk factors for Parkinson's disease and parkinsonism: the Geoparkinson study. Occup Environ Med 64, 666–672. https://doi.org/10.1136/oem.2006.027003.

Dore, J., Ehrlich, S.D., Levenez, F., Pellecchia, M.T., Alberti, A., Bertrand, L., Bork, P., Costea, P.I., Sunagawa, S., Guarner, F., et al. (2015). IHMS_SOP 07 V1: Standard operating procedure for fecal samples DNA extraction, Protocol H. International Human Microbiome Standards.

Dorsey, E.R., Elbaz, A., Nichols, E., Abbasi, N., Abd-Allah, F., Abdelalim, A., Adsuar, J.C., Ansha, M.G., Brayne, C., Choi, J.-Y.J., et al. (2018). Global, regional, and national burden of Parkinson's disease, 1990–2016: a systematic analysis for the Global Burden of Disease Study 2016. The Lancet Neurology 17, 939–953. https://doi.org/10.1016/S1474-4422(18)30295-3.

Drokhlyansky, E., Smillie, C.S., Van Wittenberghe, N., Ericsson, M., Griffin, G.K., Eraslan, G., Dionne, D., Cuoco, M.S., Goder-Reiser, M.N., Sharova, T., et al. (2020). The Human and Mouse Enteric Nervous System at Single-Cell Resolution. Cell 182, 1606-1622.e23. https://doi.org/10.1016/j.cell.2020.08.003.

Fernagut, P.O., Diguet, E., Bioulac, B., and Tison, F. (2004). MPTP potentiates 3-nitropropionic acid-induced striatal damage in mice: reference to striatonigral degeneration. Exp Neurol 185, 47–62. https://doi.org/10.1016/j.expneurol.2003.09.014.

Fleming, S.M., Ekhator, O.R., and Ghisays, V. (2013). Assessment of Sensorimotor Function in Mouse Models of Parkinson's Disease. J Vis Exp 50303. https://doi.org/10.3791/50303.

Garcia, P., Youssef, I., Utvik, J.K., Florent-Béchard, S., Barthélémy, V., Malaplate-Armand, C., Kriem, B., Stenger, C., Koziel, V., Olivier, J.-L., et al. (2010). Ciliary Neurotrophic Factor Cell-Based Delivery Prevents Synaptic Impairment and Improves Memory in Mouse Models of Alzheimer's Disease. J Neurosci 30, 7516–7527. https://doi.org/10.1523/JNEUROSCI.4182-09.2010.

Garcia, P., Jürgens-Wemheuer, W., Uriarte Huarte, O., Michelucci, A., Masuch, A., Brioschi, S., Weihofen, A., Koncina, E., Coowar, D., Heurtaux, T., et al. (2022). Neurodegeneration and neuroinflammation are linked, but independent of alpha-synuclein inclusions, in a seeding/spreading mouse model of Parkinson's disease. Glia https://doi.org/10.1002/glia.24149.

Gerhardt, S., and Mohajeri, M.H. (2018). Changes of Colonic Bacterial Composition in Parkinson's Disease and Other Neurodegenerative Diseases. Nutrients 10, 708. https://doi.org/10.3390/nu10060708.

Gorecki, A.M., Preskey, L., Bakeberg, M.C., Kenna, J.E., Gildenhuys, C., MacDougall, G., Dunlop, S.A., Mastaglia, F.L., Akkari, P.A., Koengten, F., et al. (2019). Altered Gut Microbiome in Parkinson's Disease and the Influence of Lipopolysaccharide in a Human α-Synuclein Over-Expressing Mouse Model. Front Neurosci 13, 839. https://doi.org/10.3389/fnins.2019.00839.

Gorell, J.M., Peterson, E.L., Rybicki, B.A., and Johnson, C.C. (2004). Multiple risk factors for Parkinson's disease. Journal of the Neurological Sciences 217, 169–174. https://doi.org/10.1016/j.jns.2003.09.014.

Guyenet, S.J., Furrer, S.A., Damian, V.M., Baughan, T.D., La Spada, A.R., and Garden, G.A. (2010). A Simple Composite Phenotype Scoring System for Evaluating Mouse Models of Cerebellar Ataxia. J Vis Exp https://doi.org/10.3791/1787.

Heeney, D.D., Gareau, M.G., and Marco, M.L. (2018). Intestinal Lactobacillus in health and disease, a driver or just along for the ride? Curr Opin Biotechnol 49, 140–147. https://doi.org/10.1016/j.copbio.2017.08.004.

Heintz-Buschart, A., Pandey, U., Wicke, T., Sixel-Döring, F., Janzen, A., Sittig-Wiegand, E., Trenkwalder, C., Oertel, W.H., Mollenhauer, B., and Wilmes, P. (2018). The nasal and gut microbiome in Parkinson's disease and idiopathic rapid eye movement sleep behavior disorder. Mov Disord 33, 88–98. https://doi.org/10.1002/mds.27105.

Hirschberg, S., Gisevius, B., Duscha, A., and Haghikia, A. (2019). Implications of Diet and The Gut Microbiome in Neuroinflammatory and Neurodegenerative Diseases. International Journal of Molecular Sciences 20, 3109. https://doi.org/10.3390/ijms20123109.

Johansson, M.E.V., Larsson, J.M.H., and Hansson, G.C. (2011). The two mucus layers of colon are organized by the MUC2 mucin, whereas the outer layer is a legislator of host–microbial interactions. PNAS 108, 4659–4665. https://doi.org/10.1073/pnas.1006451107.

Johansson, M.E.V., Sjövall, H., and Hansson, G.C. (2013). The gastrointestinal mucus system in health and disease. Nat Rev Gastroenterol Hepatol 10, 352–361. https://doi.org/10.1038/nrgastro.2013.35.

Kahle, P.J., Neumann, M., Ozmen, L., Müller, V., Jacobsen, H., Schindzielorz, A., Okochi, M., Leimer, U., Putten, H. van der, Probst, A., et al. (2000). Subcellular Localization of Wild-Type and Parkinson's Disease-Associated Mutant α-Synuclein in Human and Transgenic Mouse Brain. J. Neurosci. 20, 6365–6373. https://doi.org/10.1523/JNEUROSCI.20-17-06365.2000.

Kahle, P.J., Neumann, M., Ozmen, L., Müller, V., Odoy, S., Okamoto, N., Jacobsen, H., Iwatsubo, T., Trojanowski, J.Q., Takahashi, H., et al. (2001). Selective insolubility of alpha-synuclein in human Lewy body diseases is recapitulated in a transgenic mouse model. Am. J. Pathol. 159, 2215–2225. https://doi.org/10.1016/s0002-9440(10)63072-6.

Keller, D., Erö, C., and Markram, H. (2018). Cell Densities in the Mouse Brain: A Systematic Review. Frontiers in Neuroanatomy 12, 83. https://doi.org/10.3389/fnana.2018.00083.

Keller, J.N., Mark, R.J., Bruce, A.J., E. Blanc, Rothstein, J.D., Uchida, K., Waeg, G., and Mattson, M.P. (1997). 4-Hydroxynonenal, an aldehydic product of membrane lipid peroxidation, impairs glutamate transport and mitochondrial function in synaptosomes. Neuroscience 80, 685–696. https://doi.org/10.1016/S0306-4522(97)00065-1.

Keshavarzian, A., Green, S.J., Engen, P.A., Voigt, R.M., Naqib, A., Forsyth, C.B., Mutlu, E., and Shannon, K.M. (2015). Colonic bacterial composition in Parkinson's disease. Movement Disorders 30, 1351–1360. https://doi.org/10.1002/mds.26307.

Kouroupi, G., Taoufik, E., Vlachos, I.S., Tsioras, K., Antoniou, N., Papastefanaki, F., Chroni-Tzartou, D., Wrasidlo, W., Bohl, D., Stellas, D., et al. (2017). Defective synaptic connectivity and axonal neuropathology in a human iPSC-based model of familial Parkinson's disease. PNAS 114, E3679–E3688. https://doi.org/10.1073/pnas.1617259114.

Lauwers, E., Debyser, Z., Van Dorpe, J., De Strooper, B., Nuttin, B., and Baekelandt, V. (2003). Neuropathology and Neurodegeneration in Rodent Brain Induced by Lentiviral Vectormediated Overexpression of α-Synuclein. Brain Pathology 13, 364–372. https://doi.org/10.1111/j.1750-3639.2003.tb00035.x.

Li, W., Wu, X., Hu, X., Wang, T., Liang, S., Duan, Y., Jin, F., and Qin, B. (2017). Structural changes of gut microbiota in Parkinson's disease and its correlation with clinical features. Sci. China Life Sci. 60, 1223–1233. https://doi.org/10.1007/s11427-016-9001-4.

Lieu, C.A., Chinta, S.J., Rane, A., and Andersen, J.K. (2013). Age-Related Behavioral Phenotype of an Astrocytic Monoamine Oxidase-B Transgenic Mouse Model of Parkinson's Disease. PLOS ONE 8, e54200. https://doi.org/10.1371/journal.pone.0054200.

Lin, R., Sun, Y., Mu, P., Zheng, T., Mu, H., Deng, F., Deng, Y., and Wen, J. (2020). Lactobacillus rhamnosus GG supplementation modulates the gut microbiota to promote butyrate production, protecting against deoxynivalenol exposure in nude mice. Biochemical Pharmacology 175, 113868. https://doi.org/10.1016/j.bcp.2020.113868.

Magne, F., Gotteland, M., Gauthier, L., Zazueta, A., Pesoa, S., Navarrete, P., and Balamurugan, R. (2020). The Firmicutes/Bacteroidetes Ratio: A Relevant Marker of Gut Dysbiosis in Obese Patients? Nutrients 12. https://doi.org/10.3390/nu12051474.

Mao, X., Ou, M.T., Karuppagounder, S.S., Kam, T.-I., Yin, X., Xiong, Y., Ge, P., Umanah, G.E., Brahmachari, S., Shin, J.-H., et al. (2016). Pathological α-synuclein transmission initiated by binding lymphocyte-activation gene 3. Science 353. https://doi.org/10.1126/science.aah3374.

Maraki, M.I., Yannakoulia, M., Stamelou, M., Stefanis, L., Xiromerisiou, G., Kosmidis, M.H., Dardiotis, E., Hadjigeorgiou, G.M., Sakka, P., Anastasiou, C.A., et al. (2019). Mediterranean diet adherence is related to reduced probability of prodromal Parkinson's disease. Movement Disorders 34, 48–57. https://doi.org/10.1002/mds.27489.

Mariat, D., Firmesse, O., Levenez, F., Guimarăes, V., Sokol, H., Doré, J., Corthier, G., and Furet, J.-P. (2009). The Firmicutes/Bacteroidetes ratio of the human microbiota changes with age. BMC Microbiology 9, 123. https://doi.org/10.1186/1471-2180-9-123.

Marras, C., Canning, C.G., and Goldman, S.M. (2019). Environment, lifestyle, and Parkinson's disease: Implications for prevention in the next decade. Mov Disord 34, 801–811. https://doi.org/10.1002/mds.27720.

Martens, E.C., Chiang, H.C., and Gordon, J.I. (2008). Mucosal Glycan Foraging Enhances Fitness and Transmission of a Saccharolytic Human Gut Bacterial Symbiont. Cell Host Microbe 4, 447–457. https://doi.org/10.1016/j.chom.2008.09.007.

Martín, R., Miquel, S., Ulmer, J., Kechaou, N., Langella, P., and Bermúdez-Humarán, L.G. (2013). Role of commensal and probiotic bacteria in human health: a focus on inflammatory bowel disease. Microbial Cell Factories 12, 71. https://doi.org/10.1186/1475-2859-12-71.

Martínez Leo, E.E., and Segura Campos, M.R. (2020). Effect of ultra-processed diet on gut microbiota and thus its role in neurodegenerative diseases. Nutrition 71, 110609. https://doi.org/10.1016/j.nut.2019.110609.

McMurdie, P.J., and Holmes, S. (2013). phyloseq: An R Package for Reproducible Interactive Analysis and Graphics of Microbiome Census Data. PLOS ONE 8, e61217. https://doi.org/10.1371/journal.pone.0061217.

Miller, A.L., Bessho, S., Grando, K., and Tükel, Ç. (2021). Microbiome or Infections: Amyloid-Containing Biofilms as a Trigger for Complex Human Diseases. Frontiers in Immunology 12, 514. https://doi.org/10.3389/fimmu.2021.638867.

Mischley, L.K., Lau, R.C., and Bennett, R.D. (2017). Role of Diet and Nutritional Supplements in Parkinson's Disease Progression. Oxid Med Cell Longev 2017. https://doi.org/10.1155/2017/6405278.

Murakami, T.C., Mano, T., Saikawa, S., Horiguchi, S.A., Shigeta, D., Baba, K., Sekiya, H., Shimizu, Y., Tanaka, K.F., Kiyonari, H., et al. (2018). A three-dimensional single-cell-resolution whole-brain atlas using CUBIC-X expansion microscopy and tissue clearing. Nat Neurosci 21, 625–637. https://doi.org/10.1038/s41593-018-0109-1.

Nag, N., and Jelinek, G.A. (2019). More Research Is Needed on Lifestyle Behaviors That Influence Progression of Parkinson's Disease. Frontiers in Neurology 10. .

Nations, U. LIFESTYLE DISEASES: An Economic Burden on the Health Services (United Nations).

Nerius, M., Doblhammer, G., and Tamgüney, G. (2020). GI infections are associated with an increased risk of Parkinson's disease. Gut 69, 1154–1156. https://doi.org/10.1136/gutjnl-2019-318822.

Neumann, M., Steimle, A., Grant, E.T., Wolter, M., Parrish, A., Willieme, S., Brenner, D., Martens, E.C., and Desai, M.S. (2021). Deprivation of dietary fiber in specific-pathogen-free mice promotes susceptibility to the intestinal mucosal pathogen Citrobacter rodentium. Gut Microbes 13, 1966263. https://doi.org/10.1080/19490976.2021.1966263.

Oksanen, J., Blanchet, F.G., Friendly, M., Kindt, R., Legendre, P., McGlinn, D., Minchin, P.R., O'Hara, R.B., Simpson, G.L., Solymos, P., et al. (2020). vegan: Community Ecology Package.

Paiva, I., Pinho, R., Pavlou, M.A., Hennion, M., Wales, P., Schütz, A.-L., Rajput, A., Szegő, É.M., Kerimoglu, C., Gerhardt, E., et al. (2017). Sodium butyrate rescues dopaminergic cells from alpha-synuclein-induced transcriptional deregulation and DNA damage. Human Molecular Genetics 26, 2231–2246. https://doi.org/10.1093/hmg/ddx114.

Plöger, S., Stumpff, F., Penner, G.B., Schulzke, J.-D., Gäbel, G., Martens, H., Shen, Z., Günzel, D., and Aschenbach, J.R. (2012). Microbial butyrate and its role for barrier function in the gastrointestinal tract. Annals of the New York Academy of Sciences 1258, 52–59. https://doi.org/10.1111/j.1749-6632.2012.06553.x.

Poewe, W., Seppi, K., Tanner, C.M., Halliday, G.M., Brundin, P., Volkmann, J., Schrag, A.-E., and Lang, A.E. (2017). Parkinson disease. Nat Rev Dis Primers 3, 1–21. https://doi.org/10.1038/nrdp.2017.13.

Qualman, S.J., Haupt, H.M., Yang, P., and Hamilton, S.R. (1984). Esophageal Lewy bodies associated with ganglion cell loss in achalasia. Similarity to Parkinson's disease. Gastroenterology 87, 848–856. .

Quast, C., Pruesse, E., Yilmaz, P., Gerken, J., Schweer, T., Yarza, P., Peplies, J., and Glöckner, F.O. (2013). The SILVA ribosomal RNA gene database project: improved data processing and web-based tools. Nucleic Acids Res 41, D590–D596. https://doi.org/10.1093/nar/gks1219.

Rampelli, S., Schnorr, S.L., Consolandi, C., Turroni, S., Severgnini, M., Peano, C., Brigidi, P., Crittenden, A.N., Henry, A.G., and Candela, M. (2015). Metagenome Sequencing of the Hadza Hunter-Gatherer Gut Microbiota. Current Biology 25, 1682–1693. https://doi.org/10.1016/j.cub.2015.04.055.

Riva, A., Kuzyk, O., Forsberg, E., Siuzdak, G., Pfann, C., Herbold, C., Daims, H., Loy, A., Warth, B., and Berry, D. (2019). A fiber-deprived diet disturbs the fine-scale spatial architecture of the murine colon microbiome. Nat Commun 10, 4366. https://doi.org/10.1038/s41467-019-12413-0.

Rivière, A., Selak, M., Lantin, D., Leroy, F., and De Vuyst, L. (2016). Bifidobacteria and Butyrate-Producing Colon Bacteria: Importance and Strategies for Their Stimulation in the Human Gut. Front Microbiol 7, 979. https://doi.org/10.3389/fmicb.2016.00979.

Sampson, T.R., Debelius, J.W., Thron, T., Janssen, S., Shastri, G.G., Ilhan, Z.E., Challis, C., Schretter, C.E., Rocha, S., Gradinaru, V., et al. (2016). Gut Microbiota Regulate Motor Deficits and Neuroinflammation in a Model of Parkinson's Disease. Cell 167, 1469-1480.e12. https://doi.org/10.1016/j.cell.2016.11.018.

Sampson, T.R., Challis, C., Jain, N., Moiseyenko, A., Ladinsky, M.S., Shastri, G.G., Thron, T., Needham, B.D., Horvath, I., Debelius, J.W., et al. (2020). A gut bacterial amyloid promotes α-synuclein aggregation and motor impairment in mice. ELife 9, e53111. https://doi.org/10.7554/eLife.53111.

Scheperjans, F., Aho, V., Pereira, P.A.B., Koskinen, K., Paulin, L., Pekkonen, E., Haapaniemi, E., Kaakkola, S., Eerola-Rautio, J., Pohja, M., et al. (2015). Gut microbiota are related to Parkinson's disease and clinical phenotype. Movement Disorders 30, 350–358. https://doi.org/10.1002/mds.26069.

Schroeder, B.O., Birchenough, G.M.H., Ståhlman, M., Arike, L., Johansson, M.E.V., Hansson, G.C., and Bäckhed, F. (2018). Bifidobacteria or Fiber Protects against Diet-Induced Microbiota-Mediated Colonic Mucus Deterioration. Cell Host & Microbe 23, 27-40.e7. https://doi.org/10.1016/j.chom.2017.11.004.

Shannon, K.M., Keshavarzian, A., Dodiya, H.B., Jakate, S., and Kordower, J.H. (2012). Is alpha-synuclein in the colon a biomarker for premotor Parkinson's disease? Evidence from 3 cases. Mov Disord 27, 716–719. https://doi.org/10.1002/mds.25020.

Sharma, S., Taliyan, R., and Singh, S. (2015). Beneficial effects of sodium butyrate in 6-OHDA induced neurotoxicity and behavioral abnormalities: Modulation of histone deacetylase activity. Behavioural Brain Research 291, 306–314. https://doi.org/10.1016/j.bbr.2015.05.052.

Shen, T., Yue, Y., He, T., Huang, C., Qu, B., Lv, W., and Lai, H.-Y. (2021). The Association Between the Gut Microbiota and Parkinson's Disease, a Meta-Analysis. Frontiers in Aging Neuroscience 13, 40. https://doi.org/10.3389/fnagi.2021.636545.

Sidebotham, E.L., Woodward, M.N., Kenny, S.E., Lloyd, D.A., Vaillant, C.R., and Edgar, D.H. (2001). Assessment of protein gene product 9.5 as a marker of neural crest-derived precursor cells in the developing enteric nervous system. Pediatr Surg Int 17, 304–307. https://doi.org/10.1007/s003830100599.

Silva, Y.P., Bernardi, A., and Frozza, R.L. (2020). The Role of Short-Chain Fatty Acids From Gut Microbiota in Gut-Brain Communication. Frontiers in Endocrinology 11. .

Singh, Y., El-Hadidi, M., Admard, J., Wassouf, Z., Schulze-Hentrich, J.M., Kohlhofer, U., Quintanilla-Martinez, L., Huson, D., Riess, O., and Casadei, N. (2019). Enriched Environmental Conditions Modify the Gut Microbiome Composition and Fecal Markers of Inflammation in Parkinson's Disease. Front Neurosci 13, 1032. https://doi.org/10.3389/fnins.2019.01032.

St. Laurent, R., O'Brien, L.M., and Ahmad, S.T. (2013). Sodium butyrate improves locomotor impairment and early mortality in a rotenone-induced Drosophila model of Parkinson's disease. Neuroscience 246, 382–390. https://doi.org/10.1016/j.neuroscience.2013.04.037.

Stadlbauer, V., Engertsberger, L., Komarova, I., Feldbacher, N., Leber, B., Pichler, G., Fink, N., Scarpatetti, M., Schippinger, W., Schmidt, R., et al. (2020). Dysbiosis, gut barrier dysfunction and inflammation in dementia: a pilot study. BMC Geriatrics 20, 248. https://doi.org/10.1186/s12877-020-01644-2.

Stokholm, M.G., Danielsen, E.H., Hamilton-Dutoit, S.J., and Borghammer, P. (2016). Pathological α-synuclein in gastrointestinal tissues from prodromal Parkinson disease patients. Annals of Neurology 79, 940–949. https://doi.org/10.1002/ana.24648.

Tailford, L.E., Crost, E.H., Kavanaugh, D., and Juge, N. (2015). Mucin glycan foraging in the human gut microbiome. Frontiers in Genetics 6, 81. https://doi.org/10.3389/fgene.2015.00081.

Tillerson, J.L., and Miller, G.W. (2003). Grid performance test to measure behavioral impairment in the MPTP-treated-mouse model of parkinsonism. Journal of Neuroscience Methods 123, 189–200. https://doi.org/10.1016/S0165-0270(02)00360-6.

Tillerson, J.L., Caudle, W.M., Reverón, M.E., and Miller, G.W. (2002a). Detection of Behavioral Impairments Correlated to Neurochemical Deficits in Mice Treated with Moderate Doses of 1-Methyl-4-phenyl-1,2,3,6-tetrahydropyridine. Experimental Neurology 178, 80–90. https://doi.org/10.1006/exnr.2002.8021.

Tillerson, J.L., Caudle, W.M., Reverón, M.E., and Miller, G.W. (2002b). Detection of Behavioral Impairments Correlated to Neurochemical Deficits in Mice Treated with Moderate Doses of 1-Methyl-4-phenyl-1,2,3,6-tetrahydropyridine. Experimental Neurology 178, 80–90. https://doi.org/10.1006/exnr.2002.8021.

Tytgat, H.L.P., Nobrega, F.L., Oost, J. van der, and Vos, W.M. de (2019). Bowel Biofilms: Tipping Points between a Healthy and Compromised Gut? Trends in Microbiology 27, 17–25. https://doi.org/10.1016/j.tim.2018.08.009.

Unger, M.M., Spiegel, J., Dillmann, K.-U., Grundmann, D., Philippeit, H., Bürmann, J., Faßbender, K., Schwiertz, A., and Schäfer, K.-H. (2016). Short chain fatty acids and gut microbiota differ between patients with Parkinson's disease and age-matched controls. Parkinsonism Relat Disord 32, 66–72. https://doi.org/10.1016/j.parkreldis.2016.08.019.

Vaikath, N.N., Hmila, I., Gupta, V., Erskine, D., Ingelsson, M., and El-Agnaf, O.M.A. (2019). Antibodies against alpha-synuclein: tools and therapies. J Neurochem 150, 612–625. https://doi.org/10.1111/jnc.14713.

de Vos, W.M. (2015). Microbial biofilms and the human intestinal microbiome. Npj Biofilms Microbiomes 1, 1–3. https://doi.org/10.1038/npjbiofilms.2015.5.

Wakabayashi, K., Takahashi, H., Takeda, S., Ohama, E., and Ikuta, F. (1988). Parkinson's disease: the presence of Lewy bodies in Auerbach's and Meissner's plexuses. Acta Neuropathol 76, 217–221. https://doi.org/10.1007/BF00687767.

Wakabayashi, K., Takahashi, H., Ohama, E., and Ikuta, F. (1990). Parkinson's disease: an immunohistochemical study of Lewy body-containing neurons in the enteric nervous system. Acta Neuropathol 79, 581–583. https://doi.org/10.1007/BF00294234.

Wakabayashi, K., Takahashi, H., Ohama, E., Takeda, S., and Ikuta, F. (1993). Lewy bodies in the visceral autonomic nervous system in Parkinson's disease. Adv Neurol 60, 609–612. .

Wang, L., Li, S., Jiang, Y., Zhao, Z., Shen, Y., Zhang, J., and Zhao, L. (2021). Neuroprotective effect of Lactobacillus plantarum DP189 on MPTP-induced Parkinson's disease model mice. Journal of Functional Foods 85, 104635. https://doi.org/10.1016/j.jff.2021.104635.

Warner, T.T., and Schapira, A.H.V. (2003). Genetic and environmental factors in the cause of Parkinson's disease. Annals of Neurology 53, S16–S25. https://doi.org/10.1002/ana.10487.

Yadav, N., Thakur, A.K., Shekhar, N., and Ayushi (2021). Potential of Antibiotics for the Treatment and Management of Parkinson's Disease: An Overview. Current Drug Research Reviews 13, 166–171. .

Yan, Y., Ren, S., Duan, Y., Lu, C., Niu, Y., Wang, Z., Inglis, B., Ji, W., Zheng, Y., and Si, W. (2021). Gut microbiota and metabolites of α-synuclein transgenic monkey models with early stage of Parkinson's disease. Npj Biofilms Microbiomes 7, 1–9. https://doi.org/10.1038/s41522-021-00242-3.

Yang, W., Hamilton, J.L., Kopil, C., Beck, J.C., Tanner, C.M., Albin, R.L., Ray Dorsey, E., Dahodwala, N., Cintina, I., Hogan, P., et al. (2020). Current and projected future economic burden of Parkinson's disease in the U.S. Npj Parkinsons Dis. 6, 1–9. https://doi.org/10.1038/s41531-020-0117-1.

Zhang, J., Pho, V., Bonasera, S.J., Holtzman, J., Tang, A.T., Hellmuth, J., Tang, S., Janak, P.H., Tecott, L.H., and Huang, E.J. (2007). Essential function of HIPK2 in TGFβ-dependent survival of midbrain dopamine neurons. Nat Neurosci 10, 77–86. https://doi.org/10.1038/nn1816.

Zhang, Y., Granholm, A.-C., Huh, K., Shan, L., Diaz-Ruiz, O., Malik, N., Olson, L., Hoffer, B.J., Lupica, C.R., Hoffman, A.F., et al. (2012). PTEN deletion enhances survival, neurite outgrowth and function of dopamine neuron grafts to MitoPark mice. Brain 135, 2736–2749. https://doi.org/10.1093/brain/aws196.

3.3 Figures

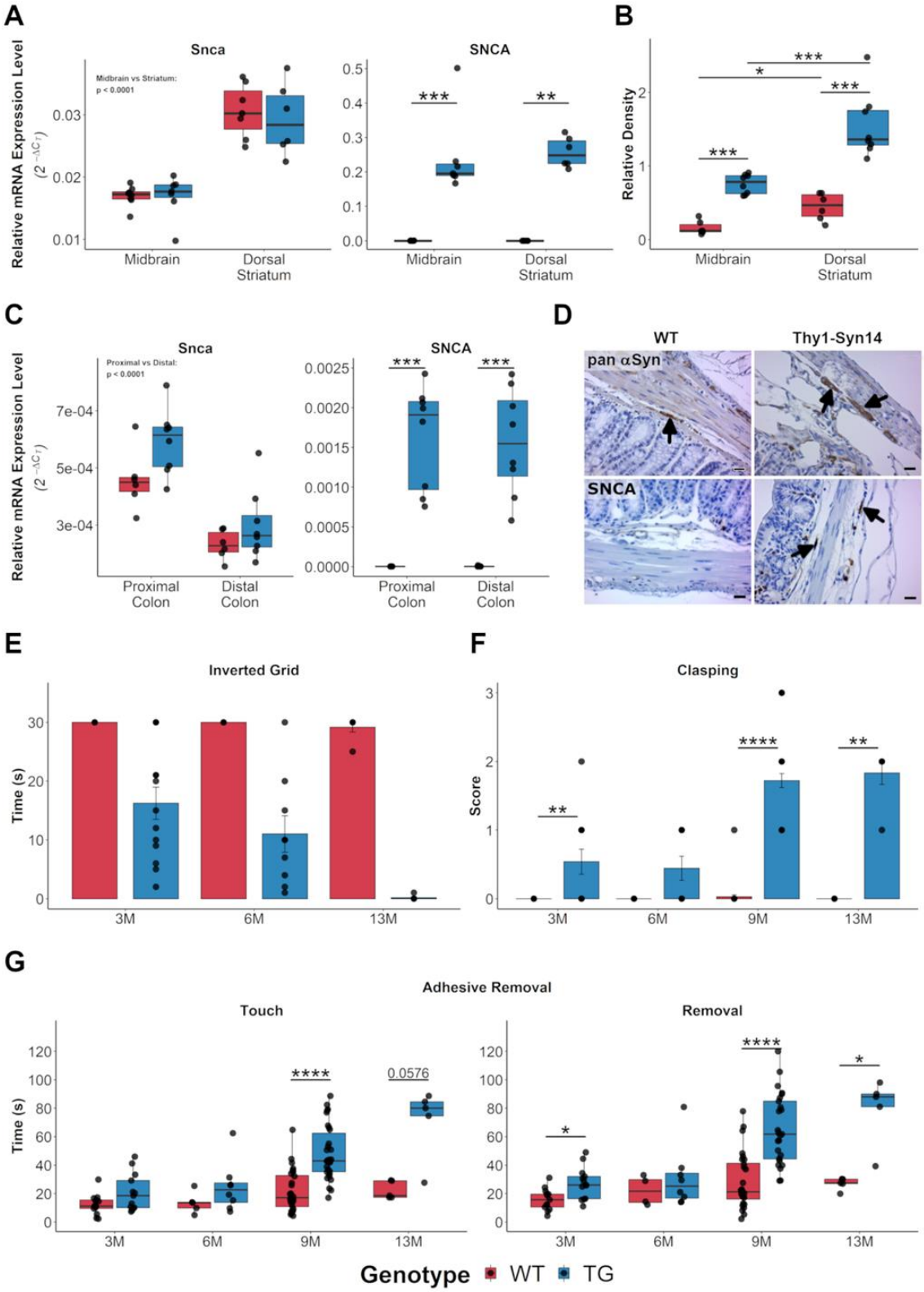
A
Snca
SNCA
Midbrain vs Striatum:
p < 0.0001
Relative mRNA Expression Level
Midbrain
Dorsal Striatum
B
Relative Density
C
Snca
SNCA
Proximal vs Distal:
p < 0.0001
Proximal Colon
Distal Colon
D
WT
Thy1-Syn14
pan αSyn
SNCA
E
Inverted Grid
Time (s)
3M
6M
13M
F
Clasping
Score
9M
G
Adhesive Removal
Touch
Removal
0.0576
Genotype
WT
TG

Figure 1 | Thy1-Syn14 mice have pronounced alpha-synuclein and motor impairment phenotypes

(A) Relative mRNA expression levels for *Snca* (left panel) do not differ between Thy1-Syn14 (TG, blue) mice and wild-type littermates (WT, red), but are significantly different between ventral midbrain and dorsal striatum. *SNCA* (right panel) is only expressed in TG mice and at identical levels between regions. Mice were 9 months old. Normalized to *Gapdh.*

(B) Relative density measures from Western blots for pan-αSyn in the ventral midbrain and dorsal striatum. Mice were 9 months old. Normalized to α-tubulin. See also **Figure S2**.

(C) Relative mRNA expression levels for *Snca* (left panel) do not significantly differ between Thy1-Syn14 (TG, blue) mice and wild-type littermates (WT, red), but are significantly different between proximal and distal colon regions. *SNCA* (right panel) is only expressed in TG mice at identical levels between regions. Mice were 9 months old. Normalized to *Gapdh.*

(D) Representative images (Scale bar: 25µm) from immunohistochemical stainings showing that SNCA in enteric neurons (arrow, right lower panel) is only expressed in TG animals, while both WT and TG mice express pan-αSyn (top row panel, black arrows). Mice were 9 months old.

(E-G) Animals were tested at different ages (3M, 6M, 9M*, 13M) for gross and fine motor skills by (E) inverted grid (*not for 9M), (F) hindlimb clasping, and (G) adhesive removal. All tests show a progressive increase in motor deficits. Each age group was a separate cohort. The results for 9M are the baseline results of the experimental cohort.

Stats: Mann-Whitney U, corrected for FDR; *, $p < 0.05$, **, $p < 0.01$, ***, $p < 0.001$, ****,$p < 0.0001$

WT, wild-type littermates; TG, Thy1-Syn14 animals, 3M, 3 months old; 6M, 6 months old; 9M, 9 months old; 13M, 13 months old

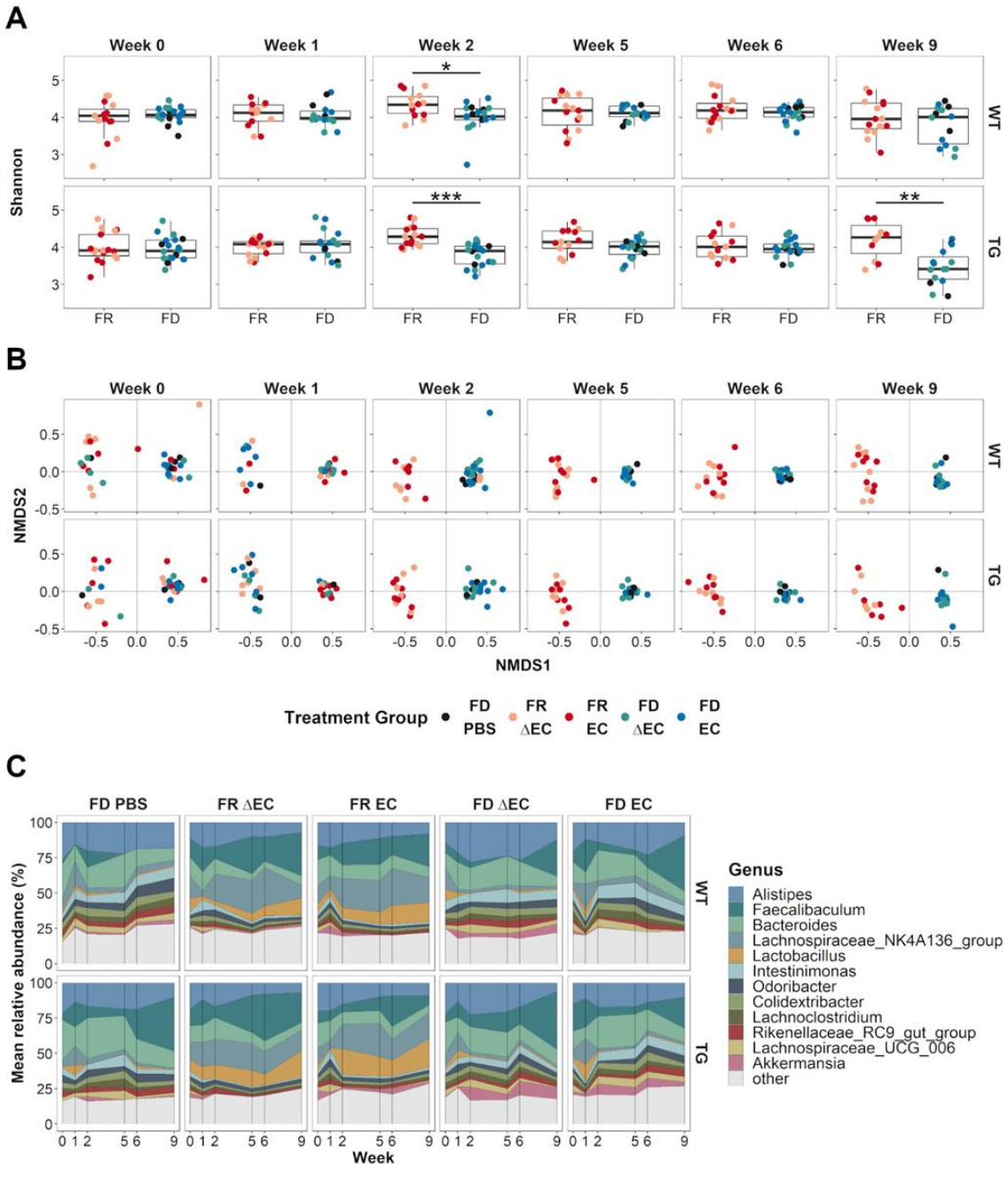
A
Week 0
Week 1
Week 2
Week 5
Week 6
Week 9
Shannon
WT
TG
FR
FD
*
***
**
B
NMDS2
NMDS1
Treatment Group
FD PBS
FR ΔEC
FR EC
FD ΔEC
FD EC
C
Mean relative abundance (%)
Week
Genus
Alistipes
Faecalibaculum
Bacteroides
Lachnospiraceae_NK4A136_group
Lactobacillus
Intestinimonas
Odoribacter
Colidextribacter
Lachnoclostridium
Rikenellaceae_RC9_gut_group
Lachnospiraceae_UCG_006
Akkermansia
other

Figure 2 | Longitudinal changes in microbial diversity and composition shifts are dietary driven

(A) Boxplots illustrating alpha diversity for the two diet challenges at different time points and both genotypes separately. The absence of dietary fibre (FD) reduced microbial diversity significantly at week 2 in WT ($p < 0.05$) and TG ($p < 0.001$) animals. At week 2 we started the gavages. In TG animals, microbial diversity is again significantly ($p < 0.01$) reduced at week 9. *Stats*: Mann-Whitney U corrected for FDR; *, $p < 0.05$; **, $p < 0.01$; ***, $p < 0.001$.

(B) Non-metric multi-dimensional scaling (NMDS) representations for beta diversity showing the different treatment groups facetted by genotype (row) and the different time points (week, column). We observe a composition shift leading to two homogeneous clusters by week 2. This separation came from the dietary challenges.

(C) Temporal distribution of relative abundance for the 12 most abundant and relevant taxa on the genus level for weeks 0 (baseline), 1, 2, 5, 6 and 9. Both WT (top row) and TG (bottom row) mice showed similar changes in relative abundance for the different taxa. Differences were observed between the diet challenge groups.

See also **Figure S3.**

WT, wild-type littermates; TG, Thy1-Syn14 mice; FD, fibre deprived; FR, fibre rich; PBS, phosphate buffered saline solution; ΔEC, curli-KO E. coli; EC, wild-type curli expressing E. coli

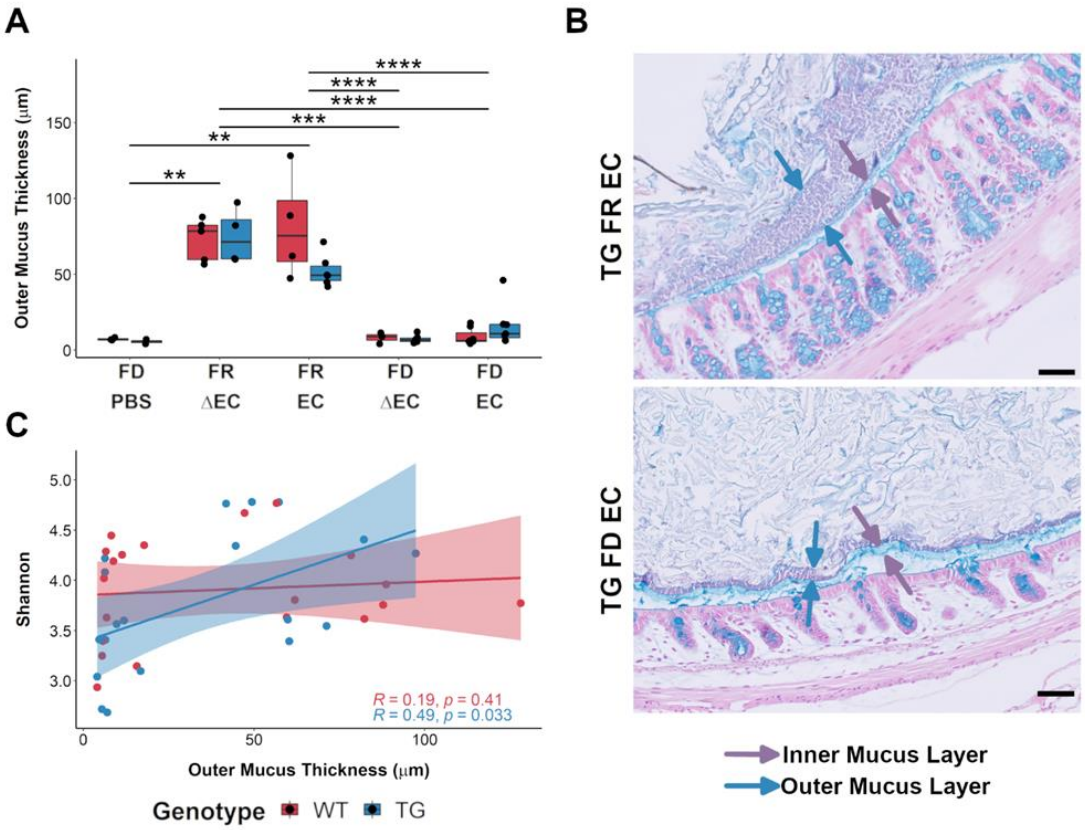
A
Outer Mucus Thickness (μm)
150
100
50
0
****
****
****
***
**
**
FD PBS
FR ΔEC
FR EC
FD ΔEC
FD EC
B
TG FR EC
TG FD EC
Inner Mucus Layer
Outer Mucus Layer
C
Shannon
5.0
4.5
4.0
3.5
3.0
R = 0.19, p = 0.41
R = 0.49, p = 0.033
0
50
100
Outer Mucus Thickness (μm)
Genotype WT TG

Figure 3 | Microbiome-mediated outer mucus erosion is associated to reduced diversity

(A) Boxplot of outer mucus thickness measurements. The FD challenge causes a vast reduction in outer mucus thickness. Stats: Mann-Whitney U test, corrected for FDR; **, $p < 0.01$; ***, $p < 0.001$; ****; $p < 0.0001$.

(B) Representative images illustrating the differences in outer mucus erosion between FR (top) and FD (bottom) challenged mice. The red arrows delimit the outer mucus layer.

(C) Scatterplots of Spearman rank tests comparing alpha diversity (y-axis) and mucus thickness (x-axis) in both genotypes separately. There is a significant positive correlation between microbial diversity and mucus thickness in Thy1-Syn14 animals independent of the other challenges. Stats: Spearman rank test. See also **Figure S8.**

WT, wild-type littermates; TG, Thy1-Syn14; FD, fibre deprived; FR, fibre rich; PBS, phosphate buffered saline solution; ΔEC, curli-KO E. coli; EC, wild-type curli expressing E. coli

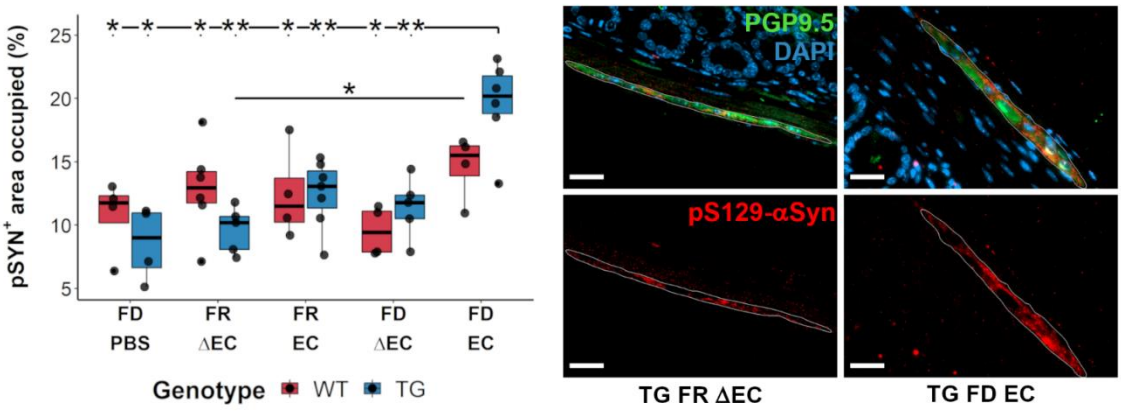
pSYN+ area occupied (%)
25
20
15
10
5
FD PBS
FR ΔEC
FR EC
FD ΔEC
FD EC
Genotype
WT
TG
PGP9.5
DAPI
pS129-αSyn
TG FR ΔEC
TG FD EC

Figure 4 | Curli-driven phospho-synuclein accumulation in fibre deprived challenged Thy1-Syn14 mice

Boxplot illustrating the changes of area occupied by pS129-αSyn^{+} forms in ganglions of the myenteric plexus of the colon. Only TG mice on the combined challenge have an increased area occupied for pS129-αSyn^{+} forms. Stats: Mann-Whitney U test, not corrected for FDR. Representative images below, illustrate the average differences between FR ΔEC and FD EC challenged Thy1-Syn14 mice. Besides the area occupied, the pS129-αSyn^{+} particles are also bigger in FD EC challenged mice. See also **Figure S9.**

WT, wild-type littermates; TG, Thy1-Syn14; FD, fibre deprived; FR, fibre rich; PBS, phosphate buffered saline solution; ΔEC, curli-KO E. coli; EC, wild-type curli expressing E. coli

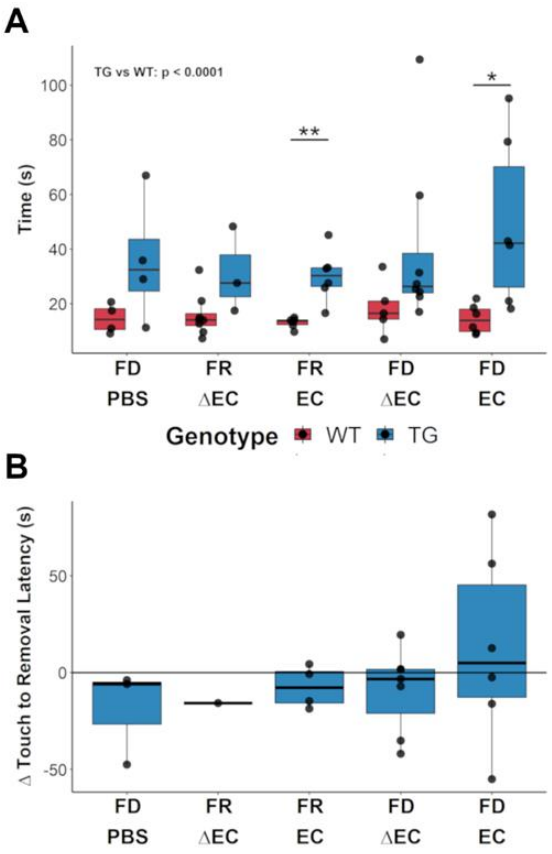
A
TG vs WT: p < 0.0001
Time (s)
100
80
60
40
20
**
*
FD PBS
FR ΔEC
FR EC
FD ΔEC
FD EC
Genotype
WT
TG
B
Δ Touch to Removal Latency (s)
50
0
-50
FD PBS
FR ΔEC
FR EC
FD ΔEC
FD EC

Figure 5 | Challenge effect on motor impairment in a subset of Thy1-Syn14 mice despite of an already strong transgene driven phenotype

(A) Boxplots illustrating the latency for removal in the different treatment groups (x-axis) for WT (red) and TG (blue) animals after 9 weeks. The results shown are for the first paw and from the first replicate. WT animals do not show any difference. TG mice on the other hand that have been FD EC challenges showed greater latency to remove the adhesive tape. There are significant in the FR EC and FD EC groups between WT and TG mice. Stats: Mann-Whitney U test, not corrected for FDR; *, $p < 0.05$; **, $p < 0.01$.

(B) Summary plot for TG animals illustrating how the adhesive removal performance changed from baseline to endpoint when focusing on the time difference from touch to removal. Most animals improved in performance from baseline to endpoint. Only the FD EC group shows for 3 out of 6 animals a performance drop. Note: for the TG FR ΔEC group only one animal performed normally and is therefore not representative. (FD PBS: n=3, FR ΔEC: n=1, FR EC: n=5, FD ΔEC: n=6, FD EC: n=6).

WT, wild-type littermates; TG, Thy1-Syn14; FD, fibre-deprived; FR, fibre-rich (normal chow); PBS, phosphate buffered saline; ΔEC, curli-KO E. coli; EC, wild-type curli expressing E. coli

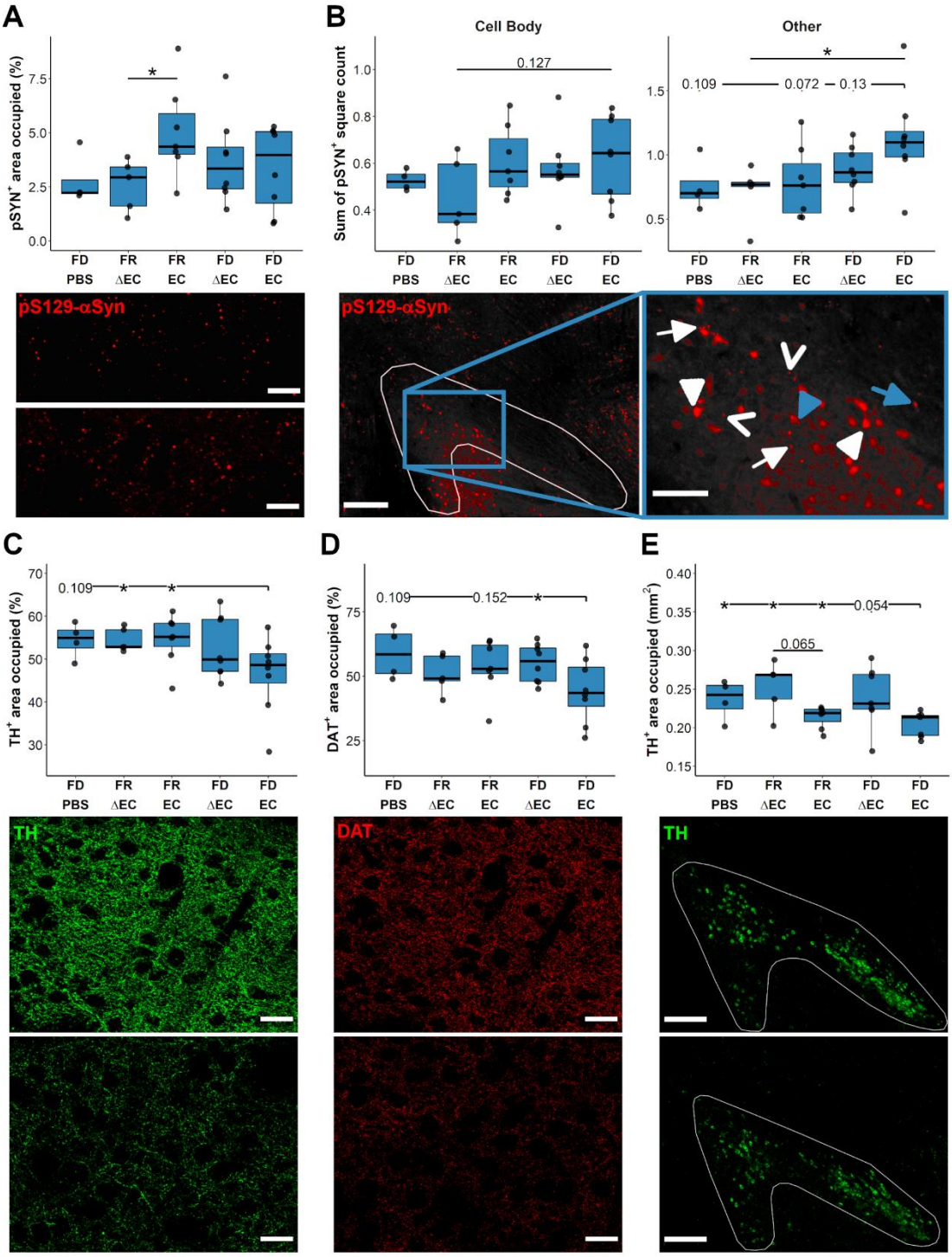
A
B
Cell Body
Other
pSYN+ area occupied (%)
Sum of pSYN+ square count
0.127
0.109
0.072
0.13
FD PBS
FR ΔEC
FR EC
FD ΔEC
FD EC
pS129-αSyn
C
D
E
TH+ area occupied (%)
DAT+ area occupied (%)
TH+ area occupied (mm2)
0.109
0.152
0.054
0.065
TH
DAT

Figure 6 | Curli-driven nigrostriatal pathological changes in Thy1-Syn14 mice are exacerbated after fibre deprivation

(A - B) Quantification and representative images of immunofluorescent pS129-αSyn stainings of the (A) dorsal striatum and (B) the SNpc.

(A) The pS129-αSyn^{+} area occupied is increased under the EC challenge. The diet challenge does contribute to lesser extent. The representative images (40X, scale bar: 50µm) below, illustrate the differences in pS129-αSyn accumulations between FR ΔEC and FR EC challenged TG mice.

(B) In the SNpc we distinguished between accumulations in cell bodies (left panel) and other forms (right panel) based of cellular morphology. See Material and Methods for details on relative quantification. Again, in EC challenged animals, we found increased pS129-αSyn^{+} accumulation. For other forms (see details in the main text) the dietary challenge appeared to exacerbate the EC pathology. The representative images (left: 10X tiles, scale bar: 250µm; right: zoom in, scale bar: 100µm) below illustrate the different observed forms of pS129-αSyn^{+} accumulations (see details on the different forms in main text).

(C - E) Quantification and representative images for (C) TH and (D) DAT in the dorsal striatum and (E) TH in the SNpc.

(C-D) FD EC transgenic animals exhibit a decrease in fibre and synaptic density. The representative high magnification (40X, scale bar: 50µm) images below illustrate more pronounced differences between FR ΔEC and FD EC transgenic animals.

(E) In the SNpc, curli drives neurodegeneration independently of the diet. FD does however exacerbate the pathology. The representative images (10X; scale bar: 250µm) illustrate the average differences between FR ΔEC and FD EC transgenic animals.

Stats: Mann-Whitney U test, not corrected for FDR

SNpc, substantia nigra pars compacta; FD, fibre-deprived (diet); FR, fibre-rich (diet) (normal chow); PBS, phosphate buffered saline; ΔEC, curli-KO E. coli; EC, wild-type curli expressing E. coli

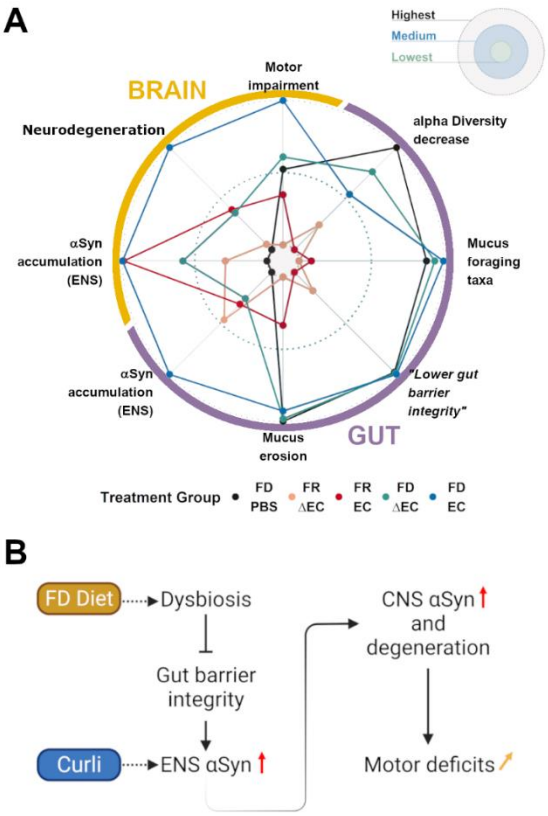
A
Highest
Medium
Lowest
BRAIN
Motor impairment
Neurodegeneration
alpha Diversity decrease
αSyn accumulation (ENS)
Mucus foraging taxa
αSyn accumulation (ENS)
"Lower gut barrier integrity"
Mucus erosion
GUT
Treatment Group
FD PBS
FR ΔEC
FR EC
FD ΔEC
FD EC
B
FD Diet
Dysbiosis
Gut barrier integrity
Curli
ENS αSyn
CNS αSyn and degeneration
Motor deficits

Figure 7 | A multi-challenged driven sequence of events for PD progression

(A) Radar plot of the total output for each challenge group in Thy1-Syn14 mice. The centre of the plot defines the treatment with the lowest and the outline the one that showed the highest effect on Thy1-Syn14 mice. Overall, the combination of FD and EC has the greatest impact on αSyn overexpressing mice. View main text for more details.

(B) Scheme of a potential sequence of events based on the results in this study. FD challenge leads to changes in the microbiome (dysbiosis), which in turn affects the gut barrier integrity and consequently facilitates the interaction of curli with the submucosa and the plexuses. As a result, αSyn abnormally accumulates. This is further seen in the brain where we observed αSyn accumulation, accompanied by neurodegeneration in the nigrostriatal pathway. these changes impact the locomotion and exacerbate the already strong motor deficits in Thy1-Syn14 mice.

CNS, central nervous system; ENS, enteric nervous system; FD, fibre-deprived; FR, fibre-rich (normal chow); PBS, phosphate buffered saline; ΔEC, curli-KO E. coli; EC, wild-type curli expressing E. coli

4 Pathological changes in the pedunculopontine nucleus and locus coeruleus after fiber deprivation and Curli exposure

4.1 Preface

The Substantia Nigra pars compacta (SNpc) and the dorsal striatum are the hallmark regions affected in PD. Neurodegeneration and consequently the depletion of dopamine trafficking in the nigrostriatal pathway is the pathognomonic mechanism manifesting in the typical clinical motor symptoms of the disease. Braak's spreading hypothesis, however, suggests that αSyn inclusions are found in regions preceding the nigrostriatal pathway decades before the appearance of clinical motor symptoms (Braak et al., 2003b, 2003a). It posits that the intracerebral diease process starts in the dorsal motor nucleus of the vagus (DMV) and continues to spread to higher regions of the brainstem before reaching midbrain structures (Braak et al., 2003b, 2003a). Amongst these regions are the locus coeruleus (LC) and the pedunculopontine nucleus (PPN).

In the previous chapter, I mentioned the role of the gut-brain-axis in disease progression and how αSyn can spread from the enteric nervous system (ENS) to lower brainstem structures, such as the DMV, LC and PPN. Due to non-validated methodological limits, I did not include my analysis of these structures in that publication.

Therefore, the following results have to be taken with caution and the quantitative analyses have to be seen as an approximation of the actual neuropathological changes. I limit the value of the results to such because our experimental protocol was initially not foreseen to analyse these regions (see Material and Methods in Chapter 3). Most protocols, for the analysis of

brainstem structures, use coronal sections of 20-30µm (Kim et al., 2019; Kroeger et al., 2017; Schmidt et al., 2019; Thompson and Felsen, 2013; Zhou et al., 2008).

There were two main problems I faced to analyse these regions using our standard preparation protocol:

1) Sagittal sectioning

   To my knowledge there are no comparative studies analysing the different regions using sagittal sections. Consequently, a reference atlas had to be created to distinguish between the different lateromedial levels.

2) 50µm thick sections

   The thickness of the sections made it difficult to

   a) capture the regions of interest

   and

   b) get the same level for every sample

The following Material and Methods will focus on the elaborate approach allowing an approximative morphometric quantification of the LC and PPN. Additionally, to simplify the analysis, the focus was kept on the Thy1-Syn14 animals, identical to what was done in Schmit et al., 2022.

Looking into these regions was initially suggested by Prof. Dr. Wolfgang Oertel after discussions with Prof. Paul Wilmes (co-supervisor). All subsequent work, from immunofluorescent staining, microscopy, morphometric atlas creation, analysis and figure generation was performed by myself.

Additional information can be found in **Appendix B**.

4.2 Material and Methods

Morphometric atlas

These morphometric atlases were created to allow an approximative quantification in the pedunculopontine nucleus (PPN) and the locus coeruleus (LC). This allowed me to group the acquired microscopy pictures from the experimental samples (see Material and Methods from **"Pathogenic effects of fibre deprivation and Curli in Parkinson's disease"**) according to their lateral-to-medial levels.

The preparation of the brain sections was performed as described before (Garcia et al., 2022; Schmit et al., 2022) with a minor adjustment. Fixed hemibrains were cut at 30µm and not 50µm. The subsequent Immunofluorescence stainings were performed as previously described (Garcia et al., 2022; Schmit et al., 2022). To stain for cholinergic neurons in the PPN, the polyclonal goat anti-ChAT antibody (ab144P, Merck Millipore, 1:500) and for noradrenergic neurons in the LC, the polyclonal rabbit anti-TH antibody (AB152, Merck Millipore, 1:000) were used. The former was coupled to a donkey anti-goat Alexa Fluor® 488 (ab150133, Abcam, 1:1000) and the latter to a goat anti-rabbit Alexa Fluor® 647 (ab150063, Abcam, 1:1000).

The procedure was the same for both regions (**Supplementary Figure 1**). A consecutive series of sections were stained either for ChAT (PPN) or TH (LC). The images were acquired with a Zeiss AxioImager Z1 upright microscope as described before (Garcia et al., 2022; Schmit et al., 2022). For the PPN, I acquired 2x2 tile images at 10x magnification per tile, while for the LC is acquired 1x2 tile images at 10x magnification.

The collected images were further compared to the reference atlas from Allen Brain Atlas (https://mouse.brain-map.org/experiment/thumbnails/100042147?image_type=atlas) to confirm the regions of interest.

For the PPN, I retained 23 sequential images (**Supplementary Figure 2**), and for the LC, 13 sequential images (**Supplementary Figure 3**). Next, the images were grouped by morphologically comparable levels. In Image J, the grouped images were stacked, superposed accordingly and a maximum projection image was generated. Based on this image, the regions of interest (ROI) was defined. This ROI was then used to 1) adjust XY-coordinates and orientation of the images from the experimental samples and 2) measure the relative area occupied of either cholinergic or noradrenergic neurons.

4.3 Results

In the pedunculopontine nucleus and locus coeruleus the combination of bacterial Curli and fiber deprivation leads to a comparable pattern of changes observed in the nigrostriatal pathway

The study by Schmit et al., 2022 elaborated on the sequence of events after mice, particularly transgenic Thy1-Syn14 mice, were fibre-deprived and exposed to bacterial Curli. In the CNS they reported that particularly the combination of both challenges led to an exacerbation of neuronal loss and increased levels of pS129-αSyn^{+} accumulations in the nigrostriatal pathway. It was proposed that these observations were a consequence of a retrograde propagation of abnormal forms of αSyn from the gut to the brain. It was therefore of great interest to further investigate the impact of these challenges on regions preceding the nigrostriatal pathway.

Pedunculopontine nucleus

The pedunculopontine nucleus (PPN) is greatly affected in PD patients and is involved in various locomotor mechanisms (Pahapill and Lozano, 2000). While it has a heterogeneous neuronal population, it densely innervates thalamic structures, the subthalamic nucleus (STN) and the SNpc almost exclusively via cholinergic projections (Pahapill and Lozano, 2000). It has been shown that the PPN connections to the SNpc and the ventral tegmental area (VTA) alter dopamine release to the striatum, further affecting cortical and thalamic structures which get input from the striatum. Hence, changes to the PPN can have a crucial impact on the nigrostriatal pathway and its relayed structures.

Here, the cholinergic neuron population of the PPN were of interest. Therefore the choline acetyltransferase (ChAT) marker was used, which is highly abundant in cholinergic neurons and their projections (Ichikawa et al., 1997). After the images were mapped and grouped according to the reference atlas, the relative area occupied by ChAT^{+} cell bodies was measured. The results indicate that the combination of both bacterial Curli and fiber deprivation have the greatest impact and cause a minor but detectable loss of cholinergic neurons in the PPN (**Figure 1A,B**). The representative images (**Figure 1C**) capture this difference between TG FR ΔEC and TG FD EC mice. To note is that even though the differences were greater to the TG FD PBS mice (**Figure 1B**), it was more relevant to compare the TG FR ΔEC and TG FD EC groups since FD was a challenge and ΔEC is considered a negative control for EC.

Changes in αSyn were investigated by targeting pS129-αSyn. I observed that the bacterial Curli challenge had the greatest impact on pS129-αSyn$^+$ accumulations (**Figure 2**). However, compared to the SNpc and dorsal striatum results from Schmit et al., 2022 (Figure 6A,B), fibre-deprivation alone appears to already affect the accumulation of pS129-αSyn (**Figure 2A)**. In combination, however, I observed, on average, the highest accumulations of pS129-αSyn$^+$. When looking at the pS129-αSyn$^+$ cell bodies and other forms separately, it appeared that actually pS129-αSyn$^+$ cell bodies were overall less frequent in presence of dietary fibre and independent of the bacterial Curli challenge. However, when combined, αSyn pathology was exacerbated. (**Figure 2A**, left panel). The increase of "Other" pS129-αSyn$^+$ forms was mainly driven by the Curli exposure and did not seem to be exacerbated under fibre-deprivation (**Figure 2A**, right panel) similar to what has been observed in the dorsal striatum (Schmit et al., 2022, Figure 6). Conformationally, "other" pS129-αSyn$^+$ forms ranged from small spheroids (**Figure 2E**, white open arrow head) to dense bead-like varicosities (**Figure 2E**, white arrow). Latter, oftentimes resembled Lewy neurites based fluorescent intensity and shape, similar to what is observed in post-mortem PD tissue (Del Tredici et al., 2002). In more rare cases they were even more of a corkscrew-like shape (**Figure 2A**, blue open arrowhead). In bodies, two types of pS129-αSyn$^+$ accumulations were observed: nuclear (majority) and cytoplasmic spheroids.

Locus coeruleus

In PD, cell loss in the LC, which projects into the caudal PPN (Jones and Yang, 1985; Martinez-Gonzalez et al., 2011), can be as high as 93% in the most severe cases (Giguère et al., 2018; Oertel et al., 2019). The LC is involved in a variety of basic physiological function. In PD, the loss of neurons in the LC is associated with both non-motor and motor symptoms (Bari et al., 2020).

The noradrenergic neurons express tyrosine hydroxylase (TH) (Weihe et al., 2006). Therefore, an anti-TH antibody was used to investigate neuronal changes in the LC. The results showed that, similar to what was already observed in the PPN, the combination of bacterial Curli and fibre-deprivation led to increased loss of TH$^+$ neurons in the LC (**Figure 3A**). The two low values observed for the FR ΔEC mice is most likely a consequence of the above elaborated technical limits and the reduced number of sections containing the LC. Consequently, the representative images were chosen based on matching latero-medial depth. In **Figure 3B**, the images are from a medially located LC plan and depict rather extreme differences observed between combinatorial challenged (FD EC) and control mice (FD PBS).

Overall, there was a striking similarity between the patterns observed here and the results from the nigrostriatal pathway in Schmit et al., 2022. Nevertheless, as mentioned above, these results have to be taken with caution and viewed as quantitative approximations due to the aforementioned methodological limits.

4.4 Figures

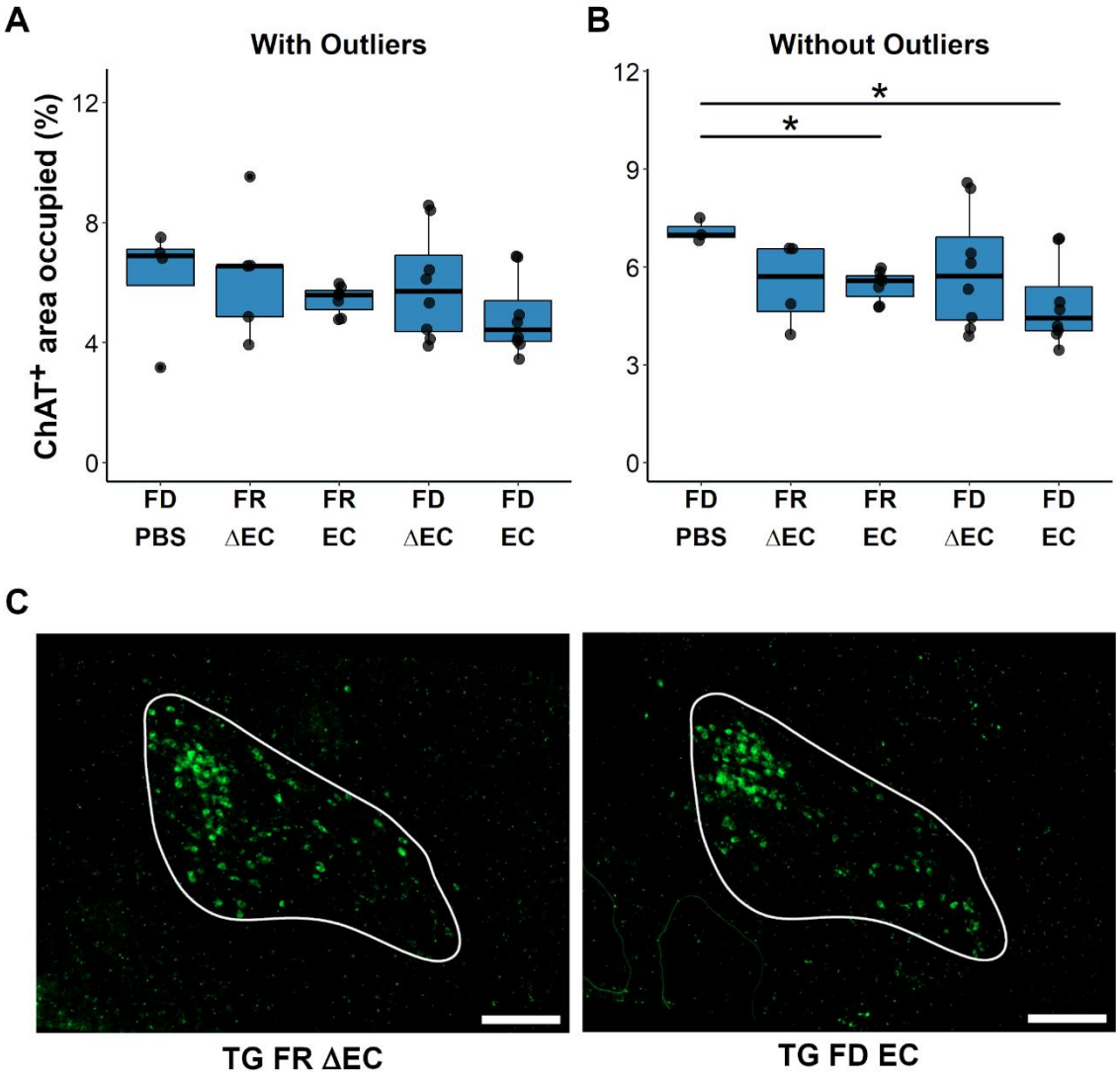
A
With Outliers
ChAT+ area occupied (%)
0
4
8
12
FD PBS
FR ΔEC
FR EC
FD ΔEC
FD EC
B
Without Outliers
0
3
6
9
12
*
*
FD PBS
FR ΔEC
FR EC
FD ΔEC
FD EC
C
TG FR ΔEC
TG FD EC

Figure 9 | Loss of cholinergic neurons in the pedunculopontine nucleus upon combining challenges in transgenic animals

(A - B) Assessment of relative area occupied of $ChAT^+$ neurons in the pedunculopontine nucleus (A) including outliers and (B) after the removal of outliers. (Stats: Mann-Whitney U, not FDR corrected for multiple comparison)

(C) Representative images (10x tiles, scale bar: 250µm) of the area occupied of $ChAT^+$ neurons in the pedunculopontine nucleus in FR ΔEC and FD EC transgenic animals

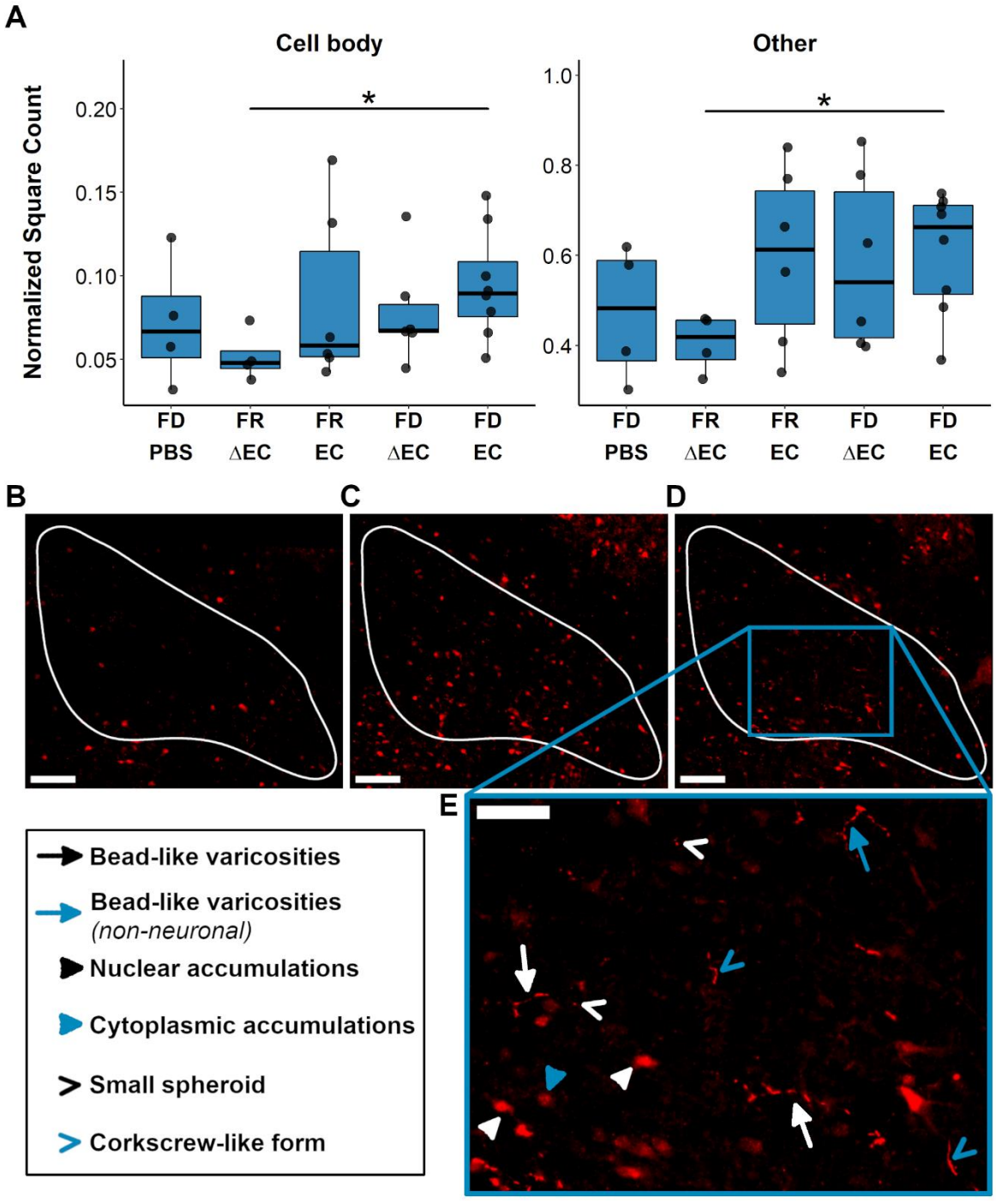
A
Cell body
Other
Normalized Square Count
0.20
0.15
0.10
0.05
1.0
0.8
0.6
0.4
*
*
FD PBS
FR ΔEC
FR EC
FD ΔEC
FD EC
B
C
D
E
Bead-like varicosities
Bead-like varicosities (non-neuronal)
Nuclear accumulations
Cytoplasmic accumulations
Small spheroid
Corkscrew-like form

Figure 10 | Phosphorylated alpha-synuclein accumulations in the PPN are mainly increased in curli challenged transgenic animals

(A) Curli is the main driver for the accumulations of pS129-aSyn^{+} accumulations in the PPN. Accumulations on the cell bodies additionally appear to be increased under fibre-deprivation. (Stats: Mann-Whitney U, not FDR corrected for multiple comparison)

(B) Representative images of the PPN for TG FR ΔEC mice (10x, Scale bar: 150µm). Neither pS129-αSyn^{+} cell bodies nor other pS129-αSyn^{+} forms are notably increased in these animals.

(C) Representative images of the PPN for TG FR EC mice (10x, Scale bar: 150µm). This image shows an exceptionally high count of pS129-αSyn^{+} cell bodies. However, the amount of other pS129-αSyn^{+} forms reflects overall observations and is comparable to what was seen in TG FD EC mice.

(D) Representative images of the PPN for TG FD EC mice (10x, Scale bar: 150µm). This image shows a rather low count of pS129-αSyn^{+} cell bodies for this group. It does reflect the overall amount of other pS129-αSyn^{+} forms observed in these mice.

(E) Zoom in of the picture (D) (Scale bar:100µm). Details in the main text.

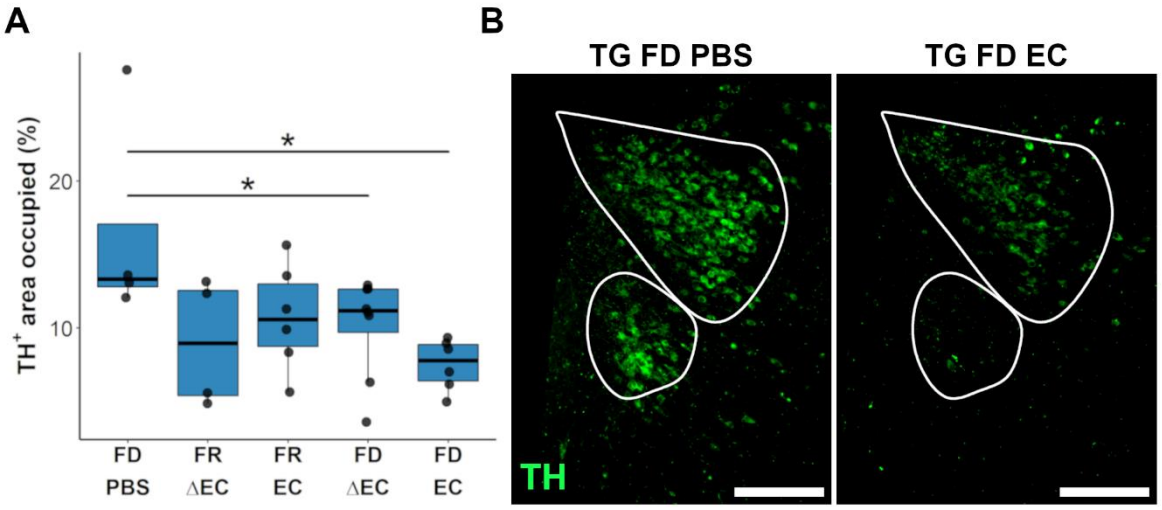
A
B
TG FD PBS
TG FD EC
TH+ area occupied (%)
20
10
*
*
FD PBS
FR ΔEC
FR EC
FD ΔEC
FD EC
TH

Figure 11 | Curli and fibre deprivation lead to loss of TH+ neurons in the Locus coeruleus

(A) Boxplot illustrating the approximative quantitation assessment of TH+ neurons of the Locus coeruleus. (Stats: Mann-Whitney U, not FDR corrected for multiple comparison)

(B) Representative images (10X tiles, scale bar: 250μm) illustrating more extreme cases comparing FD PBS to FD EC transgenic mice.

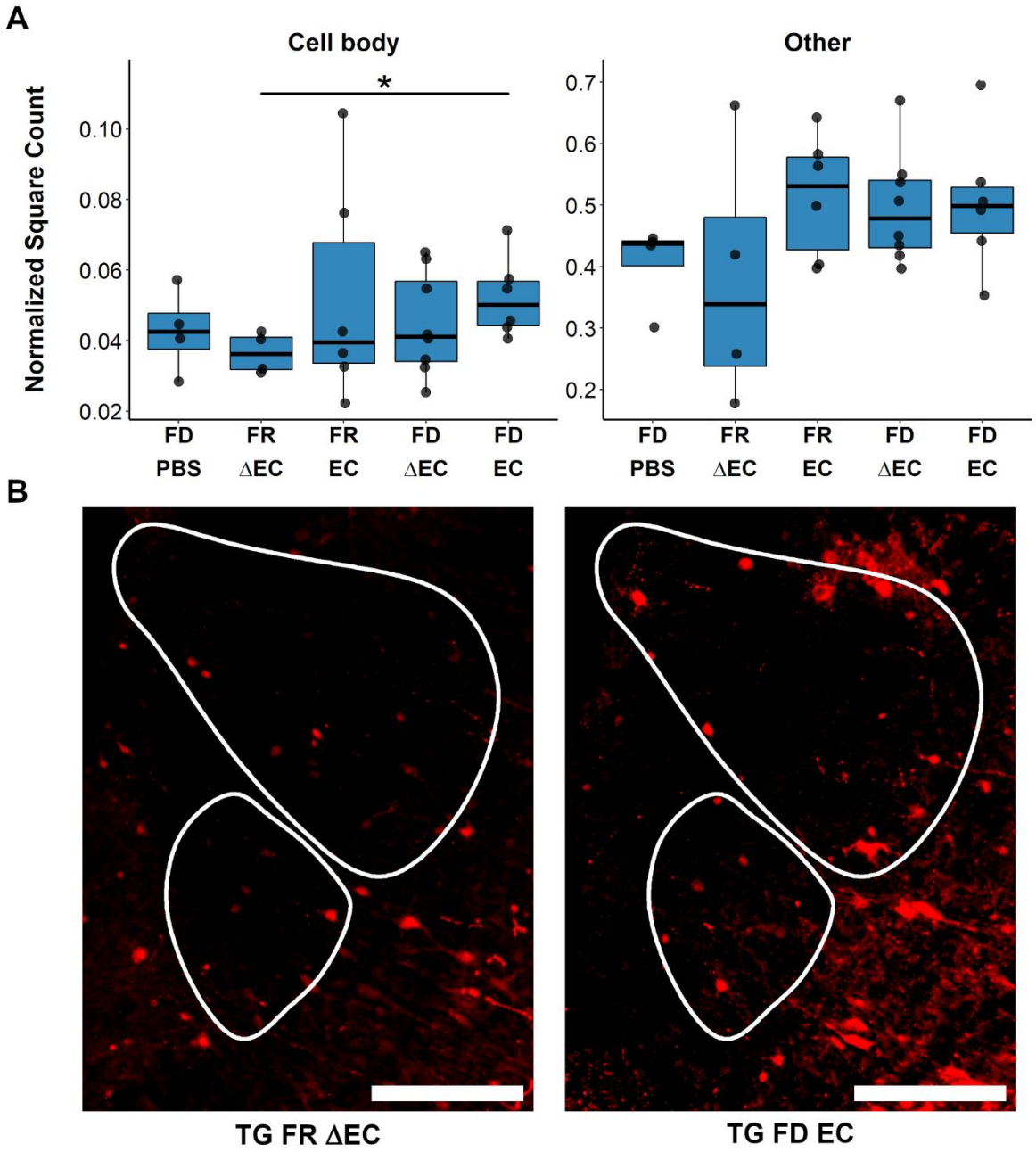
A
Cell body
Other
Normalized Square Count
*
0.10
0.08
0.06
0.04
0.02
0.7
0.6
0.5
0.4
0.3
0.2
FD PBS
FR ΔEC
FR EC
FD ΔEC
FD EC
B
TG FR ΔEC
TG FD EC

Figure 12 | Curli is the main driver of phosphorylated αSyn in the Locus coeruleus

(A) Curli is the main driver of pS129-αSyn^{+} accumulations in the LC. Accumulations of other forms, more dense and aggregated moieties, appear to be increased under fibre-deprivation. (Stats: Mann-Whitney U, not FDR corrected for multiple comparison)

(B) Representative images of pS129-αSyn staining in TG FR ΔEC and TG FD EC mice (10X tiles, Scale bar:250µm). Aggregated forms are almost completely absent in the TG FR ΔEC animals. Expecially striking are the surrounding areas, which are intensily pS129-αSyn+ in TG FD EC mice.

5 An archaeal compound as a driver of Parkinson's disease pathogenesis

Jean-Pierre Trezzi, Velma TE Aho, Christian Jäger, Oskar Hickl, Benoit Kunath, Mélanie H Thomas, **Kristopher J Schmit**, Pierre Garcia, Alessia Sciortino, Camille Martin-Gallausiaux, Rashi Halder, Oihane Uriarte Huarte, Tony Heurtaux, […], Manuel Buttini, […], Paul Wilmes

Submitted to Nature

5.1 Preface

Microbial changes in PD are well documented. However, understanding the underlying mechanisms of host-microbes interactions is to this date very limited. Multi-omic approaches help to shed light on these complex matters. Our team developed a multi-omics workflow to investigate fecal samples from PD, iRBD and healthy controls on the DNA, RNA, protein and metabolite levels.

Metabolomics analysis identified two unknown compounds increased in PD and iRBD patients, of which one was subsequently identified as 2-hydroxypyridine (2-HP). The compound was tested in different *in vitro* systems and *in vivo*.

The following manuscript has been submitted to Nature and once it is accepted for review, will be available as pre-print on the Nature servers.

I was involved in the *in vivo* part of this study: I participated in study design and writing of the animal ethics protocol, and assisted in the experimental procedures led by Mélanie Thomas and Pierre Garcia (results shown in Figure 3 and Extended Data Figure 9). Additionally, I assisted Dr. Jean-Pierre Trezzi in the early stages of the project to prepare human stool samples for extraction. Additionally, we received funding from the Jean Think Foundation to finance the initial steps of the *in vivo* experiments.

Supplementary data can be found in **Appendix C**.

5.2 Publication

Title

An archaeal compound as a driver of Parkinson's disease pathogenesis

Authors/Affiliation

Jean-Pierre Trezzi[1,2§], Velma T. E. Aho[1§], Christian Jäger[1], Sebastian Schade[3,4], Annette Janzen[5], Oskar Hickl[1], Benoit Kunath[1], Mélanie H. Thomas[1,6], Kristopher J. Schmit[1,6], Pierre Garcia[1,6], Alessia Sciortino[1,6], Camille Martin-Gallausiaux[1], Rashi Halder[1], Oihane Uriarte Huarte[1,6], Tony Heurtaux[6,7], Ursula Heins-Marroquin[1], Gemma Gomez-Giro[1], Katrin Weidenbach[8], Léa Delacour[1], Cédric C. Laczny[1], Polina V. Novikova[1], Javier Ramiro-Garcia[1], Randolph R. Singh[1,9], Begoña Talavera Andújar[1], Laura A. Lebrun[1], Annegrait Daujeumont[1], Janine Habier[1], Xiangyi Dong[1], Floriane Gavotto[1], Anna Heintz-Buschart[10], NCER-PD Consortium, Jochen G. Schneider[1,11], Nico Jehmlich[12], Martin von Bergen[12], Emma L. Schymanski[1], Ruth A. Schmitz[8], Jens C. Schwamborn[1], Enrico Glaab[1], Carole L. Linster[1], Toshimori Kitami[13], Manuel Buttini[1,6], Patrick May[1], Claudia Trenkwalder[4,14], Wolfgang Oertel[5], Brit Mollenhauer[3,4], Paul Wilmes[1,7*]

1. Luxembourg Centre for Systems Biomedicine, University of Luxembourg, Esch-sur-Alzette, Luxembourg
2. Integrated Biobank of Luxembourg, Luxembourg Institute of Health, Dudelange, Luxembourg
3. Department of Neurology, University Medical Center Göttingen, Göttingen, Germany
4. Paracelsus-Elena-Klinik, Kassel, Germany
5. Department of Neurology, Philipps-University Marburg, Marburg, Germany
6. Luxembourg Center of Neuropathology (LCNP), Dudelange, Luxembourg
7. Department of Life Sciences and Medicine, Faculty of Science, Technology and Medicine, University of Luxembourg, Belvaux, Luxembourg
8. Christian-Albrechts-Universität zu Kiel, Kiel, Germany
9. Unité Contamination Chimique des Ecosystèmes Marins, IFREMER (Institut Français de Recherche pour l'Exploitation de la Mer), Nantes, France
10. Biosystems Data Analysis, Swammerdam Institute for Life Sciences, Faculty of Science, University of Amsterdam, Amsterdam, The Netherlands
11. Departments of Internal Medicine and Psychiatry and Psychotherapy, Saarland University Medical Center at Homburg/Saar, Homburg, Germany
12. Helmholtz-Zentrum für Umweltforschung – UFZ GmbH, Department Molekulare Systembiologie, Leipzig, Germany
13. RIKEN Center for Integrative Medical Sciences, Kanagawa, Japan
14. Department of Neurosurgery, University Medical Center Göttingen, Göttingen, Germany

§ These authors contributed equally to this work
* Corresponding author: Paul Wilmes, paul.wilmes@uni.lu, (+352) 46 66 44 6188

Abstract

Patients with Parkinson's disease (PD) exhibit differences in their gut microbiomes compared to healthy individuals (Benakis et al., 2020; Boertien et al., 2019; Romano et al., 2021). Although differences have most commonly been described in the abundances of bacterial taxa, viruses and archaea have also been implicated (Qian et al., 2020; Romano et al., 2021; Rosario et al., 2021). Mechanistic links between gut microbes and PD pathogenesis remain elusive but could involve molecules that promote α-synuclein aggregation (Benakis et al., 2020; Fang et al., 2020). Here, we show that 2-hydroxypyridine (2-HP) represents a key molecule for the pathogenesis of PD. We observe significantly elevated 2-HP levels in faecal samples from patients with PD or its prodrome, idiopathic REM sleep behaviour disorder (iRBD), compared to healthy controls. 2-HP is correlated with the archaeal species *Methanobrevibacter smithii* and with genes involved in methane metabolism, and it is detectable in isolate cultures of *M. smithii*. We demonstrate that 2-HP is selectively toxic to transgenic α-synuclein overexpressing yeast and increases α-synuclein aggregation in a yeast model as well as in human induced pluripotent stem cell derived enteric neurons. It also exacerbates PD-related motor symptoms, α-synuclein aggregation, and striatal degeneration when injected intrastriatally in transgenic mice overexpressing human α-synuclein. Our results highlight the effect of an archaeal molecule in relation to the gut-brain axis, which is critical for the diagnosis, prognosis and treatment of Parkinson's disease.

Main

Changes to the gut microbiome have been implicated in the pathogenesis of idiopathic conditions such as cancer, autoimmune, metabolic, and neurodegenerative diseases. For all, incidences have been rising in the past decades (Sung et al., 2021; Matson et al., 2021; Fan and Pedersen, 2021; Dorsey et al.; Miyauchi et al., 2022; Fang et al., 2020). However, the causal mechanisms remain largely elusive, not least for disorders such as Parkinson's disease (PD), where connections between distal body sites (the gut) and organs classically associated with the disease (the brain) are not obvious. Nevertheless, as the hub of exposures to microbiome-derived molecules, the gut represents a main candidate site for the initiation of pathogenic processes which may subsequently spread systemically, for example via the gut-brain axis (Fang et al., 2020; Hawkes et al., 2007).

Cross-sectional studies have highlighted microbial community differences in the gut of PD patients compared to healthy control subjects (Benakis et al., 2020; Fang et al., 2020; Romano et al., 2021). Changes in microbial abundances have also been identified in patients with idiopathic rapid eye movement sleep behaviour disorder (iRBD) (Heintz-Buschart et al., 2018), which is recognized as a prodromal stage of α-synucleinopathies (Högl et al., 2018). A smaller number of studies have explored specific molecules, such as faecal short-chain fatty acids (SCFAs) (Aho et al., 2021; Unger et al., 2016), or used multi-omic and computational approaches to identify microbial genes or functions which may be enriched or depleted in PD (Baldini et al., 2020; Qian et al., 2020; Rosario et al., 2021). However, although agreement exists in relation to taxa found to be enriched in PD including the genera Akkermansia, Bifidobacterium and Lactobacillus (Boertien et al., 2019; Romano et al., 2021), there is currently no consensus on the functional impact of these microbes on PD pathogenesis, or even whether their role is causal or not.

Multi-omic approaches that provide detailed information on the functional attributes of the microbiome are essential for understanding the molecular links between microbes and disease (Heintz-Buschart and Wilmes, 2018). Here, we performed an integrated multi-omic analysis of faecal samples from PD and iRBD patients and healthy control subjects to systematically investigate the functional consequences of altered gut microbiota in PD. Untargeted metabolomics results

revealed an initially unidentified candidate molecule, which was significantly enriched in PD and iRBD and which we identified as 2-hydroxypyridine (2-HP; tautomer: 2-pyridone). We characterized the effects of this molecule in cellular and animal models of PD pathogenesis, which uncovered an effect on relevant α-synuclein aggregation, and an association with hydrogenotrophic methanogenic archaea which were identified as the likely source.

Integrated multi-omic analyses

Using our previously developed methodological framework (Heintz-Buschart et al., 2016; Roume et al., 2013), we performed a systematic multi-omic analysis of DNA, RNA, proteins, and metabolite fractions isolated from flash-frozen faecal samples obtained from 46 PD and 27 iRBD patients as well as 49 healthy controls (Extended Data Fig 1, Extended Data Table 1a). Statistical comparisons were performed for seven data types: taxonomically and functionally annotated metagenomic (MG), metatranscriptomic (MT) and metaproteomic (MP) data, as well as metabolite data (Extended Data Fig 2, Supplementary Tables 1-3, Supplementary Discussion). Taxonomic comparisons revealed no differences in alpha diversity with any data type or metric, while beta diversity differed significantly between cases (subjects with either PD or iRBD) and controls in MT and MG data when adjusted for age and sex (Extended Data Fig 3a-b, Supplementary Table 4). Many previously reported differences between specific microbial taxa were replicated, particularly in the MT data (Extended Data Fig 3c-d, Supplementary Tables 5-6). This data type also had the largest number of differentially abundant features in functionally annotated data (Extended Data Fig 3e-f, Supplementary Tables 7-8), highlighting the importance of using multiple omic datasets instead of focusing on DNA-based analyses. Metabolite comparisons highlighted significantly elevated levels of two unidentified compounds in iRBD and PD (Fig 1a-b, Extended Data Fig 4a, Supplementary Table 9). An integrated analysis of all omic datasets (Extended Data Fig 5, Supplementary Table 10) also selected these compounds among the features that best differentiate between cases and controls.

The first unidentified metabolite was significantly correlated with disease duration in PD patients (P=0.025 for Pearson correlation, P=0.001 for Spearman correlation; Extended Data Fig 4b, Supplementary Table 11). This metabolite was annotated as 2-hydroxypyridine by matching its electron ionization mass spectrum against publicly available mass spectral libraries (e.g. http://gmd.mpimp-golm.mpg.de/). Finally, a commercially available chemical standard was used for definitive identification by its mass spectral fingerprint and retention index. We further validated the difference in 2-HP between PD patients and controls with targeted metabolomics (Fig 1c) using 60 additional faecal samples (30 PD, 30 controls, Extended Data Table 1b).

2-HP is a microbial degradation product of chlorpyrifos (Uniyal et al., 2021), a pesticide known to increase the risk of PD (Freire and Koifman, 2012). We explored our faecal LC-MS/MS data for the presence of this pesticide but did not detect it or related molecules (Supplementary Tables 12-16, Supplementary Discussion). However, in comparisons with other data types (Extended Data Fig 4d-f, Supplementary Tables 17-19, Supplementary Discussion), 2-HP was significantly correlated with the metagenomic (MG) and metatranscriptomic (MT) abundances of archaea, specifically of *Methanobrevibacter smithii* (P=0.006 in MT and P=0.014 in MG relative abundances with fdr-adjusted Pearson correlation; Fig 1d, Extended Data Fig 4d, Supplementary Table 17). *M. smithii*, a hydrogenotrophic methanogen, is the most abundant archaeal species in the human gastrointestinal tract (Mohammadzadeh et al., 2022). It is associated with constipation (Vandeputte et al., 2016b), which is also a common early non-motor symptom of PD (Warnecke et al., 2022). Although *M. smithii* exhibited a numerically higher mean relative abundance in PD and iRBD subjects in taxon data, the difference to controls was not statistically significant in any omic dataset (Extended Data Fig 6a-c, Supplementary Tables 5-6). This could be due to the overall low levels of archaea in the gut, and the fact that our methodological workflow was not optimised for archaeal detection. However, a significant increase in the genus Methanobrevibacter in PD was previously reported in a meta-analysis combining 16S rRNA gene amplicon data from nine studies (Romano et al., 2021). Furthermore, we detected a significantly higher abundance of this genus in faecal samples from another independent large

Parkinson's disease cohort from Luxembourg (NCER-PD cohort (Baldini et al., 2020; Extended Data Table 1c, Extended Data Fig 6d, Supplementary Table 20).

The second unidentified metabolite, which was elevated in iRBD compared to PD or controls, was identified as β-glutamate. We found it to also be correlated with *M. smithii* relative abundance (fdr-adjusted P = 0.001 for Pearson correlation of relative abundance in MT data and P < 0.001 in MG data; Extended Data Fig 4d, Supplementary Table 17). β-glutamate is a known archaeal osmolyte (Robinson et al., 2001), thereby further supporting a connection between PD and archaeal metabolism. 2-HP and β-glutamate were also positively correlated (Extended Data Fig 4e, Supplementary Table 18). Other signals that were highly correlated with both 2-HP and β-glutamate were analytes with such low abundances in the samples that structure elucidation based on electron ionization mass spectrum interpretation was not possible.

We hypothesized that archaeal metabolism could be the main source of the increased 2-HP levels in PD and iRBD patients' faecal samples. One potential source could be the cofactor of the enzyme 5,10-methenyltetrahydromethanopterin hydrogenase (Hmd), which is produced by hydrogenotrophic methanogenic archaea, as this cofactor contains a 2-pyridone structure (Schick et al., 2012). To confirm the presence of 2-HP in M. smithii, we measured it in isolate cultures of this species, as well as of an environmental methanogenic archaeal species not found in the gut, Methanosarcina mazei. 2-HP was detectable in cells of both species, with higher levels at mid-exponential compared to late-exponential phase (Fig 1e).

We additionally quantified 2-HP in cerebrospinal fluid (CSF) and plasma samples from a subset of subjects. It was not detectable in CSF but was detectable at low levels in plasma (Extended Data Fig 4c), although concentrations did not differ between cases and controls. This indicates that 2-HP can pass from the gut to circulation and could therefore trigger systemic effects beyond the gut. Based on computational prediction with three different tools (Lee et al., 2003; Li et al., 2005; Liu et al., 2014), it can also penetrate the blood-brain-barrier with high confidence.

2-HP shares a substructure with the curlicide/pilicide FN075, which contains a ring-fused 2-pyridone (Horvath et al., 2012). This compound inhibits fibrillation of the

amyloidogenic curli protein CsgA, but stimulates α-synuclein amyloid fibre formation (Horvath et al., 2012). Based on this common substructure, we hypothesized that 2-HP could also influence α-synuclein aggregation, providing a potential mechanistic connection to PD pathogenesis, and prompting us to study the effect of 2-HP on α-synuclein aggregation and neurotoxicity.

2-hydroxypyridine and α-synuclein

One of the main histopathological hallmarks of PD is the formation of intracellular inclusions known as Lewy bodies, the main constituent of which is α-synuclein (Burré et al., 2018). We used multiple experimental approaches, including an in vivo model, to explore the connection between 2-HP and α-synuclein aggregation.

First, we used a yeast model overexpressing human α-synuclein, HiTox. In agreement with human PD pathology, galactose-inducible expression of α-synuclein in yeast leads to cytosolic α-synuclein aggregation and severe growth defects by disrupting vesicle trafficking, mitochondrial function and lipid homeostasis (Fanning et al., 2019; Su et al., 2010; Vincent et al., 2018; Willingham et al., 2003). These phenotypes have been translated in human-derived cell models, demonstrating the strength of this model to study cellular α-synuclein-induced cytotoxicity (Mazzulli et al., 2016; Vincent et al., 2018). Based on preliminary testing, micromolar concentrations had no detectable effects, and a range of 1 mM to 100 mM was chosen for the subsequent experiments. We confirmed that at these levels, 2-HP exacerbates α-synuclein-induced toxicity in the HiTox model in a dose-dependent manner (Fig 2a, Extended Data Fig 7a). Growth defects were already seen at 1 mM, and a 100 mM concentration was almost lethal. In contrast, the control strain, which does not express human α-synuclein, showed a slight growth improvement in the presence of higher doses of 2-HP. Under non-inducing conditions, both strains showed only a mild growth defect at 100 mM (Extended Data Fig 7a-b), confirming that 2-HP is toxic only when the strain expresses human α-synuclein. We additionally tested two related compounds, namely 3-hydroxypyridine (3-HP) and 4-hydroxypyridine (4-HP). 4-HP had only a mild effect on the HiTox strain at 30 mM and above, while 3-HP was very toxic to both strains at concentrations above 10 mM

(Extended Data Fig 7c). Based on this, 2-HP has the clearest dose-response effect when compared to the two other hydroxypyridine isomers. Furthermore, microscopic inspection of the HiTox strain under moderately toxic conditions (30 mM 2-HP) revealed a significant increase in cells with cytosolic α-synuclein aggregates in comparison to the control conditions (Fig 2b-c). Taken together, our results demonstrate that 2-HP stimulates α-synuclein aggregation and exacerbates its cytotoxic effect in the HiTox yeast model.

To further evaluate the toxicity of 2-HP in human induced pluripotent stem cell (iPSC)-derived enteric nervous system (ENS) neurons (Fattahi et al., 2016) (Extended Data Fig 8a-b), we treated ENS cells with 60 µM 2-HP, the highest concentration that did not severely impair cell viability in preliminary dose tests. After 120 hours of exposure, we did not observe a significant decrease in the viability of the cultures (Extended Data Fig 8c). However, we observed a significant increase in both total and fibrillated α-synuclein (Fig 2d-e) with a concomitant increase in the apoptotic marker cleaved-caspase 3 (CC3) (Extended Data Fig 8d-e), supporting that exposure to 2-HP also drives α-synuclein accumulation in ENS neurons.

Finally, we explored the effects of 2-HP on the central nervous system (CNS) in vivo using an established experimental approach for studying the effect of α-synuclein toxicity-promoting agents in mice (Garcia et al., 2022; Luk et al., 2012b). We performed intrastriatal injections of 100 mM 2-HP into a mouse model overexpressing human wild-type SNCA (hSNCA) under the transcriptional control of the neuronal Thy1 promoter, and wild-type littermate controls. The concentration was selected based on previous literature of neurodegeneration-inducing molecules for which the dose used in stereotaxic injections in vivo is typically 100 x higher than the one used in vitro (Desbène et al., 2012). The mice were all heterozygous for the transgene, males, and 2-3 months old. Two months after the injection, we observed that fine motor skills, assessed with the adhesive removal test(Bouet et al., 2009), were significantly impaired in hSNCA mice injected with 2-HP compared to those injected with vehicle solution without 2-HP (Fig 3a). To determine the pathological basis of the impairment, we measured the relative levels of tyrosine-hydroxylase (TH), a marker for dopaminergic neurons and their projecting fibres into the dorsal striatum (Garcia et al., 2022). We found that TH was

significantly reduced in the dorsal striatum, and somewhat reduced in the substantia nigra pars compacta (SNpc) in the 2-HP injected hSNCA mice (Fig 3b-c). We also measured S129 phosphorylated α-synuclein (phospho-αSyn), the most commonly used marker to identify α-synuclein inclusions (Vaikath et al., 2019), in synaptic boutons (striatum, substantia nigra) and in cell body profiles in different brain regions of mice in our study cohort. We found a decrease of phospho-αSyn in the dorsal striatum of 2-HP-injected transgenic mice, possibly reflecting the structural neuronal injury induced in this region by 2-HP (Extended Data Fig 9a). We observed no significant effect in the SNpc, where a longer timespan between injection and analysis may be necessary to elicit an effect (Extended Data Fig 9b). Interestingly, in the prefrontal cortex, a brain region neuronally connected to the dorsal striatum, we observed a significant increase in the number of intracellular α-synuclein inclusions in 2-HP injected transgenic mice compared to their control counterparts (Extended Data Fig 9c).

Discussion

In mammals, 2-HP is a known metabolite of pyridine (Damani et al., 1982). While pyridine ring structures are commonly present in biological systems and in man-made compounds, such as drugs and pesticides, unsubstituted pyridine is not common in nature (Gupta et al., 2019). We initially hypothesized that the 2-HP we measured in faecal samples could originate from bacterial breakdown of the pesticide chlorpyrifos, where 2-HP is an established intermediate product (Uniyal et al., 2021). However, we did not detect chlorpyrifos or other related compounds in our faecal metabolomic data. Instead, our results indicate an association of 2-HP and the archaeal species *Methanobrevibacter smithii* as well as methanogenesis-related genes on the metagenomic and metatranscriptomic level. Moreover, we found β-glutamate, which is also linked to archaeal metabolism (Robinson et al., 2001) to be statistically significantly different between PD, iRBD, and healthy control samples. At present, there is no established biosynthetic pathway for 2-HP in *Methanobrevibacter smithii* or in any other organism, but many hydrogenotrophic methanogenic archaea produce a cofactor which has a 2-pyridone structure (Schick et al., 2012). We detected 2-HP in methanoarchaeal cells, suggesting that there is a metabolic process that produces this compound.

Our results show that 2-HP has effects relevant to PD pathogenesis in several model systems: increased α-synuclein aggregation in a humanized yeast model and in human iPSC-derived enteric neurons, and exacerbated behavioural symptoms and neuropathological changes in a mouse model of PD. 2-HP has not been widely studied in mammals previously, and there are no reported neurotoxic effects thus far. However, a ring-fused 2-pyridone compound (FN075) was shown to increase α-synuclein aggregation through a mechanism that involves the formation of oligomers with a flexible solvent-exposed C-terminal end; these oligomers then drive α-synuclein fibrillation (Horvath et al., 2012). Injection of FN075 into the striatum or the substantia nigra of mice also causes PD-like behavioural, metabolic and neuropathological changes, and these changes are absent in mice that do not produce α-synuclein (Chermenina et al., 2015)(Chermenina et al., 2015). An analogous mechanism could explain our in vitro and in vivo findings concerning 2-HP and α-synuclein.

We detected 2-HP at highest concentrations in faecal samples compared to plasma or CSF, implicating the gut as a likely anatomic origin. This is in line with Braak's dual hit hypothesis (Hawkes et al., 2007), which posits that in PD α-synuclein aggregation begins in the gut and spreads from the enteric nervous system to the central nervous system. Furthermore, the presence of 2-HP in plasma, combined with our prediction that it can likely pass the blood-brain barrier, represents another potential route for spreading. We hypothesize that 2-HP could act together with other PD-influencing microbial mechanisms. This would be parallel to the gut microbiome-dependent process, which has been described in mouse models of PD using the pesticide/insecticide rotenone, administered via intrastriatal injections (Dodiya et al., 2020; Perez-Pardo et al., 2019). For example, intestinal barrier disruption due to mucus erosion by *Akkermansia muciniphila* (Desai et al., 2016), a microbe that is often reported to be increased in PD patients (Heintz-Buschart et al., 2018; Romano et al., 2021), could lead to increased exposure to harmful microbial metabolites, such as 2-HP produced by *Methanobrevibacter smithii*. This would then drive α-synuclein aggregation, initiating or exacerbating PD pathogenesis. In this context, it has not escaped our attention that a mechanism involving Methanobrevibacter smithii represents a first known example for a clear role for archaea in a human disease pathogenesis.

Methods

Patient cohorts and sampling

Individuals with PD (n = 46) or iRBD (n = 27) and healthy control subjects (n = 49) were recruited from two study sites in Germany (Paracelsus-Elena Klinik, Kassel, and Philipps-University, Marburg). The studies conformed to the Declaration of Helsinki and the ethical guidelines of the respective institutions (Kassel: approved by the ethics committee of the Physician's Board Hesse, Germany (FF 89/2008), and the DeNoPa trial registered at the German Register for Clinical trials (DRKS00000540); Marburg: approved by the ethics committee of the Medical Faculty of the Philipps-University, Marburg, Germany (46/14)). All subjects provided informed written consent. The sample analysis was approved by the Comité National d'Ethique de Recherche of Luxembourg (reference no.: 140174_ND). For the targeted validation measurements of our main metabolomics finding, we used a set of DeNoPa cohort samples consisting of 25 later-time point samples from individuals included in the main multi-omic analyses, and 35 samples from previously unmeasured individuals. Further details on recruitment, inclusion and exclusion criteria and clinical data collection are provided in the Supplementary methods.

For both cohorts, faecal samples were collected at the clinic via a stool specimen collector (MedAuxil) and collection tubes (Sarstedt), as previously described(Heintz-Buschart et al., 2018). Samples were immediately flash-frozen on dry ice after collection. Samples were subsequently stored at –80 °C and shipped on dry ice. For the Kassel cohort, blood and cerebrospinal fluid samples were also obtained, as described previously (Mollenhauer et al., 2016).

Extractions from faecal samples were performed according to a previously published protocol (De Saedeleer et al., 2021; Roume et al., 2013), conducted on a customized robotic system (Tecan Freedom EVO 200); see Supplementary methods for additional details.

Metagenomic and metatranscriptomic sequencing

For metagenomics, all DNA samples were subjected to random shotgun sequencing. Following DNA isolation, 200-300 ng of DNA was sheared using a Bioruptor NGS (Diagenode) with 30s ON and 30s OFF for 20 cycles. Sequencing libraries were prepared using the TruSeq Nano DNA library preparation kit (Illumina) following the manufacturer's protocol, with 350 bp average insert size.

For metatranscriptomics, 1 µg of isolated RNA was rRNA-depleted using the RiboZero kit (Illumina, MRZB12424). Library preparation was performed using the TruSeq Stranded mRNA library preparation kit (Illumina) following the manufacturer's protocol, apart from omitting the initial steps for mRNA pull down.

For metagenomic and metatranscriptomic analyses, the qualities of the libraries were checked using a Bioanalyzer (Agilent) and quantified using Qubit (Invitrogen). Libraries were sequenced on an Illumina NextSeq500 instrument with 2x150 bp read length.

Metaproteomics

Following isolation, 20 µl of protein extracts were processed using the paramagnetic bead approach with SP3 carboxylate coated beads (Bannuscher et al., 2020; Hughes et al., 2019); further details are provided in the Supplementary methods. The resulting peptide lysates were analysed on a Q Exactive HF instrument (Thermo Fisher Scientific) equipped with a TriVersa NanoMate source (Advion) in LC chip coupling mode. Peptide lysates were injected on a trapping column (Acclaim PepMap 100 C18, 3 µm, nanoViper, 75 µm x 2 cm, Thermo Fisher Scientific) with 5 µL/min by using 98% water/2% ACN 0.5% trifluoroacetic acid, and separated on an analytical column (Acclaim PepMap 100 C18, 3 µm, nanoViper, 75 µm x 25 cm, Thermo Fisher Scientific) with a flow rate of 300 nl/min. The mobile phase was comprised of 0.1% formic acid in water (A) and 80 % ACN/0.08 % formic acid in water (B). Full MS spectra (350–1,550 m/z) were acquired in the Orbitrap at a resolution of 120,000 with automatic gain control (AGC) and a target value of 3×106 ions.

Metabolomics

Untargeted GC-MS and SCFA measurements from faecal samples were performed according to a previously published protocol (De Saedeleer et al., 2021). Details for untargeted LC-MS measurements from faecal samples are provided in the Supplementary methods.

For targeted 2-HP detection in faecal samples, polar metabolites were extracted as follows: 500 µL of MilliQ water was added to 50 mg of faecal matter. Samples were homogenized using a Precellys24 homogenizer (Bertin Technologies): 6000 rpm, 1x30 s at 0 to 5 °C. Plasma and CSF as well as further sample preparation of samples and measurement parameters were performed as previously described (Glaab et al., 2019). For unambiguous identification and precise quantification of 2-HP, concentrations were determined using a standard addition approach. Aliquots of the same sample (faecal sample, plasma or CSF, with added internal standards: pentanedioic acid-D6, [U-13C]-ribitol and tridecanoic acid-D25) were separately spiked with different concentrations of 2-HP (10, 50, 100, 150 and 200 µmol/l) to extrapolate compound levels. Derivatization and GC-MS measurements were performed as reported before.

All GC-MS chromatograms were processed using MetaboliteDetector, v3.220190704 (Hiller et al., 2009). Compounds were initially annotated by retention time and mass spectrum using an in-house mass spectral library. Internal standards were added at the same concentration to every medium sample to correct for uncontrolled sample losses and analyte degradation during metabolite extraction. The data was normalized by using the response ratio of the integrated peak area of the analyte and the integrated peak area of the internal standard.

Bioinformatics and statistics for multi-omics

Metagenomic and metatranscriptomic sequencing data were analysed using the IMP pipeline, version 01.07.2020 (https://git-r3lab.uni.lu/IMP/imp3, tag 6f1badf7), using the HPC facilities (Varrette et al., 2014) of the University of Luxembourg. Metagenomic and metatranscriptomic reads were quality-controlled and co-assembled, ORFs predicted, reads and contigs taxonomically annotated, and ORFs functionally annotated as

previously described (Narayanasamy et al., 2016). Protein libraries were generated from the IMP output and used for protein identification on a per sample basis using SearchGUI (Barsnes and Vaudel, 2018) (v. 3.3.20). Further details are provided in the Supplementary methods.

All statistical analyses and visualizations were performed in R(Team, 2021) (v. 4.1.0) using targets(Landau, 2021) (v. 0.8.1) for workflow management and knitr(Xie, 2014, 2015, 2021) (v. 1.36) for reporting. Unless otherwise specified, false discovery rates were used for multiple comparison correction. Differential abundance comparisons were performed with DESeq2 (adjusted for age and sex) for metagenomic and metatranscriptomic data, and with ANOVA (adjusted for age and sex) and two-sided t-tests (not corrected for confounders) for the metabolomic and metaproteomic data. Integrated multi-omic testing was implemented with the DIABLO workflow from mixOmics(Rohart et al., 2017) (v. 6.17.29). Additional details are provided in the Supplementary methods.

2-HP detection in methanoarchaeal cultures

The archaea *Methanosarcina mazei* (DSM #3647) and *Methanobrevibacter smithii* (DSM #861) were cultivated under anaerobic conditions in closed serum bottles containing 50 mL minimal medium complemented with 1 mM sodium sulphide, 2 mM cysteine and ampicillin to avoid bacterial contamination(Ehlers et al., 2002). As carbon and energy sources, 150 mM methanol for *M. mazei* and H2/CO2 (80:20) in the gas atmosphere for *M. smithii* were added. Cultures were incubated at 37 °C. For monitoring growth, the turbidity at 600 nm was measured using an Ultraspec 2100 Pro Photometer (Amersham Biosciences) Cell numbers were determined in parallel using a Thoma cell counting chamber. Cells were harvested in mid and late exponential phase by centrifugation at 2,455 x g for 20 min and 4 °C. The cell pellets were resuspended in 0.9 % sodium chloride solution and centrifuged again (21,130 x g, 10 min, 4°C). All samples were stored at -80 °C. 2-HP was measured using targeted GC-MS, with sample quantities normalized for cell counts; full details are provided in the Supplementary methods.

Yeast model

The human SNCA gene was cloned into pAG306GAL-ccdB-EGFP and pAG304GAL-ccdB-EGFP plasmids using the Gateway cloning system (Alberti et al., 2007). Yeast cells were transformed with the constructs using the standard polyethylene glycol/lithium acetate protocol (Gietz and Woods, 2002). The PDR5 gene was subsequently replaced by URA3 marker in the HiTox and control strains followed by selection in synthetic complement (SC) media lacking uracil using the same transformation protocol(Gietz and Woods, 2002). Gene integration or disruption was verified by PCR. Strain details are provided in the Supplementary methods.

Four fresh single colonies of the HiTox strain and its respective control strain were inoculated from SC-2% glucose plates into 5 mL SC-2% raffinose (SCR) and incubated overnight with shaking (200 rpm) at 30 °C for 20 h. Cultures were subsequently diluted to OD 0.5 and 2 µL of culture was added to 78 µL 2-HP containing media to a final optical density of 0.0125 in a 384-well microplate. 2-HP was diluted in SC-2% raffinose/galactose (SCR/SCG) and tested at different concentrations (1-100 mM). Finally, plates were measured in a microplate reader (TECAN™ Infinite M200Pro), at an interval of 10 minutes during 72 h at 30 °C. Yeast growth phenotyping was performed as previously described74. For better comparability between batches, strains and methods, the final biomass was corrected using the GATHODE software(Jung et al., 2015). The OD600 at 48 h was recorded for biomass quantification, with the means and standard deviations calculated from four biological replicates.

To evaluate α-synuclein aggregation, one single colony was inoculated in 5 mL SCR (α-syn 'off') and incubated at 30 °C overnight. The following day, 1 mL of culture was transferred into an sample tube and cells were centrifuged. Pellets were resuspended with SCG (α-syn 'on') in presence or absence of 30 mM 2-HP and incubated at 30 °C. After 24 h, cells were visualized using a Nikon Microscope (100x oil). Ten pictures per condition were randomly taken. The total number of cells and cells showing aggregates were manually quantified in ImageJ. Statistical significance between conditions was determined using an unpaired two-sided t-test in R.

Enteric neuron model

Enteric neurons were derived from human induced pluripotent stem cells (hiPSCs) following a previously published protocol (Fattahi et al., 2016); the full details are available in the Supplementary methods.

For cytotoxicity testing, enteric neurons were detached with accutase (Sigma) after 21 days of culturing in 6-well plates. The cells were replated into 96-well plates coated with poly-ornithine/laminin/fibronectin as described in the Supplementary methods. They were then maintained under differentiating conditions until day 31, when they were treated with 2-HP (Sigma,) at 1 µM, 3 µM, 6 µM, 10 µM, 30 µM, 60 µM, 100 µM, 300 µM, 600 µM, 1 mM and 3 mM. 2-HP was reconstituted to 10 mM in the differentiation medium. Cells were treated for 24h, then assessed using a tetrazolium assay for viability; see Supplementary methods for details.

For immunostaining, enteric neurons were replated into 96-well imaging plates (Cell Carrier Ultra, Perkin Elmer) after three weeks in culture. Cells were maintained under differentiating conditions until day 31, when they were treated with 60 µM 2-HP for 72 h and 120 h. After treatment, cells were immunostained with α-synuclein antibody (NOVUS biologicals, NBP1-05194, 1:1000), α-synuclein filament antibody (Abcam, ab20953, 1:5000), TUJ1 (Millipore, AB9354, 1:600) and cleaved caspase-3 (Asp175) antibody (CST, 9661, 1:200) and imaged to quantify each marker (full details in the Supplementary methods). Differences were evaluated using one-way ANOVA with the mean values of three independent replicates and a two-sided Dunn's multiple comparison test at each time point versus the untreated using Graphpad Prism (v. 9).

Mouse model

A transgenic mouse line, B6.D2-Tg(Thy1-SNCA)14Pjk (Line 14), which overexpresses human wildtype α-synuclein under the transcriptional control of the Thy1 promoter, was used (Kahle et al., 2000, 2001). Genotyping of the mice is described in the Supplementary methods. The mice were all heterozygous for the transgene, males, and 2-3 months old. Between 6 and 14 mice were used for each analysis. Mice had access to food and water ad libitum and were exposed to a regular 12h-day-night cycle. Mice were

injected intracranially with 100 mM 2-HP (Sigma), or PBS vehicle solution (control mice), in volumes of 2 µL, within the right dorsal striatum; full details of the injection protocol are provided in the Supplementary methods.

At two months post-injection, motor function was evaluated with the adhesive removal test (Bouet et al., 2009). Briefly, animals were placed in a round transparent arena for one minute for habituation. Rectangular white tape, 3 x 5 mm was placed on the left forepaw (expected to be affected by injection of 2-HP into the right dorsal striatum). The time intervals to first touch and removal of the tape were recorded. The test was performed twice, sequentially, for each mouse, and times for both measures were averaged. The sequence of the mice being tested was randomized, and the experimenter was blinded to their genotype and treatment.

After behavioural evaluation, the mice were deeply anesthetised (i.p. injection of medetomidine, 1mg/kg and ketamine, 100 mg/kg) and then euthanised by transcardial perfusion with PBS. Brains were removed from the skull and post-fixed in fresh phosphate-buffered 4% paraformaldehyde for 48 h at 4 °C, then stored in PBS with 0.05% sodium azide (as a preservative) at 4 °C, before being processed for immunofluorescence analysis.

Immunofluorescent stainings on 50 µm sections, generated with a Leica VT 100 vibratome, were performed following a standard protocol (Ashrafi et al., 2017). Briefly, sections were first washed in PBS with 0.1% Triton X100 (TX100). They were subsequently treated with a permeabilization solution (PBS + 1.5% TX100 + 3% H2O2) for 30 minutes. This was followed by washing with PBS + 0.1% TX100. To prevent unspecific antibody binding, the sections were then incubated for 1 h in PBS + 0.1% TX100 with 5% BSA. After one short washing step, sections were incubated with the first antibodies diluted in antibody solution (PBS + 0.1% TX100 + 2% BSA) overnight at room temperature (RT) on an orbital shaker. The following antibodies were used: anti-α-synuclein (aSyn, phosphorylated at S129; Prothena Biosciences Inc., 11A5; 1:1000), anti-tyrosine hydroxylase (TH; Abcam, ab76442/Merck (Sigma-Aldrich), AB152; 1:1000). The sections were double-stained for TH and S129 phosphorylated α-synuclein (phospho-αSyn). The next day, sections were washed with PBS + 0.1% TX100 to remove any excess of the first antibody. Sections were then incubated with a secondary antibody in

antibody solution for 2 h at RT on an orbital shaker. Finally, sections were washed with PBS + 0.1% TX100 (at least 3 times for 10 mins), then mounted on Superfrost™ (ThermoFisher Scientific) slides, left to dry, and finally covered with a cover-slip using Fluoromount-G® (Invitrogen).

Imaging of the sections was performed using a Zeiss AxioImager Z1 upright microscope, coupled to a "Colibri" LED system, and an Mrm3 digital camera for image capture using the Zeiss ZEN 2 Blue software. Measurements were performed on blinded sections, and codes were broken only after all measurements were completed. TH-positive signals were quantified in the dorsal striatum and substantia nigra pars compacta, and phospho-aSyn in these two regions as well as the prefrontal cortex; details of the quantifications for each region and antibody are given in the Supplementary methods.

Behaviour and neuropathology data were analysed with Graphpad Prism (v. 9). All datasets passed normality tests and were analysed by ANOVA followed by Tukey's or Dunn's post hoc tests.

The animal study was approved by the University of Luxembourg Animal Experimentation Ethics Committee (LUPA 2020/26) and the overseeing Luxembourg Government authorities (Ministry of Health and Ministry of Agriculture).

Data availability

The datasets generated by this study are available in the following repositories: metagenomic and metatranscriptomic data at the NCBI BioProject collection with the ID PRJNA782492 (http://www.ncbi.nlm.nih.gov/bioproject/782492), metaproteomic data at the Proteomics Identifications (PRIDE) database with accession number PXD031457 (https://www.ebi.ac.uk/pride/archive/projects/PXD031457), and metabolomic data at MetaboLights with ID MTBLS5092 (https://www.ebi.ac.uk/metabolights/MTBLS5092). Due to privacy restrictions, clinical and demographic data are available on request from the corresponding author. NCER-PD clinical and 16s rRNA amplicon sequencing data are available on request from https://www.parkinson.lu/research-participation.

Code availability

The IMP pipeline, which was used for analysis of metagenomic and metatranscriptomic data, is available at https://gitlab.lcsb.uni.lu/IMP/imp3. The R code used for statistical analyses and visualisations is available at https://gitlab.lcsb.uni.lu/ESB/mibipa-2-hp.

Acknowledgements

We thank the staff of the Luxembourg Centre for Systems Biomedicine (LCSB), particularly the sequencing platform and the metabolomics platform, for running the sequencing and metabolomic analyses. The microscopy for the yeast experiments was performed at the LCSB bio-imaging platform. The bioinformatics presented in this paper were carried out using the HPC facilities(Varrette et al., 2014) of the University of Luxembourg.

This project has received funding from the European Research Council (ERC) under the European Union's Horizon 2020 research and innovation programme (grant agreement No. 863664), and was further supported by the Luxembourg National Research Fund (FNR) CORE/16/BM/11333923 (MiBiPa) and CORE/15/BM/10404093 (microCancer/MUST), and the Michael J. Fox Foundation under grant IDs 14701 (MiBiPa-PLUS) and MJFF-019228 (PARKdiet), as well as the Parkinson's Foundation (MiBiPa Saliva), to P.W.

K.J.S. is a recipient of an FNR pre-doctoral fellowship (FNR AFR 12515776). A.S. is supported by PARK-QC DTU (PRIDE17/12244779/PARK-QC), and B.T.A. by MICROH DTU (PRIDE17/11823097). E.L.S. acknowledges funding support for the ATTRACT Fellowship A18/BM/12341006. The work of R.A.S. was conducted with financial support of the DFG as part of the CRC1182 “Origin and function of metaorganisms" Z2 project. E.G. acknowledges support by the FNR as part NCER-PD (FNR11264123), the ERA-Net ERACOSySMed JTC-2 project PD-Strat (INTER/11651464), and from the European Union’s Horizon 2020 research and innovation programme under the grant no. ERAPERMED 2020-314 for the project DIGI-PD. P.M. was supported by the FNR funded National Centre of Excellence in Research on Parkinson’s disease (NCER-PD, FNR11264123), CORE MiRisk-PD (C17/BM/11676395), and the INTER ‘ProtectMove’ (INTER/DFG/19/1442937) grants. Finally, the authors thank Prof. Michel Mittelbronn, who is funded by a PEARL grant (FNR PEARL P16/BM/11192868), as well as the Jean Think Foundation, Luxembourg, for their support.

Author information

These authors contributed equally: Jean-Pierre Trezzi, Velma T. E. Aho.

Contributions

Conceptualisation: J.P.T., A.H.-B., W.O., B.M., P.W. Patient recruitment, clinical coordination, and sampling: S.S., A.J., C.T., W.O., B.M. Project management: L.D., C.C.L. Multi-omic data generation: J.P.T., C.J., R.H., R.R.S., B.T.A., L.A.L., A.D., J.H., X.D., F.G., N.J., M.v.B., E.L.S. Bioinformatics and statistics: J.P.T., V.T.E.A, C.J., O.H., B.K., P.V.N., J.R.G., R.R.S., B.T.A., E.L.S., E.G., A.H.B., P.M. Experimental work: M.H.T., K.J.S., P.G., A.S., C.M-G., O.U.H., T.H., U.H.-M., G.G.G., K.W., R.A.S., J.C.S., C.L.L., T.K., M.B., Initial manuscript draft: J.P.T., V.T.E.A, P.W. Extensive review and editing: C.C.L., A.H.-B., J.G.S. All authors read and approved of the submitted version.

Ethics declarations

Competing interests

J.P.T. and P.W. are inventors in two patent applications, the first one with the numbers No. LU101477, No. PCT/EP2020/081855, EP20820786.0, US17/776,001, CA3,157,474 and the second one with No. LU101476, No. PCT/EP2020/081832, EP20820785.2, US17/776,010.

Additional information

Supplementary information

Supplementary information is available for this paper.

Corresponding author

Correspondence should be addressed to Paul Wilmes (paul.wilmes@uni.lu).

References

Benakis, C. et al. The microbiome-gut-brain axis in acute and chronic brain diseases. Curr. Opin. Neurobiol. 61, 1–9 (2020).

Boertien, J. M., Pereira, P. A. B., Aho, V. T. E. & Scheperjans, F. Increasing comparability and utility of gut microbiome studies in Parkinson's disease: A systematic review. J. Park. Dis. (2019) doi:10.3233/JPD-191711.

Romano, S. et al. Meta-analysis of the Parkinson's disease gut microbiome suggests alterations linked to intestinal inflammation. Npj Park. Dis. 7, 1–13 (2021).

Qian, Y. et al. Gut metagenomics-derived genes as potential biomarkers of Parkinson's disease. Brain 143, 2474–2489 (2020).

Rosario, D. et al. Systematic analysis of gut microbiome reveals the role of bacterial folate and homocysteine metabolism in Parkinson's disease. Cell Rep. 34, 108807 (2021).

Fang, P., Kazmi, S. A., Jameson, K. G. & Hsiao, E. Y. The microbiome as a modifier of neurodegenerative disease risk. Cell Host Microbe 28, 201–222 (2020).

Sung, H. et al. Global Cancer Statistics 2020: GLOBOCAN Estimates of incidence and mortality worldwide for 36 cancers in 185 countries. CA. Cancer J. Clin. 71, 209–249 (2021).

Matson, V., Chervin, C. S. & Gajewski, T. F. Cancer and the microbiome—Influence of the commensal microbiota on cancer, immune responses, and immunotherapy. Gastroenterology 160, 600–613 (2021).

Fan, Y. & Pedersen, O. Gut microbiota in human metabolic health and disease. Nat. Rev. Microbiol. 19, 55–71 (2021).

Dorsey, E. R., Sherer, T., Okun, M. S. & Bloem, B. R. The emerging evidence of the Parkinson pandemic. J. Park. Dis. 8, S3–S8.

Miyauchi, E., Shimokawa, C., Steimle, A., Desai, M. S. & Ohno, H. The impact of the gut microbiome on extra-intestinal autoimmune diseases. Nat. Rev. Immunol. 1–15 (2022) doi:10.1038/s41577-022-00727-y.

Hawkes, C. H., Tredici, K. D. & Braak, H. Parkinson's disease: a dual-hit hypothesis. Neuropathol. Appl. Neurobiol. 33, 599–614 (2007).

Heintz-Buschart, A. et al. The nasal and gut microbiome in Parkinson's disease and idiopathic rapid eye movement sleep behavior disorder. Mov. Disord. 33, 88–98 (2018).

Högl, B., Stefani, A. & Videnovic, A. Idiopathic REM sleep behaviour disorder and neurodegeneration — an update. Nat. Rev. Neurol. 14, 40–55 (2018).

Unger, M. M. et al. Short chain fatty acids and gut microbiota differ between patients with Parkinson's disease and age-matched controls. Parkinsonism Relat. Disord. 32, 66–72 (2016).

Aho, V. T. E. et al. Relationships of gut microbiota, short-chain fatty acids, inflammation, and the gut barrier in Parkinson's disease. Mol. Neurodegener. 16, (2021).

Baldini, F. et al. Parkinson's disease-associated alterations of the gut microbiome predict disease-relevant changes in metabolic functions. BMC Biol. 18, 62 (2020).

Heintz-Buschart, A. & Wilmes, P. Human gut microbiome: Function matters. Trends Microbiol. 26, 563–574 (2018).

Roume, H. et al. A biomolecular isolation framework for eco-systems biology. ISME J. 7, 110–121 (2013).

Heintz-Buschart, A. et al. Integrated multi-omics of the human gut microbiome in a case study of familial type 1 diabetes. Nat. Microbiol. 2, 1–13 (2016).

Uniyal, S., Sharma, R. K. & Kondakal, V. New insights into the biodegradation of chlorpyrifos by a novel bacterial consortium: Process optimization using general factorial experimental design. Ecotoxicol. Environ. Saf. 209, 111799 (2021).

Freire, C. & Koifman, S. Pesticide exposure and Parkinson's disease: Epidemiological evidence of association. NeuroToxicology 33, 947–971 (2012).

Mohammadzadeh, R., Mahnert, A., Duller, S. & Moissl-Eichinger, C. Archaeal key-residents within the human microbiome: characteristics, interactions and involvement in health and disease. Curr. Opin. Microbiol. 67, 102146 (2022).

Vandeputte, D. et al. Stool consistency is strongly associated with gut microbiota richness and composition, enterotypes and bacterial growth rates. Gut 65, 57–62 (2016).

Warnecke, T., Schäfer, K.-H., Claus, I., Del Tredici, K. & Jost, W. H. Gastrointestinal involvement in Parkinson's disease: pathophysiology, diagnosis, and management. Npj Park. Dis. 8, 1–13 (2022).

Robinson, P., Neelon, K., Schreier, H. J. & Roberts, M. F. β-glutamate as a substrate for glutamine synthetase. Appl. Environ. Microbiol. 67, 4458–4463 (2001).

Schick, M. et al. Biosynthesis of the iron-guanylylpyridinol cofactor of [Fe]-hydrogenase in methanogenic archaea as elucidated by stable-isotope labeling. J. Am. Chem. Soc. 134, 3271–3280 (2012).

Li, H. et al. Effect of selection of molecular descriptors on the prediction of blood-brain barrier penetrating and nonpenetrating agents by statistical learning methods. J. Chem. Inf. Model. 45, 1376–1384 (2005).

Lee, S. K. et al. The PreADME Approach: Web-based program for rapid prediction of physico-chemical, drug absorption and drug-like properties. EuroQSAR 2002 Des. Drugs Crop Prot. Process. Probl. Solut. 2003, 418–420 (2003).

Liu, H. et al. AlzPlatform: An Alzheimer's disease domain-specific chemogenomics knowledgebase for polypharmacology and target identification research. J. Chem. Inf. Model. 54, 1050–1060 (2014).

Horvath, I. et al. Mechanisms of protein oligomerization: Inhibitor of functional amyloids templates α-synuclein fibrillation. J. Am. Chem. Soc. 134, 3439–3444 (2012).

Burré, J., Sharma, M. & Südhof, T. C. Cell biology and pathophysiology of α-synuclein. Cold Spring Harb. Perspect. Med. 8, (2018).

Willingham, S., Outeiro, T. F., DeVit, M. J., Lindquist, S. L. & Muchowski, P. J. Yeast genes that enhance the toxicity of a mutant huntingtin fragment or α-synuclein. Science 302, 1769–1772 (2003).

Fanning, S. et al. Lipidomic analysis of α-synuclein neurotoxicity identifies stearoyl CoA desaturase as a target for Parkinson treatment. Mol. Cell 73, 1001-1014.e8 (2019).

Su, L. J. et al. Compounds from an unbiased chemical screen reverse both ER-to-Golgi trafficking defects and mitochondrial dysfunction in Parkinson's disease models. Dis. Model. Mech. 3, 194–208 (2010).

Vincent, B. M. et al. Inhibiting stearoyl-CoA desaturase ameliorates α-synuclein cytotoxicity. Cell Rep. 25, 2742-2754.e31 (2018).

Mazzulli, J. R., Zunke, F., Isacson, O., Studer, L. & Krainc, D. α-Synuclein–induced lysosomal dysfunction occurs through disruptions in protein trafficking in human midbrain synucleinopathy models. Proc. Natl. Acad. Sci. U. S. A. 113, 1931–1936 (2016).

Fattahi, F. et al. Deriving human ENS lineages for cell therapy and drug discovery in Hirschsprung's disease. Nature 531, 105–109 (2016).

Garcia, P. et al. Neurodegeneration and neuroinflammation are linked, but independent of alpha-synuclein inclusions, in a seeding/spreading mouse model of Parkinson's disease. Glia (2022) doi:10.1002/glia.24149.

Luk, K. C. et al. Pathological α-synuclein transmission initiates Parkinson-like neurodegeneration in nontransgenic mice. Science 338, 949–953 (2012).

Desbène, C. et al. Critical role of cPLA2 in Aβ oligomer-induced neurodegeneration and memory deficit. Neurobiol. Aging 33, 1123.e17–29 (2012).

Bouet, V. et al. The adhesive removal test: a sensitive method to assess sensorimotor deficits in mice. Nat. Protoc. 4, 1560–1564 (2009).

Vaikath, N. N. et al. Antibodies against alpha-synuclein: tools and therapies. J. Neurochem. 150, 612–625 (2019).

Damani, L. A. et al. Species differences in the metabolic C - and N -oxidation, and N - methylation of [14 C]pyridine in vivo. Xenobiotica 12, 527–534 (1982).

Gupta, N., O'Loughlin, E. J. & Sims, G. K. Microbial degradation of pyridine and pyridine derivatives. in Microbial Metabolism of Xenobiotic Compounds (ed. Arora, P. K.) vol. 10 1–31 (Springer Singapore, 2019).

Chermenina, M. et al. Single injection of small-molecule amyloid accelerator results in cell death of nigral dopamine neurons in mice. Npj Park. Dis. 1, 15024 (2015).

Dodiya, H. B. et al. Chronic stress-induced gut dysfunction exacerbates Parkinson's disease phenotype and pathology in a rotenone-induced mouse model of Parkinson's disease. Neurobiol. Dis. 135, 104352 (2020).

Perez-Pardo, P. et al. Role of TLR4 in the gut-brain axis in Parkinson's disease: a translational study from men to mice. Gut 68, 829–843 (2019).

Desai, M. S. et al. A dietary fiber-deprived gut microbiota degrades the colonic mucus barrier and enhances pathogen susceptibility. Cell 167, 1339-1353.e21 (2016).

Mollenhauer, B. et al. Monitoring of 30 marker candidates in early Parkinson disease as progression markers. Neurology 87, 168–177 (2016).

De Saedeleer, B. et al. Systematic characterization of human gut microbiome-secreted molecules by integrated multi-omics. ISME Commun. 1, 1–6 (2021).

Hughes, C. S. et al. Single-pot, solid-phase-enhanced sample preparation for proteomics experiments. Nat. Protoc. 14, 68–85 (2019).

Bannuscher, A. et al. A multi-omics approach reveals mechanisms of nanomaterial toxicity and structure–activity relationships in alveolar macrophages. Nanotoxicology 14, 181–195 (2020).

Glaab, E. et al. Integrative analysis of blood metabolomics and PET brain neuroimaging data for Parkinson's disease. Neurobiol. Dis. 124, 555–562 (2019).

Hiller, K. et al. MetaboliteDetector: Comprehensive analysis tool for targeted and nontargeted GC/MS based metabolome analysis. Anal. Chem. 81, 3429–3439 (2009).

Varrette, S., Bouvry, P., Cartiaux, H. & Georgatos, F. Management of an academic HPC cluster: The UL experience. in 2014 International Conference on High Performance Computing Simulation (HPCS) 959–967 (2014). doi:10.1109/HPCSim.2014.6903792.

Narayanasamy, S. et al. IMP: a pipeline for reproducible reference-independent integrated metagenomic and metatranscriptomic analyses. Genome Biol. 17, (2016).

Barsnes, H. & Vaudel, M. SearchGUI: A highly adaptable common interface for proteomics search and de novo engines. J. Proteome Res. 17, 2552–2555 (2018).

Team, R. C. R: A language and environment for statistical computing. (R Foundation for Statistical Computing, 2021).

Landau, W. M. The targets R package: a dynamic Make-like function-oriented pipeline toolkit for reproducibility and high-performance computing. J. Open Source Softw. 6, 2959 (2021).

Xie, Y. knitr: A General-Purpose Package for Dynamic Report Generation in R. (2021).

Xie, Y. Dynamic Documents with R and knitr. (Chapman and Hall/CRC, 2015).

Xie, Y. knitr: A Comprehensive Tool for Reproducible Research in R. in Implementing Reproducible Computational Research (eds. Stodden, V., Leisch, F. & Peng, R. D.) (Chapman and Hall/CRC, 2014).

Rohart, F., Gautier, B., Singh, A. & Le Cao, K.-A. mixOmics: An R package for 'omics feature selection and multiple data integration. PLoS Comput. Biol. 13, e1005752 (2017).

Ehlers, C., Veit, K., Gottschalk, G. & Schmitz, R. A. Functional organization of a single nif cluster in the mesophilic archaeon Methanosarcina mazei strain Gö1. Archaea 1, 143–150 (2002).

Alberti, S., Gitler, A. D. & Lindquist, S. A suite of Gateway® cloning vectors for high-throughput genetic analysis in Saccharomyces cerevisiae. Yeast Chichester Engl. 24, 913–919 (2007).

Gietz, R. D. & Woods, R. A. Transformation of yeast by lithium acetate/single-stranded carrier DNA/polyethylene glycol method. Methods Enzymol. 350, 87–96 (2002).

Jung, P. P., Christian, N., Kay, D. P., Skupin, A. & Linster, C. L. Protocols and programs for high-throughput growth and aging phenotyping in yeast. PLoS ONE 10, (2015).

Kahle, P. J. et al. Selective insolubility of α-synuclein in human Lewy body diseases Is recapitulated in a transgenic mouse model. Am. J. Pathol. 159, 2215–2225 (2001).

Kahle, P. J. et al. Subcellular localization of wild-type and Parkinson's disease-associated mutant α-synuclein in human and transgenic mouse brain. J. Neurosci. 20, 6365–6373 (2000).

Ashrafi, A. et al. Absence of regulator of G-protein signaling 4 does not protect against dopamine neuron dysfunction and injury in the mouse 6-hydroxydopamine lesion model of Parkinson's disease. Neurobiol. Aging 58, 30–33 (2017).

5.3 Figures

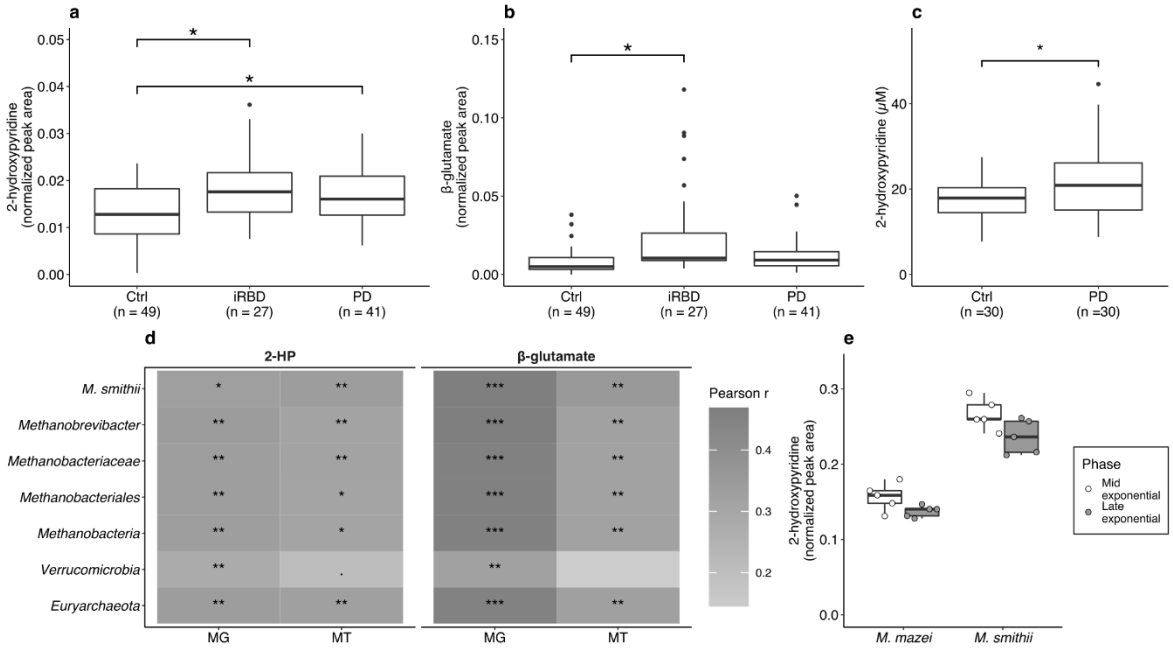
a
b
c
d
e
2-hydroxypyridine (normalized peak area)
β-glutamate (normalized peak area)
2-hydroxypyridine (μM)
Ctrl (n = 49)
iRBD (n = 27)
PD (n = 41)
Ctrl (n =30)
PD (n =30)
2-HP
β-glutamate
M. smithii
Methanobrevibacter
Methanobacteriaceae
Methanobacteriales
Methanobacteria
Verrucomicrobia
Euryarchaeota
MG
MT
Pearson r
M. mazei
M. smithii
Phase
Mid exponential
Late exponential

Figure 1. Metabolite differences between patients with PD and iRBD and control subjects, and findings connecting the results to the gut archaeal species *Methanobrevibacter smithii*.

a. Normalized peak area of 2-hydroxypyridine (2-HP) in faecal extracts of PD and iRBD patients and control subjects (Ctrl). **b**. Normalized peak area of β-glutamate in faecal extracts from PD and iRBD patients and control subjects. **c.** Validation of differential concentration of 2-HP in faecal extracts with targeted metabolomics. **d.** Pearson correlations of relative abundances of taxa with 2-HP and β-glutamate, trimmed to taxa with the most overlap between different data analysis strategies (complete results: Extended Data Fig 4d and Supplementary Table 17); MG = metagenomic data, MT = metatranscriptomic data. **e.** 2-HP in cells of the archaeal species *Methanobrevibacter smithii* (*M. smithii*) and *Methanosarcina mazei* (*M. mazei*); five biological replicates, normalized by cell count prior to measurement. In a-c, *P*-values reflect unpaired t-tests corrected for multiple comparisons across all metabolites; * $P < 0.05$. In all box plots: box hinges: 1st and 3rd quartiles; whiskers: hinge to highest/lowest values that is within 1.5*IQR of hinge.

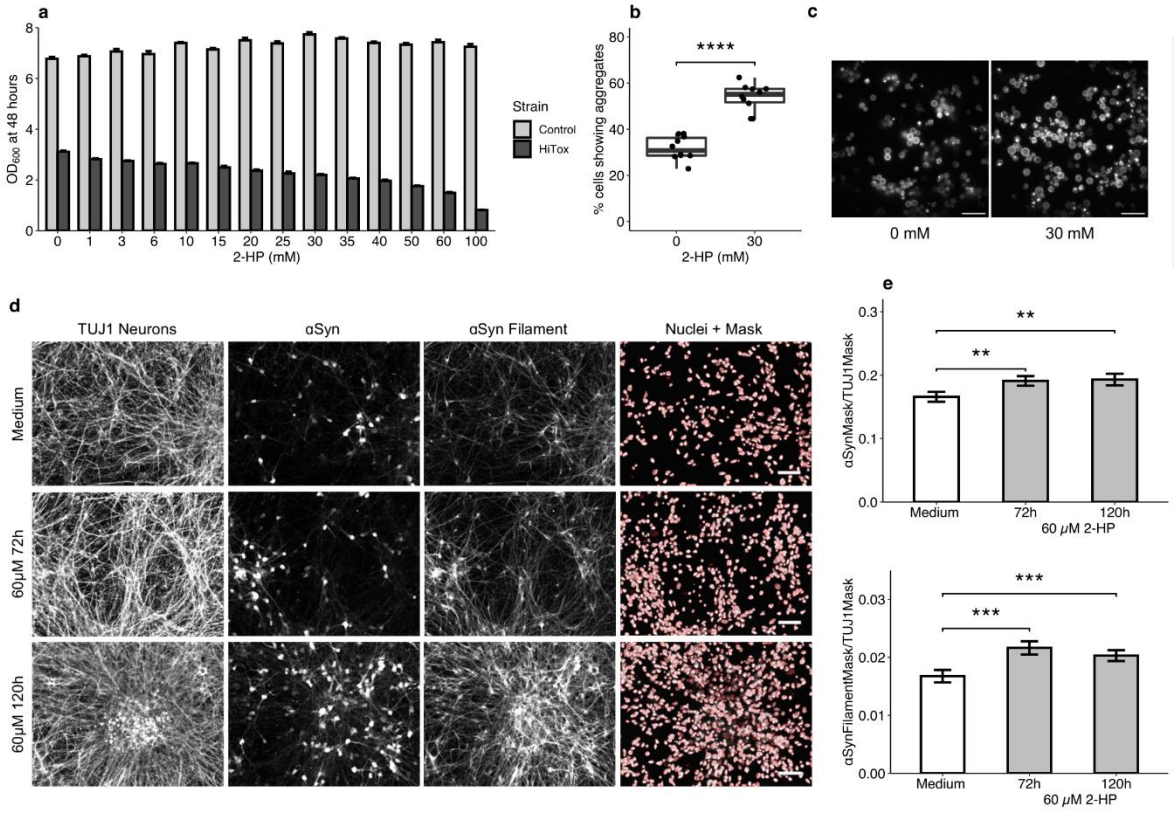
a
b
c
d
e
OD600 at 48 hours
2-HP (mM)
Strain
Control
HiTox
% cells showing aggregates
****
0 mM
30 mM
TUJ1 Neurons
αSyn
αSyn Filament
Nuclei + Mask
Medium
60μM 72h
60μM 120h
αSynMask/TUJ1Mask
αSynFilamentMask/TUJ1Mask
Medium
72h
120h
60 μM 2-HP
**
***

Figure 2. Effects of 2-hydroxypyridine in human α-synuclein expressing yeast model and in human induced pluripotent stem cell (hIPSC) derived enteric neurons.

a. Dose-response assay in α-synuclein expressing yeast cells (HiTox) and control strain (Ctrl); showing means and standard deviations calculated from four biological replicates for each strain. **b.** Microscopy-based quantification of yeast cells exhibiting α-synuclein aggregates (based on 10 pictures per condition). Box hinges: 1st and 3rd quartiles; whiskers: hinge to highest/lowest values that is within 1.5*IQR of hinge. **c.** Representative microscopy images of HiTox cells after 24 h treatment with 30 mM 2-HP; scale bar: 20 µm. **d**. High-content imaging of hIPSC derived enteric neurons, showing total α-synuclein (αSyn), α-synuclein filament (αSyn Filament), TUJ1-positive neurons and Hoechst-positive nuclei (with a representation of the mask applied to segment the nuclei); scale bar: 100 µm. **e.** Total α-synuclein and filamentous α-synuclein normalized to the amounts of TUJ1-positive neurons (mean ± SEM of three independent neuronal differentiations; 8 wells per condition and 30 fields per well quantified for each). * $P < 0.05$, ** $P < 0.01$, *** $P < 0.001$, **** $P < 0.0001$.

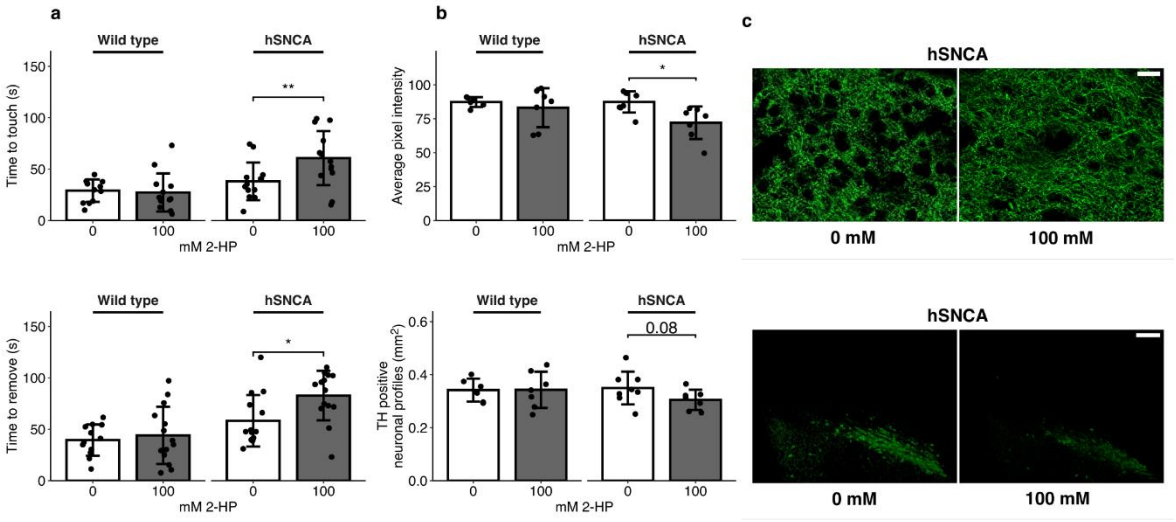
a
Wild type
hSNCA
Time to touch (s)
150
100
50
0
**
0
100
0
100
mM 2-HP
b
Wild type
hSNCA
Average pixel intensity
100
75
50
25
0
*
0
100
0
100
mM 2-HP
c
hSNCA
0 mM
100 mM
Wild type
hSNCA
Time to remove (s)
150
100
50
0
*
0
100
0
100
mM 2-HP
Wild type
hSNCA
TH positive neuronal profiles (mm²)
0.6
0.4
0.2
0.0
0.08
0
100
0
100
mM 2-HP
hSNCA
0 mM
100 mM

Figure 3. Effects of intrastriatally injected 2-hydroxypyridine on fine motor behaviour and the dopaminergic neuron marker tyrosine hydroxylase (TH) in transgenic mice overexpressing human α-synuclein.

a. Fine motor behaviour of mice 2 months after 2-HP injection, measured using the adhesive removal test (time to touch: upper panel, time to remove: lower panel); hSNCA: human α-synuclein overexpressing transgenic mice; n of mice = 12-14 per group. **b.** Quantification of TH-positive structures in the nigro-striatal circuit of hSNCA mice at 2 months after 100 mM 2-HP injection; Upper panel: TH-positive axons in the dorsal striatum; lower panel: TH-positive neurons in the substantia nigra pars compacta; n of mice = 6-8 per group. **c.** Microphotographs showing examples for 0 mM and 100mM in hSNCA mice only; upper panel: dorsal striatum (scale bar: 25 µm); lower panel: substantia nigra pars compacta (scale bar: 200 µm). All bar plots show mean and standard deviation. * $P < 0.05$, ** $P < 0.01$.

6 Neurodegeneration and neuroinflammation are linked, but independent of alpha-synuclein inclusions, in a seeding/spreading mouse model of Parkinson's disease

Pierre Garcia, Wiebke Jürgens-Wemheuer, Oihane Uriarte Huarte, […], Eric Koncina, Djalil Coowar, Tony Heurtaux, Enrico Glaab, Rudi Balling, […], Felix Kleine-Borgmann, Michel Mittelbronn, Marek Ostaszewski, **Kristopher J Schmit**, Manuel Buttini

Published in Glia on 29th January 2022

6.1 Preface

PD is a multifactorial disorder clinically characterized by different motor and non-motor dysfunctions, and pathologically characterized by the loss of dopaminergic neurons and Lewy body formations. The formation of Lewy bodies, thus, a gain of function of αSyn and its prion-like spreading ability is still considered the main pathogenic event in PD.

However, over the last years, it is strongly debated if these toxic αSyn aggregating forms are the only event triggering PD pathogenesis. Neuroinflammation has been proposed as an additional player in PD pathogenesis. We were particularly interested in the disease progression timeline of these different events.

To mimic the spreading of αSyn, we injected preformed fibrils (PFFs) of αSyn into the dorsal striatum of wild-type mice, and followed its spreading across brain regions over time. We were interested in the underlying mechanisms contributing to PD pathology. Especially early events were of interest to us and so we compared early (13dpi) to late events (90dpi). We used classical neuropathological techniques to identify the different PD pathologies such as aSyn aggregation and neuronal death and microgliosis. Additionally, we performed transcriptomics on nigral tissue to identify crucial pathways in PD pathogenesis at different timepoints.

The manuscript was published in Glia (IF (2020) 7.452) on 29th January 2022.

I was the lead researcher on the transcriptomic analysis for this project. I also assisted in the interpretation of the data, generated the corresponding figures and tables (Figures 6-9, Figures S4-S7, Table S2-S6), and assisted in manuscript writing. I am, together with my colleagues Pierre Garcia, Wiebke Jürgens-Wemheuer and Oihane Uriarte Huarte, first co-author of this publication.

Supplementary material can be found in **Appendix D.**

.

6.2 Publication

Title

Neurodegeneration and neuroinflammation are linked, but independent of alpha-synuclein inclusions, in a seeding/spreading mouse model of Parkinson's disease

Authors & Affiliations

Pierre Garcia[1,2]*, Wiebke Jürgens-Wemheuer[1,3]*, Oihane Uriarte Huarte[1,2]*, Alessandro Michelucci[1,4], Annette Masuch[5], Simone Brioschi[5], Andreas Weihofen[6], Eric Koncina[7], Djalil Coowar[1], Tony Heurtaux[2,7], Enrico Glaab[1], Rudi Balling[1], Carole Sousa[4], Tony Kaoma[4], Nathalie Nicot[4], Tatjana Pfander[3], Walter Schulz-Schaeffer[3], Ahmad Allouche[8], Nicolas Fischer[8], Knut Biber[5], Felix Kleine-Borgmann[2,4,9], Michel Mittelbronn[1,2,4,7,9,10], Marek Ostaszewski[1], Kristopher J. Schmit[1,2]*, Manuel Buttini[1,2]

*Authors contributed equally

[1] Luxembourg Centre for Systems Biomedicine, University of Luxembourg, Esch-sur-Alzette, Luxembourg
[2] Luxembourg Center of Neuropathology, Dudelange, Luxembourg
[3] Institute of Neuropathology, Saarland University Clinic (UKS), Homburg, Germany
[4] Department of Cancer Research, Luxembourg Institute of Health, Strassen, Luxembourg
[5] Department of Psychiatry, University of Freiburg Medical Center, Freiburg, Germany
[6] Biogen, Cambridge, Massachusetts, USA
[7] Department of Life Science and Medicine, University of Luxembourg, Esch-sur-Alzette, Luxembourg
[8] SynAging SAS, Vandoeuvre-lès-Nancy, France
[9] Faculty of Science, Technology and Medicine, University of Luxembourg, Esch-sur-Alzette, Luxembourg
[10] National Center of Pathology (NCP), Laboratoire National de Santé, Dudelange, Luxembourg

Corresponding author : Manuel Buttini, manuel.buttini@uni.lu, (+352) 4666446183

Keywords

alpha-synuclein spreading, disease pathways, microgliosis, neurodegeneration, neuroinflammation, Parkinson's disease, transcriptional profiling, translational

Abstract

A key pathological process in Parkinson's disease (PD) is the transneuronal spreading of α-synuclein. Alpha-synuclein (α-syn) is a presynaptic protein that, in PD, forms pathological inclusions. Other hallmarks of PD include neurodegeneration and microgliosis in susceptible brain regions. Whether it is primarily transneuronal spreading of α-syn particles, inclusion formation, or other mechanisms, such as inflammation that cause neurodegeneration in PD is unclear. We used a model of spreading of α-syn induced by striatal injection of α-syn preformed fibrils into the mouse striatum to address this question. We performed quantitative analysis for α-syn inclusions, neurodegeneration, and microgliosis in different brain regions, and generated gene expression profiles of the ventral midbrain, at two different timepoints after disease induction. We observed significant neurodegeneration and microgliosis in brain regions not only with, but also without α-syn inclusions. We also observed prominent microgliosis in injured brain regions that did not correlate with neurodegeneration nor with inclusion load. Using longitudinal gene expression profiling, we observed early gene expression changes, linked to neuroinflammation that preceded neurodegeneration, indicating an active role of microglia in this process. Altered gene pathways overlapped with those typical of PD. Our observations indicate that α-syn inclusion formation is not the major driver in the early phases of PD-like neurodegeneration, but that microglia, activated by diffusible, oligomeric α-syn, may play a key role in this process. Our findings uncover new features of α-syn induced pathologies, in particular microgliosis, and point to the necessity for a broader view of the process of α-syn spreading.

Introduction

Protein misfolding and aggregation are central pathological processes in neurodegenerative diseases, where they are believed to play a key role in driving the pathology (Chiti & Dobson, 2017; Selkoe, 2003). Proteins such as the amyloid beta peptide (Aβ) and tau in Alzheimer's disease (AD), TAR DNA-binding protein 43 (TDP43) in motor neuron disease, prion in Creutzfeldt-Jakob disease, and finally alpha-synuclein (α-syn) in Parkinson's disease (PD), are all examples of physiologically occurring proteins that, upon pathological misfolding, form oligomers, fibrils, and extracellular (Aβ, prion) or intracellular (TDP43, tau, α-syn) deposits, and injure neurons in the process (Goedert, 2015; Ross & Poirier, 2004; Scheckel & Aguzzi, 2018). An important property of these disease-associated proteins is their ability to self-propagate, a process first described in prion diseases, in which disease-associated misfolding proteins induce the disease when transposed into a susceptible recipient host (Scheckel & Aguzzi, 2018; Walker & Jucker, 2015). They do so by acting as a seed and corrupting the endogenous form of the protein, leading it to aggregate and form, over time, inclusions along interconnected neuronal pathways (Jucker & Walker, 2018; Mezias et al., 2020). The “spreading hypothesis” posits that misfolded/aggregated particles of a disease protein move trans-synaptically from neuron to neuron, causing dysfunction and damage along the way (Goedert, 2015; Mezias et al., 2020). Major support for this hypothesis comes from two observations. First, the neuropathological studies by Braak and colleagues, staging tau inclusions in AD (Braak & Braak, 1995), and Lewy inclusions in PD (Braak et al., 2003), suggest a progression, starting first in a population of susceptible neurons, of proteinaceous intraneuronal inclusions, a process that takes place over decades. Second, postmortem studies of PD patients that had received striatal fetal neuron transplants to combat dopamine loss, revealed Lewy bodies in a subset of the grafted neurons, indicating a spreading of abnormal α-syn from the diseased neurons of the recipient to those of the donor (Brundin et al., 2016; Chu & Kordower, 2010). Alpha-syn is a presynaptic protein that normally is involved in the regulation of the synaptic vesicle cycle (Bendor et al., 2013; Burre et al., 2018). Its involvement in PD was discovered when it was identified as an essential component of a PD pathological hallmark, the Lewy body (Spillantini et al., 1998), and when mutations in its gene, as well as dupli- or triplication thereof, were shown to lead to hereditary forms of the disease (Lin & Farrer, 2014;

Singleton & Hardy, 2019). Its prion-like spreading properties have been demonstrated in in vitro and in vivo model systems, using intracranial injection of Lewy-body containing brain extracts, of viral-construct mediated α-syn overexpression, or administration of pre-formed fibrils (PFFs) from recombinant α-syn as seeds, to induce spreading and progressive aggregation (Chu et al., 2019) (Luk et al., 2012; Luna & Luk, 2015; Rey et al., 2016; Ulusoy et al., 2013). The role of α-syn spreading and inclusion formation in PD pathogenesis is still unclear, since no correlation between PD symptoms and α-syn inclusion load was consistently found (Dijkstra et al., 2014; Espay & Marras, 2019; Jellinger, 2009a, 2009b). Different possibilities that could explain what ultimately causes neuronal dysfunction and injury and, hence, neurological symptoms, have surfaced (Poewe et al., 2017; Surmeier et al., 2017b). Oligomers, rather than deposited forms of α-syn, may be more neurotoxic that deposited forms (Bengoa-Vergniory et al., 2017; Walsh & Selkoe, 2004). While some studies report the toxicity of α-syn oligomers, notably through activation of microglia (Bengoa-Vergniory et al., 2017; Helwig et al., 2016), others contend only inclusions cause neuronal dysfunction and injury (Abdelmotilib et al., 2017; Osterberg et al., 2015). In this study, we addressed this issue by inducing α-syn seeding/ spreading in wildtype mice (Luk et al., 2012). We used intracranial administration of recombinant murine α-syn PFFs to induce α-syn spreading and inclusion formation in the brain, and examined neurodegeneration and microgliosis in regions with α-syn inclusions and, importantly, in those without. We observed neurodegeneration in both cases, indicating that neuronal injury can occur independently of the formation of α-syn inclusions. Because neuroinflammation has emerged as a key player in neurodegenerative disease (Hammond et al., 2019), and because microglia are the main cellular effectors of this process (Crotti & Ransohoff, 2016; Wolf et al., 2017), we measured microgliosis in our model. We noticed, in regions with or without inclusions, a surprisingly strong microgliosis (4–5 over baseline), which far surpassed that observed after administration of neurotoxins such as the dopaminergic lesioning agent 6-hydroxydopamine (6-OHDA). In contrast to mice injected with 6-OHDA, neurodegeneration and microgliosis did not correlate with each other in the brains of α-syn PFFs injected mice. Moreover, by measuring gene expression profiles after striatal α-syn PFF injection, we observed numerous changes in inflammation-related genes and pathways, and an unusual microglial molecular

activation profile that preceded neurodegeneration and pointed toward an involvement of these cells in the process. We also saw that key PD pathways were recapitulated in this model. These findings indicated that, in the α-syn seeding/spreading mouse model, microgliosis does not occur primarily as a response to neuronal damage, but as part of a response that occurs independently of α-syn inclusion formation. Our results demonstrate that PD-like neurodegeneration can occur in the absence of α-syn inclusions, and thus that PD-like pathology is more than just the progressive formation of such inclusions. It may involve spreading of other, more soluble forms of toxic aggregates, such as oligomers, that could induce an excessive microglial response. We believe these results add an important aspect on how the pathogenic properties of "prion-like" α-syn should be viewed, highlight an important role of microglia in the process, and stress the translational relevance of the α-syn seeding/spreading model.

Results

Western blot and electron microscopy characterization of α-syn moieties

A non-denaturing blot of the α-syn moieties used in this study is shown in Figure S1 (upper panel). For striatal injections, α-syn oligomers were used non-sonicated, whereas α-syn PFFs were sonicated. Based on their Western blot (WB) profile, the oligomer preparation was composed mainly of monomers, dimers, and trimers, as well as higher molecular weight species. The sonicated PFFs were composed mainly of monomers and dimers, and higher molecular weight species. When compared to their non-sonicated counterparts, sonicated PFFs seemed to have less of all these components, consistent with a shearing effect of sonication that produces smaller α-syn fragments, which may then act as seeds. Electron microscopy confirmed the presence of different sized moieties in the different preparations. At the ultrastructural level (Figure S1, lower panels), we observed that oligomers were mostly composed of small globular assemblies, unsonicated PFFs were formed of highly complex large agglomerates, and a number of smaller assemblies, and sonicated PFFs were mostly composed of small fibrillar fragments. Because we wanted to follow the original protocol of Luk et al. (Luk et al., 2012), no effort was made to purify particular α-syn moieties. In addition, defining the pathobiological properties of the different moieties, while also making sure these moieties stayed stable in their respective conformation over the whole course of an experiment, was beyond the scope of the present study. Other studies have looked at that issue (Grozdanov et al., 2019; Peelaerts et al., 2015; Rey et al., 2019). We were instead focused on determining whether the pathologies resulting from intracerebral injection of the moieties we used resulted in translationally relevant PDlike phenotypes, and on understanding underlying mechanisms of neurodegeneration.

Striatal injection of PFFs causes bilateral α-syn inclusions in multiple brain regions

Because we wanted to capture the early features of α-syn spreading associated pathologies, we decided to focus our investigations on time points when these pathologies have not peaked yet (Luk et al., 2012). Since α-syn inclusions have been suggested to be a major driver of PDlike pathology (Abdelmotilib et al., 2017; Spillantini

& Goedert, 2018), we first looked at the appearance of such inclusions in our model. To determine if striatal injection of murine α-syn PFF reliably induced propagation of fibrillar α-syn in our mice, we performed immunohistochemistry against pSER129- α-syn on sections of both brain hemispheres 13 and 90 days after they had been injected with PFFs (13 and 90 dpi). Immunostaining for pSER129- α-syn is the most commonly used approach to detect α-syn inclusions in rodent or human brain tissues (Vaikath et al., 2019). At an early time point after α-syn PFF administration (13 dpi), we only detected few pSER129-α-syn positive inclusions in frontal cortex, amygdala, and SN, and a few more in the ipsilateral striatum (Figure S2). However, at 90 dpi, we observed robust appearance of pSER129- α-syn positive cellular and neuritic inclusions ipsi- and contralaterally, in the same brain regions (Figure 1a). Quantitation of image area occupied revealed median coverage of 10% for the ipsilateral frontal cortex, 5% for the contralateral frontal cortex, 8% for the ipsilateral amygdala, 4.2% for the contralateral amygdala, and 12% for the ipsilateral SN. No or very few α-syn inclusions were found in the contralateral SN and striatum, and no inclusions in either side of the hippocampus. Cells containing inclusions had neuronal morphology. In the ipsilateral SN, fluorescent double staining for pSER129-α-syn and TH, a marker for dopaminergic neurons in the SN, showed that 85% of inclusions colocalized with TH-positive neurons, indicating that most, if not all, inclusions were localized in neurons. To determine if pSER129-α-syn positive inclusions were Proteinase-K resistant, we performed a Paraffin-Embedded Tissue blot (Kramer & Schulz-Schaeffer, 2007; Milber et al., 2012). We observed numerous pSER129-α-syn positive signals in these tissue sections (Figure 1b), indicating that most inclusions were proteinase-K resistant. Inclusions are not the only α-syn species that have been suggested to be linked to neurodegeneration in PD. To determine if regions without detectable α-syn inclusions, such as the hippocampus, were still affected by abnormal α-syn after injection of PFFs, we performed a proximity ligation assay (Malaplate-Armand et al., 2006). This assay has been used for detecting oligomeric forms of α-syn in human (Roberts et al., 2015) and mouse models of PD (Ulusoy et al., 2015). We observed greatly enhanced signal intensity in the hippocampi of PFF-injected mice than in those of control mice (Figure 1c), indicating the presence of abnormal levels of oligomeric α-syn in that region. Overall, the pattern of α-syn inclusions we observed 90 dpi matched that described at a similar time point by Luk et

al. (2012) (Luk et al., 2012). The robust appearance of intracellular α-syn inclusions in this model, at just 90 dpi after injection of PFFs, opened up the possibility of analyzing how they are associated with other pathological hallmarks, such as neurodegeneration and –inflammation, and which of these events precedes the other.

Striatal injection of PFFs causes bilateral synaptic loss and unilateral dopaminergic neuron injury that was independent of α-syn inclusions

We set out to determine to what extent the presence of neuronal α-syn deposition was linked to neurodegeneration, 90 dpi after striatal administration of PFFs. First, we analyzed synaptic degeneration in the hippocampus and frontal cortex. In these brain regions, we measured the level of the presynaptic protein synaptophysin. Synaptophysin is a good marker for synaptic integrity (Buttini et al., 2005; Calhoun et al., 1996; Zhan et al., 1993), and pathological synaptic alterations have been reported in PD post-mortem tissues (Bellucci et al., 2016). Roughly 60% of PD patients suffer from cognitive impairments and dementia (Aarsland et al., 2017), indicating that their hippocampus and their higher cortical association areas are affected. Addition to PFFs to cultured primary hippocampal neurons was reported to affect these neurons' synaptic integrity and function (Wu et al., 2019). Thus, we measured synaptophysin ipsi- and contralaterally in these brain regions in mice 90 days after PFF administration (Figure 2). We found, in both regions, a highly significant, bilateral 20%–25% reduction of this protein in PFF-injected mice. Interestingly, we noticed this decrease in the absence of α-syn inclusions in the hippocampus. The α-syn oligomers though (Figure 1) in that region colocalized with synaptophysin loss. Next, we examined the SN, because it contains dopaminergic neurons that are one of the most susceptible population in PD. We measured the area occupied by tyrosine hydroxylase (TH)-positive neuronal profiles in the SN ipsilaterally, where α-syn inclusions were present (see above), but also contralaterally, which was without such inclusions. We found a statistically significant 16% decrease of TH-positive neurons in the ipsilateral SN, but not so in the contralateral SN (Figure 2). To determine if striatal axonal projections of dopaminergic neurons were affected in our model, we analyzed the morphological integrity of these projections and

their synaptic terminals. We observed, 90 dpi, a significant decrease in TH-positive axonal fibers as well as in dopamine transporter (DAT) positive synaptic terminals, in the ipsilateral, but not the contralateral striatum. We did not find any sign of degeneration in the striatum or SN at 13 dpi (Figure S3, 3 first rows). To confirm ipsilateral striatal injury, we measured the neurotransmitter dopamine (DA) in dissected ipsi- and contralateral striata of PFF injected and PBS control mice (n = 8–12/group). We found a significant decrease in ipsilateral striatum of PFF mice compared their ipsilateral PBS controls (19.5+/-5.8 vs. 27.5+/-7.3 pmol/mg; p = .02 by ANOVA followed by Sidak's post hoc, results are means +/- SD), but no difference between contralateral striatum of PFF mice compared to their compared their ipsilateral PBS controls (27.3+/-3.7 pmol/mg vs. 28.5+/-5.7 pmol/mg). This substantiated our histological observations.

Striatal injection of α-syn PFFs caused profound microgliosis in different brain regions that was independent of α-syn inclusions

Microglia, the local CNS innate immune defense cells (Michelucci et al., 2018), react rapidly to CNS infection or injury. Functional imbalance of these cells can precipitate disease outcomes (Biber et al., 2014; Crotti & Ransohoff, 2016; Wolf et al., 2017). While strong microgliosis has been reported in PD and models thereof (Doorn et al., 2012; Joers et al., 2017; Tan et al., 2020), the role of these cells in disease initiation and progression is poorly understood. To better understand the role of microglia in the context of α-syn spreading, and more precisely to determine if these cells have a role in driving the neurodegeneration we observed, we first analyzed their response using a specific marker (Iba1), in mouse brains after injection of α-syn PFFs. We observed a surprisingly strong (4–5 times over control) microgliosis in different brain regions (bilaterally in frontal cortex, amygdala, SN) at 90 dpi. The microgliosis was present in brain regions with inclusions, but also those without (hippocampus) or very little (contralateral SN) inclusions (Figure 3). While no significant Iba1 increase was seen at 90 dpi in the ipsilateral striatum in PFF injected mice, microglial Cluster-of- Differentiation 68 (CD68), a marker for phagocytic activity, was increased in that location, indicating that these cells, while having a different kind of response, were still activated. No

significant microgliosis was observed in the SN at 13 dpi (Figure S2, lower row). Microglia in PFF-injected mice had thickened, though still ramified, processes, and an intensely stained cell soma. In the cerebellum, which was devoid of α-syn deposits in all mice, we could not detect any differences in Iba1 positive microglia between PFF-injected and control PBS injected mice (not shown). Our observations indicate that a robust, widespread microglial reaction is an important part of the α-syn spreading process, and warranted further investigation into the pathological implications of that reaction.

Neurodegeneration and microgliosis correlated neither with α-syn deposition, nor with each other

To gain insight into the pathological properties of α-syn inclusions, we correlated the inclusion load with neurodegeneration and with microgliosis measured locally in frontal cortex and SN. We found that inclusion load correlated with neither of the two (Figure 4). Thus, neurodegeneration as well as microgliosis induced by α-syn PFFs are probably independent of α-syn deposition. The strong microgliosis in different brain regions after administration of PFFs prompted us to look into this observation further. In the brain, microglia react rapidly to tissue injury to control the damage and clear up cell debris (Fu et al., 2014; Wolf et al., 2017). Thus, microglial reaction is typically secondary to an underlying neurodegenerative process, and, as a consequence, increase of microglial reaction is directly associated with decrease of neuronal integrity. For instance, we have observed that microglial reaction (measured on Iba1 immunostained sections) correlated negatively with TH neuron loss in the ipsilateral SN after unilateral lesioning by 6-OHDA (Figure 4b2), and with synapse or dendritic loss in the cortex after lesioning with the excitotoxin kainic acid (Jaeger et al., 2015). After intracerebral injection of α-syn PFF though, we found that microglial reaction was not only much stronger than after injection of neurotoxins (4–5 vs. 2–3 over control), but also failed to correlate with measures of neurodegeneration (TH neuron loss in the SN, synaptophysin in the cortex and hippocampus) (Figure 4b). This observation indicates that the microglial reaction to α-syn spreading may be a direct response to factors produced during that process, and not just a secondary response to neuronal degeneration.

Microglia across several brain regions reacted strongly to striatal injection of α-syn oligomers

Several studies have indicated that microglia are activated in vitro by α-syn oligomers (Hughes et al., 2019; Kim et al., 2013). As described above, we have observed the presence of α-syn oligomers, notably in the hippocampus, after striatal injection of α-syn PFFs. To test whether α-syn oligomers could be the factor that led to a strong microglial reaction during the α-syn spreading process, we injected such oligomers into the same location as the PFFs, the dorsal striatum. Just 13 dpi, we observed, on Iba1 stained sections, a strong microglial reaction in the ipsilateral striatum, frontal cortex, and hippocampus (Figure 5). Qualitatively, the reaction was even stronger than 90 dpi after PFF injection. We did not move forward in quantifying this reaction and its consequences, since our goal was just to show that microglia react to the injection α-syn oligomers, even in regions distant to the injection site, and because the number of animals used to test this was only three per group. Further studies will investigate these issues. Thus, microglial cells in vivo respond strongly to α-syn oligomers, and further analyzing the possible role of these cells was warranted.

Transcriptional profiling of ventral midbrain revealed most gene expression changes occur 13 days after α-syn PFF injection

To investigate the molecular underpinnings of the neurodegeneration and the microglial response accompanying α-syn spreading, we generated a gene expression profile from ventral midbrain of PFF injected and control mice using the Affymetrix gene expression profiling platform. Because microglial response typically starts early after an insult (Michelucci et al., 2018; Tansey & Romero-Ramos, 2019), we analyzed the midbrain gene expression profiles 13 dpi (no neurodegeneration) and 90 dpi (neurodegeneration in the ipsilateral striatum and midbrain) after striatal α-syn PFF injection. We focused on two comparisons of ventral midbrain gene expression profiles: 1. Ipsilateral midbrain of PFF-injected mice (ipsi PFF, with degeneration of nigral TH neurons and their striatal projections) versus ipsilateral midbrain of control PBS-injected mice (ipsi PBS); 2. Ipsilateral midbrain of PFF-injected mice versus contralateral midbrain of the same, PFF-

injected, mice (contra PFF, without loss of nigral TH neurons and their striatal projections). We figured that these two comparisons would be best suited to reveal relevant gene expression changes. Venn diagrams for the number of DEGs that emerged in the comparisons between the two time (13 and 90 dpi) are shown in Figure S4. The heatmaps are shown in Figure S5. By comparing ipsi PFF to ipsi PBS, applying a cut-off of $p < .05$, we found a total of 3.584 significant DEGs at 13 dpi, and significant 2.990 DEGs at 90 dpi, with 960 overlapping DEGs between the two time points. After correcting for multiple hypothesis testing at a cut-off of $pfp < 0.1$, we found 308 DEGs at 13 dpi, and 94 DEGs at 90 dpi, with 37 DEGs overlapping between the two times points. The majority of overlapping DEGs showed enhanced expression at 13 dpi, but reduced expression at 90 dpi. By comparing ipsi PFF to contra PFF, we found 4.268 significant DEGs at 13 dpi, and 3.976 DEGs at 90 dpi, with 1312 overlapping DEGs. At $pfp < 0.1$, we found 674 DEGs at 13 dpi, and 688 DEGs at 90 dpi, with 210 overlapping DEGs. At 13 dpi, we found a similar number of DEGs with enhanced versus reduced expression, but at 90 dpi, we saw that most DEGs were, interestingly, had reduced expression. To capture all potentially relevant molecular changes, we used the all DEGs with $p < .05$ for the subsequent analyses. Taken together, these two comparisons indicate that enhanced gene expression changes occurred in the ventral midbrains of both hemispheres at 13 dpi, possibly setting the stage for the subsequent pathological events. In contrast, at 90 dpi, in the ipsilateral midbrain, most DEGs dial their expression level back, indicating a reduction in gene transcription, while the major pathological events now appear to take place at the protein level, and are measurable with quantitative histology (see above).

Gene set enrichment revealed early involvement of inflammation in the α-syn seeding/ spreading process

To investigate which molecular pathways underlie the α-syn spreading process and its associated pathologies, in particular microgliosis, we generated an enrichment map based on a Gene-Set Enrichment Analysis (GSEA, see Materials and Methods, Section 2) for Biological Processes (BP, see Materials and Methods, Section 2). To obtain a global view of the BPs alterations during the evolution of α-syn spreading induced pathologies,

we used manual curation to group gene sets into biologically meaningful gene-set clusters associated with high order pathological processes (Figure 6). Our first observation was that, in ipsilateral midbrains of PFF injected mice compared to those of PBS-injected ones, 261 BPs were enriched at 13 dpi, but, surprisingly none at 90 dpi. In contrast, we observed that, at 90 dpi, all BPs in ipsilateral midbrains of PFF injected mice versus those of PBS-injected ones (total of 1067 BPs), showed reduced gene activity. This observation indicates a significant shift from enhanced to greatly reduced transcriptional activity in the time frame between 13 and 90 dpi, and confirms the observations on DEGs depicted in Figure S5. We then observed that many gene set clusters with enhanced transcriptional activity at 13 dpi in ipsi PFF were associated with inflammation/immune processes (Figure 6, upper panels), while gene set clusters associated with similar profiles had reduced transcriptional activity at 90 dpi, in particular compared to ipsi PBS (Figure 6, lower left panel). This indicated that, after an initially enhanced activity of genes regulating inflammation/immune responses, that activity was strongly reduced at a stage when pathology was histologically detectable. Another interesting observation we made was that some gene set clusters containing BPs associated with reduced gene activity at 90 dpi, were related to dopaminergic neuron function (e.g., catecholamine/ dopamine metabolic processes, locomotor behavior, regulation of synaptic transmission regulation of signaling pathways upon growth factor stimulus). The reduced gene activity in midbrain dopaminergic neurons was likely a reflection of their pathological demise. Taken together, these observations point to an important role for inflammatory/immune processes in the initiation and, possibly, progression of neurodegeneration in the context of α-syn spreading.

Gene expression changes based on cell type confirmed early microglial response to α-syn seeding/ spreading

To identify the immune cell type(s) active in the inflammatory response to α-syn seeding/spreading, we attributed all DEGs of ipsi PFF versus ipsi PBS and ipsi PFF versus contra PFF to cell types, using a widely used public database (see Materials and Methods, Section 2). We found that the majority of DEGs with increased expression at

13 dpi were microglial, whereas many of these DEGs had decreased expression at 90 dpi (Figure 7a). We also looked at the 20 top DEGs and their cellular source for each time points after PFF injection (Figure 7b). At 13 dpi, in both the ipsi PFF versus ipsi PBS as well as the ipsi PFF versus contra PFF comparison, we observed that the majority of these 20 DEGs with enhanced expression were microglial (ipsi PFF versus ipsi PBS: 9 out of 20, or 45%, ipsi PFF versus contra PFF: 8 out of 20, or 40%). This indicates a strong gene expression activity of these cells, well before pathological changes can be detected histologically. In contrast, at 90 dpi, we observed that only 1 out of 20 (5%) DEGs was microglial in both comparisons (ipsi PFF versus ipsi PBS, ipsi PFF versus contra PFF). Here, the majority (>50%) of DEGs in the ipsi PFF versus ipsi PBS comparison were neuronal. The observation that the majority of DEGs at 13 dpi were microglial confirmed an early response of these cells to α-syn spreading.

Unusual microglial molecular signature, induced by striatal injection of α-syn PFFS, preceded neurodegeneration

Recent studies using transcriptomics technologies have shed light on microglial activation profiles at baseline and in disease models. In one study (Uriarte Huarte et al., 2021), single-cell transcriptomics in mouse nigro-striatal brain regions revealed an enrichment of a microglia subtype with an “immune-alerted” expression signature of 68 genes, and 2 other subtypes (homeostatic, intermediate) with a much smaller number of signature genes. A list of the DEGs in our study that overlap with the genes for these microglial subtypes is given in Table S3. At 13 dpi, 20 microglial ipsi PFF versus ipsi PBS DEGs, and 21 microglial ipsi PFF versus contra PFF DEGs were of the “immune-alerted” class. In contrast, at 90 dpi, the corresponding numbers were 9 microglial DEGs for ipsi PFF versus ipsi PBS, and 7 for ipsi PFF versus contra PFF. At both time points, the number of DEGs for other microglial subtypes (homeostatic, intermediate) was, for both comparisons, less than 5 (Table S3). This indicated a predominant participation of “immune-alerted” microglia in the α-syn seeding/spreading model. In neurological disease and models thereof, the term “disease-associated microglia” (DAM) defines molecular microglial states, as reflected by a gene expression signature, that are

associated with these diseases and may modulate their pathologies (Hakim et al., 2021; Hammond et al., 2019; Keren-Shaul et al., 2017; Mathys et al., 2017; Mrdjen et al., 2018; Tay et al., 2018; Uriarte Huarte et al., 2021). Some DAM genes show expression changes common to many diseases, while others may only change in a specific disease, or at specific time points across one or many diseases. There is little information on such microglial states for PD. It is beyond the scope of our study to compare our data with all the available DAM gene expression profiles. One study though (Holtman et al., 2015) presents a meta-analysis of aged mice and four different mouse neurological disease models. We compared our DEG datasets to each of these models, and the Venn Diagrams are shown in Figure S6. We then extracted the overlapping microglia genes from the five models in that study, and found a core DAM signature of 50 genes. We compared our datasets with those DAM core genes and found that, at 13 dpi, almost double as many genes overlap with these core genes than at 90 dpi. Venn diagrams illustrating these results are shown in Figure 8, and the list of overlapping genes are found in Table S4. Further studies, in particular on single microglial cells, will have to determine how that number changes over the course of the disease. To look at more unique characteristics of the microglial gene signature in the α-syn seeding/spreading model, we looked at individual genes typically associated with inflammation during neurodegeneration (Table S5). Curiously, there were no changes, at 13 or 90 dpi, in the expressions of Il1b, Il6, Ccl2, Tnfa, or Nos2, genes that are often involved in inflammation. Gene expression was enhanced for Cybb, Ptgs2, and Cxcl10. NADPH oxidase 2 (Nox2), coded by Cybb, generates free oxygen radicals, which can harm neurons (Ma et al., 2017). Cyclooxygenase 2 (Cox2), coded by Ptgs2, generates arachidonic acid metabolites, some of which have been reported to be neurotoxic (Figueiredo-Pereira et al., 2016) or form neurotoxic dopamine-quinone adducts (Teismann et al., 2003). Thus, this may be the mediators of the neurodegeneration observed in ipsi PFF midbrains at 90 dpi. Other microglial activation markers whose products may be involved in promoting pathology were Mrc1, Cd68, Tyrobd, Trem2, Tlr2, P2ry6, and Aif1, which showed increased expression at 13 dpi and/or 90 dpi. Mrc1, Cd68, P2ry6, Aif1 gene products are all involved in phagocytic processes and/or signal transduction (Bhattacharya & Biber, 2016; Janda et al., 2018; Ransohoff & El Khoury, 2015). We had observed CD68 upregulation by immunostaining in the striatal projection

area of dopaminergic neurons (Figure 3), indicating that the arrays' results reflect actual gene product changes. The Tlr2 gene product is a receptor for α-syn, an interaction that elicits the production of microglial neurotoxins (Kim et al., 2016). Tyrobp and the gene for its receptor, Trem2, whose product is involved, among other processes in the regulation of microglial phagocytosis (Konishi & Kiyama, 2018), also showed enhanced expression. Finally, to see if there was an astroglial and peripheral immune cell involvement in the α-syn seeding/spreading model, we listed gene expression data for typical markers of these cells from our gene expression dataset (Table S6). Enhanced expression of a series of astroglial genes in ipsi PFF midbrain indicates a reaction of these cells. Enhanced expression of Ptprc, which codes for CD45, a marker that can be both expressed by microglia and invading macrophages, and of Cd4, which codes for the helper T cell antigen CD4, in the same region, indicated possible infiltration of peripheral immune cells that could contribute to neuronal injury (Brochard et al., 2009; Harms et al., 2017; Kannarkat et al., 2013). Overall, we tentatively conclude that a unique molecular signature in the ipsilateral ventral midbrain at 13 dpi underlies the initial molecular events that lead to the neurodegeneration we observed at 90 dpi. Since neurodegeneration in the contralateral SN has been reported at later time points after PFF injection previously (Luk et al., 2012), in one study even in the absence of α-syn inclusions (Paumier et al., 2015), one can speculate that, at a point past 13dpi, the same molecular signature appears there as well. Our data indicate that inflammatory events, in particular those associated with microglia, but not α-syn inclusion formation, could be initiators of neurodegeneration in the context of α-syn spreading in the model used in our study.

Translational relevance assessment

Finally, we evaluated the translational value of the main pathological changes we observed in the α-syn seeding/spreading model in this study. Pathologically, Braak staging indicates α-syn spreading (Braak et al., 2004), and the presence of important microgliosis, detectable by medical imaging, are happening at early stages of PD (Terada et al., 2016). Hence, at that level of investigation, evidence suggests that the α-syn

seeding/spreading model holds translational value. There is however, to our knowledge, no studies systematically comparing the transcriptional profile of the ventral midbrain in the α-syn seeding/spreading model to that of the SN in different stages of PD. There are numerous studies describing transcriptional profiles of the SN in PD, and comparing them all to our data is beyond the scope of this study. We therefore picked two studies that seemed particularly pertinent: one study lays out the transcriptional profiles of different Braak stages in PD (Dijkstra et al., 2015), and another one presents a meta-analysis study of end-stage PD studies (Glaab & Schneider, 2015). We limited our analysis to comparing DEGs between the ipsi PFF versus ipsi PBS brain sides with human databases, since we did not expect the comparison of ipsi PFF versus contra PFF, (done to reveal molecular features of activated microglia in the presence (ipsi PFF) versus the absence (contra PFF) of neurodegeneration) with those databases to reveal translationally meaningful information. Venn diagrams of overlapping DEGs of the α-syn model with different stages of PD were not very informative, as they revealed anywhere from around 300 to a bit less than 700 overlaps (Figure S6). Overlapping DEGs revealed no pattern and were seemingly random (list not shown). In studies comparing mouse models of inflammatory diseases with their human counterparts, analysis of overlapping DEGs also show poor similarities (Seok et al., 2013). However, a follow-up meta-analysis, looking at pathways and biologically meaningful gene sets, revealed great similarities between the same mouse models and human inflammatory conditions (Takao & Miyakawa, 2015). Similar observations were made when comparing transcriptome profiles of Alzheimer's disease mouse models with those of Alzheimer brains (Wan et al., 2020). We thus proceeded to investigate overlapping pathways between the α-syn seeding/ spreading model and different stages of PD. To do this, we used the PD map online tool (Fujita et al., 2014) (see Materials and Methods, Section 2). By selecting pathways that were significantly represented in at least one of the human databases, as well as in at least one of the two mouse model datasets, we found 15 highly PD-relevant pathways that were shared between the model and PD (Figure 9). Among those, “neuroinflammation” (highest score) and “microglial phagocytosis” were noteworthy, reinforcing the role of microglia in this PD mouse model and in human. While the pathways identified in the mouse model were, perhaps not unexpectedly (see Discussion, Section 4), not completely overlapping in extent and directionality of change,

the similarities were surprisingly close. We thus tentatively conclude that the α-syn seeding/ spreading mouse model of PD provides a valuable preclinical tool to study disease mechanisms, as well as the efficacy of experimental therapeutics, in particular if they relate to microglial-mediated neuroinflammation.

Discussion

In this study, we have used a seeding/spreading model of α-syn, based on striatal injection of α-syn PFFs in the mouse brain, to investigate key questions on how two major pathological features of PD, α-syn inclusion formation and neuroinflammation, contribute to neurodegeneration. Using a transcriptomics approach, we also shed light into the molecular underpinning the disease process in this model. We provide evidence that:

1. α-syn inclusion formation did not correlate with neurodegeneration in areas with inclusions;
2. An exceptionally strong microglial response was seen across different brain regions, but this response did also not correlate with neurodegeneration;
3. The most likely driver of the microglial response were diffusible α-syn oligomers;
4. Gene expression changes indicative of early neuroinflammatory events in the ventral midbrain, in particular in microglia, appeared before nigro-striatal degeneration, and microglial factors could be the driver for downstream neurodegeneration;
5. A translational relevance analysis revealed that 15 key molecular pathways that change in the model overlap with those found altered in PD, with neuroinflammation scoring at the top.

Our study provides novel insights into underlying pathological processes of α-syn spreading mediated PD-like neuronal injury, and stress the value of the α-syn spreading model for investigation of disease mechanisms and preclinical testing of therapeutics. We undertook this study because it is unclear how different pathological processes relate to each other in PD. In particular, it is debated whether α-syn inclusion formation is the main driving force in disease initiation and progression, or whether other processes, such as neuroinflammation are (Brundin & Melki, 2017; Surmeier et al., 2017a; Walsh & Selkoe, 2016). The Braak hypothesis (Braak et al., 2003) posits that α-

syn inclusion pathology starts in lower motor nuclei of the brainstem (e.g., Dorsal Motor Nucleus of the Vagus), or even in the PNS, then gradually moves upwards and, in doing so, causes various PD symptoms, from early non-motor to later motor and cognitive and psychiatric ones, to appear. More direct evidence for the importance of α-syn spreading in inducing PD-like disease comes from experimental models. In rodent or primate models, direct injection, in different brain regions, of PD brain tissue, isolated Lewy bodies, PFF made out of recombinant α-syn, or viral vector driven local overexpression of α-syn, induces a variety of PD-related pathologies, including α-syn spreading and inclusion formation along connected neurons (Rey et al., 2016). Peripheral PFF injections, such as intramuscular, intestinal, or intravenous have been reported to also lead to PD-like pathologies in the brain of rodents (Ayers et al., 2017; Holmqvist et al., 2014; Peelaerts et al., 2015; Sacino et al., 2014). These studies have cemented, experimentally, the process of "prion-like" propagation and inclusion formation of α-syn. The mechanism of this process has been investigated in in vitro systems. Cultured neurons secrete as well as take up circulating α-syn, and various underlying mechanisms have been proposed, such as unusual forms of endo- and exocytosis, or nanotubes (Rodriguez et al., 2018; Vasili et al., 2019). Ingested, presumably misfolded α-syn, corrupts its endogenous counterpart and leads it to form pathological inclusions (Spillantini & Goedert, 2018). Glial cells have also been reported to take up α-syn, and, in some cases, this can lead to pathological inclusions, as is the case for oligodendrocytes in Multiple System Atrophy (Filippini et al., 2019). Microglia, in particular, have recently been shown to uptake and degrade abnormal α-syn, a process facilitated by through the formation of intercellular connections that distribute the "work-load" through a microglial cellular network (Scheiblich et al., 2021). The toxic potential of inclusions has also been investigated in vivo. In a mouse model of α-syn spreading, where inclusion formation was followed in vivo by multi-photon laser microscopy, the formation of intraneuronal inclusion was reported to coincide with neuronal dysfunction (Osterberg et al., 2015). Another study has shown a weak correlation between loss of TH neurons in the SN and a global score of inclusion load after striatal PFF injection in both mice and rats, but a strong correlation between the two measures after direct injection of PFFs into the SN of rats (Abdelmotilib et al., 2017). Thus, it is tempting to conclude that α-syn inclusions are a major driver of PD pathology. But a closer look at other evidence reveals

several unresolved questions in this otherwise elegant picture. In post-mortem brain tissues of early or late PD, the correlation between α-syn inclusion (Lewy body) load and nigral degeneration is unclear (Jellinger, 2009a, 2009b). Across different studies looking at various brain structures affected in PD, α-syn inclusions have been reported in areas with high, moderate, or no neuronal loss (Jellinger, 2009b). Some PD patients, including some familial forms, have PD symptoms and loss of nigral neurons without detectable α-syn inclusions (Surmeier et al., 2017b). Interestingly, one study, comparing Incipient Lewy Body Disease (ILBD) to PD autopsy material, reported that neuronal loss precedes α-syn inclusion formation in the SN (Milber et al., 2012). In mice injected with α-syn PFFs into the pedunculopontine nucleus, appearance of inclusions was not related to strength or extent of neuronal connection of that brain region (Henrich et al., 2020). In a rodent models where spreading is driven by viral overexpression of α-syn in the Dorsal Motor Nucleus of the Vagus, while intact neuronal architecture was essential for the spreading process to happen, neurodegeneration and inclusion formation were also found to be independent processes (Ulusoy et al., 2015). Non-fibrillar forms of misfolded α-syn, notably oligomers, diffusing for long distances have been suggested to drive neuronal dysfunction and degeneration (Bengoa-Vergniory et al., 2017; Walsh & Selkoe, 2016). In our study, we indeed found evidence of neurodegeneration that was independent of inclusions, and, in the hippocampus, even appeared in the complete absence of them, but in the presence of oligomers. Published evidence suggests that the hippocampus remains devoid of α-syn inclusions even 180 days after PFF injection into the striatum (Luk et al., 2012). Our data therefore does 954 GARCIA ET AL. not support the notion of a direct relationship between the formation of α-syn inclusions and neurodegeneration, but rather indicate that the α-syn spreading process may lead to the formation of pathological oligomers, at least in the early stages of the disease. Pathologically misfolded α-syn can drive neuronal injury in PD by different means, including mitochondrial dysfunction, oxidative stress, endoplasmic reticulum stress and lysosomal dysfunction, disequilibrium in cytosolic Ca2+, neurotoxic oxidized dopamine, disruption of axonal transport, and, notably, neuroinflammation (Rocha et al., 2018). The relative contribution of these different processes to neuronal demise is unclear. Neuroinflammation has received particular attention because of its widespread involvement in various neurological diseases and the potential for therapeutic

modulation (Hirsch & Standaert, 2020; Lema Tome et al., 2013; Tansey & Romero-Ramos, 2019). The major cellular mediators of this process are microglia. Microglia are a particular kind of myeloid cells that originate from the yolk sack and populate the nervous system during early stages of development, where they act as the innate, resident immune cells (Michelucci et al., 2018; Ransohoff & El Khoury, 2015). During development and under normal conditions, they modulate nervous system homeostasis, prune synapses, and regulate their formation. Under pathological conditions, they act as the primary line of defense against infectious organisms, and clear endogenous tissue debris after injury (Michelucci et al., 2018; Ransohoff & El Khoury, 2015; Wolf et al., 2017). They undergo a substantial morphological and functional transition to activated, or reactive, microglia, which makes them functionally equivalent to macrophages (Michelucci et al., 2018). Evidence suggests though that, in many neurological conditions, they are not only reacting to disease, but also drive tissue injury (Ransohoff & El Khoury, 2015). This pathological process is, in particular in PD, incompletely understood. While microglial activation can be induced by neuronal injury and/or misfolded and aggregated protein, notably α-syn oligomers or fibrils (Fellner et al., 2013), it is still unclear how and when microglial activation damages healthy tissue and exacerbates the neurological disease process. In PD, a strong microgliosis is observed post mortem in the SN (Croisier et al., 2005; Joers et al., 2017). Longitudinal imaging studies with PET ligands demonstrated an early microglial activation in various regions beyond the SN, such as cortex, hippocampus, basal ganglia, and pons, but no correlation with other pathological measures, including clinical scores, of PD emerged (Gerhard et al., 2006; Terada et al., 2016). Interestingly, in striatal fetal grafts implanted in PD patients (Chu & Kordower, 2010), microglia activation was observed years before the appearance of α-syn inclusions (Olanow et al., 2019). In different toxin-induced PD rodent models, microgliosis was reported to precede, coincide, or follow the appearance of neuronal demise (Joers et al., 2017), while in a transgenic human α-syn model (Watson et al., 2012), and in rats injected with PFFs into the striatum (Duffy et al., 2018), microgliosis, measured histologically, was shown to precede neurodegeneration. These studies are based mainly, if not exclusively, on the observation of morphological changes of microglial response using immunostaining techniques for generic cell markers. While informative, the detection of morphological

changes indicating microglial activation does not yield enough information on the actual physiological or molecular profile of these cells. Microglia commonly have a spectrum of activation states that may change over the course of the disease (Ransohoff, 2016). Recent gene expression profiling approaches have revealed a bewildering complexity in microglial heterogeneity (Crotti & Ransohoff, 2016; Dubbelaar et al., 2018; Uriarte Huarte et al., 2021). Evidence suggests a "core" gene expression profile response that is associated with every neurodegeneration condition, while expression changes of a more restricted set of genes may be specific for each condition, leading to the concept of disease-specific microglial signatures, or "disease-associated microglia" (DAM) (Dubbelaar et al., 2018). Our study provides new insights into the molecular underpinnings of neuroinflammation preceding neuronal injury in the PD-like context of α-syn spreading, and highlights a microglial gene signature that may drive neurodegeneration. First, we show, at the level of gene expression, that neuroinflammation-linked processes were activated, and that many microglial genes had increased expression levels early (13 dpi), which then were downregulated later (90 dpi) after PFF injection. Microglia genes that code for factors that could cause neurodegeneration showed increased expression 13 dpi only in the ipsilateral midbrain, where TH loss was observed later, at 90 dpi. Among these were Cybb, which codes for NAPDH oxidase 2, an enzyme that catalyzes the production of tissue harming free radicals (Ma et al., 2017), and Ptgs2, which codes for cyclooxygenase 2 (Cox2), an enzyme that forms prostanoids from arachidonic acid, some of which are neurotoxic (Figueiredo-Pereira et al., 2016; Hsieh et al., 2011). Tlr2, Trem2, and Tyrobp RNAs showed increased levels in our model at 13 dpi. Many genes linked to microglial activation are regulated by Tyrobp, a tyrosine kinase binding protein that binds to Trem2. The Tyrobp/ Trem2 pair triggers pathways that are involved in the inhibition of TLR-mediated inflammation, and in the modulation of phagocytosis (Konishi & Kiyama, 2018). In prodromal PD, enhanced TLR2 immunoreactivity on microglia was observed, whereas in late stage PD, it wasn't (Doorn et al., 2014), indicating that, just like in our model, the microglial response happens in early phases of the disease and changes over time. Alpha-syn, in particular in its oligomeric form, activates microglia in vitro through Toll-like receptors (Fellner et al., 2013; Kim et al., 2013), and targeting TLR2 by immunotherapy was shown to be beneficial in α-syn pathology models (Kim et al., 2018).

The absence of increased gene expression of common proinflammatory mediators such as Il1b and Tnfa in our α-syn spreading model is puzzling, since these are factors associated with most, if not all, inflammatory conditions. Of note though is that we also did not observe enhanced expression of these factors when primary microglia were exposed to our α-syn PFFs, while they responded strongly to bacterial lipopolysaccharide (not shown). It is possible tough that the increased expression for these genes was missed and occurs at a time point after PFF injection that we have not looked at. Future studies will have to focus on isolated microglia and use the latest transcriptional technology in a longitudinal fashion in this model to better GARCIA ET AL. 955 understand the specific microglial response, in particular the response of microglial subtypes. It is crucial to demonstrate the translational relevance of a rodent model by drawing parallels between the disease manifestations and mechanisms observed in it with those found in human. Our comparative analysis of molecular pathways altered in the α-syn seeding/ spreading model revealed several overlaps of disease-relevant pathways with the pathways that change in different stages of PD. There was no absolute 1–1 overlap of any of the two mouse datasets with any of the human datasets, but this may not be surprising. One of the limitations of rodent models is that studies are typically done in inbred strains (genetically identical subjects that are homozygotes in all loci), whereas humans are genetically quite heterogeneous. One can thus expect more variation in human than in the typical inbred strain mouse model. Another one is that, in the field of chronic neurological diseases, it is necessary to compress a disease that in human takes decades to develop into the comparatively short lifespan of a mouse. The similarities we saw though between the α-syn seeding/spreading model and PD are encouraging. Taken together, our data indicate that, at least in the initial period of PD-like disease progression that is associated with α-syn spreading, non-deposited pathological forms of α-syn, such as oligomers, may drive neurodegeneration in different brain regions via their action on microglia. Activated microglia respond early, before neurodegeneration is apparent, by producing potentially neurotoxic compounds. Our findings contribute toward answers to unresolved questions around neuroinflammation in PD (Hirsch & Standaert, 2020), and have important implications for the design of therapeutic interventions during the early stages of the disease.

Materials and Methods

Expression and purification of recombinant murine α-Syn, and generation of pre-formed fibrils (PFFs), and of oligomers

Expression and purification of recombinant murine α-syn and generation of PFFs were performed as described (Weihofen et al., 2019). PFFs were stored aliquoted at -80°C until use. For the preparation of oligomers, recombinant α-syn was purchased from Analytik Jena (Jena, Germany). Oligomers were generated as described (Almandoz- Gil et al., 2018; Malaplate-Armand et al., 2006), by incubating soluble α-syn in 10 mM Tris–HCl, 100 mM NaCl under continuous shaking in an Eppendorf Thermomixer at 650 rpm and 37°C for 24 h, then stored aliquoted at 2 mg/ml at -80°C until use.

Western blot of α-syn PFFs and oligomers

The composition of α-syn PFFs and oligomers was checked by nondenaturing Western Blot. Three different concentrations of oligomers of PFFs (10, 100, and 500 ng), were loaded on 4%–10% Precast Gel Mini Protean TGX (BioRad) according to manufacturer's instructions. To reveal α-syn bands, anti-synuclein antibody clone 4D6 (Covance) was used at 1:2000 dilution (2 h at RT incubation), followed by IRDyeR 800 CW donkey anti-mouse, diluted 1:10,000 (1 h at RT incubation). Image was captured with a LI-COR Bioscience C-Digit Chemoluminescence scanner.

Electron microscopy of a-syn PFFs and oligomers

Samples were prepared for transmission electron microscopy by negative staining using a direct application method (Doane, 1987). The Formvar/carbon coated 100 mesh copper grids (EMS, FCF100H-CU, Lot# 190405) were charged using a glow discharge apparatus (Cressington 208: 10s at HT10 0.1 bar). This renders the carbon surface negatively charged and allows the sample and stain to spread more effectively (Hayat & Miller, 1990). To load the samples (diluted to 0.2–0.5 µg/µl in PBS), a 2 µl drop was placed directly onto the carbon coated grid for 1 min without drying, and excess volume was blotted off the grid with a piece of filter paper, then the samples were let to air-dry

under a hood. Then the grids were washed three times, to remove salts, by applying a small (100 µl) droplet of sterile purified water (Millipore) to the sample side of the grid. Excess water was blotted off the grid with a piece of filter paper, and the samples were let to air-dry. The samples were then stained with aqueous 2% uranyl acetate for 20 s. Excess liquid was blotted off the grid surface with filter paper, and the grid was let to dry. The samples were then examined and photographed in a scanning electron microscope (Zeiss GeminiSEM 300) using a scanning transmission electron detector at an accelerating voltage of 20 Kv.

Animals

All 3- to 6-month-old C57Bl/6J mice were purchased from Jackson via Charles River (Bois-des-Oncins, France), or Janvier Labs (Le- Genet-St.-Isle, France). Mice were housed in individually-ventilated cages (IVC) in a conventional animal facility of the University of Luxembourg, or in the facility of SynAging, in Vandeouvre-les-Nancy, France. All animal studies were in agreement with the requirements of the EU Directive 2010/63/EU and Commission recommendation 2007/526/EC. Male and female mice were housed, separated by sex, under a 12 h–12 h dark/light cycle with ad libitum access to water and food (#2016, Harlan, Horst, NL). For time point of 90 dpi PFF injections (see below), the youngest mice were used, for time point 13 dpi PFF injections, the oldest mice were used, so that, at euthanasia, all the mice were of comparable age (6–6.5 months). Animals were otherwise randomly and equitably assigned to groups. For quantitative histology (see below), ten-eleven mice/group were injected and all were quantified, and for transcriptional profiling, six mice/group were injected and all were profiled. Such sample numbers are similar or higher than the ones used in the original study by Luk et al (Luk et al., 2012), and have proven sufficient in previous studies on different models of neurodegeneration, while also keeping in line with the rule of the “3Rs” (Buttini et al., 1999; Buttini et al., 2005; Cabeza- Arvelaiz et al., 2011; Jaeger et al., 2015; Miller et al., 2007). Animals used for 6-hydroxydopamine injection have been described elsewhere (Ashrafi et al., 2017). For injections of α-syn oligomers, three mice/ group were used, as this experiment was for qualitative purpose only (see results). Animal studies were

approved by the institutional Animal Experimentation Ethics Committee of the University of Luxembourg and the responsible Luxembourg government authorities (Ministry of Health, Ministry of Agriculture). Alternatively, experiments done at the SynAging site were approved by ethics committee “Comité d'Ethique Lorrain en Matière d'Expérimentation Animale”, and by the governmental agency the “Direction Départementale de la Protection des Populations de Meurthe et Moselle- Domaine Expérimentation Animale”.

Striatal injections of α-syn PFFs, α-syn oligomers, and 6-hydroxydopamine

Alpha-syn PFFs were sonicated in a sonicating waterbath (Branson 2510, Danbury, CT) for 2 h at RT, keeping the temperature constant at 25°C by adding ice as needed, or using the Bioruptor UCD 300 (Diagenode, Seraing, Belgium) with 30 cycles of 15 s ON/15 s OFF at 4°C. Sonicated PFFs were kept on ice and used within 10 h. Mice were injected under isoflurane anesthesia (2%) on a heating pad. A 1 cm long mid-line scalp incision was made into the desinfected surgical area and a 0.5 mm hole drilled unilaterally into the skull using stereotaxic coordinates for striatum according to the Mouse Brain Atlas of Franklin and Paxinos (Paxinos & Franklin, 2008). Ten µg of PFFs, or just PBS solution (control mice) were administered, in volumes of 2 µl, within the right dorsal striatum at the following relative-to-bregma coordinates: anterior +0.5 mm, lateral +2.1 mm; depth +3.2 mm. The 24-gauge blunt tip needle of the Hamilton syringe (7105KH, Bonaduz, CH) was inserted down 3.3 mm for 10 s to form an injection pocket, and the needle remained in place for 2 min before and after the injection procedure. The hole was covered with bonewax (Lukens, Arlington, VA), and the wound closed using 7 mm Reflex wound clips (Fine Science Tools, Heidelberg, Germany). Two % xylocaine gel was applied to the wound, and mice were allowed to recover from anesthesia before being put back into their home cages. The day of injection of PFFs was named day 0. Same coordinates and a similar procedure were used for 6-OHDA or α-syn oligomers injections. Striatal injection of 6-OHDA has been described elsewhere (Ashrafi et al., 2017). Striatal injections of α-syn oligomers were done with 4 µg oligomers in 2 µl vehicle. Control mice received the same volume of vehicle (see above). Mice were euthanized in a deep

anesthesia (i.p. injection of Medetomidin, 1 mg/kg and Ketamin, 100 mg/kg) by transcardial transfusion with PBS. PFF-injected mice were euthanized either at day 13 (13 dpi) or at day 90 (90 dpi) after striatal injections ("day 0": day of injection). Mice injected with oligomers or with 6-OHDA were euthanized at 13 dpi.

Tissue extraction and preparation

For immunohistochemistry, extracted brains were fixed in in 4% buffered PFA for 48 h and kept in PBS with 0.1% NaN3 until they were cut with a vibratome (VT1000 S from Leica) into sagittal 50 µm free-floating sections. Before the staining procedure, sections were kept at -20°C in a cryoprotectant medium (1:1 vol/vol PBS/ethylene glycol, 10 g/L polyvinyl pyrrolidone). Alternatively, for dopamine measurement or RNA extraction, after removal from the skull, brains were dissected on ice into regions. Isolated striatum and ventral midbrain were quickly weighted, then snap-frozen on dry ice until further processing. Extraction and measurement of striatal dopamine (DA) has been described elsewhere (Jager et al., 2016). Briefly, after homogenization and derivatization, striatal metabolites were measured with a gas-chromatography/ mass-spectrometry set-up (Agilent 7890B GC – Agilent 5977A MSD, Santa Clara, CA). Absolute level of DA were determined using an internal standard, 2-(3,4-Dihydroxyphenyl)ethyl-1,1,2,2-d4- amine HCl (D-1540, C/D/N isotopes, Pointe-Claire, Canada). For RNA extraction from the ventral midbrain, the RNEasy Universal Kit (Quiagen) was used. After homogenization of midbrain tissues in a Retsch MM 400 device (2 min at 22 Hz, Haan, Germany). RNA concentrations and integrity were determined using a Nanodrop 2000c (Thermo Scientific) and a BioAnalyzer 2100 (Agilent), respectively. Purified RNAs were considered of sufficient quality if their RNA Integrity Number (RIN) was above 8.5, their 260/230 absorbance ratio > 1, and their 260/280 absorbance ratio = 2.

Single and double-label immunohistochemistry

Immunostaining procures followed standard protocols, as described (Buttini et al., 1999; Buttini et al., 2005). All stainings, except those for proteinase-K resistant α-syn inclusions

(see below), were performed on free-floating 50 µm-thick sections. Table S1 lists all primary and secondary antibodies used in this study, as well as their dilutions. All other reagents were from Sigma unless indicated otherwise. All antibody incubations were at room temperature, except for the anti-synaptophysin antibody, which was incubated at 4°C. Sections were washed 3 in PBS between each incubation step. To block endogenous peroxidases and for permeabilization, sections were incubated with 3% H2O2 vol/vol and 1.5% Triton 100 vol/vol for 30 min. For immoperoxidase staining with anti-synuclein antibody, this step was followed by an epitope unmasking step with 75% vol/vol formic acid for 5 min. To avoid unspecific antibody binding, sections were incubated with 5% serum (Vector Laboratories, Burlingame, CA) or 5% BSA wt/vol in PBS for 1 h before they were incubated with the respective primary antibody, or antibodies in case of double labeling. The following day, sections were incubated with a secondary antibody for 1–2 h (fluorophore-coupled for immunofluorescence, or biotinylated for immunoperoxidase). Singly or doubly fluorescently stained sections were mounted on Superfrost plus slides (Thermoscientific, Walham, MA), air-dried, and coverslipped using ProLong Gold antifade mounting medium (Life technologies, Darmstadt, Germany). For immunoperoxidase staining, antibody binding was visualized using an ABC Vectastain Kit (Vector Laboratories), followed by detection with diaminobenzidine (Merck) and H2O2 as peroxidase substrates. Sections were mounted, dried overnight and coverslipped with Neo-mount (Merck) after soaking in Neo-clear xylene substitute (Merck) for 10 min. Visualization of Proteinase-K resistant α-synuclein inclusions was done by Paraffin-Embedded Tissue blot (PET blot) on 3 µm paraffin sections mounted on nitrocellulose membrane (0.45 µm, BioRad), as previously (Kramer & Schulz-Schaeffer, 2007).

Proximity ligation assay

Protocol for proximity ligation assay (PLA) was adapted for free floating sections. All reactants were prepared according manufacturer's recommendations (Duolink, Sigma) and incubation times were as described (Trifilieff et al., 2011). Washes were performed in 24-well plates at RT, and reactions volumes were 40 µl at 37°C. First, 20 µg of anti-pSER129- α-syn mouse monoclonal 11E5 antibody (Prothena Biosciences, see Table S1)

were conjugated with either plus or minus oligonucleotide probes according manufacturer's recommendations, and stored 4°C until use. Free floating sections were washed in PBS and permeabilized as described above. Blocking was performed with DuoLink blocking solution for 2 h at RT. Sections were incubated overnight with both plus and minus probe-linked antibody (1:1 1/750 in Duolink antibody diluent solution). For ligation of the probes, after washing of the probelinked antibodies (2 5 min in Duolink's Buffer A), the ligationligase solution was added and incubated for 30 min at 37°C. For detection, after washing of the ligation-ligase solution (2 5 min in Duolink's Buffer A), sections were incubated with the amplification polymerase solution for 2.5 h at 37°C. Sections were washed in Buffer B for 10min, and in Buffer B 0.01 for a minute prior to mounting, then dried in the dark, and coverslipped. Z-stacks of pictures were acquired at 40 with a Zeiss LabA1 microscope, a maximum intensity projection was created using the Zen Blue 2012 software (Zeiss).

Quantitative neuropathology on immunostained sections

Imaging of peroxidase-labeled sections for pSER129-α-syn, and of fluorescently labeled sections for tyrosine-hydroxylase (TH), dopamine transporter (DAT), or ionized calcium binding adaptor molecule 1 (Iba1), was done using a Zeiss LabA1 microscope, coupled to a Zeiss Axiocam MRm3 digital camera, and to a PC running the Zeiss Zen Blue 2012 software. Alpha-syn inclusions were visualized by immunostaining for pSER129-α-syn. For the quantitation of α-syn inclusions in the frontal cortex and the amygdala (basolateral nucleus), two immunoperoxidase labeled (see above) sections/animal were imaged, using the 10 objective (frontal cortex) or the 20 objective (amygdala). A total of four-six images was collected for each region (10 objective, 2 1.52 mm2 each image), and digitized. After manually drawing regions of interests and thresholding, the percent image area occupied by immunopositive structures was determined using the ImageJ v. 1.45 (NIH, Bethesda, MD) public domain software. All values obtained from sections of the same animal were averaged. For the quantitation of α-syn inclusions in the SN, double immunostainings for TH and pSER129-α-syn were performed using one section of each hemibrain for each animal. TH staining was used to locate the SN, and images

were acquired at 10 magnification. Percent overlap of pSER129- α-syn signal within the TH immunopositive area was calculated using ImageJ. For the quantitation of synaptophysin-positive synaptic terminals, two fluorescently stained sections, selected randomly for each hemibrain, from each animal were viewed by a Zeiss LSM 710 laser-scanning confocal microscope, using a 20 objective and a software magnification zoom factor was used to obtain images of 180 180 µm2 each. From each of the two hemibrains of all animals, a total of four-six images were collected from the frontal cortex, and four from the hippocampal pyramidal region. Images were then transferred to a PC personal computer, and average intensity of positive presynaptic terminals was quantified for each image using the ImageJ software. Values from individual animals were averaged. This method to quantify synaptic integrity has been validated by electron microscopy quantitation of synaptic densities in a previous study (Buttini et al., 2005). The quantitation of degeneration of TH positive neurons in the SN has been described, and results obtained with this approach have been shown to correlate with stereological cell counts (supplemental material in Ashrafi et al. (2017)). For the quantitation of striatal TH-positive neuronal fibers and of DAT-positive synaptic terminal, two doubly labeled sections with anti-TH and anti-DAT were used from each hemibrain for all animals. A total of six to nine 40 pictures (223.8 167.7 µm2 each) of the dorsal striatum, from two-three sections per hemibrain, were acquired using the optical sectioning system Apotome.2 (Zeiss). The percent area occupied by TH and DAT was determined using Image J software and averaged for each mouse. For the quantitation of microglial activation in the hippocampus and frontal cortex, two randomly selected sections/hemibrain for each animal were labeled for the microglial marker Iba1. For the frontal cortex, a total of six/hemibrain, and, for the hippocampus, a total of three-four images/hemibrain were collected with a 40x objective (223.8 167.7 µm2 each image). Digitized images were transferred to a PC, and, with ImageJ v. 1.45, after thresholding, average area occupied by Iba1-positive microglia was measured. All values obtained from sections of the same animal were averaged. For the quantitation of the microglial activation in the SN, TH, and Iba1- double-labeled sections were imaged with a 10 objective. Average area covered by TH-positive neurons in control mice was used to determine the region of interest, restricted to the SN, to measure microglial activation. Four subregions of the SN were imaged and quantified for each hemibrain of

each mouse (Ashrafi et al., 2017). Iba1 immunopositive cells were quantified within each subregions, averaged for each of them, and converted in mm2. For each mouse, the sum of the four averaged subregions was used as a measure of microglial activation. All quantitative neuropathological analyses were performed blinded on coded sections, and, for each of the measurements, codes were only broken when quantification for that measure in all animals was complete. For all measures, the ipsilateral and contralateral values of PBS-injected control mice were similar (no statistical difference detected), thus these values were grouped. Statistics on quantitative histological data were done using the GraphPad Prism 8 software. Neurodegeneration and microgliosis measurements were analyzed by ANOVA followed by Dunnett's post hoc for all datasets, which were all parametric. Figures 2 and 3 are mixed graphs of bars and scattergrams. Bars represent means +/- SD, and points in the scatters represent the individual animal values. Pearson's test was used for linear correlations, except for correlations involving α-syn inclusion load (non-parametric dataset), for which Spearman's rank was used. Adjusted P values smaller than 5% were considered significant for all tests.

Microarray analysis and calculation of differentially expressed genes

GeneChip Mouse Gene 2.0ST Arrays (Affymetrix) were used for transcriptional profiling. Total RNAs (150 ng) were processed using the Affymetrix GeneChip® WT PLUS Reagent Kit according to the manufacturer's instructions (Manual Target Preparation for GeneChip® Whole Transcript [WT] Expression Arrays P/N 703174 Rev. 2). In this procedure, adapted from (Bougnaud et al., 2016), the purified, sense-strand cDNA is fragmented by uracil-DNA glycosylase (UDG) and apurinic/apyrimidinic endonuclease 1 (APE 1) at the unnatural dUTP residues and breaks the DNA strand. The fragmented cDNA was labeled by terminal deoxynucleotidyl transferase (TdT) using the Affymetrix proprietary DNA labeling reagent that is covalently linked to biotin; 5.5 µg of single-stranded cDNA are required for fragmentation and labeling, then 3.5 µg of labeled DNA + hybridization controls were injected into an Affymetrix cartridge. Microarrays were then incubated in the Affymetrix Oven with rotation at 60 rpm for 16 h at 45°C, then the arrays were washed and scanned with the Affymetrix® GeneChip® Scanner 3000, based

on the following protocol: UserGuide GeneChip® Expression Wash, Stain and Scan for Cartridge Arrays P/N 702731 Rev. 4, which generated the Affymetrix raw data CEL files containing hybridization raw signal intensities were imported into the Partek GS software. First, probe intensities were summarized to gene expression signals using Partek default options (GCcontent adjustment, RMA background correction, quantile normalization, log2 transformation and summarization by means). For statistical analysis, the normalized and log2 transformed data was loaded into the R/Bioconductor statistical environment. The rank product (Package: RankProd) approach was chosen to determine the differentially expressed genes (DEGs) (Breitling et al., 2004; Del Carratore et al., 2017; Hong et al., 2006). Rank product statistics were computed, since they have been shown to enable a robust non-parametric analysis of microarray datasets with limited number of samples (Breitling et al., 2004). Estimated p-values and pfp (percentage of false prediction) values were determined and used as nominal and adjusted significance scores, respectively. Pfp scores estimate the significance of differential expression after adjusting for multiple hypothesis testing, and can have values larger than 1. The chosen significance cut-offs were p-value <.05 and pfp < 0.1. A cut-off (pfp < 0.1 instead of <.05) was chosen to avoid loss of information for the subsequent enrichment analysis, which combines several genes below this threshold to enable detection of pathway alterations. No minimal fold change threshold was applied. For visualization of differential gene expression, Venn diagrams and heatmaps were generated using the VennDiagram and gplots packages, respectively, in R. Data pre-processing included removal of all transcripts missing gene IDs and duplicated entries (after ranking). Mouse “Gene Symbols” were used to calculate the overlapping DEGs between the different comparisons. Diagrams were generated for the following criteria and comparisons: (a) 13 and 90 dpi - ipsiPFF versus ipsiPBS (p-value <.05); (b) 13 and 90 dpi – ipsiPFF versus ipsiPBS (pfp < 0.1); (c) 13 and 90 dpi - ipsiPFF versus contraPFF (p-value <.05); (d) 13 and 90 dpi – ipsiPFF versus contraPFF (pfp < 0.1). In a second step, we were interested in investigating the expression direction of the overlapping transcripts between the early to late timepoint. Therefore, we extracted the probe IDs, matched the individual lists and grouped them into high and low expressed transcripts. Then, the above mentioned Venn diagrams were generated with these newly generated lists. Heatmaps were generated using the heatmap.2 function for ipsiPFF versus ipsiPBS and

ipsiPFF versus contraPFF for p-value <.05 and pfp < 0.1 at 13 and 90 dpi, respectively. The log2-transformed data matrix was used to plot. Additionally, we applied hierarchical top down clustering (cor and hclust basic R functions) and the data matrix was scaled row-by-row generating Z-scores.

Gene set enrichment analysis (GSEA)

The enrichment analysis for GO terms (biological processes [BP] only) was performed using the GUI (graphical user interface) version GSEA (version 3.0) published by the Broad Institute (download: http://software.broadinstitute.org/gsea/downloads.jsp) (Subramanian et al., 2005). All parameters were set to default in GSEA, except "Collapse dataset to gene symbols" was set to "false", "Permutation type" was set to "gene_set" and "Max size: excluding larger sets" was set to "250". One optimization step was introduced: a customized GMT/GMX file was generated in R/Bioconductor with mouse NCBI EntryzIDs as gene identifiers. This file was used as the "Gene sets database" in GSEA. The resulting enrichment scores (ES) were obtained applying the weighted Kolmogorov–Smirnov-like statistics. ES reflect the level to which a gene set is overrepresented among the top up- or down-regulated genes in a ranked gene list, then, the ES statistic was normalized (normalized enrichment scores, NES) as described (Subramanian et al., 2005). Finally, the p-value significance scores were adjusted for multiple hypothesis testing (Benjamini, 1995) to provide final FDR scores. A network map of the enrichment analysis results was generated using Cytoscape (Shannon et al., 2003). The mapping parameters used in Cytoscape were: p-value <.05, FDR Q-value <0.1 (default setting is 1) and Overlap >0.5. The enrichment map was automatically launched from GSEA and created in Cytoscape. In the enrichment maps, nodes represent enriched gene sets associated with BPs, and edges the degree of similarity between them using the overlap coefficient (threshold >0.5). Further curation of gene sets was done manually. Since gene sets with similar gene compositions tend to group together, such gene set clusters were easily identifiable. Nodes grouped into more than one gene cluster according to this procedure were assigned to the most overlapping cluster, that

is, the cluster they were associated with by a shorter sequence of connecting edges in the ontology graph. All software used are given in Table S2.

Identification of cellular source of DEGs

For the identification of the cellular source of specific DEGs, the public database GSE52564 (https://www.ncbi.nlm.nih.gov/geo/query/ acc.cgi?acc=GSE52564) was used. An easily accessible online resource of this database is found here: https://www.brainrnaseq. org/. Data were filtered based on FPKM values relative to the sum of FPKM per gene across different cell types. The filter criteria focused on isolating genes that were specifically expressed by individual cell types or cell type groups (mixed glial cells (e.g., for instance microglia and astrocytes), mixed oligodendrocytes (e.g., myelinated, precursors, and newly formed oligodendrocytes), and pan-cellular (e.g., expressed in all cell types). The selection criteria were:

Group description	***Inclusion criteria***	***Exclusion criteria***
Single cell type	≥40%	>26.6% other cell types
More than one cell type	∑%CellType >50% + not in single cell type	>15% all other cell types
Pan cellular expression	All <20% + not in single or more than one cell type	

Datasets were finally checked for their uniqueness to each specific group. No overlaps were found.

Characterization of microglial molecular profile

Overlaps were determined using the “calculate.overlap” function of the VennDiagram-package in R, and, in select analyses, diagrams were generated with the “ggvenn” function of the package with the same name. Datasets from (Uriarte et al., 2021) were from Table S2 of that study. Datasets from (Holtman et al., 2015) were from Table S3 of that study. The datasets of that study were analyzed each separately (for each of the

mouse models) and compared to our datasets. Then an overall overlap was generated from all the datasets in that study, to extract a “disease-associated” microglial core gene signature, which was termed “disease-associated microglia” (DAM) signature. This resulting dataset of 50 genes was compared to our datasets, to generate overlaps and Venn diagrams.

Translational relevance assessment: comparison of DEGs and of pathways between the α-syn seeding/spreading model and different stages of PD

To generate overlaps and Venn diagrams of our data with PD human databases, datasets from two studies were used: (Dijkstra et al., 2015) (GSE49036), and (Glaab & Schneider, 2015). Gene symbols of these datasets were first changed to mouse gene symbols using the “convert_human_to_mouse” function of the NicheNet-package (Browaeys et al., 2020). Then the same procedure to generate overlaps and Venn diagram was applied as described above. To compare pathways between the mouse model used in this study and PD, the PD map (https://pdmap.uni.lu/minerva/) on the MINERVA platform was used (Gawron et al., 2016; Hoksza et al., 2019). All datasets were prepared appropriately before analysis. In short, a list of DEGs per dataset containing ‘Gene Symbols’ and the respective log-fold changes was produced. First, Gene symbols had to be under the format proposed by the HUGO Gene Nomenclature Committee (HGNC). For mouse datasets, gene symbols were converted using the “convert_mouse_to_human” function from the NicheNet-package in R. Next, log-fold changes were altered as follows: arranged in decreasing order, all positive log-fold-changes were divided by the highest positive log-fold-change and analogous for the negative log-fold-changes. Finally, each DEG list in a tab delimited format was uploaded to https://pdmap.uni.lu/minerva/ and the integrated GSEA plugin was activated. To visualize directionality of changes, the number and expression changes of DEGs in each pathway that mapped to the PD map was simply categorized as “Up” or “Down”, based on the original expression data. This was done by accessing the hits information in the PD map for the significantly altered gene sets, using the API calls of the MINERVA Platform that is hosting the map (https://minerva-web.lcsb.uni.lu).The extracted information was distilled to keep multi-

hit genes as unique hits only. The generated point plots allowed to differentiate between number or counts of DEGs and the expression directionality of those genes for pathways that were significantly altered in at least one of the datasets (human or mouse).

Acknowledgments

Wiebke Jürgens-Wemheuer and Kristopher J. Schmit were recipients, respectively, of a post-doctoral (FNR AFR 5712281), and a pre-doctoral (FNR AFR 12515776) fellowship from the Luxembourg National Research Fond. Michel Mittelbronn thanks the Luxembourg National Research Fond for support (FNR PEARL P16/BM/11192868). The authors thank Laurent Vallar (Luxembourg Institute of Health) for help with gene expression arrays, Christian Jaeger (Luxembourg Centre for Systems Biomedicine) for dopamine measurements, Eliezer Masliah (University of California, San Diego) for advice, Thierry Pillot and Violette Koziel (SynAging, France) for synuclein oligomers and advice, Yuting Liu (Biogen) for purifying recombinant murine α-syn, Alessia Sciortino (University of Luxembourg) for help with Electron Microscopy sample preparation, Wagner Zago (Prothena Biosciences) for providing the 11A5 antibody.

Conflict of interest

Andreas Weihofen is affiliated with Biogen. The author has no financial interests to declare. Ahmad Allouche and Nicolas Fischer were affiliated with SynAging SAS, now with ETAP-labs. These authors have no financial interests to declare. Annette Masuch is currently affiliated with Anklam Extrakt GmbH. The author has no financial interests to declare. Knut Biber is currently affiliated with AbbVie Pharmaceutical Research and Development. The author has no financial interests to declare.

Authors contribution

Pierre Garcia, Wiebke Jürgens-Wemheuer, Djalil Coowar, and Manuel Buttini, designed the study. Pierre Garcia, Wiebke Jürgens- Wemheuer, Oihane Uriarte Huarte, Annette Masuch, Simone Brioschi, Eric Koncina, Tony Heurtaux, Andreas Weihofen, Carole Sousa, Alessandro Michelucci, Felix Kleine-Borgmann, Tatjana Pfander, Ahmad Allouche, Nicolas Fischer, and Manuel Buttini did the experiments (stereotactic surgery, tissue processing, stainings, imaging, RNA extraction). Tony Kaoma, Nathalie Nicot generated the microarray data. Kristopher J Schmit, Enrico Glaab analyzed the microarray data. Pierre Garcia, Wiebke Jürgens-Wemheuer, Oihane Uriarte Huarte, Kristopher J Schmit,

Rudi Balling, Walter Schulz-Schaeffer, Knut Biber, Michel Mittelbronn, Manuel Buttini analyzed and interpreted the data. Kristopher J. Schmit and Marek Ostaszewski did the translational relevance analysis. Manuel Buttini wrote the paper. All authors read and approved the final manuscript. All authors have approved of the contents of this manuscript and provided consent for publication.

Ethics statement

Animal studies performed at the Luxembourg Centre for Systems Biomedicine were approved by the institutional Animal Experimentation Ethics Committee of the University of Luxembourg, and the responsible Luxembourg government authorities (Ministry of Health, Ministry of Agriculture). Alternatively, experiments done at the SynAging site were approved by ethics committee “Comité d'Ethique Lorrain en Matière d'Expérimentation Animale”, and by the governmental agency the “Direction Départementale de la Protection des Populations de Meurthe et Moselle- Domaine Expérimentation Animale”. All followed EU directive 2010/63/EU.

Data availability statement

Original datasets and list of genes from comparative analyses are available upon any reasonable request to the correspondence author (manuel.buttini@uni.lu). The GEO accession number of the microarray expression data is GSE15571. (https://www.ncbi.nlm.nih.gov/geo/ query/acc.cgi?acc=GSE155716).

References

Aarsland, D., Creese, B., Politis, M., Chaudhuri, K. R., Ffytche, D. H., Weintraub, D., & Ballard, C. (2017). Cognitive decline in Parkinson disease. Nature Reviews. Neurology, 13(4), 217–231.

Abdelmotilib, H., Maltbie, T., Delic, V., Liu, Z., Hu, X., Fraser, K. B., Moehle, M. S., Stoyka, L., Anabtawi, N., Krendelchtchikova, V., Volpicelli-Daley, L., & West, A. (2017). Alpha-synuclein fibril-induced inclusion spread in rats and mice correlates with dopaminergic neurodegeneration. Neurobiology of Disease, 105, 84–98.

Almandoz-Gil, L., Ingelsson, M., & Bergstrom, J. (2018). Generation and characterization of stable alpha-Synuclein oligomers. Methods in Molecular Biology, 1779, 61–71.

Ashrafi, A., Garcia, P., Kollmus, H., Schughart, K., Del Sol, A., Buttini, M., & Glaab, E. (2017). Absence of regulator of G-protein signaling 4 does not protect against dopamine neuron dysfunction and injury in the mouse 6-hydroxydopamine lesion model of Parkinson's disease. Neurobiology of Aging, 58, 30–33.

Ayers, J. I., Brooks, M. M., Rutherford, N. J., Howard, J. K., Sorrentino, Z. A., Riffe, C. J., & Giasson, B. I. (2017). Robust central nervous system pathology in transgenic mice following peripheral injection of alpha-synuclein fibrils. Journal of Virology, 91(2), e02095–16.

Bellucci, A., Mercuri, N. B., Venneri, A., Faustini, G., Longhena, F., Pizzi, M., Missale, C., & Spano, P. (2016). Review: Parkinson's disease: From synaptic loss to connectome dysfunction. Neuropathology and Applied Neurobiology, 42(1), 77–94.

Bendor, J. T., Logan, T. P., & Edwards, R. H. (2013). The function of alphasynuclein. Neuron, 79(6), 1044–1066.

Bengoa-Vergniory, N., Roberts, R. F., Wade-Martins, R., & Alegre- Abarrategui, J. (2017). Alpha-synuclein oligomers: A new hope. Acta Neuropathologica, 134(6), 819–838.

Benjamini, Y. H. Y. (1995). Controlling the false discovery rate: A practical and powerful approach to multiple testing. Journal of the Royal Statistical Society. Sries B (Methodological), 57(1), 289–300.

Bhattacharya, A., & Biber, K. (2016). The microglial ATP-gated ion channel P2X7 as a CNS drug target. Glia, 64(10), 1772–1787.

Biber, K., Owens, T., & Boddeke, E. (2014). What is microglia neurotoxicity (not)? Glia, 62(6), 841–854.

Bougnaud, S., Golebiewska, A., Oudin, A., Keunen, O., Harter, P. N., Mader, L., Azuaje, F., Fritah, S., Stieber, D., Kaoma, T., Vallar, L., Brons, N. H. C., Daubon, T., Miletic, H., Sundstrom, T., Herold-Mende, C., Mittelbronn, M., Bjerkvig, R., & Niclou, S. P. (2016). Molecular crosstalk between tumour and brain parenchyma instructs histopathological features in glioblastoma. Oncotarget, 7(22), 31955–31971.

Braak, H., & Braak, E. (1995). Staging of Alzheimer's disease-related neurofibrillary changes. Neurobiology of Aging, 16(3), 278–284.

Braak, H., Del Tredici, K., Rub, U., de Vos, R. A., Jansen Steur, E. N., & Braak, E. (2003). Staging of brain pathology related to sporadic Parkinson's disease. Neurobiology of Aging, 24(2), 197–211.

Braak, H., Ghebremedhin, E., Rub, U., Bratzke, H., & Del Tredici, K. (2004). Stages in the development of Parkinson's disease-related pathology. Cell and Tissue Research, 318(1), 121–134.

Breitling, R., Armengaud, P., Amtmann, A., & Herzyk, P. (2004). Rank products: A simple, yet powerful, new method to detect differentially regulated genes in replicated microarray experiments. FEBS Letters, 573(1–3), 83–92.

Brochard, V., Combadiere, B., Prigent, A., Laouar, Y., Perrin, A., Beray- Berthat, V., & Hunot, S. (2009). Infiltration of CD4+ lymphocytes into the brain contributes to neurodegeneration in a mouse model of Parkinson disease. The Journal of Clinical Investigation, 119(1), 182–192.

Browaeys, R., Saelens, W., & Saeys, Y. (2020). NicheNet: Modeling intercellular communication by linking ligands to target genes. Nature Methods, 17(2), 159–162.

Brundin, P., Ma, J., & Kordower, J. H. (2016). How strong is the evidence that Parkinson's disease is a prion disorder? Current Opinion in Neurology, 29(4), 459–466.

Brundin, P., & Melki, R. (2017). Prying into the prion hypothesis for Parkinson's disease. The Journal of Neuroscience, 37(41), 9808–9818.

Burre, J., Sharma, M., & Sudhof, T. C. (2018). Cell biology and pathophysiology of alpha-Synuclein. Cold Spring Harbor Perspectives in Medicine, 8(3), a024091.

Buttini, M., Masliah, E., Barbour, R., Grajeda, H., Motter, R., Johnson- Wood, K., Khan, K., Seubert, P., Freedman, S., Schenk, D., & Games, D. (2005). Beta-amyloid immunotherapy prevents synaptic degeneration in a mouse model of Alzheimer's disease. The Journal of Neuroscience, 25(40), 9096–9101.

Buttini, M., Orth, M., Bellosta, S., Akeefe, H., Pitas, R. E., Wyss-Coray, T., Mucke, L., & Mahley, R. W. (1999). Expression of human apolipoprotein E3 or E4 in the brains of Apoe-/- mice: Isoform-specific effects on neurodegeneration. The Journal of Neuroscience, 19(12), 4867– 4880.

Cabeza-Arvelaiz, Y., Fleming, S. M., Richter, F., Masliah, E., Chesselet, M. F., & Schiestl, R. H. (2011). Analysis of striatal transcriptome in mice overexpressing human wild-type alpha-synuclein supports synaptic dysfunction and suggests mechanisms of neuroprotection for striatal neurons. Molecular Neurodegeneration, 6, 83.

Calhoun, M. E., Jucker, M., Martin, L. J., Thinakaran, G., Price, D. L., & Mouton, P. R. (1996). Comparative evaluation of synaptophysin-based methods for quantification of synapses. Journal of Neurocytology, 25(12), 821–828.

Chiti, F., & Dobson, C. M. (2017). Protein misfolding, amyloid formation, and human disease: A summary of progress over the last decade. Annual Review of Biochemistry, 86, 27–68.

Chu, Y., & Kordower, J. H. (2010). Lewy body pathology in fetal grafts. Annals of the New York Academy of Sciences, 1184, 55–67.

Chu, Y., Muller, S., Tavares, A., Barret, O., Alagille, D., Seibyl, J., Tamagnan, G., Marek, K., Luk, K. C., Trojanowski, J. Q., Lee, V. M. Y., & Kordower, J. H. (2019). Intrastriatal alpha-synuclein fibrils in monkeys: Spreading, imaging and neuropathological changes. Brain, 142(11), 3565–3579.

Croisier, E., Moran, L. B., Dexter, D. T., Pearce, R. K., & Graeber, M. B. (2005). Microglial inflammation in the parkinsonian substantia nigra: Relationship to alpha-synuclein deposition. Journal of Neuroinflammation, 2, 14.

Crotti, A., & Ransohoff, R. M. (2016). Microglial physiology and pathophysiology: Insights from genome-wide transcriptional profiling. Immunity, 44(3), 505–515.

Del Carratore, F., Jankevics, A., Eisinga, R., Heskes, T., Hong, F., & Breitling, R. (2017). RankProd 2.0: A refactored bioconductor package for detecting differentially expressed features in molecular profiling datasets. Bioinformatics, 33(17), 2774–2775.

Dijkstra, A. A., Ingrassia, A., de Menezes, R. X., van Kesteren, R. E., Rozemuller, A. J., Heutink, P., & van de Berg, W. D. (2015). Evidence for immune response, axonal dysfunction and reduced endocytosis in the substantia nigra in early stage Parkinson's disease. PLoS One, 10(6), e0128651.

Dijkstra, A. A., Voorn, P., Berendse, H. W., Groenewegen, H. J., Netherlands Brain, B., Rozemuller, A. J., & van de Berg, W. D. (2014). Stage-dependent nigral neuronal loss in incidental Lewy body and Parkinson's disease. Movement Disorders, 29(10), 1244–1251.

Doane, F. W. A. N. (1987). Electron microscopy in diagnostic virology. Cambridge University Press.

Doorn, K. J., Lucassen, P. J., Boddeke, H. W., Prins, M., Berendse, H. W., Drukarch, B., & van Dam, A. M. (2012). Emerging roles of microglial activation and non-motor symptoms in Parkinson's disease. Progress in Neurobiology, 98(2), 222–238.

Doorn, K. J., Moors, T., Drukarch, B., van de Berg, W., Lucassen, P. J., & van Dam, A. M. (2014). Microglial phenotypes and toll-like receptor 2 in the substantia nigra and hippocampus of incidental Lewy body disease cases and Parkinson's disease patients. Acta Neuropathologica Communications, 2, 90.

Dubbelaar, M. L., Kracht, L., Eggen, B. J. L., & Boddeke, E. (2018). The kaleidoscope of microglial phenotypes. Frontiers in Immunology, 9, 1753.

Duffy, M. F., Collier, T. J., Patterson, J. R., Kemp, C. J., Luk, K. C., Tansey, M. G., Paumier, K. L., Kanaan, N. M., Luke-Fischer, D., Polinksi, N. K., Barth, O. L., Howe, J. W., Vaikath, N. N., Majbour, N. K., El-Agnaf, O. M. A., & Sortwell, C. E. (2018). Lewy body-like alpha-synuclein inclusions trigger reactive microgliosis prior to nigral degeneration. Journal of Neuroinflammation, 15(1), 129.

Espay, A. J., & Marras, C. (2019). Clinical Parkinson disease subtyping does not predict pathology. Nature Reviews. Neurology, 15(4), 189–190.

Fellner, L., Irschick, R., Schanda, K., Reindl, M., Klimaschewski, L., Poewe, W., Wenning, G. K., & Stefanova, N. (2013). Toll-like receptor 4 is required for alpha-synuclein dependent activation of microglia and astroglia. Glia, 61(3), 349–360.

Figueiredo-Pereira, M. E., Corwin, C., & Babich, J. (2016). Prostaglandin J2: A potential target for halting inflammation-induced neurodegeneration. Annals of the New York Academy of Sciences, 1363, 125–137.

Filippini, A., Gennarelli, M., & Russo, I. (2019). Alpha-Synuclein and glia in Parkinson's disease: A beneficial or a detrimental duet for the endolysosomal system? Cellular and Molecular Neurobiology, 39(2), 161–168.

Fu, R., Shen, Q., Xu, P., Luo, J. J., & Tang, Y. (2014). Phagocytosis of microglia in the central nervous system diseases. Molecular Neurobiology, 49(3), 1422–1434.

Fujita, K. A., Ostaszewski, M., Matsuoka, Y., Ghosh, S., Glaab, E., Trefois, C., Crespo, I., Perumal, T. M., Jurkowski, W., Antony, P. M., Diederich, N., Buttini, M., Kodama, A., Satagopam, V. P., Eifes, S., Del Sol, A., Schneider, R., Kitano, H., & Balling, R. (2014). Integrating pathways of Parkinson's disease in a molecular interaction map. Molecular Neurobiology, 49(1), 88–102.

Gawron, P., Ostaszewski, M., Satagopam, V., Gebel, S., Mazein, A., Kuzma, M., Zorzan, S., McGee, F., Otjacques, B., Balling, R., & Schneider, R. (2016). MINERVA-a platform for visualization and curation of molecular interaction networks. NPJ Systems Biology and Applications, 2, 16020.

Gerhard, A., Pavese, N., Hotton, G., Turkheimer, F., Es, M., Hammers, A., Eggert, K., Oertel, W., Banati, R. B., & Brooks, D. J. (2006). In vivo imaging of microglial activation

with [11C](R)-PK11195 PET in idiopathic Parkinson's disease. Neurobiology of Disease, 21(2), 404–412.

Glaab, E., & Schneider, R. (2015). Comparative pathway and network analysis of brain transcriptome changes during adult aging and in Parkinson's disease. Neurobiology of Disease, 74, 1–13.

Goedert, M. (2015). Neurodegeneration. Alzheimer's and Parkinson's diseases: The prion concept in relation to assembled Abeta, tau, and alpha-synuclein. Science, 349(6248), 1255555.

Grozdanov, V., Bousset, L., Hoffmeister, M., Bliederhaeuser, C., Meier, C., Madiona, K., Pieri, L., Kiechle, M., McLean, P. J., Kassubek, J., Behrends, C., Ludolph, A. C., Weishaupt, J. H., Melki, R., & Danzer, K. M. (2019). Increased immune activation by pathologic alpha-synuclein in Parkinson's disease. Annals of Neurology, 86(4), 593–606.

Hakim, R., Zachariadis, V., Sankavaram, S. R., Han, J., Harris, R. A., Brundin, L., Enge, M., & Svensson, M. (2021). Spinal cord Injury induces permanent reprogramming of microglia into a disease-associated state which contributes to functional recovery. The Journal of Neuroscience, 41(40), 8441–8459.

Hammond, T. R., Dufort, C., Dissing-Olesen, L., Giera, S., Young, A., Wysoker, A., Walker, A. J., Gergits, F., Segel, M., Nemesh, J., Marsh, S. E., Saunders, A., Macosko, E., Ginhoux, F., Chen, J., Franklin, R. J. M., Piao, X., McCarroll, S. A., & Stevens, B. (2019). Single-cell RNA sequencing of microglia throughout the mouse lifespan and in the injured brain reveals complex cell-state changes. Immunity, 50(1), 253–271.

Hammond, T. R., Marsh, S. E., & Stevens, B. (2019). Immune signaling in neurodegeneration. Immunity, 50(4), 955–974.

Harms, A. S., Delic, V., Thome, A. D., Bryant, N., Liu, Z., Chandra, S., Jurkuveniate, A., & West, A. B. (2017). Alpha-synuclein fibrils recruit peripheral immune cells in the rat brain prior to neurodegeneration. Acta Neuropathologica Communications, 5(1), 85.

Hayat, M. A. M., & Miller, S. E. (1990). Negative Staining. McGraw-Hill.

Helwig, M., Klinkenberg, M., Rusconi, R., Musgrove, R. E., Majbour, N. K., El-Agnaf, O. M., Ulusoy, A., & Di Monte, D. A. (2016). Brain propagation of transduced alpha-synuclein involves non-fibrillar protein species and is enhanced in alpha-synuclein null mice. Brain, 139(3), 856–870.

Henrich, M. T., Geibl, F. F., Lakshminarasimhan, H., Stegmann, A., Giasson, B. I., Mao, X., Dawson, V. L., Dawson, T. M., Oertel, W., & Surmeier, D. J. (2020). Determinants of seeding and spreading of alpha-synuclein pathology in the brain. Science Advances, 6(46), eabc2487.

Hirsch, E. C., & Standaert, D. G. (2020). Ten unsolved questions about neuroinflammation in Parkinson's disease. Movement Disorders, 36, 16–24.

Hoksza, D., Gawron, P., Ostaszewski, M., Smula, E., & Schneider, R. (2019). MINERVA API and plugins: Opening molecular network analysis and visualization to the community. Bioinformatics, 35(21), 4496–4498.

Holmqvist, S., Chutna, O., Bousset, L., Aldrin-Kirk, P., Li, W., Bjorklund, T., Wang, Z.-Y., Roybon, L., Melki, R., & Li, J. Y. (2014). Direct evidence of Parkinson pathology spread from the gastrointestinal tract to the brain in rats. Acta Neuropathologica, 128(6), 805–820.

Holtman, I. R., Raj, D. D., Miller, J. A., Schaafsma, W., Yin, Z., Brouwer, N., Wes, P. D., Moller, T., Orre, M., Kamphuis, W., Hol, E. M., Boddeke, E. W. G. M., & Eggen, B. J. (2015). Induction of a common microglia gene expression signature by aging and neurodegenerative conditions: A co-expression meta-analysis. Acta Neuropathologica Communications, 3, 31.

Hong, F., Breitling, R., McEntee, C. W., Wittner, B. S., Nemhauser, J. L., & Chory, J. (2006). RankProd: A bioconductor package for detecting differentially expressed genes in meta-analysis. Bioinformatics, 22(22), 2825–2827.

Hsieh, Y. C., Mounsey, R. B., & Teismann, P. (2011). MPP(+)-induced toxicity in the presence of dopamine is mediated by COX-2 through oxidative stress. Naunyn-Schmiedeberg's Archives of Pharmacology, 384(2), 157–167.

Hughes, C. D., Choi, M. L., Ryten, M., Hopkins, L., Drews, A., Botia, J. A., Iljina, M., Rodrigues, M., Gagliano, S. A., Gandhi, S., Bryant, C., & Klenerman, D. (2019).

Picomolar concentrations of oligomeric alphasynuclein sensitizes TLR4 to play an initiating role in Parkinson's disease pathogenesis. Acta Neuropathologica, 137(1), 103–120.

Jaeger, C., Glaab, E., Michelucci, A., Binz, T. M., Koeglsberger, S., Garcia, P., Trezzi, J.-P., Ghelfi, J., Balling, R., & Buttini, M. (2015). The mouse brain metabolome: Region-specific signatures and response to excitotoxic neuronal injury. The American Journal of Pathology, 185(6), 1699– 1712.

Jaeger, C., Hiller, K., & Buttini, M. (2016). Metabolic profiling and quantification of neurotransmitters in mouse brain by gas chromatography-mass spectrometry. Current Protocols in Mouse Biology, 6(3), 333–342.

Janda, E., Boi, L., & Carta, A. R. (2018). Microglial phagocytosis and its regulation: A therapeutic target in Parkinson's disease? Frontiers in Molecular Neuroscience, 11, 144.

Jellinger, K. A. (2009a). A critical evaluation of current staging of alphasynuclein pathology in Lewy body disorders. Biochimica et Biophysica Acta, 1792(7), 730–740.

Jellinger, K. A. (2009b). Formation and development of Lewy pathology: A critical update. Journal of Neurology, 256(3), 270–279.

Joers, V., Tansey, M. G., Mulas, G., & Carta, A. R. (2017). Microglial phenotypes in Parkinson's disease and animal models of the disease. Progress in Neurobiology, 155, 57–75.

Jucker, M., & Walker, L. C. (2018). Propagation and spread of pathogenic protein assemblies in neurodegenerative diseases. Nature Neuroscience, 21(10), 1341–1349.

Kannarkat, G. T., Boss, J. M., & Tansey, M. G. (2013). The role of innate and adaptive immunity in Parkinson's disease. Journal of Parkinson's Disease, 3(4), 493–514.

Keren-Shaul, H., Spinrad, A., Weiner, A., Matcovitch-Natan, O., Dvir- Szternfeld, R., Ulland, T. K., David, E., Baruch, K., Lara-Astaiso, D., Toth, B., Itzkovitz, S., Colonna, M., Schwartz., M., & Amit, I. (2017). A unique microglia type associated with restricting development of Alzheimer's disease. Cell, 169(7), 1276–1290.

Kim, C., Ho, D. H., Suk, J. E., You, S., Michael, S., Kang, J., Lee, S. J., Masliah, E., Hwang, D., Lee, H. J., & Lee, S. J. (2013). Neuron-released oligomeric alpha-synuclein is an endogenous agonist of TLR2 for paracrine activation of microglia. Nature Communications, 4, 1562.

Kim, C., Lee, H. J., Masliah, E., & Lee, S. J. (2016). Non-cell-autonomous neurotoxicity of alpha-synuclein through microglial toll-like receptor 2. Exp Neurobiol, 25(3), 113–119.

Kim, C., Spencer, B., Rockenstein, E., Yamakado, H., Mante, M., Adame, A., Fields, J. A., Masliah, D., Iba, M., Lee, H. J., Rissman, R. A., Lee, S. J., & Masliah, E. (2018). Immunotherapy targeting toll-like receptor 2 alleviates neurodegeneration in models of synucleinopathy by modulating alpha-synuclein transmission and neuroinflammation. Molecular Neurodegeneration, 13(1), 43.

Konishi, H., & Kiyama, H. (2018). Microglial TREM2/DAP12 signaling: A double-edged sword in neural diseases. Frontiers in Cellular Neuroscience, 12, 206.

Kramer, M. L., & Schulz-Schaeffer, W. J. (2007). Presynaptic alpha-synuclein aggregates, not Lewy bodies, cause neurodegeneration in dementia with Lewy bodies. The Journal of Neuroscience, 27(6), 1405–1410.

Lema Tome, C. M., Tyson, T., Rey, N. L., Grathwohl, S., Britschgi, M., & Brundin, P. (2013). Inflammation and alpha-synuclein's prion-like behavior in Parkinson's disease–is there a link? Molecular Neurobiology, 47(2), 561–574.

Lin, M. K., & Farrer, M. J. (2014). Genetics and genomics of Parkinson's disease. Genome Medicine, 6(6), 48.

Luk, K. C., Kehm, V., Carroll, J., Zhang, B., O'Brien, P., Trojanowski, J. Q., & Lee, V. M. (2012). Pathological alpha-synuclein transmission initiates Parkinson-like neurodegeneration in nontransgenic mice. Science, 338(6109), 949–953.

Luna, E., & Luk, K. C. (2015). Bent out of shape: Alpha-synuclein misfolding and the convergence of pathogenic pathways in Parkinson's disease. FEBS Letters, 589(24), 3749–3759.

Ma, M. W., Wang, J., Zhang, Q., Wang, R., Dhandapani, K. M., Vadlamudi, R. K., & Brann, D. W. (2017). NADPH oxidase in brain injury and neurodegenerative disorders. Molecular Neurodegeneration, 12(1), 7.

Malaplate-Armand, C., Florent-Bechard, S., Youssef, I., Koziel, V., Sponne, I., Kriem, B., Leininger-Muller, B., Olivier, J. L., Oster, T., & Pillot, T. (2006). Soluble oligomers of amyloid-beta peptide induce neuronal apoptosis by activating a cPLA2-dependent sphingomyelinaseceramide pathway. Neurobiology of Disease, 23(1), 178–189.

Mathys, H., Adaikkan, C., Gao, F., Young, J. Z., Manet, E., Hemberg, M., De Jager, P., Ransohoff, R. M., Regev, A., & Tsai, L. H. (2017). Temporal tracking of microglia activation in neurodegeneration at single-cell resolution. Cell Reports, 21(2), 366–380.

Mezias, C., Rey, N., Brundin, P., & Raj, A. (2020). Neural connectivity predicts spreading of alpha-synuclein pathology in fibril-injected mouse models: Involvement of retrograde and anterograde axonal propagation. Neurobiology of Disease, 134, 104623.

Michelucci, A., Mittelbronn, M., & Gomez-Nicola, D. (2018). Microglia in health and disease: A unique immune cell population. Frontiers in Immunology, 9, 1779.

Milber, J. M., Noorigian, J. V., Morley, J. F., Petrovitch, H., White, L., Ross, G. W., & Duda, J. E. (2012). Lewy pathology is not the first sign of degeneration in vulnerable neurons in Parkinson disease. Neurology, 79(24), 2307–2314.

Miller, R. M., Kiser, G. L., Kaysser-Kranich, T., Casaceli, C., Colla, E., Lee, M. K., Palaniappan, C., & Federoff, H. J. (2007). Wild-type and mutant alpha-synuclein induce a multi-component gene expression profile consistent with shared pathophysiology in different transgenic mouse models of PD. Experimental Neurology, 204(1), 421–432.

Mrdjen, D., Pavlovic, A., Hartmann, F. J., Schreiner, B., Utz, S. G., Leung, B. P., Lelios, I., Heppner, F. L., Kipnis, J., Merkler, D., Greter, M., & Becher, B. (2018). High-dimensional single-cell mapping of central nervous system immune cells reveals distinct myeloid subsets in health, aging, and disease. Immunity, 48(2), 380–395.

Olanow, C. W., Savolainen, M., Chu, Y., Halliday, G. M., & Kordower, J. H. (2019). Temporal evolution of microglia and alpha-synuclein accumulation following foetal grafting in Parkinson's disease. Brain, 142(6), 1690–1700.

Osterberg, V. R., Spinelli, K. J., Weston, L. J., Luk, K. C., Woltjer, R. L., & Unni, V. K. (2015). Progressive aggregation of alpha-synuclein and selective degeneration of lewy inclusion-bearing neurons in a mouse model of parkinsonism. Cell Reports, 10(8), 1252–1260.

Paumier, K. L., Luk, K. C., Manfredsson, F. P., Kanaan, N. M., Lipton, J. W., Collier, T. J., Steece-Collier, K., Kemp, C. J., Celano, S., Schulz, E., Sandoval, I. M., Fleming, S., Dirr, E., Polinksi, N. K., Trojanowski, J. Q., Lee, V. M., & Sortwell, C. E. (2015). Intrastriatal injection of pre-formed mouse alpha-synuclein fibrils into rats triggers alpha-synuclein pathology and bilateral nigrostriatal degeneration. Neurobiology of Disease, 82, 185–199.

Paxinos, G., & Franklin, K. (2008). The mouse brain atlas in stereotactic coordinates (3rd ed.). Elsevier Academic Press.

Peelaerts, W., Bousset, L., Van der Perren, A., Moskalyuk, A., Pulizzi, R., Giugliano, M., Van den Haute, C., Melki, R., & Baekelandt, V. (2015). Alpha-synuclein strains cause distinct synucleinopathies after local and systemic administration. Nature, 522(7556), 340–344.

Poewe, W., Seppi, K., Tanner, C. M., Halliday, G. M., Brundin, P., Volkmann, J., Schrag, A. E., & Lang, A. E. (2017). Parkinson disease. Nature Reviews Disease Primers, 3, 17013.

Ransohoff, R. M. (2016). A polarizing question: Do M1 and M2 microglia exist? Nature Neuroscience, 19(8), 987–991.

Ransohoff, R. M., & El Khoury, J. (2015). Microglia in health and disease. Cold Spring Harbor Perspectives in Biology, 8(1), a020560.

Rey, N. L., Bousset, L., George, S., Madaj, Z., Meyerdirk, L., Schulz, E., Steiner, J. A., Melki, R., & Brundin, P. (2019). Alpha-synuclein conformational strains spread, seed and target neuronal cells differentially after injection into the olfactory bulb. Acta Neuropathologica Communications, 7(1), 221

Rey, N. L., George, S., & Brundin, P. (2016). Review: Spreading the word: Precise animal models and validated methods are vital when evaluating prion-like behaviour of alpha-synuclein. Neuropathology and Applied Neurobiology, 42(1), 51–76.

Roberts, R. F., Wade-Martins, R., & Alegre-Abarrategui, J. (2015). Direct visualization of alpha-synuclein oligomers reveals previously undetected pathology in Parkinson's disease brain. Brain, 138(6), 1642–1657.

Rocha, E. M., De Miranda, B., & Sanders, L. H. (2018). Alpha-synuclein: Pathology, mitochondrial dysfunction and neuroinflammation in Parkinson's disease. Neurobiology of Disease, 109, 249–257.

Rodriguez, L., Marano, M. M., & Tandon, A. (2018). Import and export of misfolded alpha-synuclein. Frontiers in Neuroscience, 12, 344.

Ross, C. A., & Poirier, M. A. (2004). Protein aggregation and neurodegenerative disease. Nature Medicine, 10, 10–17.

Sacino, A. N., Brooks, M., Thomas, M. A., McKinney, A. B., Lee, S., Regenhardt, R. W., McGarvey, N. H., Ayers, J. I., Notterpek, L., Borchelt, D. R., Golde, T., & Giasson, B. I. (2014). Intramuscular injection of alphasynuclein induces CNS alpha-synuclein pathology and a rapid-onset motor phenotype in transgenic mice. Proceedings of the National Academy of Sciences of the United States of America, 111(29), 10732–10737.

Scheckel, C., & Aguzzi, A. (2018). Prions, prionoids and protein misfolding disorders. Nature Reviews. Genetics, 19(7), 405–418.

Scheiblich, H., Dansokho, C., Mercan, D., Schmidt, S. V., Bousset, L., Wischhof, L., Eikens, F., Odainic, A., Spitzer, J., Grieb, A., Schwartz, S., Dano, D., Latz, E., Melki, R., & Heneka, M. T. (2021). Microglia jointly degrade fibrillar alpha-synuclein cargo by distribution through tunneling nanotubes. Cell, 184(20), 5089–5106.

Selkoe, D. J. (2003). Folding proteins in fatal ways. Nature, 426(6968), 900–904.

Seok, J., Warren, H. S., Cuenca, A. G., Mindrinos, M. N., Baker, H. V., Xu, W., Richards, D.R, Honari, S., Moore, E. E., Minei, J. P. Cuschieri, J., Bankey, P. E., Johnson, J. L., Sperry, J., Nathens, A. B., Billiar, T. R., West, M. A., Jeschke, M. G., Klein, M. B., … Host

Response to Injury, Large Scale Collaborative Research Program. (2013). Genomic responses in mouse models poorly mimic human inflammatory diseases. Proceedings of the National Academy of Sciences of the United States of America, 110(9), 3507–3512.

Shannon, P., Markiel, A., Ozier, O., Baliga, N. S., Wang, J. T., Ramage, D., Amin, N., Schwikowski, B., & Ideker, T. (2003). Cytoscape: A software environment for integrated models of biomolecular interaction networks. Genome Research, 13(11), 2498–2504.

Singleton, A., & Hardy, J. (2019). Progress in the genetic analysis of Parkinson's disease. Human Molecular Genetics, 28(2), 215–218.

Spillantini, M. G., Crowther, R. A., Jakes, R., Hasegawa, M., & Goedert, M. (1998). Alpha-synuclein in filamentous inclusions of Lewy bodies from Parkinson's disease and dementia with Lewy bodies. Proceedings of the National Academy of Sciences of the United States of America, 95(11), 6469–6473.

Spillantini, M. G., & Goedert, M. (2018). Neurodegeneration and the ordered assembly of alpha-synuclein. Cell and Tissue Research, 373(1), 137–148.

Subramanian, A., Tamayo, P., Mootha, V. K., Mukherjee, S., Ebert, B. L., Gillette, M. A., Paulovich, P., Pomeroy, S. L., Golub, T. R., Lander, E. S., & Mesirov, J. P. (2005). Gene set enrichment analysis: A knowledgebased approach for interpreting genome-wide expression profiles. Proceedings of the National Academy of Sciences of the United States of America, 102(43), 15545–15550.

Surmeier, D. J., Obeso, J. A., & Halliday, G. M. (2017a). Parkinson's disease is not simply a prion disorder. The Journal of Neuroscience, 37(41), 9799–9807.

Surmeier, D. J., Obeso, J. A., & Halliday, G. M. (2017b). Selective neuronal vulnerability in Parkinson disease. Nature Reviews. Neuroscience, 18(2), 101–113.

Takao, K., & Miyakawa, T. (2015). Genomic responses in mouse models greatly mimic human inflammatory diseases. Proceedings of the National Academy of Sciences of the United States of America, 112(4), 1167–1172.

Tan, E. K., Chao, Y. X., West, A., Chan, L. L., Poewe, W., & Jankovic, J. (2020). Parkinson disease and the immune system - associations, mechanisms and therapeutics. Nature Reviews. Neurology, 16, 303–318.

Tansey, M. G., & Romero-Ramos, M. (2019). Immune system responses in Parkinson's disease: Early and dynamic. The European Journal of Neuroscience, 49(3), 364–383.

Tay, T. L., Sagar Dautzenberg, J., Grun, D., & Prinz, M. (2018). Unique microglia recovery population revealed by single-cell RNAseq following neurodegeneration. Acta Neuropathologica Communications, 6(1), 87.

Teismann, P., Tieu, K., Choi, D. K., Wu, D. C., Naini, A., Hunot, S., Vila, M., Jackson-Lewis, V., & Przedborski, S. (2003). Cyclooxygenase-2 is instrumental in Parkinson's disease neurodegeneration. Proceedings of the National Academy of Sciences of the United States of America, 100(9), 5473–5478.

Terada, T., Yokokura, M., Yoshikawa, E., Futatsubashi, M., Kono, S., Konishi, T., Miyajima, H., Hashizume, T., & Ouchi, Y. (2016). Extrastriatal spreading of microglial activation in Parkinson's disease: A positron emission tomography study. Annals of Nuclear Medicine, 30(8), 579–587.

Trifilieff, P., Rives, M. L., Urizar, E., Piskorowski, R. A., Vishwasrao, H. D., Castrillon, J., Schmauss, C., Slattman, M., Gullberg, M., & Javitch, J. A. (2011). Detection of antigen interactions ex vivo by proximity ligation assay: Endogenous dopamine D2-adenosine A2A receptor complexes in the striatum. BioTechniques, 51(2), 111–118.

Ulusoy, A., Musgrove, R. E., Rusconi, R., Klinkenberg, M., Helwig, M., Schneider, A., & Di Monte, D. A. (2015). Neuron-to-neuron alphasynuclein propagation in vivo is independent of neuronal injury. Acta Neuropathologica Communications, 3, 13.

Ulusoy, A., Rusconi, R., Perez-Revuelta, B. I., Musgrove, R. E., Helwig, M., Winzen-Reichert, B., & Di Monte, D. A. (2013). Caudo-rostral brain spreading of alpha-synuclein through vagal connections. EMBO Molecular Medicine, 5(7), 1119–1127.

Uriarte Huarte, O., Kyriakis, D., Heurtaux, T., Pires-Afonso, Y., Grzyb, K., Halder, R., Buttini, M., Skupin, A., Mittelbronn, M., & Michelucci, A. (2021). Single-cell transcriptomics and in situ morphological analyses reveal microglia heterogeneity across the nigrostriatal pathway. Frontiers in Immunology, 12, 639613.

Uriarte Huarte, O., Richart, L., Mittelbronn, M., & Michelucci, A. (2021). Microglia in health and disease: The strength to be diverse and reactive. Frontiers in Cellular Neuroscience, 15, 660523.

Vaikath, N. N., Hmila, I., Gupta, V., Erskine, D., Ingelsson, M., & El- Agnaf, O. M. A. (2019). Antibodies against alpha-synuclein: Tools and therapies. Journal of Neurochemistry, 150(5), 612–625.

Vasili, E., Dominguez-Meijide, A., & Outeiro, T. F. (2019). Spreading of alpha-synuclein and tau: A systematic comparison of the mechanisms involved. Frontiers in Molecular Neuroscience, 12, 107.

Walker, L. C., & Jucker, M. (2015). Neurodegenerative diseases: Expanding the prion concept. Annual Review of Neuroscience, 38, 87–103.

Walsh, D. M., & Selkoe, D. J. (2004). Oligomers on the brain: The emerging role of soluble protein aggregates in neurodegeneration. Protein and Peptide Letters, 11(3), 213–228.

Walsh, D. M., & Selkoe, D. J. (2016). A critical appraisal of the pathogenic protein spread hypothesis of neurodegeneration. Nature Reviews. Neuroscience, 17(4), 251–260.

Wan, Y. W., Al-Ouran, R., Mangleburg, C. G., Perumal, T. M., Lee, T. V., Allison, K., Swarup, V., Funk, C. C., Gaiteri, C., Allen, M., Wang, M., Neuner, S. M., Kaczorowski, C. C., Philip, V. M., Howell, G. R., Martini- Stoica, H., Zheng, H., Mei, H., Zhing, X., … Logsdon, B. A. (2020). Metaanalysis of the Alzheimer's disease human brain transcriptome and functional dissection in mouse models. Cell Reports, 32(2), 107908.

Watson, M. B., Richter, F., Lee, S. K., Gabby, L., Wu, J., Masliah, E., Effros, R. B., & Chesselet, M. F. (2012). Regionally-specific microglial activation in young mice over-expressing human wildtype alpha-synuclein. Experimental Neurology, 237(2), 318–334.

Weihofen, A., Liu, Y., Arndt, J. W., Huy, C., Quan, C., Smith, B. A., Baeriswyl, J. L., Cavegn, N., Senn, L., Su, L., Marsh, G., Auluck, P. K., Montrasio, F., Nitsch, R. M., Hirst, W. D., Cedarbaum, J. M., Pepinsky, R. B., Grimm, J., & Weinreb, P. H. (2019). Development of an aggregate-selective, human-derived alpha-synuclein antibody BIIB054 that

ameliorates disease phenotypes in Parkinson's disease models. Neurobiology of Disease, 124, 276–288.

Wolf, S. A., Boddeke, H. W., & Kettenmann, H. (2017). Microglia in physiology and disease. Annual Review of Physiology, 79, 619–643.

Wu, Q., Takano, H., Riddle, D. M., Trojanowski, J. Q., Coulter, D. A., & Lee, V. M. (2019). Alpha-synuclein (alphaSyn) preformed fibrils induce endogenous alphaSyn aggregation, compromise synaptic activity and enhance synapse loss in cultured excitatory hippocampal neurons. The Journal of Neuroscience, 39(26), 5080–5094.

Zhan, S. S., Beyreuther, K., & Schmitt, H. P. (1993). Quantitative assessment of the synaptophysin immuno-reactivity of the cortical neuropil in various neurodegenerative disorders with dementia. Dementia, 4(2), 66–74.

6.3 Figures

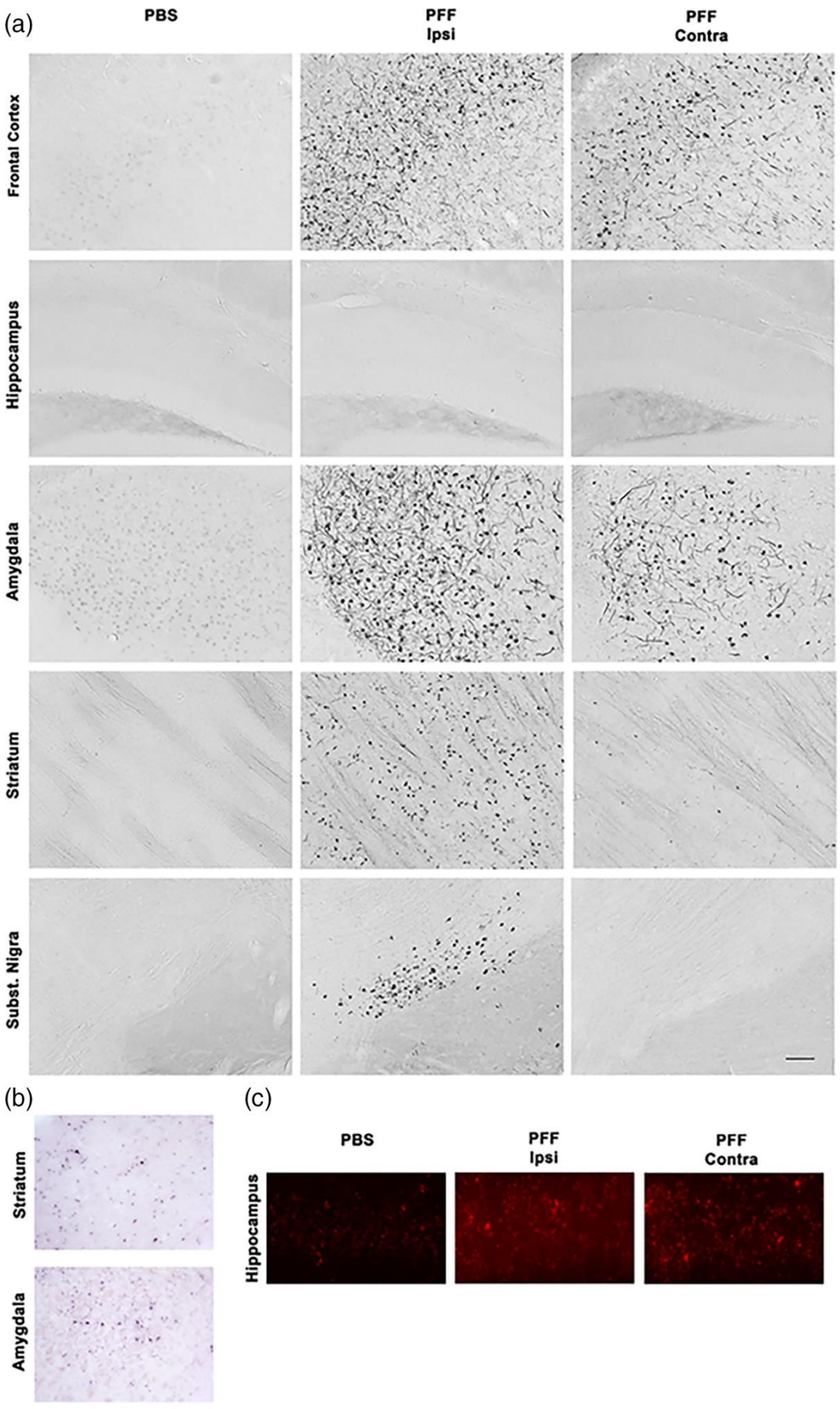
(a)
PBS
PFF Ipsi
PFF Contra
Frontal Cortex
Hippocampus
Amygdala
Striatum
Subst. Nigra
(b)
Striatum
Amygdala
(c)
PBS
PFF Ipsi
PFF Contra
Hippocampus

Figure 1: Striatal injection of murine α-syn PFFs induced α-syn inclusions in various brain regions.

Mice were euthanized 90 days after injection (90 dpi, n = 10–11/group). (a) PhosphoSER129 α-syn immunostaining showed numerous α-syn inclusions in neuritic and neuronal body structures in different brain regions. Widespread α-syn inclusions were observed bilaterally in frontal cortex and the amygdala, ipsilaterally in the striatum and the substantia nigra (SN), and only minimally in the contralateral striatum and SN. None were observed in the hippocampus. No inclusions were observed in either side of the brains of PBS-injected control mice. Pictures show the ipsilateral side of these mice. (b) Proteinase-K digestion on thin sections generated from paraffin-embedded tissue (PET) revealed the presence of digestion-resistant α-syn inclusions stained for PhosphoSER129 α-syn. Shown here are ipsilateral striatum and amygdala for illustration. (c) Proximity-ligation assay using a monoclonal PhosphoSER129 α-syn antibody showed the presence of enhanced levels of oligomeric forms of α-syn in the hippocampus of PFF-injected mice, where no inclusions could be detected 90 dpi, compared to PBS-injected controls. Scale bar = 250 μm (a), 250 μm (b), 25 μm (c)

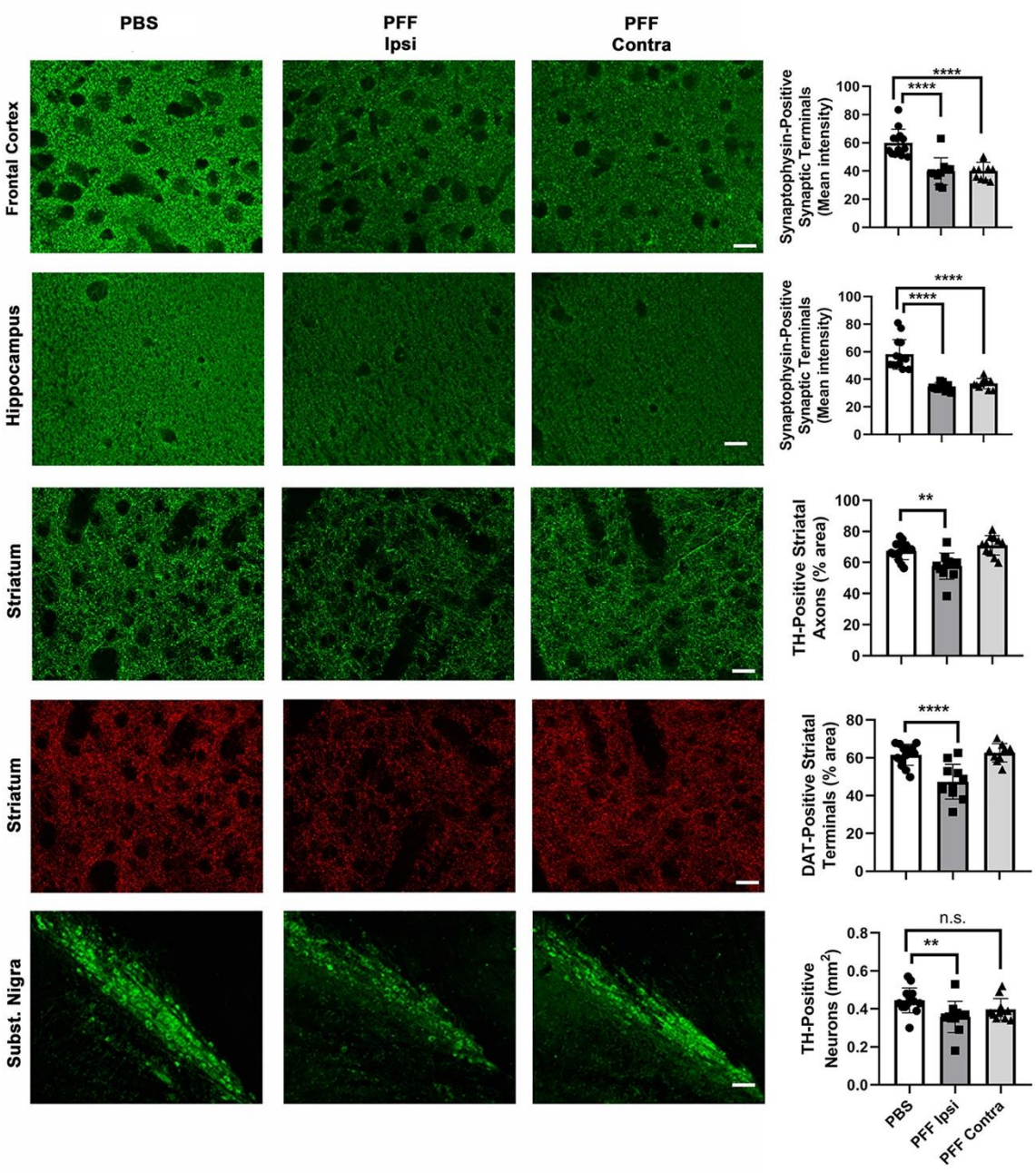
PBS
PFF Ipsi
PFF Contra
Frontal Cortex
Hippocampus
Striatum
Striatum
Subst. Nigra
Synaptophysin-Positive Synaptic Terminals (Mean intensity)
Synaptophysin-Positive Synaptic Terminals (Mean intensity)
TH-Positive Striatal Axons (% area)
DAT-Positive Striatal Terminals (% area)
TH-Positive Neurons (mm²)
****
****
****
****
**
****
n.s.
**
PBS
PFF Ipsi
PFF Contra

Figure 2: Striatal injection of murine α-syn PFFs induced neurodegeneration in various brain regions.

Mice were euthanized 90 dpi. In the frontal cortex and the hippocampus, a significant bilateral loss of synaptophysin-positive presynaptic terminals was observed (first two rows). In the striatum, a significant ispilateral loss of TH-positive axonal fibers and DAT-positive synaptic terminals was observed (3rd and 4th row). In the SN, a significant loss of TH-positive neurons was observed only ipsilaterally. For group comparisons and graphing, ipsilateral PBS measures were combined contralateral PBS measures, since they were similar. Pictures show the ipsilateral side of PBS-injected mice. ****p < .0001, **p < .01, compared to PBS controls by Dunnett's post hoc; n = 10–11/group; graphs are mixed scattergrams/bar diagrams, where points represent the individual values for each animal, and bars represent the means +/− SD; 95% confidence intervals of differences: Frontal cortex – PBS versus PFF ipsi: 11.6 to 28.7, PBS versus PFF contra: 11.42 to 28.52; hippocampus – PBS versus PFF ipsi: 16.2 to 30.5, PBS versus PFF contra: 13.9 to 28.3; striatum (TH) – PBS versus PFF ipsi: 3.56 to 16.3, PBS versus PFF contra: −9.8 to 2.9; striatum (DAT) – PBS versus PFF ipsi: 7.8 to 20.6; PBS versus PFF contra: −7.8 to 5.7; SN (TH) – PBS versus PFF ipsi: 0.002 to 0.152, PBS versus PFF contra: −0.017 to 0.112). Scale bars: 18 µm (for frontal cortical and hippocampal synaptophysin panels), 22.5 µm (for striatal TH and DAT panels), 80 µm (for Subst. Nigra panels)

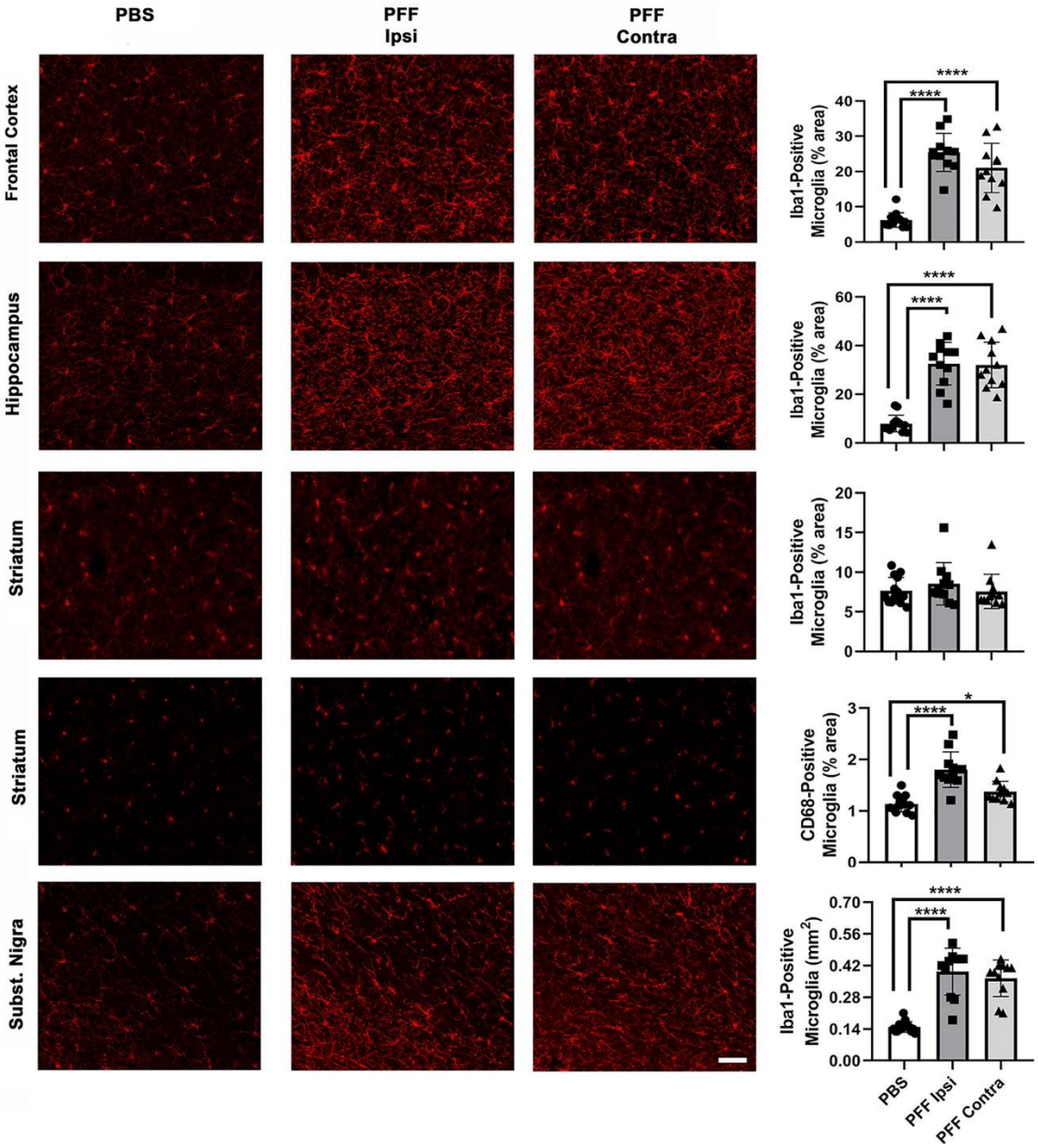
PBS
PFF Ipsi
PFF Contra
Frontal Cortex
Hippocampus
Striatum
Striatum
Subst. Nigra
Iba1-Positive Microglia (% area)
Iba1-Positive Microglia (% area)
Iba1-Positive Microglia (% area)
CD68-Positive Microglia (% area)
Iba1-Positive Microglia (mm2)
****
****
*
PBS
PFF Ipsi
PFF Contra

Figure 3: Striatal injection of murine α-syn PFFs induced widespread microgliosis in different brain regions.

Mice were euthanized 90 dpi. Panels show microgliosis measured on Iba1-stained sections of frontal cortex (upper row), hippocampus (second row), striatum (third row), and Subst. Nigra (last row), and on CD68-stained sections of striatum (4th row). A very strong microgliosis (up to 4× over control) was observed bilaterally in frontal cortex, hippocampus, and SN. No increase in Iba1 signal, but a significant bilateral increase in CD68 signal was observed in the striatum of PFF-injected mice. For group comparisons and graphing, ipsilateral PBS measures were combined contralateral PBS measures, since they were similar. Pictures show the ipsilateral side of PBS-injected mice. ****$p < .0001$, *$p < .05$, compared to PBS controls by Dunnett's post hoc; $n = 10–11$/group; graphs are mixed scattergrams/bar diagrams, where points represent the individual values for each animal, and bars represent the means +/− SD; 95% confidence intervals of differences: Frontal cortex – PBS versus PFF ipsi: −23.9 to −14.5, PBS versus PFF contra: −19.5 to −10.1; hippocampus: – PBS versus PFF ipsi: −31.5 to −17.7, PBS versus PFF contra −31.0 to −17.2; striatum (Iba1) – PBS versus PFF ipsi: −2..9 to 1.1, PBS versus PFF contra: −1.9 to 2.1; striatum (CD68) – PBS versus PFF ipsi: −0.9 to −0.4, PBS versus PFF contra: −0.5 to −0.01; SN – PBS versus PFF ipsi:-0.31 to −0.17, PBS versus PFF contra: −0.28 to −0.15. Scale bars: 22.5 µm (for all panels)

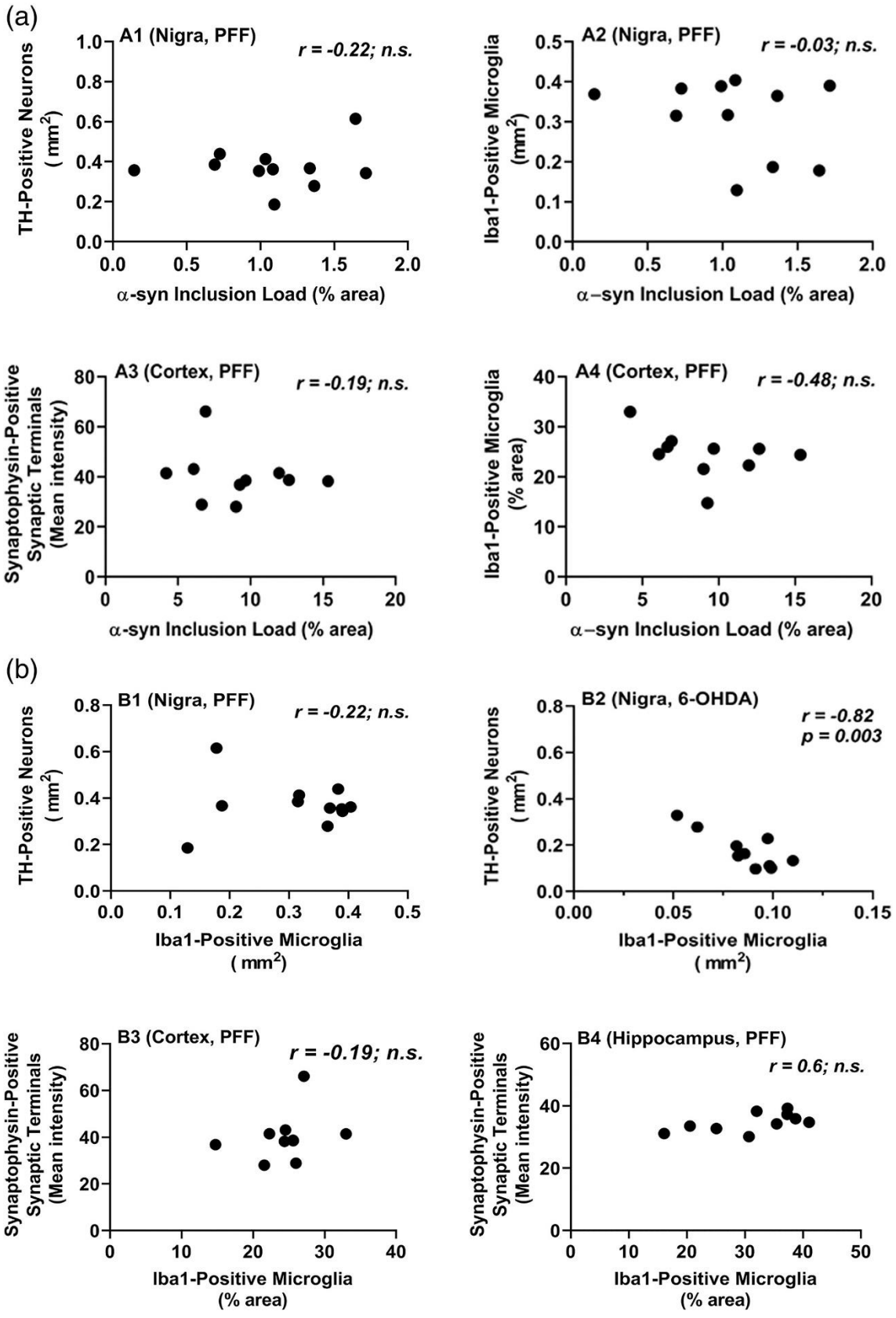
(a)
A1 (Nigra, PFF)
r = -0.22; n.s.
TH-Positive Neurons (mm2)
α-syn Inclusion Load (% area)
A2 (Nigra, PFF)
r = -0.03; n.s.
Iba1-Positive Microglia (mm2)
α−syn Inclusion Load (% area)
A3 (Cortex, PFF)
r = -0.19; n.s.
Synaptophysin-Positive Synaptic Terminals (Mean intensity)
α-syn Inclusion Load (% area)
A4 (Cortex, PFF)
r = -0.48; n.s.
Iba1-Positive Microglia (% area)
α−syn Inclusion Load (% area)
(b)
B1 (Nigra, PFF)
r = -0.22; n.s.
TH-Positive Neurons (mm2)
Iba1-Positive Microglia (mm2)
B2 (Nigra, 6-OHDA)
r = -0.82
p = 0.003
TH-Positive Neurons (mm2)
Iba1-Positive Microglia (mm2)
B3 (Cortex, PFF)
r = -0.19; n.s.
Synaptophysin-Positive Synaptic Terminals (Mean intensity)
Iba1-Positive Microglia (% area)
B4 (Hippocampus, PFF)
r = 0.6; n.s.
Synaptophysin-Positive Synaptic Terminals (Mean intensity)
Iba1-Positive Microglia (% area)

Figure 4: Different PD-related pathologies in the brains of mice injected striatally with α-syn PFFs do not correlate with each other.

Mice were euthanized 90 dpi. (a) α-syn inclusion load did no correlate with neurodegeneration (loss TH-positive neurons, A1) or with microgliosis (A2) in the SN (Nigra), nor with neurodegeneration (loss of synaptophysin-positive synaptic terminals, A3) or with microgliosis (A4) in the frontal cortex (cortex). (b) Microgliosis did not correlate with loss of TH-positive neurons in the SN after intrastriatal PFF injection, but did so after intrastriatal injection of the toxin 6-OHDA. The microgliosis, measured on Iba1-stained section, was also much higher in the Subst. Nigra of PFF-injected mice than in that of 6-OHDA-injected mice. All measures shown are from the ipsilateral brain sides; similar observations were made for the contralateral sides of PFF-injected mice. Correlation analyses were done using Spearman rank test for data set including α-syn inclusion load measures (non-parametric), and with Pearson's test for data sets with the other measures (parametric)

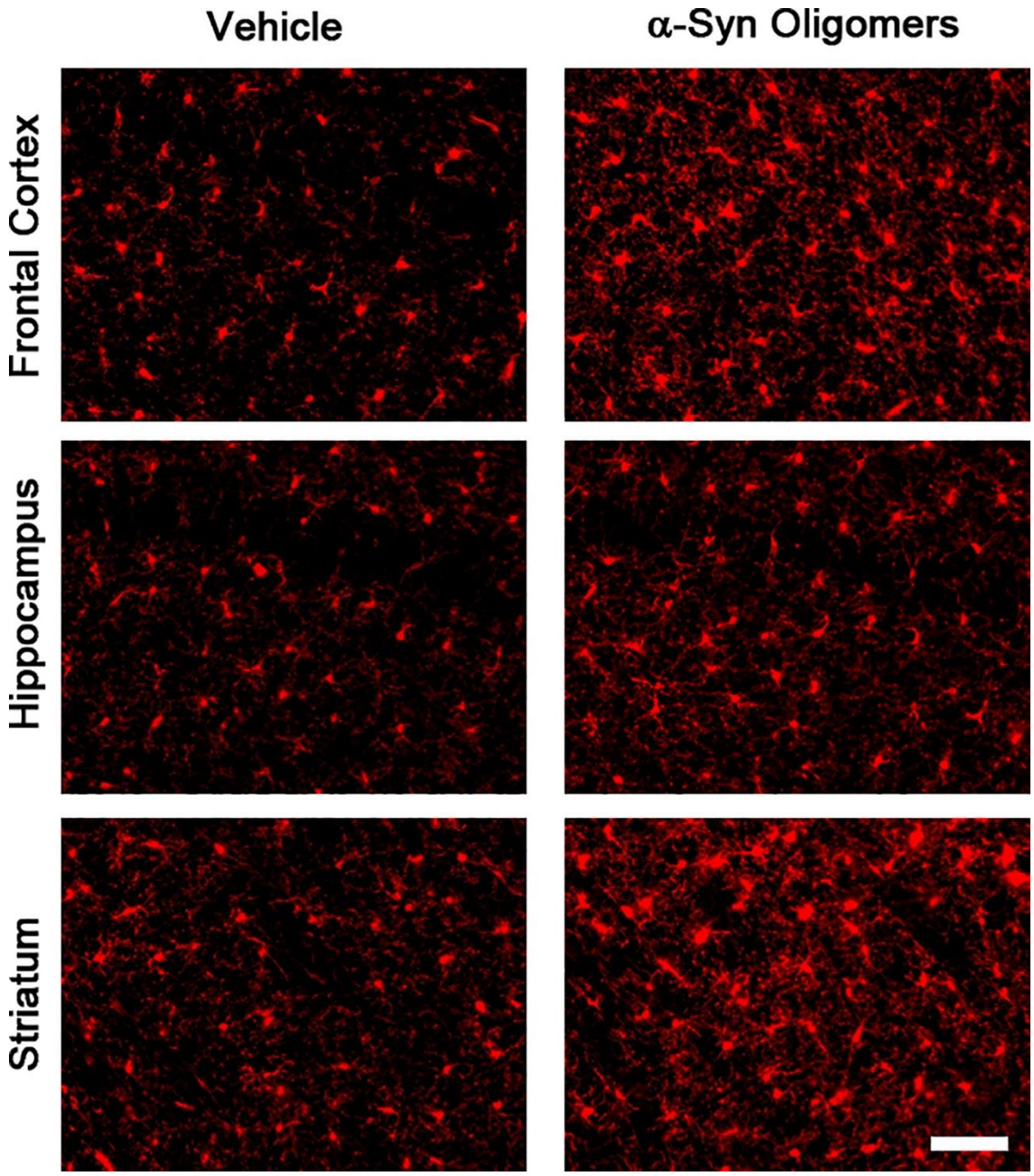
Vehicle
α-Syn Oligomers
Frontal Cortex
Hippocampus
Striatum

Figure 5: Strong microglial response after striatal injection of α-syn oligomers.

Oligomers were prepared and injections were performed as described in Materials and Methods, Section 2. A strong microgliosis was observed in different brain regions 13 dpi, confirming that these cells react strongly to oligomers. Scale bar = 40 µm

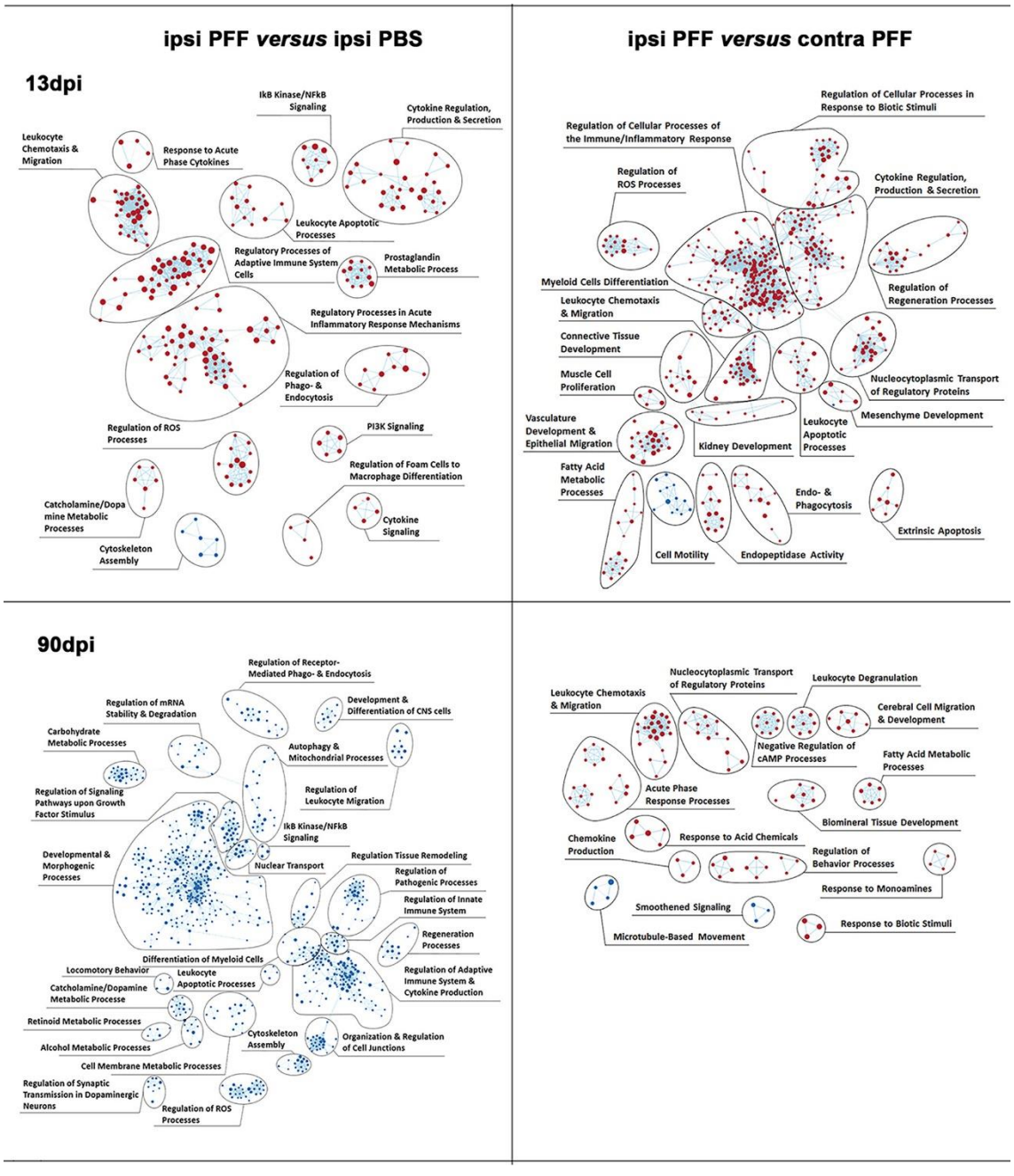
ipsi PFF versus ipsi PBS
13dpi
IkB Kinase/NFkB Signaling
Cytokine Regulation, Production & Secretion
Leukocyte Chemotaxis & Migration
Response to Acute Phase Cytokines
Leukocyte Apoptotic Processes
Regulatory Processes of Adaptive Immune System Cells
Prostaglandin Metabolic Process
Regulatory Processes in Acute Inflammatory Response Mechanisms
Regulation of Phago- & Endocytosis
Regulation of ROS Processes
PI3K Signaling
Regulation of Foam Cells to Macrophage Differentiation
Cytokine Signaling
Catcholamine/Dopamine Metabolic Processes
Cytoskeleton Assembly
ipsi PFF versus contra PFF
Regulation of Cellular Processes in Response to Biotic Stimuli
Regulation of Cellular Processes of the Immune/Inflammatory Response
Regulation of ROS Processes
Cytokine Regulation, Production & Secretion
Myeloid Cells Differentiation
Regulation of Regeneration Processes
Leukocyte Chemotaxis & Migration
Connective Tissue Development
Muscle Cell Proliferation
Nucleocytoplasmic Transport of Regulatory Proteins
Mesenchyme Development
Vasculature Development & Epithelial Migration
Kidney Development
Leukocyte Apoptotic Processes
Fatty Acid Metabolic Processes
Endo- & Phagocytosis
Extrinsic Apoptosis
Cell Motility
Endopeptidase Activity
90dpi
Regulation of Receptor-Mediated Phago- & Endocytosis
Regulation of mRNA Stability & Degradation
Development & Differentiation of CNS cells
Carbohydrate Metabolic Processes
Autophagy & Mitochondrial Processes
Regulation of Signaling Pathways upon Growth Factor Stimulus
Regulation of Leukocyte Migration
IkB Kinase/NFkB Signaling
Developmental & Morphogenic Processes
Nuclear Transport
Regulation Tissue Remodeling
Regulation of Pathogenic Processes
Regulation of Innate Immune System
Regeneration Processes
Differentiation of Myeloid Cells
Locomotory Behavior
Leukocyte Apoptotic Processes
Regulation of Adaptive Immune System & Cytokine Production
Catcholamine/Dopamine Metabolic Processe
Retinoid Metabolic Processes
Cytoskeleton Assembly
Organization & Regulation of Cell Junctions
Alcohol Metabolic Processes
Cell Membrane Metabolic Processes
Regulation of Synaptic Transmission in Dopaminergic Neurons
Regulation of ROS Processes
Nucleocytoplasmic Transport of Regulatory Proteins
Leukocyte Degranulation
Leukocyte Chemotaxis & Migration
Cerebral Cell Migration & Development
Negative Regulation of cAMP Processes
Fatty Acid Metabolic Processes
Acute Phase Response Processes
Biomineral Tissue Development
Chemokine Production
Response to Acid Chemicals
Regulation of Behavior Processes
Response to Monoamines
Smoothened Signaling
Response to Biotic Stimuli
Microtubule-Based Movement

Figure 6: Enriched inflammatory pathways precede neurodegeneration in mouse ventral midbrains after intrastriatal α-syn PFFs injection.

Enrichment map of gene expression profiles were derived from GSEA. Statistics were done by weighted Kolmogorov–Smirnov, gene set size limits were set to min15 – max250. Details of curation procedure used to group BPs (represented as dots, either red if upregulated, or blue if downregulated) into high-level functional gene set clusters of BPs of related biological function are described in Material & Methods. At 13 dpi, comparing ipsi PFF to either ipsi PBS or contra PFF, most BPs were upregulated and associated with gene sets related to immune and inflammation processes. This shows that, in the ipsilateral nigro-striatum, neuroinflammation precedes neurodegeneration (measurable at 90 dpi), and might contribute to its development. At 90 dpi, comparing ipsi PFF to ipsi PBS, all BPs, including those associated with inflammation gene sets, were downregulated, possibly reflecting the neurodegenerative process itself. Comparing ipsi PFF to contra PFF at this time point, most BPs were upregulated

(a)

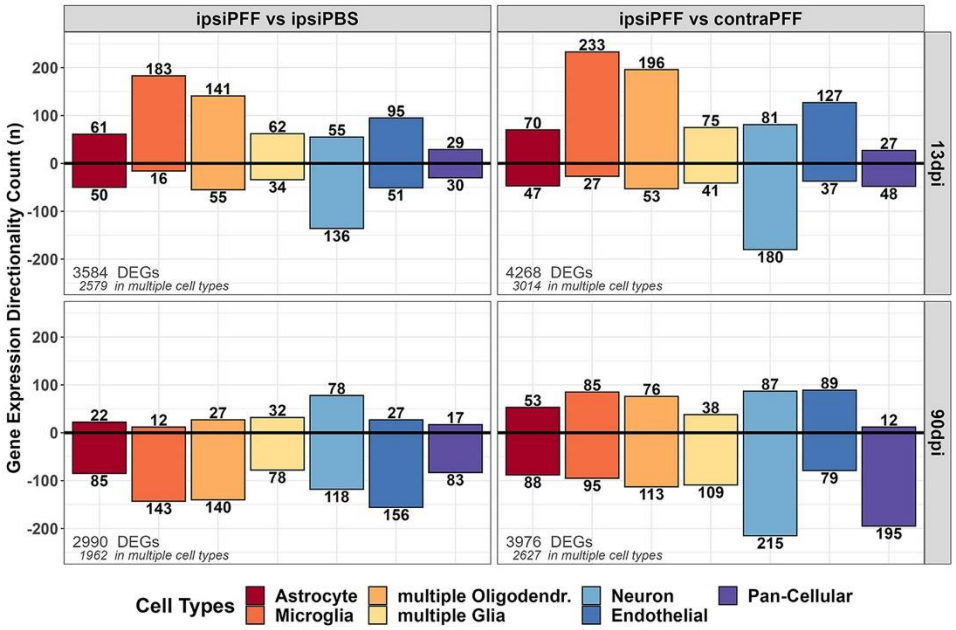

(b)

Gene Symbol	Protein Name	Cell type	FC	Pfp
	13dpi - ipsi PFF *versus* ipsi PBS			
Slc6a3	Sodium-dependent dopamine transporter	Neuron	2.600	2.94E-08
Oxt	Oxytocin	Pan cellular	-1.519	1.64E-06
Lilrb4a	Leukocyte immunoglobulin-like receptor, subfamily B, member 4A	Microglia	2.074	3.59E-06
Spp1	Osteopontin	Microglia	1.921	9.29E-06
Cst7	Cystatin F (leukocystatin)	Microglia	1.921	1.63E-05
Lpl	Lipoprotein lipase	Microglia	1.795	1.70E-05
Ccl3	Chemokine (C-C motif) ligand 3	Microglia	1.819	1.72E-05
Plin4	Perilipin 4	Neuron	1.747	5.44E-05
Clec7a	C-type lectin domain family 7 member A	Microglia	1.808	5.94E-05
Ogn	Osteoglycin	Endothelial	1.753	8.19E-05
Avp	Arginine vasopressin	Neuron	-1.149	1.30E-04
Prg4	Proteoglycan 4 (lubricin)	Astrocyte	1.777	1.72E-04
Gfap	Glial fibrillary acidic protein	Astrocyte	1.633	1.85E-04
Sim1	Single-minded homolog 1	Neuron	-1.643	1.88E-04
Sgk1	Serum/glucocorticoid regulated kinase 1	Microglia	1.675	2.00E-04
Cd68	CD68 antigen	Microglia	1.683	2.07E-04
Chrna6	Neuronal acetylcholine receptor subunit alpha-6	Neuron	1.585	2.11E-04
Zbtb16	Zinc finger and BTB domain containing 16	Neuron	1.644	2.73E-04
Tyrobp	TYRO protein tyrosine kinase binding protein	Microglia	1.628	3.48E-04
Fezf1	Fez family zinc finger protein 1	Neuron	-1.475	3.74E-04
	90dpi - ipsi PFF *versus* ips iPBS			
Slc6a3	Sodium-dependent dopamine transporter	Neuron	-2.383	1.51E-06
Gh	Growth hormone	Endothelial	2.007	1.09E-05
Th	Tyrosine hydroxylase	Neuron	-1.874	5.40E-04
Slc18a2	Synaptic vesicular amine transporter	Neuron	-1.782	1.33E-03
Chrnb3	Neuronal acetylcholine receptor subunit beta-3	Neuron	-1.748	3.72E-03
Slc5a7	High affinity choline transporter 1	Neuron	1.630	3.95E-03
Cyr61	Cysteine-rich angiogenic inducer 61	Astrocyte	-1.692	4.44E-03
Gm10754	*Unnamed protein*	Neuron	1.364	5.64E-03
Taf1d	TATA box-binding protein-associated factor RNA polymerase I	Endothelial	1.560	7.33E-03
Chrna6	Neuronal acetylcholine receptor subunit alpha-6	Neuron	-1.707	7.61E-03
Kcnj13	Inward rectifier potassium channel 13	Pan cellular	-1.556	1.38E-02
Ret	Proto-oncogene tyrosine-protein kinase receptor Ret	Neuron	-1.602	1.43E-02
Meis2	Homeobox protein Meis2	Neuron	1.434	1.43E-02
Slc13a4	Solute carrier family 13 (Sodium/sulfate symporter), member 4	OPC	-1.358	1.56E-02
Ranbp3l	RAN binding protein 3-like	Astrocyte	-1.288	2.13E-02
Mir5098	*Stem-loop RNA, non coding*	Pan cellular	1.507	2.13E-02
Aldh1a2	Aldehyde dehydrogenase family 1, member A2	Neuron	-1.442	2.16E-02
Trh	Thyrotropin releasing hormone	Astrocyte	1.436	2.34E-02
C030013G03Rik	*Unknown*	*unknown*	-1.540	2.36E-02
Prkcd	Protein kinase C delta type	Microglia	-1.368	2.45E-02

Gene Symbol	Protein Name	Cell type	FC	Pfp
	13dpi - ipsi PFF *versus* contra PFF			
Oxt	Oxytocin	Pan cellular	-2.762	2.97E-13
Slc6a3	Sodium-dependent dopamine transporter	Neuron	2.749	5.55E-10
Tmem212	Transmembrane protein 212	Astrocyte	-2.203	1.98E-09
Stoml3	Stomatin-like protein 3	Pan cellular	-2.211	1.99E-09
Lilrb4a	Leukocyte immunoglobulin-like receptor, subfamily B, 4A	Microglia	2.437	2.18E-09
Cst7	Cystatin F (leukocystatin)	Microglia	2.412	3.46E-09
Ogn	Osteoglycin	Endothelial	2.296	4.44E-09
Clec7a	C-type lectin domain family 7 member A	Microglia	2.348	8.01E-09
Ak7	Adenylate kinase 7	Astrocyte	-2.112	8.52E-09
Spp1	Osteopontin	Microglia	2.232	1.28E-08
Ccl3	Chemokine (C-C motif) ligand 3	Microglia	2.367	1.33E-08
Trh	Thyrotropin releasing hormone	Astrocyte	-2.067	2.72E-08
Cdhr3	Cadherin-related family member 3	Pancellular	-1.996	5.01E-08
Slc17a7	Vesicular glutamate transporter 1	Pan-cellular	2.288	1.10E-07
Cd68	CD68 antigen	Microglia	2.042	1.31E-07
Ccl6	Chemokine (C-C motif) ligand 6	Microglia	1.980	1.96E-06
Prg4	Proteoglycan 4 (lubricin)	Astrocyte	1.999	1.99E-06
Dynlrb2	Dynein light chain roadblock-type 2	Astrocyte	-1.815	2.40E-06
Fam183b	Protein FAM183B	Neuron	-1.889	4.02E-06
Ccl9	Chemokine (C-C motif) ligand 9	Microglia	1.838	7.89E-06
	90dpi - ipsi PFF *versus* contra PFF			
Kcnj13	Inward rectifier potassium channel 13	Pan cellular	2.556	7.66E-09
Prg4	Proteoglycan 4 (lubricin)	Astrocyte	2.593	1.03E-08
Ogn	Osteoglycin	Endothelial	2.749	1.15E-08
Slc13a4	Solute carrier family 13 (Sodium/sulfate symporter), member 4	OPC	2.330	4.82E-07
Ranbp3l	RAN binding protein 3-like	Astrocyte	2.334	4.89E-07
Crym	Ketimine reductase mu-crystallin	Pan cellular	2.193	1.06E-06
Col6a1	Collagen alpha-1(VI) chain	Neuron	2.115	1.41E-06
Rgs16	Regulator of G-protein signaling 16	Endothelial	-2.062	1.61E-06
Slitrk6	SLIT and NTRK-like protein 6	OPC	-2.139	1.91E-06
Stoml3	Stomatin-like protein 3	Pan cellular	-2.146	1.95E-06
C030013G03Rik	*Unknown*	*unknown*	-2.018	2.12E-06
Car12	Carbonic anyhydrase 12	Neuron	2.151	2.28E-06
Pomc	Pro-opiomelanocortin-alpha	Endothelial	-2.112	3.09E-06
Tcf7l2	Transcription factor 7-like 2	Oligodend.	-1.996	3.73E-06
Omd	Osteomodulin	Astrocyte	2.155	4.48E-06
Osr1	Protein odd-skipped-related 1	Pan cellular	1.998	1.43E-05
Nov	Protein NOV homolog	Neuron	2.039	1.51E-05
Trav7d-4	T cell receptor alpha variable 7D-4	Leucocyte*	-1.783	1.69E-05
Cox6a2	Cytochrome c oxidase subunit 6A2, mitochondrial	Microglia	-1.837	1.73E-05
Oxt	Oxytocin	Pan cellular	-1.835	1.85E-05

Figure 7

(a) Deconvolution of cell types for DEGs at 13 and 90 dpi after striatal injection of α-syn PFFs. Many DEGs were expressed in multiple, but not all cell types. DEGs that were expressed in all cell types are named “pan-cellular”. DEGs expressed in related cells (e.g., “multiple glia”, “multiple oligodendrocytes”), have been grouped for simplicity. The majority of DEGs, at 13dpi, expressed uniquely by one cell type were in microglia. (b) Top 20 DEGs in mouse ventral midbrain after striatal injection of α-syn PFF indicate involvement of microglia in initial pathological events. At 13 dpi, comparing ipsi PFF with ipsi PBS or contra PFF, 45% and 40%, respectively, of the top 20 DEGs were microglial. At 90 dpi, comparing ipsi PFF with ipsi PBS, 50% of top 20 DEGs were neuronal, possibly a reflection of neurodegeneration. The bottom panel lists the gene products of the gene symbols, coded proteins, the associated cell type, the fold change (FC) and the pfp of all top 20 DEGs for each comparison

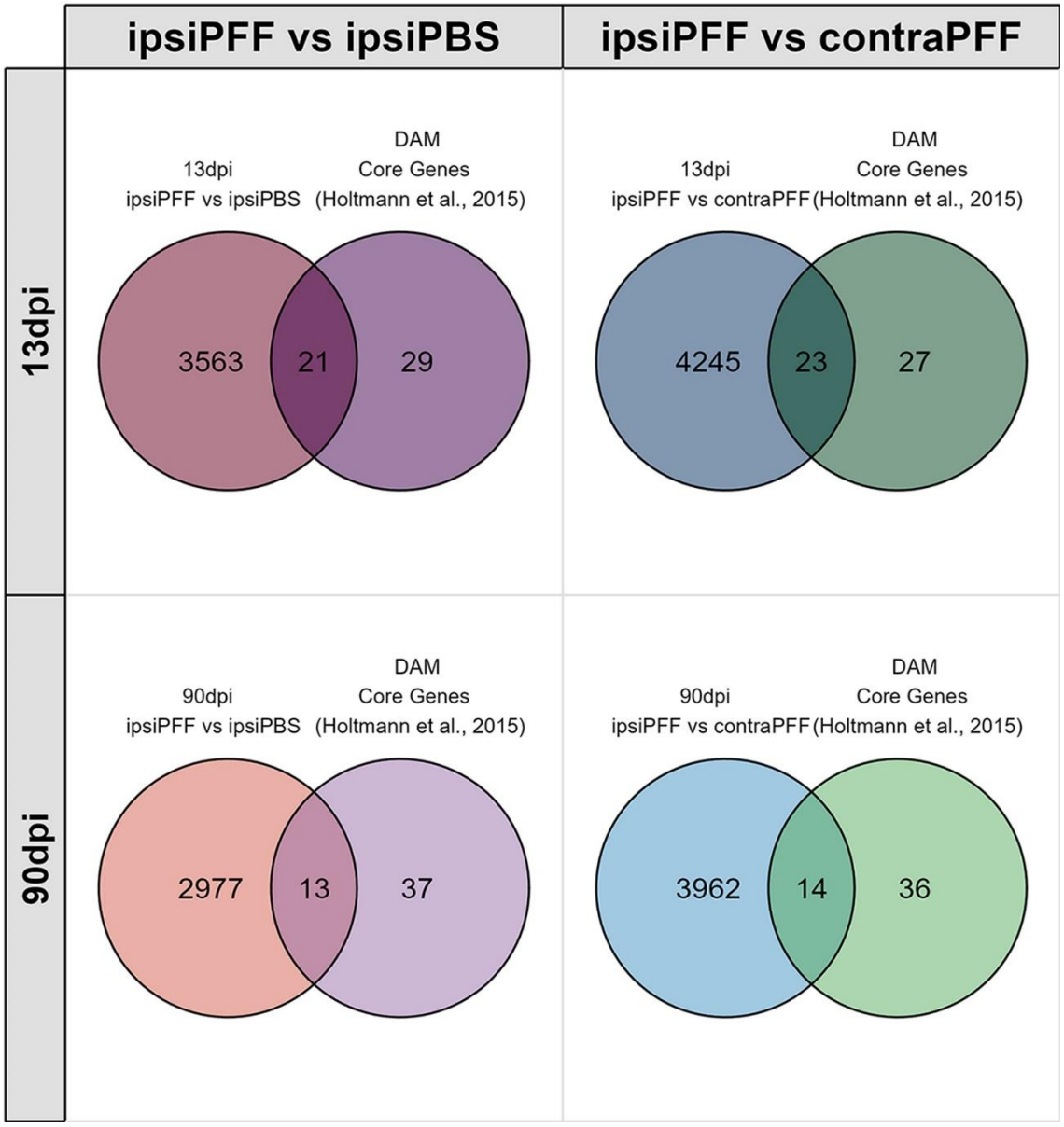
ipsiPFF vs ipsiPBS
ipsiPFF vs contraPFF
13dpi
90dpi
13dpi
ipsiPFF vs ipsiPBS
DAM
Core Genes
(Holtmann et al., 2015)
3563
21
29
13dpi
ipsiPFF vs contraPFF
DAM
Core Genes
(Holtmann et al., 2015)
4245
23
27
90dpi
ipsiPFF vs ipsiPBS
DAM
Core Genes
(Holtmann et al., 2015)
2977
13
37
90dpi
ipsiPFF vs contraPFF
DAM
Core Genes
(Holtmann et al., 2015)
3962
14
36

Figure 8: Venn diagrams of DEGs 13 and 90 dpi after striatal injections of α-syn PFFs overlapping with a core gene signature of microglia associated with five different mouse neurological disease models (disease-associated microglia, DAM).

More DEGs at 13dpi overlap with the core DAM signature than at 90 dpi. See main text for details

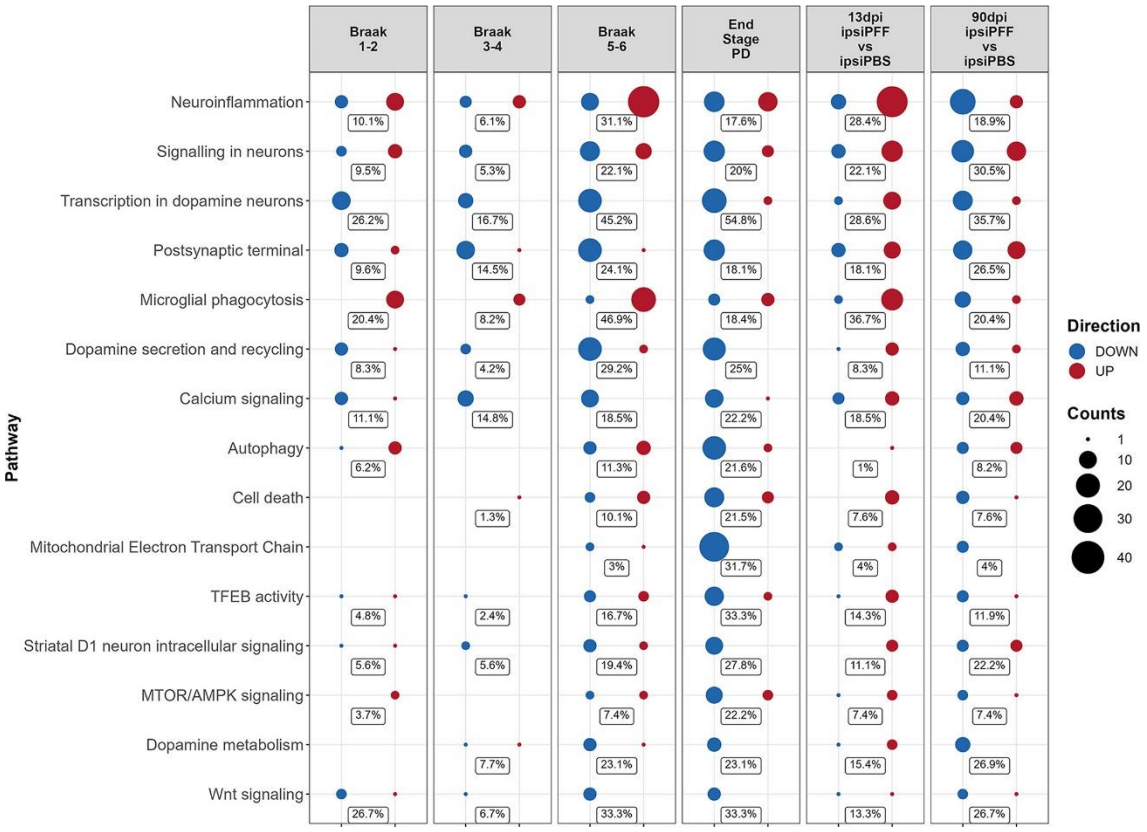
Braak 1-2
Braak 3-4
Braak 5-6
End Stage PD
13dpi ipsiPFF vs ipsiPBS
90dpi ipsiPFF vs ipsiPBS
Pathway
Neuroinflammation
Signalling in neurons
Transcription in dopamine neurons
Postsynaptic terminal
Microglial phagocytosis
Dopamine secretion and recycling
Calcium signaling
Autophagy
Cell death
Mitochondrial Electron Transport Chain
TFEB activity
Striatal D1 neuron intracellular signaling
MTOR/AMPK signaling
Dopamine metabolism
Wnt signaling
10.1%
6.1%
31.1%
17.6%
28.4%
18.9%
9.5%
5.3%
22.1%
20%
22.1%
30.5%
26.2%
16.7%
45.2%
54.8%
28.6%
35.7%
9.6%
14.5%
24.1%
18.1%
18.1%
26.5%
20.4%
8.2%
46.9%
18.4%
36.7%
20.4%
8.3%
4.2%
29.2%
25%
8.3%
11.1%
11.1%
14.8%
18.5%
22.2%
18.5%
20.4%
6.2%
11.3%
21.6%
1%
8.2%
1.3%
10.1%
21.5%
7.6%
7.6%
3%
31.7%
4%
4%
4.8%
2.4%
16.7%
33.3%
14.3%
11.9%
5.6%
5.6%
19.4%
27.8%
11.1%
22.2%
3.7%
7.4%
22.2%
7.4%
7.4%
7.7%
23.1%
23.1%
15.4%
26.9%
26.7%
6.7%
33.3%
33.3%
13.3%
26.7%
Direction
DOWN
UP
Counts
1
10
20
30
40

Figure 9: Translational relevance assessment of gene expression changes at 13 and 90 dpi after striatal injection of α-syn PFFs.

The PD map (https://pdmap.uni.lu/minerva/) was used to extract pathways from human databases (first 4 columns) and from the DEG datasets of this study (two last columns). The percentages in each row give the proportion of genes in each pathway that were found as DEGs in each dataset that were mapped. There were strong similarities between human PD gene expression changes and those found in the α-syn seeding/spreading model. See main text for details

PART IV

Discussion, Conclusion & Perspective

Discussion

The multifactorial complexity of PD poses a great challenge in research and therapy development. Various factors – genetic, environmental and lifestyle – have been associated with onset, progression and severity of the disease. Braak's spreading hypothesis provided novel conceptual insights, but did also meet criticism with Lewy pathology not necessarily reflecting PD symptomatology (Dijkstra et al., 2014; Espay and Marras, 2019). The clinical heterogeneity in PD cannot be explained by a single model (Borghammer and Van Den Berge, 2019). Hence, we have to consider that PD, even though showing the same pathological hallmarks in the SN at *post mortem*, has different origins and underlying pathways of pathogenesis.

In the last decade, the importance and potential implications of the gut microbiome in disease onset and progression have been brought to the limelight. Changes to the microbiome in PD are particularly marked by the decrease of SCFA synthesizing bacteria. Consequently, protective mechanisms are weakened, and mucosal and systemic inflammation sets in, potentially extending to the brain (Baizabal-Carvallo and Alonso-Juarez, 2020; Sampson et al., 2016). This is additionally accompanied by a weakening of the gut barrier integrity allowing various toxins or pathogens to cross the barrier and access the vasculature or the ENS. Braak and colleagues postulated that the gut could be at the origin of PD, where an exogenous pathogen would reach the submucosal and myenteric plexuses corrupting endogenous αSyn. Such turned-toxic forms would subsequently spread in a prion-like manner via the vagus nerve to subsequently spread in a caudorostral manner throughout the brain culminating in the known PD pathologies.

Fibre deprivation leads to microbial changes driving colonic outer mucus erosion and gut barrier vulnerability

Various studies have documented significant changes in the microbiome of PD patients compared to healthy controls. If these changes are at the origin or a consequence of the disease still needs to be answered. Nevertheless, it has been shown that altered microbiomes do affect disease progression (Lubomski et al., 2022) and one of the strongest microbiome modulators is diet. A "western-style", poor in vegetables and rich of processes foods, opposite to a balanced, fiber rich diet, has been associated with exacerbation of PD progression (Mischley et al., 2017). In animals, a fiber-deprived diet has been shown to cause rapid gut microbial shifts, selectively increasing potentially harmful bacteria (Desai et al., 2016; Neumann et al., 2021; Riva et al., 2019; Schroeder et al., 2018). We were able to confirm that the lack of dietary fibre did cause a diversity drop and shift, further reflected in altered Firmicutes/Bacteroidetes ratios and in various PD-associated taxa levels.

Under fiber deprived conditions, mucus foraging taxa, such as *Akkermansia* spp. and *Bacteroides* spp., move to the host's glycans as energy source found in enteric mucus layers. This consequently leads to mucus erosion, weakening of the physical barrier that the mucus layers provides and ultimately allows toxins or pathogens easier access to the different gut epithelial layers (Desai et al., 2016; Martens et al., 2008). While our study did not show immediate changes to the inner mucus due to potential compensatory mechanisms (Schroeder et al., 2018), the outer mucus layer was drastically reduced in fiber-deprived conditions. Being the habitat of resident commensal bacteria (Johansson et al., 2011), the decrease of the outer mucus layer thickness correlated with reduced microbial diversity.

In PD, SCFA-producing bacteria are reduced. Lower levels of SCFA have been associated with different physiological reactions such as constipation, inflammation and "leaky gut" (Keshavarzian et al., 2020). In our data, genera of the butyrogenic *Lachnospiraceae* family amongst others were decreased in fiber deprivation groups. Butyrate is involved in different essential regulatory processes including mucin production stimulation and gut barrier protection via the stimulation of tight junction expression (Plöger et al., 2012; Rivière et al., 2016).

Hence, under fiber-deprived conditions the enteric barrier is weakened and more susceptible to pathogenic factors as e.g. Curli.

Curli exposure drives PD pathologies, further exacerbated under fiber deprived conditions

In PD, key regulators of microbial homeostasis are decreased, whereas others potentially harmful if overgrowing are increased. One particular family which has been associated with a more severe PD phenotype and faster disease progression is Enterobacteriaceae (Barichella et al., 2019; Li et al., 2017; Scheperjans et al., 2015). Several Enterobacteriaceae members can synthesize the amyloidogenic protein Curli, known to seed αSyn aggregation *in vitro* (Sampson et al., 2020). αSyn aggregation is well documented in the ENS of PD patients (Braak et al., 2006; Wakabayashi et al., 1988, 1990). Different rodent models either treated with rotenone, MPTP or Curli have replicated PD pathologies in the gut (Chen et al., 2016; Lai et al., 2018; Pan-Montojo et al., 2010). We observed increased levels of pS129-αSyn+ forms in the myenteric plexus of mice which had been exposed to Curli producing *E. coli*. The levels were many-fold higher in transgenic mice which received the fiber-deprived diet.

Braak hypothesized that abnormal αSyn would subsequently propagate via the vagus nerve to the brain. Epidemiological studies support this hypothesis, suggesting that truncal vagotomy is a protective factor for PD (Liu et al., 2017; Svensson et al., 2015). The previously mentioned rotenone model showed that ENS pathology preceded CNS changes and propagation of αSyn after injection of PFFs into the gut wall of wild-type mice was prevented by truncal vagotomy (Kim et al., 2019; Pan-Montojo et al., 2010). While our data does not confirm the propagation via the vagus nerve to lower brainstem regions, we investigated different interconnected PD-relevant regions. Amongst the affected nuclei are the locus coeruleus, the pedunculopontine nucleus and of course the nigrostriatal pathway with the SN and striatum. These nuclei exhibit strong neuronal loss and αSyn deposits in PD (Cheng et al., 2010; Giguère et al., 2018; Hirsch et al., 1987; Oertel et al., 2019). According to Braak's pathology staging, αSyn spreads in a caudorostral manner. Kim and colleagues showed that in an incremental time-dependant manner, αSyn deposits and neurodegeneration in wild-type mice are

observed from caudal to rostral regions between 3 to 7 months (Kim et al., 2019). Our data suggests that this process is accelerated under all three pathological challenges; transgene overexpression, fiber-deprivation and Curli. We observed very similar patterns between the LC, PPN and SNpc for neurodegeneration and αSyn aggregation after only 9 weeks. More specifically, in transgenic animals, exposure to Curli was the key modulator and fiber-deprivation accelerated the pathogenic process.

Neurodegeneration and motor impairment in the absence of αSyn aggregation after 2-HP injection

Current microbiome research efforts try to further explore the functional host-microbe relationships. Using the in-house developed multi-omics approach, we identified increased levels of 2-hydroxypyridine (2-HP) in PD and idiopathic RBD patients compared to healthy controls. 2-HP is a microbial breakdown product of a known PD associated pesticide, chlorpyrifos (Freire and Koifman, 2012; Uniyal et al., 2021). Our data however did not indicate a direct link to chlorpyrifos, instead we identified the *Methanobrevibacter* species *M. smithii* to be significantly correlated with 2-HP and confirmed its expression by the archaeon. *Methanobrevibacter* is the most abundant archaeal genus in the human gut microbiota (Tyakht et al., 2013) and has been reported enriched in PD patients (Li et al., 2019; Romano et al., 2021).

2-HP is novel compound and has not been studied extensively. However, a ring-fused 2-pyridone compound (FN075) can act as seed for αSyn fibrillation (Horvath et al., 2012). Accordingly, we saw in our *in vitro* systems increased αSyn aggregation and cytotoxicity. In rodents FN075 caused different PD pathologies (Chermenina et al., 2015; Kelly et al., 2021). When injected into the striatum of wild-type mice, motor impairments appeared after 6 months and it took 3 months for dopaminergic neuron loss when FN075 was injected directly into the SN (Chermenina et al., 2015). An AAV-rat model expressing either WT αSyn or the A53T mutant αSyn injected with FN075 into the SN did neither show motor deficits nor neurodegeneration but showed increased expression and more so phosphorylation of αSyn in the SN and striatum. Our results showed neurodegeneration in the striatum and, to a more reduced extend, on the SNpc

only 2 months after 2-HP injection in Thy1-Syn14 mice. This was accompanied by significant motor impairments. Interestingly, we did not observe increases in pS129-αSyn in these brain structures, suggesting that neurodegeneration was independent of αSyn pathology.

Neuroinflammation is a trigger of neurodegeneration independent of αSyn pathology

Microbial changes have an impact on various physiological systems in humans. Changes in SCFA levels, as can be expected in PD patients, have been shown to actively modulate microglia, therefore neuroinflammation, in the CNS. Neuroinflammation, however, was not considered to actively participate in PD pathogenesis. Many studies focused on dysregulated pathways directly related to αSyn aggregation and its cytotoxicity (Fields et al., 2019; Periquet et al., 2007). However, αSyn load was found to not always correlate with disease severity or dopaminergic loss (Jellinger, 2009). Intriguingly, aggregated forms of αSyn can directly interact with microglia via TLR2 setting off an inflammatory reaction, which has been reported to potentially precede neurodegeneration (Croisier et al., 2005; Duffy et al., 2018; Kim et al., 2013; Tansey and Romero-Ramos, 2019). Unfortunately, reactive microglial population appear to not only react but also cause tissue injury (Ransohoff and El Khoury, 2015). This process is however not fully understood.

Using a PD mouse model of αSyn seeding and spreading, as described before (Luk et al., 2012), we intended to further investigate the underlying pathological events. The most relevant neuropathological findings were that αSyn inclusion load and microgliosis did not correlate with neurodegeneration. While these findings, based on immunohistochemistry, are very informative, they do not capture the dynamics and complexity of reactive microglia populations (Ransohoff, 2016; Uriarte Huarte et al., 2021). Using a microarray system, we analysed the transcriptional profile of the ventral midbrain at an early and late timepoint after injection. Our results highlight an early (13dpi) microglia dominant, reactive profile, which might be the driver of neurodegeneration. This is supported by several microglia genes, such as *Cybb*, *Ptgs2*, *Cox2m Tlr2, Trem2* and *Tyrobp,* whose expression was upregulated ipsilaterally of PFF

challenged mice. These genes have been associated with neurotoxicity and regulation of phagocytosis (Konishi and Kiyama, 2018). At 90dpi, these mice showed ipsilateral neurodegeneration.

Finally, we wanted to assess the translational relevance of our model. We loaded our data onto the *PD map* (developed at the LCSB). For comparison, we used data from different human studies (Dijkstra et al., 2015; Glaab and Schneider, 2015). We observed several overlapping pathways between the different datasets. Noteworthy are the "neuroinflammation" and "microglial phagocytosis" pathways, which again underline the role of microglia in early PD.

General conclusion and perspectives

The complexity and multi-factorial nature of PD is a continuous challenge in understanding and treating the disease. We showed that the interactions of endogenous and exogenous factors can modulate the progression of the disease and provide an explanation for the heterogeneous disease profiles between PD patients. The different mechanisms identified here and in other studies add on to the complexity, but also provide potential therapeutic target for early treatment of the disease or disease mitigation.

While having provided many new insights on PD pathogenesis in regard of progression profiles, novel disease relevant compound and early disease mechanisms, this PhD project gave rise to several important questions:

- The microbial changes caused by diet are known to influence neuroinflammation. In our study we did not yet answer this question. One might argue that the timepoint is too advanced and that microglia do not show a reactive profile anymore. As seen in our spreading and seeding model, reactive microglia is an early mechanism preceding neurodegeneration. The diet and curli model did report significant neurodegeneration, which would suggest that neuroinflammatory pathways are again downregulated. However, in this model the exposure was chronic and other factors, such as SCFA, besides different αSyn forms could contribute to inflammation. Immunohistochemistry and RNA-seq on nigral tissue could provide insights into other changes aside from αSyn aggregation in the neurodegenerative process and the gene-environment interplay of that model.

- So far we have investigated the short term consequences of 2-HP on different PD pathologies. Neurodegeneration and motor impairment were present in the absence of αSyn inclusions or aggregates. Based on our findings from the seeding/spreading model, neuroinflammation could be underlying driving mechanism. Therefore, one would need to perform an in-depth analysis for different inflammatory markers combined with transcriptomics to capture early events.

  To further investigate if 2-HP triggers αSyn spreading, a longer incubation time could provide more information on how 2-HP acts in a complex in vivo system.

  Additionally, 2-HP levels were different in stool samples of PD/iRBD patients and it is hypothesized to be a product of *Methanobrevibacter* metabolism, which indicates that the site of action is the gut. To test the impact of 2-HP via the enteric route, one could provide animals 2-HP via the drinking water or perform fecal microbiota transplants of patient material enriched in 2-HP in germ-free mice.

- The microbiome and its host have an interdependent functional relationship. Using different approaches such as single-cell or spatio-temporal sequencing could help to look into how microbes interact directly with host cells in the gut. Further, it would be important to take a closer look into the microbial changes in the mucus layer.

PART V

References

1. Abbott, R.D., Ross, G.W., Petrovitch, H., Tanner, C.M., Davis, D.G., Masaki, K.H., Launer, L.J., Curb, J.D., and White, L.R. (2007). Bowel movement frequency in late-life and incidental Lewy bodies. Movement Disorders *22*, 1581–1586. https://doi.org/10.1002/mds.21560.

2. Agim, Z.S., and Cannon, J.R. (2015). Dietary factors in the etiology of Parkinson's disease. Biomed Res Int *2015*, 672838. https://doi.org/10.1155/2015/672838.

3. Alcalay, R.N., Gu, Y., Mejia-Santana, H., Cote, L., Marder, K.S., and Scarmeas, N. (2012). The association between Mediterranean diet adherence and Parkinson's disease. Mov Disord *27*, 771–774. https://doi.org/10.1002/mds.24918.

4. Anderson, J.P., Walker, D.E., Goldstein, J.M., de Laat, R., Banducci, K., Caccavello, R.J., Barbour, R., Huang, J., Kling, K., Lee, M., et al. (2006). Phosphorylation of Ser-129 is the dominant pathological modification of alpha-synuclein in familial and sporadic Lewy body disease. J Biol Chem *281*, 29739–29752. https://doi.org/10.1074/jbc.M600933200.

5. Baizabal-Carvallo, J.F., and Alonso-Juarez, M. (2020). The Link between Gut Dysbiosis and Neuroinflammation in Parkinson's Disease. Neuroscience *432*, 160–173. https://doi.org/10.1016/j.neuroscience.2020.02.030.

6. Bari, B.A., Chokshi, V., and Schmidt, K. (2020). Locus coeruleus-norepinephrine: basic functions and insights into Parkinson's disease. Neural Regeneration Research *15*, 1006. https://doi.org/10.4103/1673-5374.270297.

7. Barichella, M., Severgnini, M., Cilia, R., Cassani, E., Bolliri, C., Caronni, S., Ferri, V., Cancello, R., Ceccarani, C., Faierman, S., et al. (2019). Unraveling gut microbiota in Parkinson's disease and atypical parkinsonism. Movement Disorders *34*, 396–405. https://doi.org/10.1002/mds.27581.

8. Bauckneht, M., Chincarini, A., De Carli, F., Terzaghi, M., Morbelli, S., Nobili, F., and Arnaldi, D. (2018). Presynaptic dopaminergic neuroimaging in REM sleep behavior disorder: A systematic review and meta-analysis. Sleep Med Rev *41*, 266–274. https://doi.org/10.1016/j.smrv.2018.04.001.

9. Bendor, J., Logan, T., and Edwards, R.H. (2013). The Function of α-Synuclein. Neuron *79*, 10.1016/j.neuron.2013.09.004. https://doi.org/10.1016/j.neuron.2013.09.004.

10. Bensaid, M., Michel, P.P., Clark, S.D., Hirsch, E.C., and François, C. (2016). Role of pedunculopontine cholinergic neurons in the vulnerability of nigral dopaminergic neurons in Parkinson's disease. Experimental Neurology *275*, 209–219. https://doi.org/10.1016/j.expneurol.2015.11.004.

11. Berg, G., Rybakova, D., Fischer, D., Cernava, T., Vergès, M.-C.C., Charles, T., Chen, X., Cocolin, L., Eversole, K., Corral, G.H., et al. (2020). Microbiome definition re-visited: old concepts and new challenges. Microbiome *8*, 103. https://doi.org/10.1186/s40168-020-00875-0.

12. Berman, J.J. (2019). Chapter 8 - Changing how we think about infectious diseases. In Taxonomic Guide to Infectious Diseases (Second Edition), J.J. Berman, ed. (Academic Press), pp. 321–365.

13. Bernheimer, H., Birkmayer, W., Hornykiewicz, O., Jellinger, K., and Seitelberger, F. (1973). Brain dopamine and the syndromes of Parkinson and Huntington. Clinical, morphological and neurochemical correlations. J Neurol Sci *20*, 415–455. https://doi.org/10.1016/0022-510x(73)90175-5.

14. Bilbo, S., and Stevens, B. (2017). Microglia: The Brain's First Responders. Cerebrum *2017*, cer-14-17. .

15. Boertien, J.M., Pereira, P.A.B., Aho, V.T.E., and Scheperjans, F. (2019). Increasing Comparability and Utility of Gut Microbiome Studies in Parkinson's Disease: A Systematic Review. Journal of Parkinson's Disease *9*, S297–S312. https://doi.org/10.3233/JPD-191711.

16. Boka, G., Anglade, P., Wallach, D., Javoy-Agid, F., Agid, Y., and Hirsch, E.C. (1994). Immunocytochemical analysis of tumor necrosis factor and its receptors in Parkinson's disease. Neurosci Lett *172*, 151–154. https://doi.org/10.1016/0304-3940(94)90684-x.

17. Borghammer, P., and Van Den Berge, N. (2019). Brain-First versus Gut-First Parkinson's Disease: A Hypothesis. J Parkinsons Dis *9*, S281–S295. https://doi.org/10.3233/JPD-191721.

18. Braak, H., and Del Tredici, K. (2017). Neuropathological Staging of Brain Pathology in Sporadic Parkinson's disease: Separating the Wheat from the Chaff. Journal of Parkinson's Disease *7*, S71–S85. https://doi.org/10.3233/JPD-179001.

19. Braak, H., Tredici, K.D., Rüb, U., de Vos, R.A.I., Jansen Steur, E.N.H., and Braak, E. (2003a). Staging of brain pathology related to sporadic Parkinson's disease. Neurobiology of Aging *24*, 197–211. https://doi.org/10.1016/S0197-4580(02)00065-9.

20. Braak, H., Rüb, U., Gai, W.P., and Del Tredici, K. (2003b). Idiopathic Parkinson's disease: possible routes by which vulnerable neuronal types may be subject to neuroinvasion by an unknown pathogen. J Neural Transm (Vienna) *110*, 517–536. https://doi.org/10.1007/s00702-002-0808-2.

21. Braak, H., de Vos, R.A.I., Bohl, J., and Del Tredici, K. (2006). Gastric alpha-synuclein immunoreactive inclusions in Meissner's and Auerbach's plexuses in cases staged for Parkinson's disease-related brain pathology. Neurosci. Lett. *396*, 67–72. https://doi.org/10.1016/j.neulet.2005.11.012.

22. Brodacki, B., Staszewski, J., Toczyłowska, B., Kozłowska, E., Drela, N., Chalimoniuk, M., and Stepien, A. (2008). Serum interleukin (IL-2, IL-10, IL-6, IL-4), TNFalpha, and INFgamma concentrations are elevated in patients with atypical and idiopathic

parkinsonism. Neurosci Lett *441*, 158–162. https://doi.org/10.1016/j.neulet.2008.06.040.

23. Brundin, P., Melki, R., and Kopito, R. (2010). Prion-like transmission of protein aggregates in neurodegenerative diseases. Nat Rev Mol Cell Biol *11*, 301–307. https://doi.org/10.1038/nrm2873.

24. Chambers, N.E., Lanza, K., and Bishop, C. (2020). Pedunculopontine Nucleus Degeneration Contributes to Both Motor and Non-Motor Symptoms of Parkinson's Disease. Frontiers in Pharmacology *10*. .

25. Chapman, M.R., Robinson, L.S., Pinkner, J.S., Roth, R., Heuser, J., Hammar, M., Normark, S., and Hultgren, S.J. (2002). Role of Escherichia coli curli operons in directing amyloid fiber formation. Science *295*, 851–855. https://doi.org/10.1126/science.1067484.

26. Chen, S.G., Stribinskis, V., Rane, M.J., Demuth, D.R., Gozal, E., Roberts, A.M., Jagadapillai, R., Liu, R., Choe, K., Shivakumar, B., et al. (2016). Exposure to the Functional Bacterial Amyloid Protein Curli Enhances Alpha-Synuclein Aggregation in Aged Fischer 344 Rats and Caenorhabditis elegans. Sci Rep *6*, 1–10. https://doi.org/10.1038/srep34477.

27. Cheng, H.-C., Ulane, C.M., and Burke, R.E. (2010). Clinical Progression in Parkinson's Disease and the Neurobiology of Axons. Ann Neurol *67*, 715–725. https://doi.org/10.1002/ana.21995.

28. Chermenina, M., Chorell, E., Pokrzywa, M., Antti, H., Almqvist, F., Strömberg, I., and Wittung-Stafshede, P. (2015). Single injection of small-molecule amyloid accelerator results in cell death of nigral dopamine neurons in mice. NPJ Parkinsons Dis *1*, 15024. https://doi.org/10.1038/npjparkd.2015.24.

29. Chu, Y., Muller, S., Tavares, A., Barret, O., Alagille, D., Seibyl, J., Tamagnan, G., Marek, K., Luk, K.C., Trojanowski, J.Q., et al. (2019). Intrastriatal alpha-synuclein fibrils in monkeys: spreading, imaging and neuropathological changes. Brain *142*, 3565–3579. https://doi.org/10.1093/brain/awz296.

30. Coon, E.A., and Singer, W. (2020). Synucleinopathies. Continuum (Minneap Minn) *26*, 72–92. https://doi.org/10.1212/CON.0000000000000819.

31. Cotillard, A., Kennedy, S.P., Kong, L.C., Prifti, E., Pons, N., Le Chatelier, E., Almeida, M., Quinquis, B., Levenez, F., Galleron, N., et al. (2013). Dietary intervention impact on gut microbial gene richness. Nature *500*, 585–588. https://doi.org/10.1038/nature12480.

32. Croisier, E., Moran, L.B., Dexter, D.T., Pearce, R.K., and Graeber, M.B. (2005). Microglial inflammation in the parkinsonian substantia nigra: relationship to alpha-synuclein deposition. Journal of Neuroinflammation *2*, 14. https://doi.org/10.1186/1742-2094-2-14.

33. Danzer, K.M., Ruf, W.P., Putcha, P., Joyner, D., Hashimoto, T., Glabe, C., Hyman, B.T., and McLean, P.J. (2011). Heat-shock protein 70 modulates toxic extracellular α-synuclein oligomers and rescues trans-synaptic toxicity. FASEB J *25*, 326–336. https://doi.org/10.1096/fj.10-164624.

34. Del Tredici, K., Rüb, U., de Vos, R.A.I., Bohl, J.R.E., and Braak, H. (2002). Where Does Parkinson Disease Pathology Begin in the Brain? Journal of Neuropathology & Experimental Neurology *61*, 413–426. https://doi.org/10.1093/jnen/61.5.413.

35. Desai, M.S., Seekatz, A.M., Koropatkin, N.M., Kamada, N., Hickey, C.A., Wolter, M., Pudlo, N.A., Kitamoto, S., Terrapon, N., Muller, A., et al. (2016). A dietary fiber-deprived gut microbiota degrades the colonic mucus barrier and enhances pathogen susceptibility. Cell *167*, 1339-1353.e21. https://doi.org/10.1016/j.cell.2016.10.043.

36. Dijkstra, A.A., Voorn, P., Berendse, H.W., Groenewegen, H.J., Netherlands Brain Bank, Rozemuller, A.J.M., and van de Berg, W.D.J. (2014). Stage-dependent nigral neuronal loss in incidental Lewy body and Parkinson's disease. Mov Disord *29*, 1244–1251. https://doi.org/10.1002/mds.25952.

37. Dijkstra, A.A., Ingrassia, A., de Menezes, R.X., van Kesteren, R.E., Rozemuller, A.J.M., Heutink, P., and van de Berg, W.D.J. (2015). Evidence for Immune Response, Axonal Dysfunction and Reduced Endocytosis in the Substantia Nigra in Early Stage Parkinson's Disease. PLoS One *10*, e0128651. https://doi.org/10.1371/journal.pone.0128651.

38. Duffy, M.F., Collier, T.J., Patterson, J.R., Kemp, C.J., Luk, K.C., Tansey, M.G., Paumier, K.L., Kanaan, N.M., Fischer, D.L., Polinski, N.K., et al. (2018). Lewy body-like alpha-synuclein inclusions trigger reactive microgliosis prior to nigral degeneration. J Neuroinflammation *15*, 129. https://doi.org/10.1186/s12974-018-1171-z.

39. Ehringer, H., and Hornykiewicz, O. (1960). [Distribution of noradrenaline and dopamine (3-hydroxytyramine) in the human brain and their behavior in diseases of the extrapyramidal system]. Klin Wochenschr *38*, 1236–1239. https://doi.org/10.1007/BF01485901.

40. Ellis, J.M., and Fell, M.J. (2017). Current approaches to the treatment of Parkinson's Disease. Bioorganic & Medicinal Chemistry Letters *27*, 4247–4255. https://doi.org/10.1016/j.bmcl.2017.07.075.

41. Emamzadeh, F.N. (2016). Alpha-synuclein structure, functions, and interactions. J Res Med Sci *21*, 29. https://doi.org/10.4103/1735-1995.181989.

42. Emmanouilidou, E., Melachroinou, K., Roumeliotis, T., Garbis, S.D., Ntzouni, M., Margaritis, L.H., Stefanis, L., and Vekrellis, K. (2010). Cell-Produced α-Synuclein Is Secreted in a Calcium-Dependent Manner by Exosomes and Impacts Neuronal Survival. J Neurosci *30*, 6838–6851. https://doi.org/10.1523/JNEUROSCI.5699-09.2010.

43. Erro, R., Brigo, F., Tamburin, S., Zamboni, M., Antonini, A., and Tinazzi, M. (2018). Nutritional habits, risk, and progression of Parkinson disease. J Neurol *265*, 12–23. https://doi.org/10.1007/s00415-017-8639-0.

44. Espay, A.J., and Marras, C. (2019). Clinical Parkinson disease subtyping does not predict pathology. Nat Rev Neurol *15*, 189–190. https://doi.org/10.1038/s41582-019-0153-9.

45. Fearnley, J.M., and Lees, A.J. (1991). Ageing and Parkinson's disease: substantia nigra regional selectivity. Brain *114 (Pt 5)*, 2283–2301. https://doi.org/10.1093/brain/114.5.2283.

46. Fellner, L., Irschick, R., Schanda, K., Reindl, M., Klimaschewski, L., Poewe, W., Wenning, G.K., and Stefanova, N. (2013). Toll-like receptor 4 is required for α-synuclein dependent activation of microglia and astroglia. Glia *61*, 349–360. https://doi.org/10.1002/glia.22437.

47. Fields, C.R., Bengoa-Vergniory, N., and Wade-Martins, R. (2019). Targeting Alpha-Synuclein as a Therapy for Parkinson's Disease. Front Mol Neurosci *12*, 299. https://doi.org/10.3389/fnmol.2019.00299.

48. Frank, D.N., St. Amand, A.L., Feldman, R.A., Boedeker, E.C., Harpaz, N., and Pace, N.R. (2007). Molecular-phylogenetic characterization of microbial community imbalances in human inflammatory bowel diseases. Proc Natl Acad Sci U S A *104*, 13780–13785. https://doi.org/10.1073/pnas.0706625104.

49. Freire, C., and Koifman, S. (2012). Pesticide exposure and Parkinson's disease: epidemiological evidence of association. Neurotoxicology *33*, 947–971. https://doi.org/10.1016/j.neuro.2012.05.011.

50. French, I.T., and Muthusamy, K.A. (2018). A Review of the Pedunculopontine Nucleus in Parkinson's Disease. Frontiers in Aging Neuroscience *10*. .

51. Garcia, P., Jürgens-Wemheuer, W., Uriarte Huarte, O., Michelucci, A., Masuch, A., Brioschi, S., Weihofen, A., Koncina, E., Coowar, D., Heurtaux, T., et al. (2022). Neurodegeneration and neuroinflammation are linked, but independent of alpha-synuclein inclusions, in a seeding/spreading mouse model of Parkinson's disease. Glia https://doi.org/10.1002/glia.24149.

52. George, J.M. (2002). The synucleins. Genome Biol *3*, reviews3002.1-reviews3002.6. .

53. Giguère, N., Burke Nanni, S., and Trudeau, L.-E. (2018). On Cell Loss and Selective Vulnerability of Neuronal Populations in Parkinson's Disease. Front Neurol *9*, 455. https://doi.org/10.3389/fneur.2018.00455.

54. Glaab, E., and Schneider, R. (2015). Comparative pathway and network analysis of brain transcriptome changes during adult aging and in Parkinson's disease. Neurobiol Dis *74*, 1–13. https://doi.org/10.1016/j.nbd.2014.11.002.

55. Goedert, M., Spillantini, M.G., Del Tredici, K., and Braak, H. (2013). 100 years of Lewy pathology. Nat Rev Neurol *9*, 13–24. https://doi.org/10.1038/nrneurol.2012.242.

56. Goetz, C.G., Tilley, B.C., Shaftman, S.R., Stebbins, G.T., Fahn, S., Martinez-Martin, P., Poewe, W., Sampaio, C., Stern, M.B., Dodel, R., et al. (2008). Movement Disorder Society-sponsored revision of the Unified Parkinson's Disease Rating Scale (MDS-UPDRS): Scale presentation and clinimetric testing results. Movement Disorders *23*, 2129–2170. https://doi.org/10.1002/mds.22340.

57. Greffard, S., Verny, M., Bonnet, A.-M., Beinis, J.-Y., Gallinari, C., Meaume, S., Piette, F., Hauw, J.-J., and Duyckaerts, C. (2006). Motor Score of the Unified Parkinson Disease Rating Scale as a Good Predictor of Lewy Body–Associated Neuronal Loss in the Substantia Nigra. Archives of Neurology *63*, 584–588. https://doi.org/10.1001/archneur.63.4.584.

58. Hazards (BIOHAZ), E.P. on B., Koutsoumanis, K., Allende, A., Alvarez-Ordóñez, A., Bolton, D., Bover-Cid, S., Chemaly, M., Davies, R., De Cesare, A., Hilbert, F., et al. (2020). Update of the list of QPS-recommended biological agents intentionally added to food or feed as notified to EFSA 12: suitability of taxonomic units notified to EFSA until March 2020. EFSA Journal *18*, e06174. https://doi.org/10.2903/j.efsa.2020.6174.

59. Hilton, D., Stephens, M., Kirk, L., Edwards, P., Potter, R., Zajicek, J., Broughton, E., Hagan, H., and Carroll, C. (2014). Accumulation of α-synuclein in the bowel of patients in the pre-clinical phase of Parkinson's disease. Acta Neuropathol *127*, 235–241. https://doi.org/10.1007/s00401-013-1214-6.

60. Hirsch, E.C., Graybiel, A.M., Duyckaerts, C., and Javoy-Agid, F. (1987). Neuronal loss in the pedunculopontine tegmental nucleus in Parkinson disease and in progressive supranuclear palsy. Proc Natl Acad Sci U S A *84*, 5976–5980. https://doi.org/10.1073/pnas.84.16.5976.

61. Hirsch, E.C., Jenner, P., and Przedborski, S. (2013). Pathogenesis of Parkinson's disease. Movement Disorders *28*, 24–30. https://doi.org/10.1002/mds.25032.

62. Hopkins, D.A., Bieger, D., deVente, J., and Steinbusch, W.M. (1996). Vagal efferent projections: viscerotopy, neurochemistry and effects of vagotomy. Prog Brain Res *107*, 79–96. https://doi.org/10.1016/s0079-6123(08)61859-2.

63. Hornykiewicz, O. (1998). Biochemical aspects of Parkinson's disease. Neurology *51*, S2-9. https://doi.org/10.1212/wnl.51.2_suppl_2.s2.

64. Horsager, J., Andersen, K.B., Knudsen, K., Skjærbæk, C., Fedorova, T.D., Okkels, N., Schaeffer, E., Bonkat, S.K., Geday, J., Otto, M., et al. (2020). Brain-first versus body-first Parkinson's disease: a multimodal imaging case-control study. Brain *143*, 3077–3088. https://doi.org/10.1093/brain/awaa238.

65. Horvath, I., Weise, C.F., Andersson, E.K., Chorell, E., Sellstedt, M., Bengtsson, C., Olofsson, A., Hultgren, S.J., Chapman, M., Wolf-Watz, M., et al. (2012). Mechanisms of protein oligomerization: inhibitor of functional amyloids templates α-synuclein fibrillation. J Am Chem Soc *134*, 3439–3444. https://doi.org/10.1021/ja209829m.

66. Hou, K., Wu, Z.-X., Chen, X.-Y., Wang, J.-Q., Zhang, D., Xiao, C., Zhu, D., Koya, J.B., Wei, L., Li, J., et al. (2022). Microbiota in health and diseases. Sig Transduct Target Ther *7*, 1–28. https://doi.org/10.1038/s41392-022-00974-4.

67. Hughes, A.J., Daniel, S.E., Kilford, L., and Lees, A.J. (1992). Accuracy of clinical diagnosis of idiopathic Parkinson's disease: a clinico-pathological study of 100 cases. J Neurol Neurosurg Psychiatry *55*, 181–184. https://doi.org/10.1136/jnnp.55.3.181.

68. Hunot, S., Dugas, N., Faucheux, B., Hartmann, A., Tardieu, M., Debré, P., Agid, Y., Dugas, B., and Hirsch, E.C. (1999). FcepsilonRII/CD23 is expressed in Parkinson's disease and induces, in vitro, production of nitric oxide and tumor necrosis factor-alpha in glial cells. J Neurosci *19*, 3440–3447. .

69. Ichikawa, T., Ajiki, K., Matsuura, J., and Misawa, H. (1997). Localization of two cholinergic markers, choline acetyltransferase and vesicular acetylcholine transporter in the central nervous system of the rat: in situ hybridization histochemistry and immunohistochemistry. Journal of Chemical Neuroanatomy *13*, 23–39. https://doi.org/10.1016/S0891-0618(97)00021-5.

70. Imamura, K., Hishikawa, N., Sawada, M., Nagatsu, T., Yoshida, M., and Hashizume, Y. (2003). Distribution of major histocompatibility complex class II-positive microglia and cytokine profile of Parkinson's disease brains. Acta Neuropathol *106*, 518–526. https://doi.org/10.1007/s00401-003-0766-2.

71. Janda, E., Boi, L., and Carta, A.R. (2018). Microglial Phagocytosis and Its Regulation: A Therapeutic Target in Parkinson's Disease? Frontiers in Molecular Neuroscience *11*. .

72. Jankovic, J., McDermott, M., Carter, J., Gauthier, S., Goetz, C., Golbe, L., Huber, S., Koller, W., Olanow, C., and Shoulson, I. (1990). Variable expression of Parkinson's disease: a base-line analysis of the DATATOP cohort. The Parkinson Study Group. Neurology *40*, 1529–1534. https://doi.org/10.1212/wnl.40.10.1529.

73. Jao, C.C., Hegde, B.G., Chen, J., Haworth, I.S., and Langen, R. (2008). Structure of membrane-bound alpha-synuclein from site-directed spin labeling and computational refinement. Proc Natl Acad Sci U S A *105*, 19666–19671. https://doi.org/10.1073/pnas.0807826105.

74. Jellinger, K. (1988). The pedunculopontine nucleus in Parkinson's disease, progressive supranuclear palsy and Alzheimer's disease. J Neurol Neurosurg Psychiatry *51*, 540–543. .

75. Jellinger, K.A. (2009). A critical evaluation of current staging of α-synuclein pathology in Lewy body disorders. Biochimica et Biophysica Acta (BBA) - Molecular Basis of Disease *1792*, 730–740. https://doi.org/10.1016/j.bbadis.2008.07.006.

76. Johansson, M.E.V., Larsson, J.M.H., and Hansson, G.C. (2011). The two mucus layers of colon are organized by the MUC2 mucin, whereas the outer layer is a legislator of host–microbial interactions. PNAS *108*, 4659–4665. https://doi.org/10.1073/pnas.1006451107.

77. Jones, B.E., and Yang, T.-Z. (1985). The efferent projections from the reticular formation and the locus coeruleus studied by anterograde and retrograde axonal transport in the rat. Journal of Comparative Neurology *242*, 56–92. https://doi.org/10.1002/cne.902420105.

78. Jovel, J., Dieleman, L.A., Kao, D., Mason, A.L., and Wine, E. (2018). Chapter 10 - The Human Gut Microbiome in Health and Disease. In Metagenomics, M. Nagarajan, ed. (Academic Press), pp. 197–213.

79. Jucker, M., and Walker, L.C. (2018). Propagation and spread of pathogenic protein assemblies in neurodegenerative diseases. Nat Neurosci *21*, 1341–1349. https://doi.org/10.1038/s41593-018-0238-6.

80. Kalaitzakis, M.E., Graeber, M.B., Gentleman, S.M., and Pearce, R.K.B. (2008). The dorsal motor nucleus of the vagus is not an obligatory trigger site of Parkinson's disease: a critical analysis of alpha-synuclein staging. Neuropathol Appl Neurobiol *34*, 284–295. https://doi.org/10.1111/j.1365-2990.2007.00923.x.

81. Kalia, L.V., and Lang, A.E. (2015). Parkinson's disease. The Lancet *386*, 896–912. https://doi.org/10.1016/S0140-6736(14)61393-3.

82. Kelly, R., Cairns, A.G., Ådén, J., Almqvist, F., Bemelmans, A.-P., Brouillet, E., Patton, T., McKernan, D.P., and Dowd, E. (2021). The Small Molecule Alpha-Synuclein Aggregator, FN075, Enhances Alpha-Synuclein Pathology in Subclinical AAV Rat Models. Biomolecules *11*, 1685. https://doi.org/10.3390/biom11111685.

83. Keshavarzian, A., Engen, P., Bonvegna, S., and Cilia, R. (2020). The gut microbiome in Parkinson's disease: A culprit or a bystander? Prog Brain Res *252*, 357–450. https://doi.org/10.1016/bs.pbr.2020.01.004.

84. van Kessel, S.P., Frye, A.K., El-Gendy, A.O., Castejon, M., Keshavarzian, A., van Dijk, G., and El Aidy, S. (2019). Gut bacterial tyrosine decarboxylases restrict levels of levodopa in the treatment of Parkinson's disease. Nat Commun *10*, 310. https://doi.org/10.1038/s41467-019-08294-y.

85. Kim, C., Ho, D.-H., Suk, J.-E., You, S., Michael, S., Kang, J., Joong Lee, S., Masliah, E., Hwang, D., Lee, H.-J., et al. (2013). Neuron-released oligomeric α-synuclein is an endogenous agonist of TLR2 for paracrine activation of microglia. Nat Commun *4*, 1562. https://doi.org/10.1038/ncomms2534.

86. Kim, S., Kwon, S.-H., Kam, T.-I., Panicker, N., Karuppagounder, S.S., Lee, S., Lee, J.H., Kim, W.R., Kook, M., Foss, C.A., et al. (2019). Transneuronal Propagation of Pathologic α-Synuclein from the Gut to the Brain Models Parkinson's Disease. Neuron *103*, 627-641.e7. https://doi.org/10.1016/j.neuron.2019.05.035.

87. Klingelhoefer, L., and Reichmann, H. (2015). Pathogenesis of Parkinson disease—the gut–brain axis and environmental factors. Nature Reviews Neurology *11*, 625–636. https://doi.org/10.1038/nrneurol.2015.197.

88. Knudsen, K., Fedorova, T.D., Hansen, A.K., Sommerauer, M., Otto, M., Svendsen, K.B., Nahimi, A., Stokholm, M.G., Pavese, N., Beier, C.P., et al. (2018). In-vivo staging of pathology in REM sleep behaviour disorder: a multimodality imaging case-control study. The Lancet. Neurology *17*. https://doi.org/10.1016/S1474-4422(18)30162-5.

89. Konishi, H., and Kiyama, H. (2018). Microglial TREM2/DAP12 Signaling: A Double-Edged Sword in Neural Diseases. Frontiers in Cellular Neuroscience *12*. .

90. Kordower, J.H., Freeman, T.B., and Olanow, C.W. (1998). Neuropathology of fetal nigral grafts in patients with Parkinson's disease. Mov Disord *13 Suppl 1*, 88–95. .

91. Kordower, J.H., Chu, Y., Hauser, R.A., Freeman, T.B., and Olanow, C.W. (2008). Lewy body–like pathology in long-term embryonic nigral transplants in Parkinson's disease. Nat Med *14*, 504–506. https://doi.org/10.1038/nm1747.

92. Kroeger, D., Ferrari, L.L., Petit, G., Mahoney, C.E., Fuller, P.M., Arrigoni, E., and Scammell, T.E. (2017). Cholinergic, Glutamatergic, and GABAergic Neurons of the Pedunculopontine Tegmental Nucleus Have Distinct Effects on Sleep/Wake Behavior in Mice. J. Neurosci. *37*, 1352–1366. https://doi.org/10.1523/JNEUROSCI.1405-16.2016.

93. Lai, F., Jiang, R., Xie, W., Liu, X., Tang, Y., Xiao, H., Gao, J., Jia, Y., and Bai, Q. (2018). Intestinal Pathology and Gut Microbiota Alterations in a Methyl-4-phenyl-1,2,3,6-tetrahydropyridine (MPTP) Mouse Model of Parkinson's Disease. Neurochem Res *43*, 1986–1999. https://doi.org/10.1007/s11064-018-2620-x.

94. Lashuel, H.A., Overk, C.R., Oueslati, A., and Masliah, E. (2013). The many faces of α-synuclein: from structure and toxicity to therapeutic target. Nat Rev Neurosci *14*, 38–48. https://doi.org/10.1038/nrn3406.

95. Leclair-Visonneau, L., Clairembault, T., Coron, E., Le Dily, S., Vavasseur, F., Dalichampt, M., Péréon, Y., Neunlist, M., and Derkinderen, P. (2017). REM sleep behavior disorder is related to enteric neuropathology in Parkinson disease. Neurology *89*, 1612–1618. https://doi.org/10.1212/WNL.0000000000004496.

96. Lee, H.-J., Suk, J.-E., Bae, E.-J., Lee, J.-H., Paik, S.R., and Lee, S.-J. (2008). Assembly-dependent endocytosis and clearance of extracellular alpha-synuclein. Int J Biochem Cell Biol *40*, 1835–1849. https://doi.org/10.1016/j.biocel.2008.01.017.

97. Li, C., Cui, L., Yang, Y., Miao, J., Zhao, X., Zhang, J., Cui, G., and Zhang, Y. (2019). Gut Microbiota Differs Between Parkinson's Disease Patients and Healthy Controls in Northeast China. Front Mol Neurosci *12*, 171. https://doi.org/10.3389/fnmol.2019.00171.

98. Li, J.-Y., Englund, E., Holton, J.L., Soulet, D., Hagell, P., Lees, A.J., Lashley, T., Quinn, N.P., Rehncrona, S., Björklund, A., et al. (2008). Lewy bodies in grafted neurons in subjects with Parkinson's disease suggest host-to-graft disease propagation. Nat Med *14*, 501–503. https://doi.org/10.1038/nm1746.

99. Li, W., Wu, X., Hu, X., Wang, T., Liang, S., Duan, Y., Jin, F., and Qin, B. (2017). Structural changes of gut microbiota in Parkinson's disease and its correlation with clinical features. Sci. China Life Sci. *60*, 1223–1233. https://doi.org/10.1007/s11427-016-9001-4.

100. Lindqvist, D., Hall, S., Surova, Y., Nielsen, H.M., Janelidze, S., Brundin, L., and Hansson, O. (2013). Cerebrospinal fluid inflammatory markers in Parkinson's disease--associations with depression, fatigue, and cognitive impairment. Brain Behav Immun *33*, 183–189. https://doi.org/10.1016/j.bbi.2013.07.007.

101. Lionnet, A., Leclair-Visonneau, L., Neunlist, M., Murayama, S., Takao, M., Adler, C.H., Derkinderen, P., and Beach, T.G. (2018). Does Parkinson's disease start in the gut? Acta Neuropathol *135*, 1–12. https://doi.org/10.1007/s00401-017-1777-8.

102. Liu, B., Fang, F., Pedersen, N.L., Tillander, A., Ludvigsson, J.F., Ekbom, A., Svenningsson, P., Chen, H., and Wirdefeldt, K. (2017). Vagotomy and Parkinson disease. Neurology *88*, 1996–2002. https://doi.org/10.1212/WNL.0000000000003961.

103. Lubomski, M., Xu, X., Holmes, A.J., Muller, S., Yang, J.Y.H., Davis, R.L., and Sue, C.M. (2022). The Gut Microbiome in Parkinson's Disease: A Longitudinal Study of the Impacts on Disease Progression and the Use of Device-Assisted Therapies. Frontiers in Aging Neuroscience *14*. .

104. Luk, K.C., Kehm, V., Carroll, J., Zhang, B., O'Brien, P., Trojanowski, J.Q., and Lee, V.M.-Y. (2012). Pathological α-synuclein transmission initiates Parkinson-like neurodegeneration in nontransgenic mice. Science *338*, 949–953. https://doi.org/10.1126/science.1227157.

105. Luna, E., and Luk, K.C. (2015). Bent out of shape: α-Synuclein misfolding and the convergence of pathogenic pathways in Parkinson's disease. FEBS Letters *589*, 3749–3759. https://doi.org/10.1016/j.febslet.2015.10.023.

106. MacLaren, D.A.A., Ljungberg, T.L., Griffin, M.E., and Clark, S.D. (2018). Pedunculopontine tegmentum cholinergic loss leads to a progressive decline in motor abilities and neuropathological changes resembling progressive supranuclear palsy. European Journal of Neuroscience *48*, 3477–3497. https://doi.org/10.1111/ejn.14212.

107. Maini Rekdal, V., Bess, E.N., Bisanz, J.E., Turnbaugh, P.J., and Balskus, E.P. (2019). Discovery and inhibition of an interspecies gut bacterial pathway for Levodopa metabolism. Science *364*, eaau6323. https://doi.org/10.1126/science.aau6323.

108. Marsili, L., Rizzo, G., and Colosimo, C. (2018). Diagnostic Criteria for Parkinson's Disease: From James Parkinson to the Concept of Prodromal Disease. Frontiers in Neurology *9*. .

109. Martens, E.C., Chiang, H.C., and Gordon, J.I. (2008). Mucosal Glycan Foraging Enhances Fitness and Transmission of a Saccharolytic Human Gut Bacterial Symbiont. Cell Host Microbe *4*, 447–457. https://doi.org/10.1016/j.chom.2008.09.007.

110. Martinez-Gonzalez, C., Bolam, J.P., and Mena-Segovia, J. (2011). Topographical Organization of the Pedunculopontine Nucleus. Front Neuroanat *5*, 22. https://doi.org/10.3389/fnana.2011.00022.

111. McGeer, P.L., Itagaki, S., Boyes, B.E., and McGeer, E.G. (1988). Reactive microglia are positive for HLA-DR in the substantia nigra of Parkinson's and Alzheimer's disease brains. Neurology *38*, 1285–1291. https://doi.org/10.1212/wnl.38.8.1285.

112. Mischley, L.K., Lau, R.C., and Bennett, R.D. (2017). Role of Diet and Nutritional Supplements in Parkinson's Disease Progression. Oxid Med Cell Longev *2017*. https://doi.org/10.1155/2017/6405278.

113. Mogi, M., Harada, M., Kondo, T., Riederer, P., Inagaki, H., Minami, M., and Nagatsu, T. (1994). Interleukin-1 beta, interleukin-6, epidermal growth factor and transforming growth factor-alpha are elevated in the brain from parkinsonian patients. Neurosci Lett *180*, 147–150. https://doi.org/10.1016/0304-3940(94)90508-8.

114. Neumann, M., Steimle, A., Grant, E.T., Wolter, M., Parrish, A., Willieme, S., Brenner, D., Martens, E.C., and Desai, M.S. (2021). Deprivation of dietary fiber in specific-pathogen-free mice promotes susceptibility to the intestinal mucosal pathogen Citrobacter rodentium. Gut Microbes *13*, 1966263. https://doi.org/10.1080/19490976.2021.1966263.

115. Oertel, W.H., Henrich, M.T., Janzen, A., and Geibl, F.F. (2019). The locus coeruleus: Another vulnerability target in Parkinson's disease. Mov Disord *34*, 1423–1429. https://doi.org/10.1002/mds.27785.

116. O'Keefe, S.J. (2019a). The association between dietary fiber deficiency and high-income lifestyle-associated diseases: Burkitt's hypothesis revisited. Lancet Gastroenterol Hepatol *4*, 984–996. https://doi.org/10.1016/S2468-1253(19)30257-2.

117. O'Keefe, S.J.D. (2019b). Plant-based foods and the microbiome in the preservation of health and prevention of disease. Am J Clin Nutr *110*, 265–266. https://doi.org/10.1093/ajcn/nqz127.

118. Pahapill, P.A., and Lozano, A.M. (2000). The pedunculopontine nucleus and Parkinson's disease. Brain *123 (Pt 9)*, 1767–1783. https://doi.org/10.1093/brain/123.9.1767.

119. Pan-Montojo, F., Anichtchik, O., Dening, Y., Knels, L., Pursche, S., Jung, R., Jackson, S., Gille, G., Spillantini, M.G., Reichmann, H., et al. (2010). Progression of Parkinson's Disease Pathology Is Reproduced by Intragastric Administration of Rotenone in Mice. PLOS ONE *5*, e8762. https://doi.org/10.1371/journal.pone.0008762.

120. Pan-Montojo, F., Schwarz, M., Winkler, C., Arnhold, M., O'Sullivan, G.A., Pal, A., Said, J., Marsico, G., Verbavatz, J.-M., Rodrigo-Angulo, M., et al. (2012). Environmental toxins trigger PD-like progression via increased alpha-synuclein release from enteric neurons in mice. Sci Rep *2*, 898. https://doi.org/10.1038/srep00898.

121. Parent, M., and Parent, A. (2010). Substantia nigra and Parkinson's disease: a brief history of their long and intimate relationship. Can J Neurol Sci *37*, 313–319. https://doi.org/10.1017/s0317167100010209.

122. Parkinson, J. (1817). An Essay on the Shaking Palsy. Neely and Jones, London.

123. Periquet, M., Fulga, T., Myllykangas, L., Schlossmacher, M.G., and Feany, M.B. (2007). Aggregated alpha-synuclein mediates dopaminergic neurotoxicity in vivo. J Neurosci *27*, 3338–3346. https://doi.org/10.1523/JNEUROSCI.0285-07.2007.

124. Poewe, W. (2008). Non-motor symptoms in Parkinson's disease. European Journal of Neurology *15*, 14–20. https://doi.org/10.1111/j.1468-1331.2008.02056.x.

125. Poewe, W., Seppi, K., Tanner, C.M., Halliday, G.M., Brundin, P., Volkmann, J., Schrag, A.-E., and Lang, A.E. (2017). Parkinson disease. Nat Rev Dis Primers *3*, 1–21. https://doi.org/10.1038/nrdp.2017.13.

126. Prusiner, S.B. (1991). Molecular biology of prion diseases. Science *252*, 1515–1522. https://doi.org/10.1126/science.1675487.

127. Rampelli, S., Schnorr, S.L., Consolandi, C., Turroni, S., Severgnini, M., Peano, C., Brigidi, P., Crittenden, A.N., Henry, A.G., and Candela, M. (2015). Metagenome Sequencing of the Hadza Hunter-Gatherer Gut Microbiota. Current Biology *25*, 1682–1693. https://doi.org/10.1016/j.cub.2015.04.055.

128. Ransohoff, R.M. (2016). A polarizing question: do M1 and M2 microglia exist? Nat Neurosci *19*, 987–991. https://doi.org/10.1038/nn.4338.

129. Ransohoff, R.M., and El Khoury, J. (2015). Microglia in Health and Disease. Cold Spring Harb Perspect Biol *8*, a020560. https://doi.org/10.1101/cshperspect.a020560.

130. Ransohoff, R.M., Schafer, D., Vincent, A., Blachère, N.E., and Bar-Or, A. (2015). Neuroinflammation: Ways in Which the Immune System Affects the Brain. Neurotherapeutics *12*, 896–909. https://doi.org/10.1007/s13311-015-0385-3.

131. Rey, N.L., Steiner, J.A., Maroof, N., Luk, K.C., Madaj, Z., Trojanowski, J.Q., Lee, V.M.-Y., and Brundin, P. (2016). Widespread transneuronal propagation of α-synucleinopathy triggered in olfactory bulb mimics prodromal Parkinson's disease. Journal of Experimental Medicine *213*, 1759–1778. https://doi.org/10.1084/jem.20160368.

132. Riva, A., Kuzyk, O., Forsberg, E., Siuzdak, G., Pfann, C., Herbold, C., Daims, H., Loy, A., Warth, B., and Berry, D. (2019). A fiber-deprived diet disturbs the fine-scale spatial architecture of the murine colon microbiome. Nat Commun *10*, 4366. https://doi.org/10.1038/s41467-019-12413-0.

133. Romano, S., Savva, G.M., Bedarf, J.R., Charles, I.G., Hildebrand, F., and Narbad, A. (2021). Meta-analysis of the Parkinson's disease gut microbiome suggests alterations linked to intestinal inflammation. Npj Parkinsons Dis. *7*, 1–13. https://doi.org/10.1038/s41531-021-00156-z.

134. Sampson, T.R., Debelius, J.W., Thron, T., Janssen, S., Shastri, G.G., Ilhan, Z.E., Challis, C., Schretter, C.E., Rocha, S., Gradinaru, V., et al. (2016). Gut Microbiota Regulate Motor Deficits and Neuroinflammation in a Model of Parkinson's Disease. Cell *167*, 1469-1480.e12. https://doi.org/10.1016/j.cell.2016.11.018.

135. Sampson, T.R., Challis, C., Jain, N., Moiseyenko, A., Ladinsky, M.S., Shastri, G.G., Thron, T., Needham, B.D., Horvath, I., Debelius, J.W., et al. (2020). A gut bacterial amyloid promotes α-synuclein aggregation and motor impairment in mice. ELife *9*, e53111. https://doi.org/10.7554/eLife.53111.

136. Scheperjans, F., Aho, V., Pereira, P.A.B., Koskinen, K., Paulin, L., Pekkonen, E., Haapaniemi, E., Kaakkola, S., Eerola-Rautio, J., Pohja, M., et al. (2015). Gut microbiota are related to Parkinson's disease and clinical phenotype. Movement Disorders *30*, 350–358. https://doi.org/10.1002/mds.26069.

137. Schmidt, K., Bari, B., Ralle, M., Washington-Hughes, C., Muchenditsi, A., Maxey, E., and Lutsenko, S. (2019). Localization of the Locus Coeruleus in the Mouse Brain. J Vis Exp 10.3791/58652. https://doi.org/10.3791/58652.

138. Schmit, K.J., Sciortino, A., Aho, V.T., Garcia, P., Rodriguez, B.P., Thomas, M.H., Gérardy, J.-J., Halder, R., Cialini, C., Heurtaux, T., et al. (2022). Dietary fiber deprivation and bacterial curli exposure shift gut microbiome and exacerbate Parkinson's disease-like pathologies in an alpha-synuclein-overexpressing mouse. 2022.03.21.485143. https://doi.org/10.1101/2022.03.21.485143.

139. Schroeder, B.O., Birchenough, G.M.H., Ståhlman, M., Arike, L., Johansson, M.E.V., Hansson, G.C., and Bäckhed, F. (2018). Bifidobacteria or Fiber Protects against Diet-Induced Microbiota-Mediated Colonic Mucus Deterioration. Cell Host & Microbe *23*, 27-40.e7. https://doi.org/10.1016/j.chom.2017.11.004.

140. Seidl, S., Santiago, J., Bilyk, H., and Potashkin, J. (2014). The emerging role of nutrition in Parkinson's disease. Frontiers in Aging Neuroscience *6*. .

141. Sekirov, I., Russell, S.L., Antunes, L.C.M., and Finlay, B.B. (2010). Gut microbiota in health and disease. Physiol Rev *90*, 859–904. https://doi.org/10.1152/physrev.00045.2009.

142. Shahrestani, J., and Das, J.M. (2021). Neuroanatomy, Auerbach Plexus (StatPearls Publishing).

143. Shannon, K.M., Keshavarzian, A., Dodiya, H.B., Jakate, S., and Kordower, J.H. (2012). Is alpha-synuclein in the colon a biomarker for premotor Parkinson's disease? Evidence from 3 cases. Mov Disord *27*, 716–719. https://doi.org/10.1002/mds.25020.

144. Sonne, J., Reddy, V., and Beato, M.R. (2022). Neuroanatomy, Substantia Nigra. In StatPearls, (Treasure Island (FL): StatPearls Publishing), p.

145. Sonnenburg, E.D., Smits, S.A., Tikhonov, M., Higginbottom, S.K., Wingreen, N.S., and Sonnenburg, J.L. (2016). Diet-induced extinction in the gut microbiota compounds over generations. Nature *529*, 212–215. https://doi.org/10.1038/nature16504.

146. Spillantini, M.G., Schmidt, M.L., Lee, V.M.-Y., Trojanowski, J.Q., Jakes, R., and Goedert, M. (1997). α-Synuclein in Lewy bodies. Nature *388*, 839–840. https://doi.org/10.1038/42166.

147. Spillantini, M.G., Crowther, R.A., Jakes, R., Hasegawa, M., and Goedert, M. (1998). alpha-Synuclein in filamentous inclusions of Lewy bodies from Parkinson's disease and dementia with lewy bodies. Proc Natl Acad Sci U S A *95*, 6469–6473. https://doi.org/10.1073/pnas.95.11.6469.

148. Sprenger, F.S., Stefanova, N., Gelpi, E., Seppi, K., Navarro-Otano, J., Offner, F., Vilas, D., Valldeoriola, F., Pont-Sunyer, C., Aldecoa, I., et al. (2015). Enteric nervous system α-synuclein immunoreactivity in idiopathic REM sleep behavior disorder. Neurology *85*, 1761–1768. https://doi.org/10.1212/WNL.0000000000002126.

149. Stokholm, M.G., Danielsen, E.H., Hamilton-Dutoit, S.J., and Borghammer, P. (2016). Pathological α-synuclein in gastrointestinal tissues from prodromal Parkinson disease patients. Annals of Neurology *79*, 940–949. https://doi.org/10.1002/ana.24648.

150. Streit, W.J., Mrak, R.E., and Griffin, W.S.T. (2004). Microglia and neuroinflammation: a pathological perspective. J Neuroinflammation *1*, 14. https://doi.org/10.1186/1742-2094-1-14.

151. Svensson, E., Horváth-Puhó, E., Thomsen, R.W., Djurhuus, J.C., Pedersen, L., Borghammer, P., and Sørensen, H.T. (2015). Vagotomy and subsequent risk of Parkinson's disease. Ann Neurol *78*, 522–529. https://doi.org/10.1002/ana.24448.

152. Tang, B., Becanovic, K., Desplats, P.A., Spencer, B., Hill, A.M., Connolly, C., Masliah, E., Leavitt, B.R., and Thomas, E.A. (2012). Forkhead box protein p1 is a transcriptional repressor of immune signaling in the CNS: implications for transcriptional dysregulation in Huntington disease. Hum Mol Genet *21*, 3097–3111. https://doi.org/10.1093/hmg/dds132.

153. Tansey, M.G., and Goldberg, M.S. (2010). Neuroinflammation in Parkinson's disease: its role in neuronal death and implications for therapeutic intervention. Neurobiol Dis *37*, 510–518. https://doi.org/10.1016/j.nbd.2009.11.004.

154. Tansey, M.G., and Romero-Ramos, M. (2019). Immune system responses in Parkinson's disease: Early and dynamic. Eur J Neurosci *49*, 364–383. https://doi.org/10.1111/ejn.14290.

155. Thompson, J.A., and Felsen, G. (2013). Activity in mouse pedunculopontine tegmental nucleus reflects action and outcome in a decision-making task. J Neurophysiol *110*, 2817–2829. https://doi.org/10.1152/jn.00464.2013.

156. Triantafyllou, K., Chang, C., and Pimentel, M. (2014). Methanogens, methane and gastrointestinal motility. J Neurogastroenterol Motil *20*, 31–40. https://doi.org/10.5056/jnm.2014.20.1.31.

157. Tyakht, A.V., Kostryukova, E.S., Popenko, A.S., Belenikin, M.S., Pavlenko, A.V., Larin, A.K., Karpova, I.Y., Selezneva, O.V., Semashko, T.A., Ospanova, E.A., et al. (2013). Human gut microbiota community structures in urban and rural populations in Russia. Nat Commun *4*, 2469. https://doi.org/10.1038/ncomms3469.

158. Ulusoy, A., Rusconi, R., Pérez-Revuelta, B.I., Musgrove, R.E., Helwig, M., Winzen-Reichert, B., and Di Monte, D.A. (2013). Caudo-rostral brain spreading of α-synuclein through vagal connections. EMBO Mol Med *5*, 1119–1127. https://doi.org/10.1002/emmm.201302475.

159. Uniyal, S., Sharma, R.K., and Kondakal, V. (2021). New insights into the biodegradation of chlorpyrifos by a novel bacterial consortium: Process optimization using general factorial experimental design. Ecotoxicology and Environmental Safety *209*, 111799. https://doi.org/10.1016/j.ecoenv.2020.111799.

160. Uriarte Huarte, O., Kyriakis, D., Heurtaux, T., Pires-Afonso, Y., Grzyb, K., Halder, R., Buttini, M., Skupin, A., Mittelbronn, M., and Michelucci, A. (2021). Single-Cell Transcriptomics and In Situ Morphological Analyses Reveal Microglia Heterogeneity Across the Nigrostriatal Pathway. Front Immunol *12*, 639613. https://doi.org/10.3389/fimmu.2021.639613.

161. Valdes, A.M., Walter, J., Segal, E., and Spector, T.D. (2018). Role of the gut microbiota in nutrition and health. BMJ *361*, k2179. https://doi.org/10.1136/bmj.k2179.

162. Van Den Berge, N., Ferreira, N., Gram, H., Mikkelsen, T.W., Alstrup, A.K.O., Casadei, N., Tsung-Pin, P., Riess, O., Nyengaard, J.R., Tamgüney, G., et al. (2019). Evidence for bidirectional and trans-synaptic parasympathetic and sympathetic propagation of alpha-synuclein in rats. Acta Neuropathol *138*, 535–550. https://doi.org/10.1007/s00401-019-02040-w.

163. Van Egroo, M., Koshmanova, E., Vandewalle, G., and Jacobs, H.I.L. (2022). Importance of the locus coeruleus-norepinephrine system in sleep-wake regulation: Implications for aging and Alzheimer's disease. Sleep Medicine Reviews *62*, 101592. https://doi.org/10.1016/j.smrv.2022.101592.

164. Vandeputte, D., Falony, G., Vieira-Silva, S., Tito, R.Y., Joossens, M., and Raes, J. (2016). Stool consistency is strongly associated with gut microbiota richness and composition, enterotypes and bacterial growth rates. Gut *65*, 57–62. https://doi.org/10.1136/gutjnl-2015-309618.

165. Varrette, S., Bouvry, P., Cartiaux, H., and Georgatos, F. (2014). Management of an academic HPC cluster: The UL experience. In 2014 International Conference on High Performance Computing Simulation (HPCS), pp. 959–967.

166. Vilar, M., Chou, H.-T., Lührs, T., Maji, S.K., Riek-Loher, D., Verel, R., Manning, G., Stahlberg, H., and Riek, R. (2008). The fold of α-synuclein fibrils. Proceedings of the National Academy of Sciences *105*, 8637–8642. https://doi.org/10.1073/pnas.0712179105.

167. Vilas, D., Iranzo, A., Tolosa, E., Aldecoa, I., Berenguer, J., Vilaseca, I., Martí, C., Serradell, M., Lomeña, F., Alós, L., et al. (2016). Assessment of α-synuclein in submandibular glands of patients with idiopathic rapid-eye-movement sleep behaviour disorder: a case-control study. Lancet Neurol *15*, 708–718. https://doi.org/10.1016/S1474-4422(16)00080-6.

168. Wakabayashi, K., Takahashi, H., Takeda, S., Ohama, E., and Ikuta, F. (1988). Parkinson's disease: the presence of Lewy bodies in Auerbach's and Meissner's plexuses. Acta Neuropathol *76*, 217–221. https://doi.org/10.1007/BF00687767.

169. Wakabayashi, K., Takahashi, H., Ohama, E., and Ikuta, F. (1990). Parkinson's disease: an immunohistochemical study of Lewy body-containing neurons in the enteric nervous system. Acta Neuropathol *79*, 581–583. https://doi.org/10.1007/BF00294234.

170. Watson, M.B., Richter, F., Lee, S.K., Gabby, L., Wu, J., Masliah, E., Effros, R.B., and Chesselet, M.-F. (2012). Regionally-specific microglial activation in young mice over-expressing human wildtype alpha-synuclein. Exp Neurol *237*, 318–334. https://doi.org/10.1016/j.expneurol.2012.06.025.

171. Weihe, E., Depboylu, C., Schütz, B., Schäfer, M.K.-H., and Eiden, L.E. (2006). Three Types of Tyrosine Hydroxylase-Positive CNS Neurons Distinguished by Dopa Decarboxylase and VMAT2 Co-Expression. Cell Mol Neurobiol *26*, 659–678. https://doi.org/10.1007/s10571-006-9053-9.

172. Whitton, P.S. (2007). Inflammation as a causative factor in the aetiology of Parkinson's disease. Br J Pharmacol *150*, 963–976. https://doi.org/10.1038/sj.bjp.0707167.

173. Wilms, H., Rosenstiel, P., Romero-Ramos, M., Arlt, A., Schäfer, H., Seegert, D., Kahle, P.J., Odoy, S., Claasen, J.H., Holzknecht, C., et al. (2009). Suppression of MAP kinases inhibits microglial activation and attenuates neuronal cell death induced by alpha-synuclein protofibrils. Int J Immunopathol Pharmacol *22*, 897–909. https://doi.org/10.1177/039463200902200405.

174. Winn, P. (2008). Experimental studies of pedunculopontine functions: Are they motor, sensory or integrative? Parkinsonism & Related Disorders *14*, S194–S198. https://doi.org/10.1016/j.parkreldis.2008.04.030.

175. Wraith, D.C., and Nicholson, L.B. (2012). The adaptive immune system in diseases of the central nervous system. J Clin Invest *122*, 1172–1179. https://doi.org/10.1172/JCI58648.

176. Wu, D.C., Jackson-Lewis, V., Vila, M., Tieu, K., Teismann, P., Vadseth, C., Choi, D.-K., Ischiropoulos, H., and Przedborski, S. (2002). Blockade of microglial activation is neuroprotective in the 1-methyl-4-phenyl-1,2,3,6-tetrahydropyridine mouse model of Parkinson disease. J Neurosci *22*, 1763–1771. .

177. Young, C.B., Reddy, V., and Sonne, J. (2021). Neuroanatomy, Basal Ganglia (StatPearls Publishing).

178. Zhou, S.-Y., Lu, Y.-X., Yao, H., and Owyang, C. (2008). Spatial organization of neurons in the dorsal motor nucleus of the vagus synapsing with intragastric cholinergic and nitric oxide/VIP neurons in the rat. Am J Physiol Gastrointest Liver Physiol *294*, G1201–G1209. https://doi.org/10.1152/ajpgi.00309.2006.

PART VI

Appendix

Appendix A

A.1 Supplementary Figures

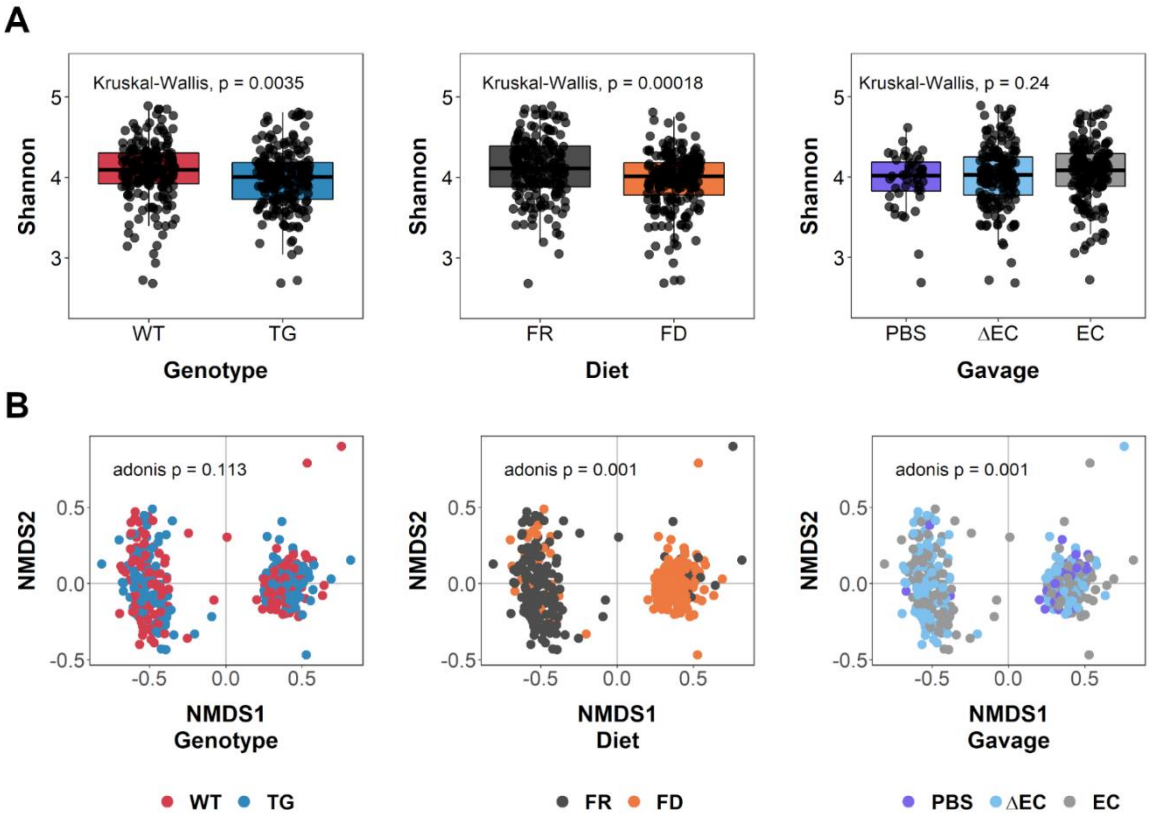

Figure S1 | Alpha and beta diversity assessment for the different challenges

(A) Boxplots for alpha diversity of the different variables/challenges. Genotype and Diet challenges were both altering alpha diversity. No significant changes were induced by gavage alone. P-values were determined using the Kruskal-Wallis test and were corrected for FDR.

(B) Non-metric multi-dimensional scaling (NMDS) plots for beta diversity of the different variables/challenges. Here Diet and Gavage appear to lead to changes in beta diversity. However, one has to take into account that the PBS gavaged mice were exclusively FD challenged. The dissimilarities were genotype independent. P-values were determined using the adonis test.

WT, wild-type littermates; TG, Thy1-Syn14; FD, fibre deprived; FR, fibre rich; PBS, phosphate buffered saline solution; ΔEC, curli-KO *E. coli*; EC, wild-type curli expressing *E. coli*

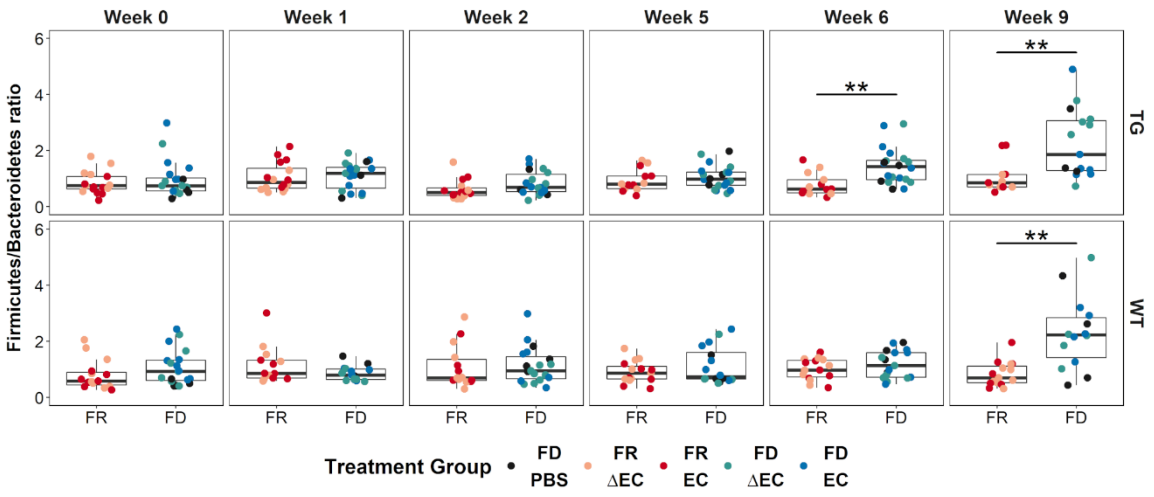

Figure S2 | Fibre-deprivation induced increased Firmicutes to Bacteroidetes ratios

Boxplots illustrating the Firmicutes to Bacteroidetes ratios for each tested time point between FR and FD challenged mice. Both genotypes show significant increases in ratios at 9 weeks. Thy1-Syn14 mice do already show significant differences at week 6.P-values were determined using the Kruskal-Wallis test and were corrected for FDR.

WT, wild-type littermates; TG, Thy1-Syn14; FD, fibre deprived; FR, fibre rich; PBS, phosphate buffered saline solution; ΔEC, curli-KO *E. coli*; EC, wild-type curli expressing *E. coli*

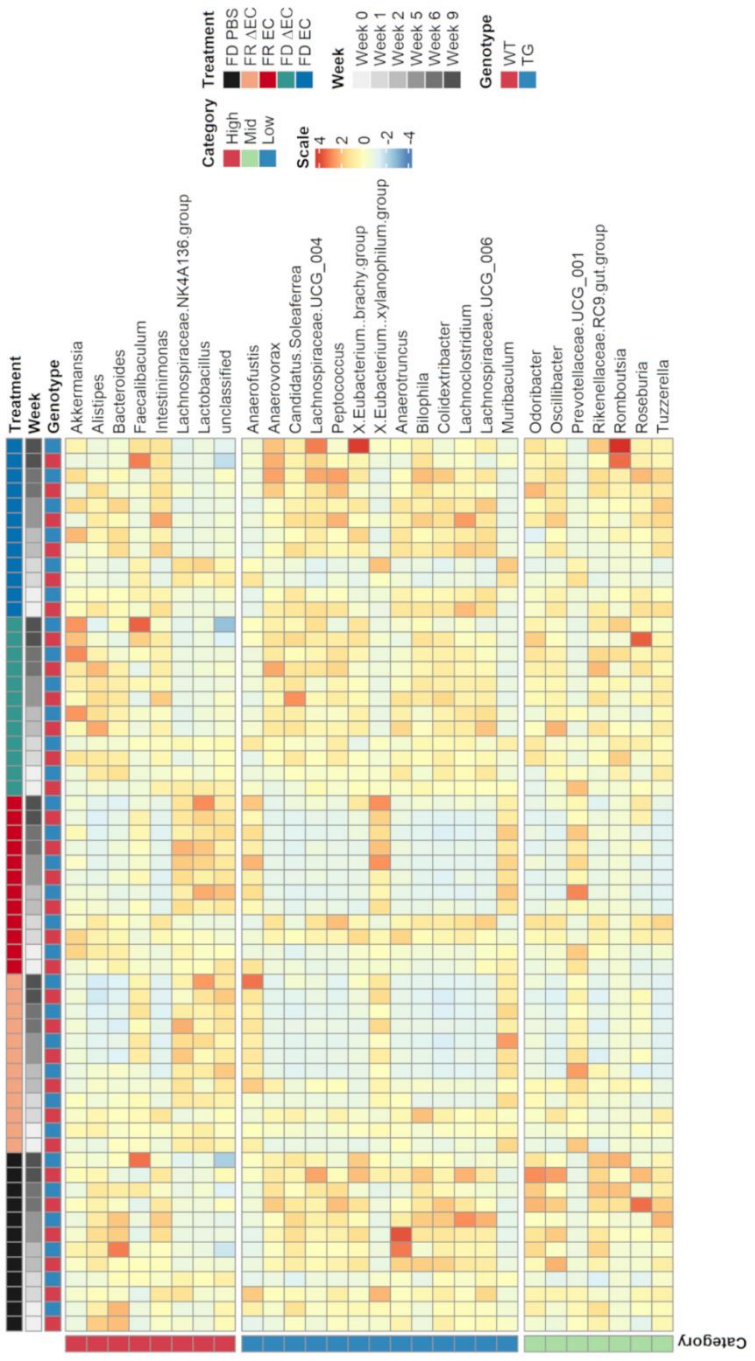

Figure S3 | Differential taxa abundance over time is diet regulated

Complex heatmap visualizing the effect of different challenges on the relative abundance changes over time. The taxa were subdivided into three different groups according to their relative abundances: High, at least for one time point there was an average relative abundance of 10% or higher for at least one treatment group; Mid, at least for one time point there was an average relative abundance between at least 1 and maximum 10% for at least one treatment group; Low, less then 1%. All data was scaled and centred per row. Main effect is seen between FR and FD challenges. For some taxa, we observed also difference between genotypes.

WT, wild-type littermates; TG, Thy1-Syn14; FD, fibre deprived; FR, fibre rich; PBS, phosphate buffered saline solution; ΔEC, curli-KO *E. coli*; EC, wild-type curli expressing *E. coli*

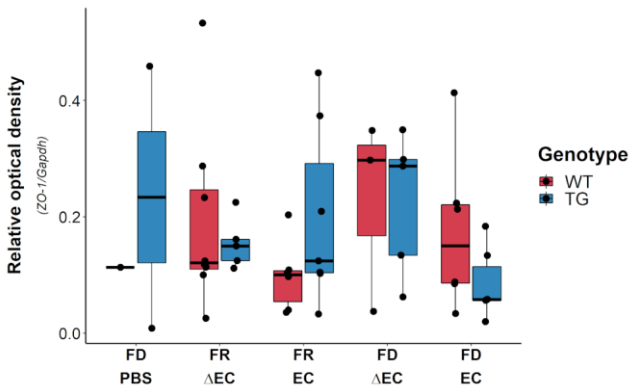

Figure S4 | Curli contributes to the loss of gut barrier integrity of the colon

Relative semi-quantitation of Western blots for ZO-1 indicate that Curli (EC groups) contributes to gut barrier integrity loss and/or a so-called "leaky gut". Due to the inner-group variability, these results should, however, be taken with caution.

WT, wild-type littermates; TG, Thy1-Syn14; FD, fibre deprived; FR, fibre rich; PBS, phosphate buffered saline solution; ΔEC, curli-KO *E. coli*; EC, wild-type curli expressing *E. coli*

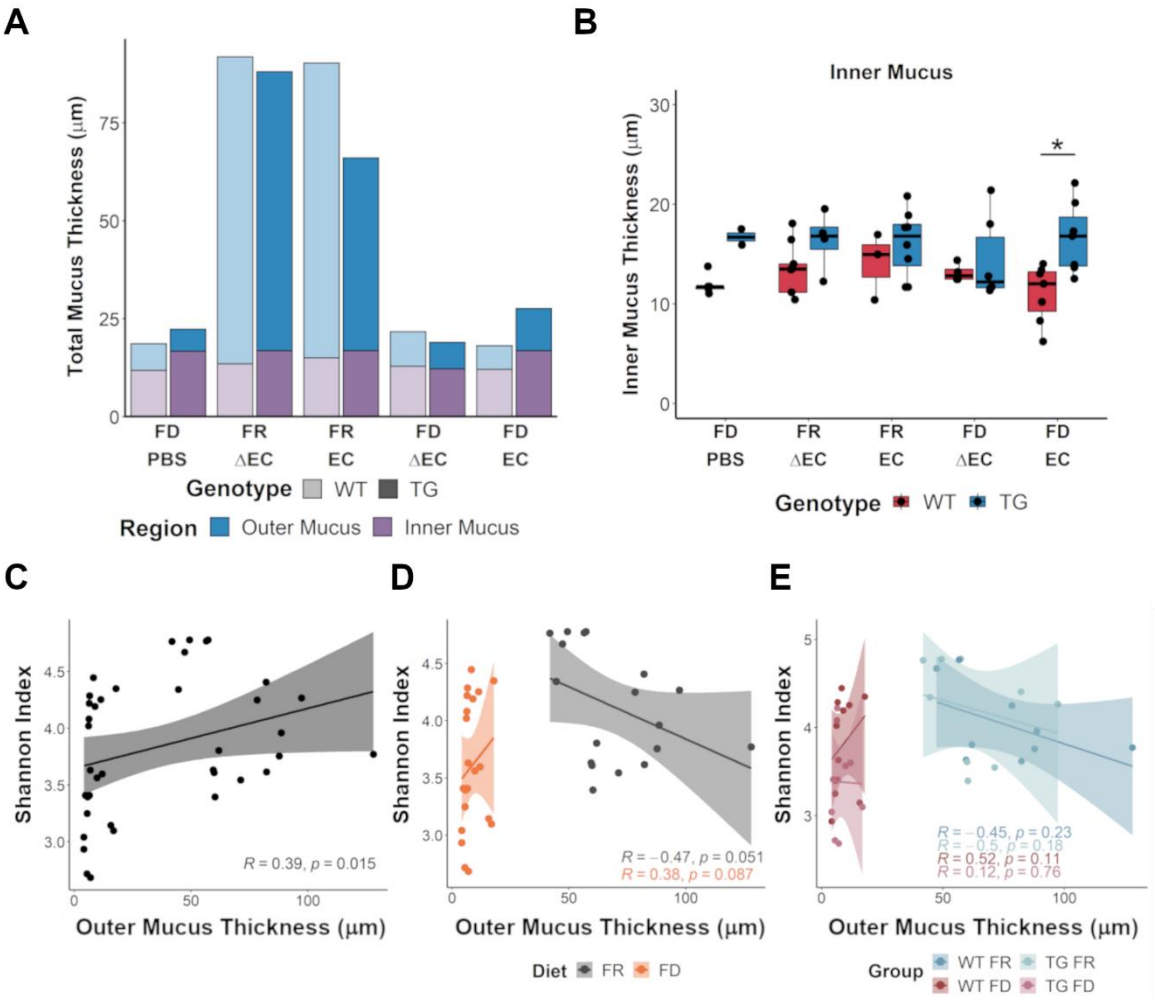

Figure S5 | Inner mucus thickness compensation and outer mucus to diversity associations

(A) Barplot illustrating the combined mucus thickness in all different treatment groups.

(B) Inner mucus thickness does not vary significantly between the different treatment groups in the separate genotypes. To note is however, the significant ticker inner mucus layer in the TG FD EC group compared to its WT equivalent. This inferred a greater compensatory/rescue mechanism in TG animals.

(C-E) Scatterplots of Spearman rank tests comparing alpha diversity (y-axis) and mucus thickness (x-axis) (C) overall, (D) for the different diet groups, and (D) combining genotype and diet groups.

WT, wild-type littermates; TG, Thy1-Syn14; FD, fibre deprived; FR, fibre rich; PBS, phosphate

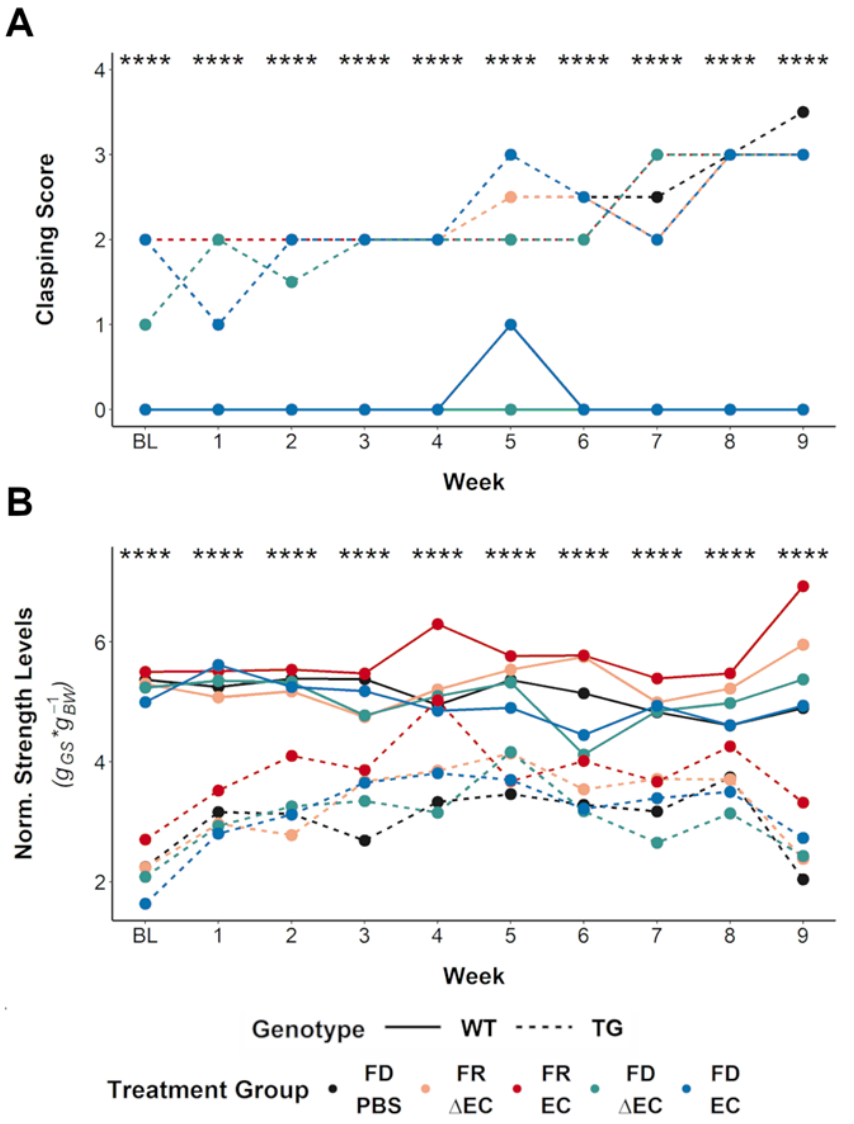
A
Clasping Score
Week
B
Norm. Strength Levels
Week
Genotype
WT
TG
Treatment Group
FD PBS
FR ΔEC
FR EC
FD ΔEC
FD EC
C
TG vs WT: p < 0.0001
Time (s)
Genotype
WT
TG
FD PBS
FR ΔEC
FR EC
FD ΔEC
FD EC

Figure S6 | Gross motor and sensorimotor functions are transgene driven

(A - B) Longitudinal gross motor function monitoring visualized in line plots indicating the median value changes for the different treatment groups. Alpha-synuclein overexpression drives motor deficits in transgenic animals.

(A) Hindlimb clasping scores increase within all transgenic groups (dotted lines) independent of their treatment. Differences between WT and TG animals were significant from baseline to week 9. All p-values were determined using the Mann-Whitney U test and FDR to correct for multiple comparison.

(B) Grip strength results confirm that there is only a difference between the genotypes and there is no observable difference due to any kind of treatment. Differences between WT and TG animals were significant from baseline to week 9. All p-values were determined using the Mann-Whitney U test and FDR to correct for multiple comparison.

(C) Boxplots illustrating the latency for touch in the different treatment groups (x-axis) for WT (red) and TG (blue) animals after 9 weeks. The time of touch refers to the sensory ability of the mice. Here we saw a clear significance between genotypes (Kruskal-Wallis, corrected for FDR; $p < 0.0001$). More specifically there are significant differences in the FR ΔEC, FR EC, and FD EC between genotypes. All p-values were determined using the Mann-Whitney U test.

*, $p < 0.05$; **, $p < 0.01$; ****, $p < 0.0001$; WT, wild-type littermates; TG, Thy1-Syn14; FD, fibre deprived; FR, fibre rich; PBS, phosphate buffered saline solution; ΔEC, curli-KO *E. coli*; EC, wild-type curli expressing *E. coli*

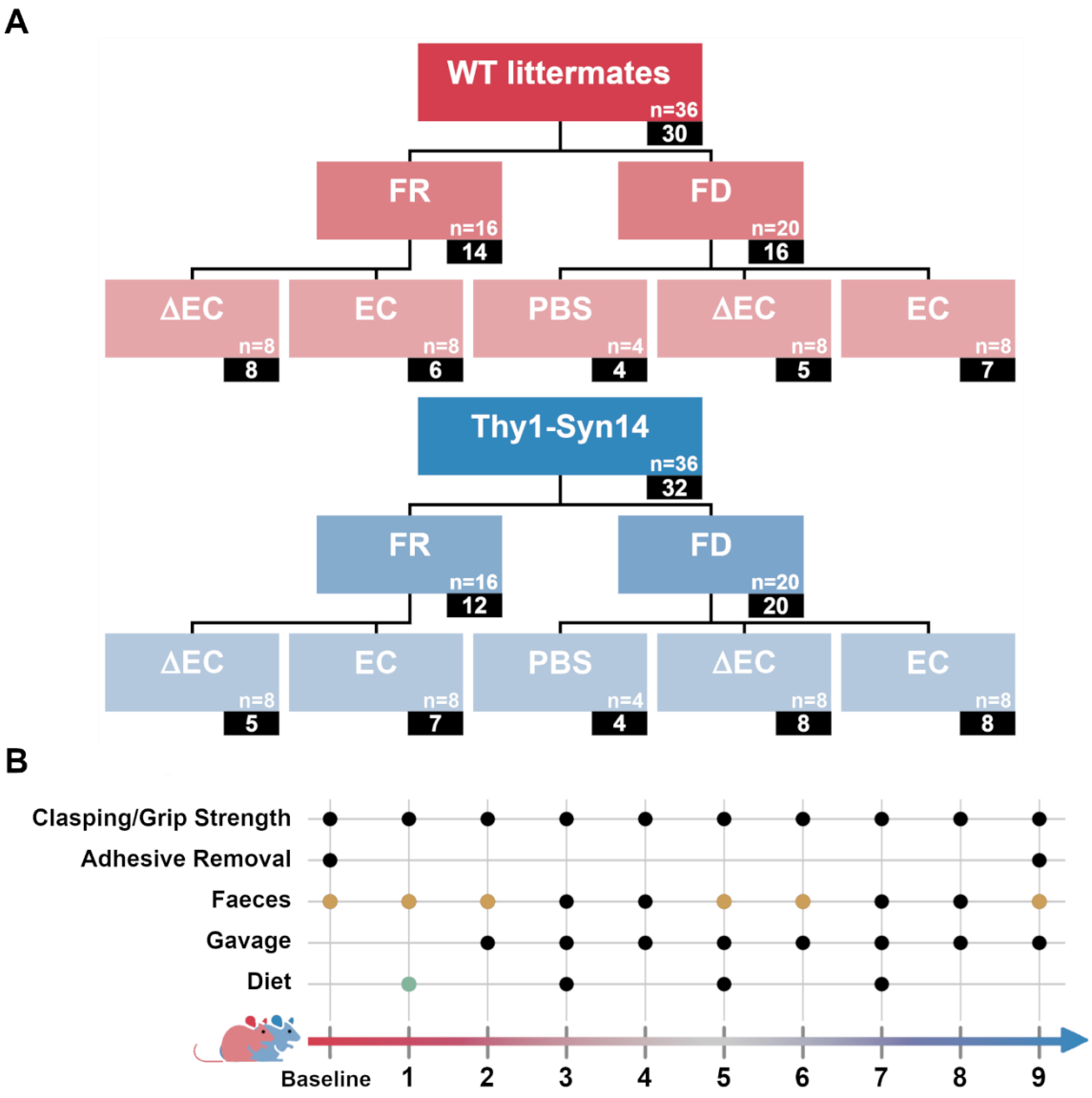

Figure S7 | Experimental design and in-life experiments

(A) Hierarchy graphs illustrating the complex experimental design. See details in Material and Methods. The white on black background numbers refer to the numbers of animals we were left with at the end of the in-life phase.

(B) Graph indicating which treatments were given or tests were performed during the in-life phase. Gross motor functions were tested weekly, while the adhesive removal test was only performed twice, at start and end of the in-life phase. Faeces were checked weekly and afterwards six time points were chosen for analysis. Mice were gavaged weekly starting at week 2 for a total 8 times and their food was changed every second week.

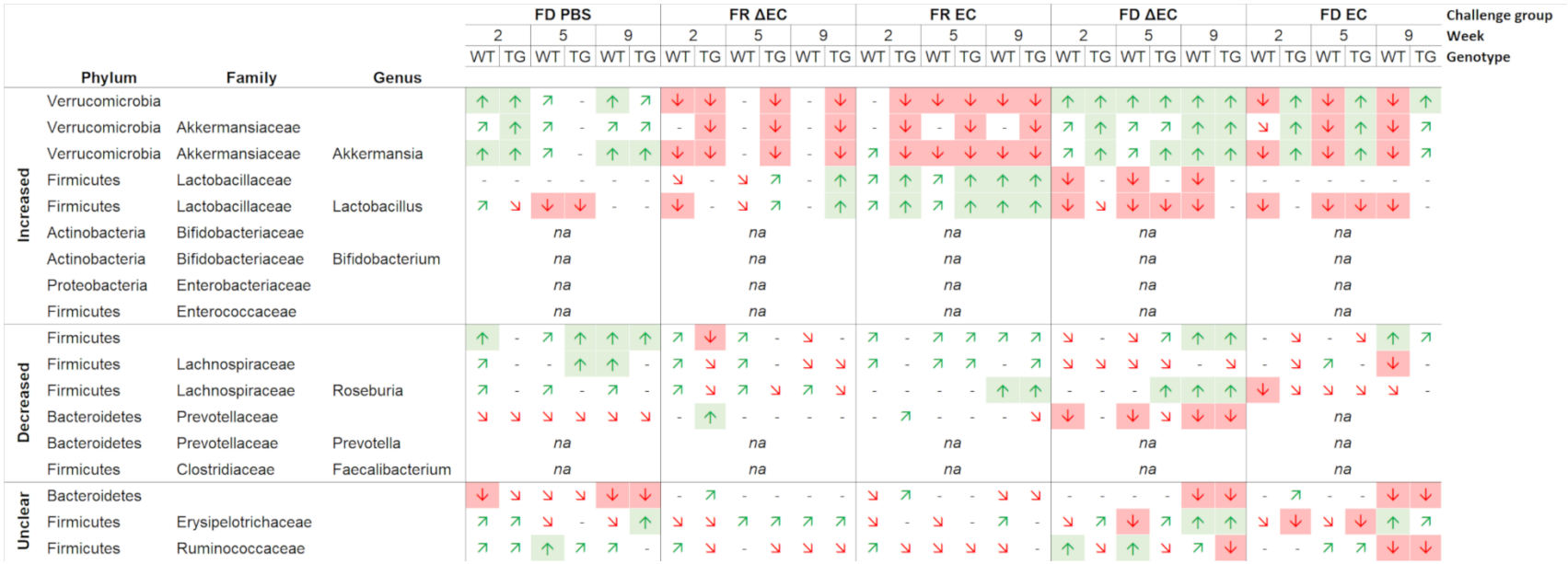

Table S1 | Comparison of the 16S rRNA sequencing results to known taxa altered in stool samples of PD patients (adapted from Boertien et al., 2019)

Appendix B

B.1 Supplementary Figures

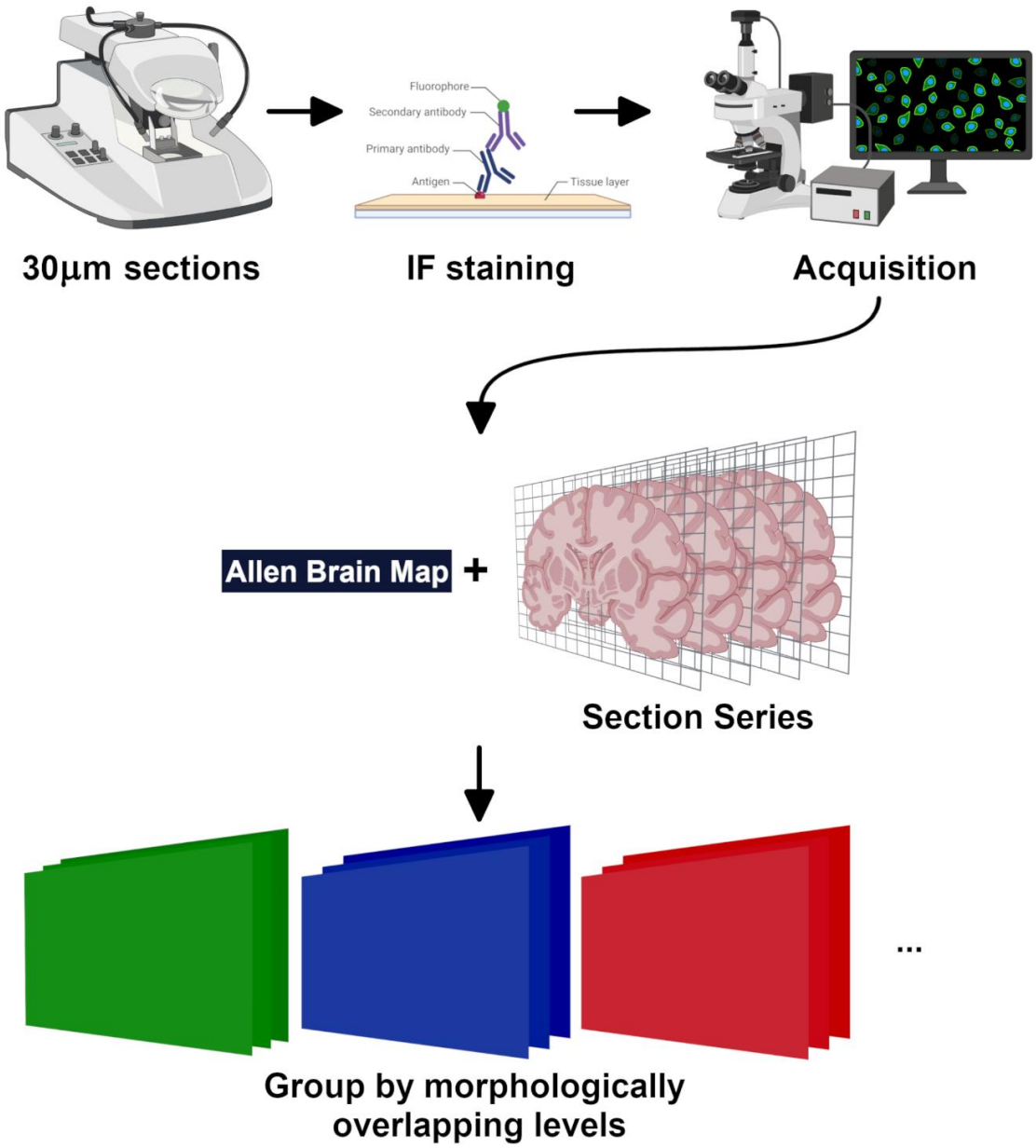

Supplementary Figure 1 | Morphometric atlas generation workflow

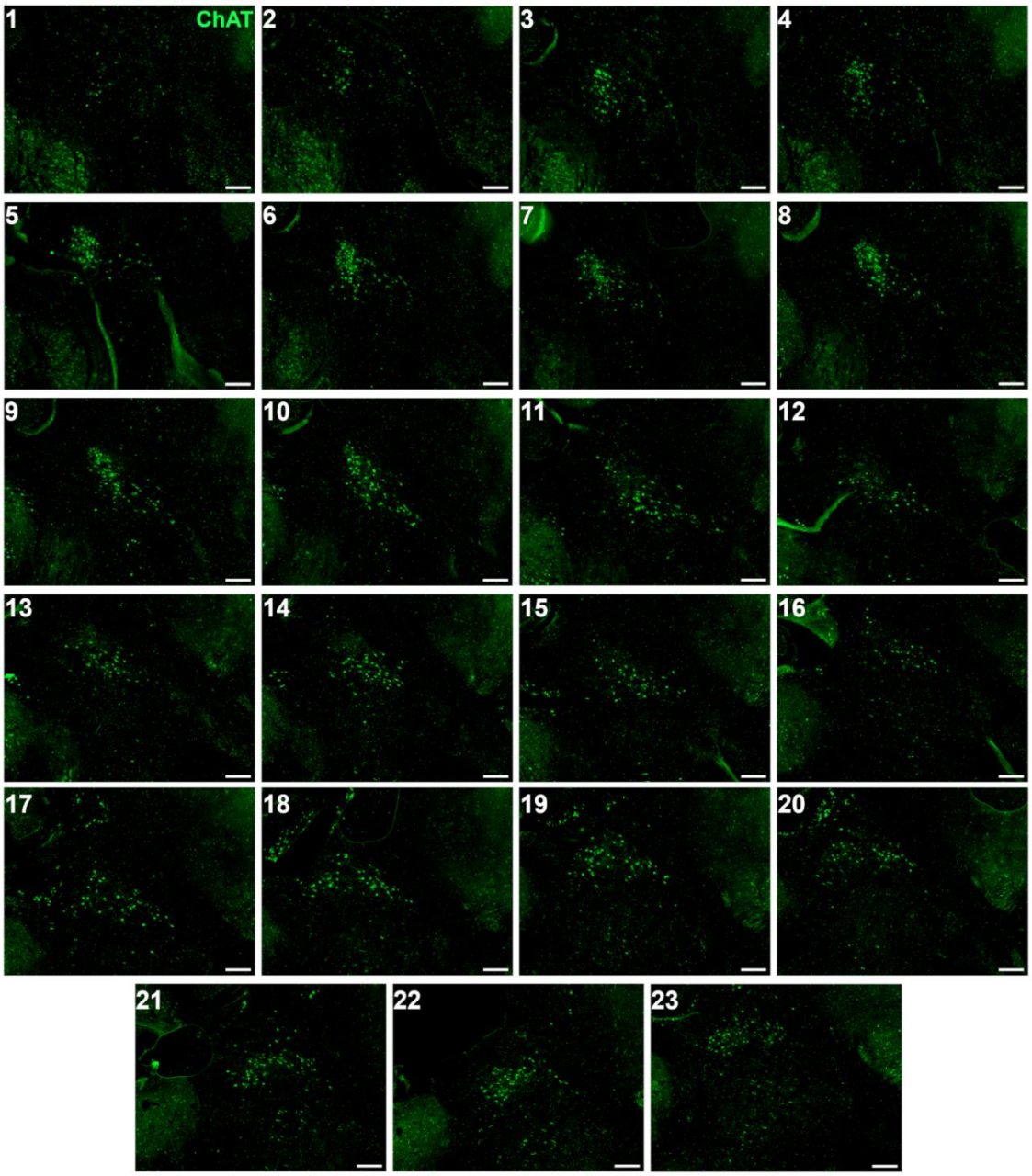

Supplementary Figure 2 | PPN morphometric atlas

Image series for cholinergic neurons of the pedunculopontine nucleus to determine morphologically distinct levels. (10x tiles; scale bar: 250μm)

.

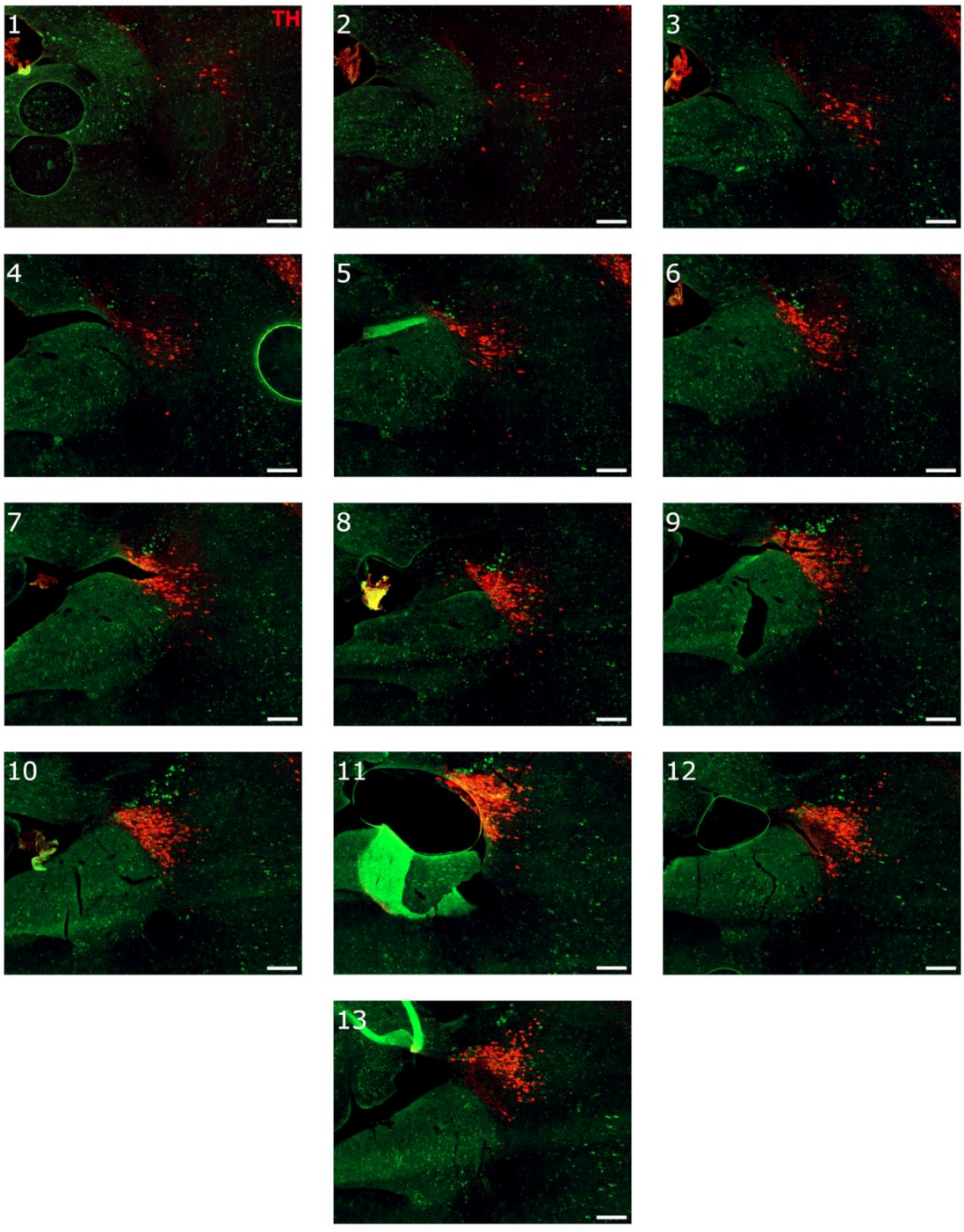

Supplementary Figure 3 | LC morphometric atlas

Image series for noradrenergic (TH positive) neurons of the locus coeruleus to determine morphologically distinct levels. (10x tiles; scale bar: 250μm)

Appendix C

C.1 Supplementary Figures

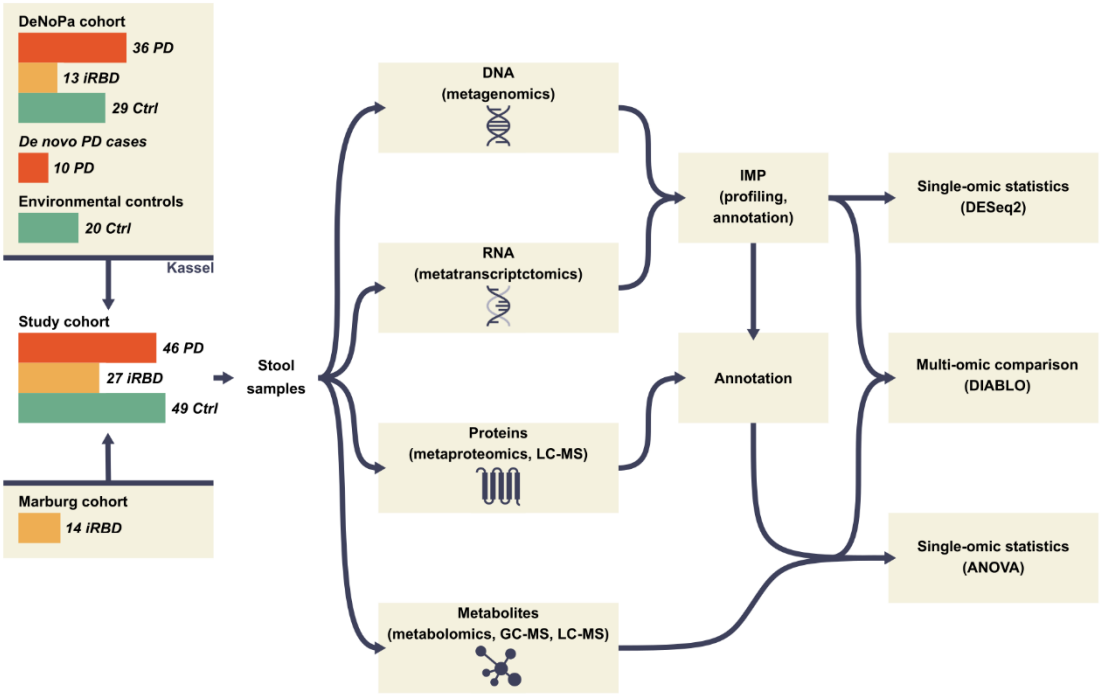

Extended Data Figure 1 | Multi-omic data analysis workflow. PD = Parkinson's disease, iRBD = idiopathic REM sleep behavior disorder, Ctrl = control subject.

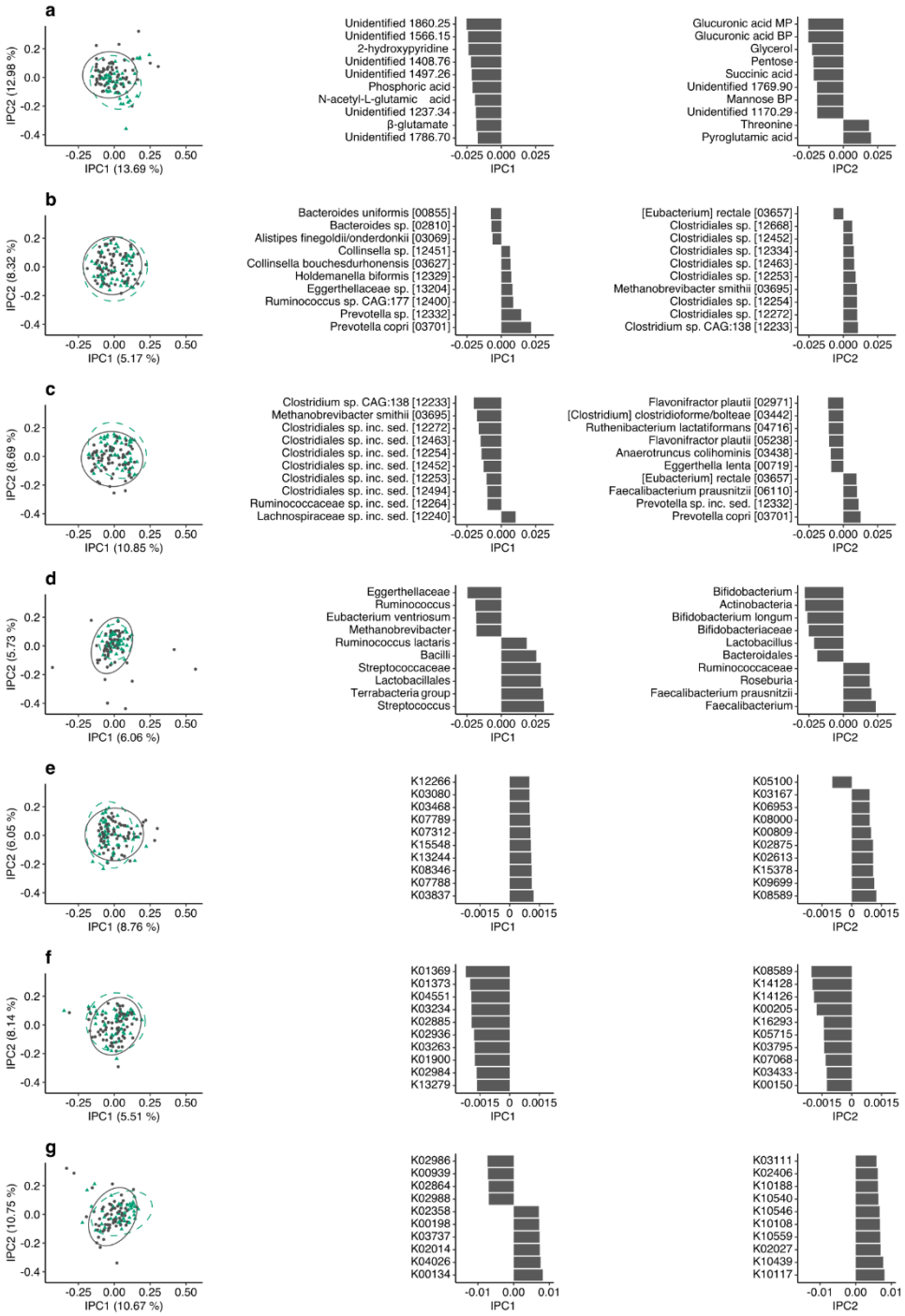

Extended Data Figure 2 | Independent Principal Component Analysis (IPCA) for each data type. Testing was performed separately for each data type, with total number of components chosen based on kurtosis. The first two components are shown for each data type regardless of total number of components. In the 1st column, green triangles and dashed line correspond to control subjects, and black circles and solid line to patients with PD or iRBD. Ellipses reflect 95% confidence. 2nd and 3rd columns show 10 features with the highest loadings. **a.** Untargeted metabolomics; showing 2/2 components, **b.** Taxonomically classified metagenomic reads; 2/3 components, **c.** Taxonomically classified metatranscriptomic reads; 2/2 components, **d.** Taxonomically classified metaproteomic spectra; 2/4 components, **e.** Functionally classified (KEGG orthologs; KOs) metagenomic reads; 2/3 components, **f.** Functionally classified (KOs) metatranscriptomic reads; 2/4 components, **g.** Functionally classified (KOs) metaproteomic spectra; 2/4 components. The numbers in taxon names (**b, c**) refer to identifiers from the mOTUs workflow. For KOs (**e-g**), details are provided in Supplementary Table 3.

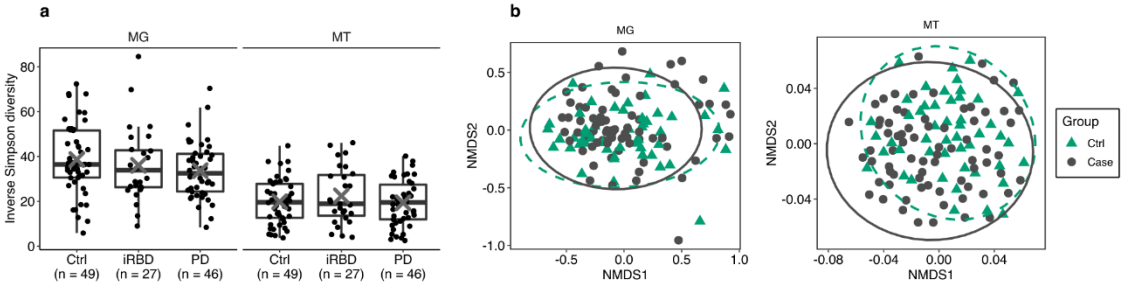

c

Level	Case/Ctrl	iRBD/Ctrl	PD/Ctrl	PD/iRBD
MG				
Phylum	0	0	0	0
Class	1	0	1	1
Order	2	2	3	4
Family	4	2	3	3
Genus	5	2	3	3
Species	7	14	4	7
MT				
Phylum	1	1	0	0
Class	2	5	1	4
Order	7	4	8	0
Family	12	4	10	4
Genus	22	12	17	2
Species	37	35	31	2
MP				
All	0	1	0	1

d

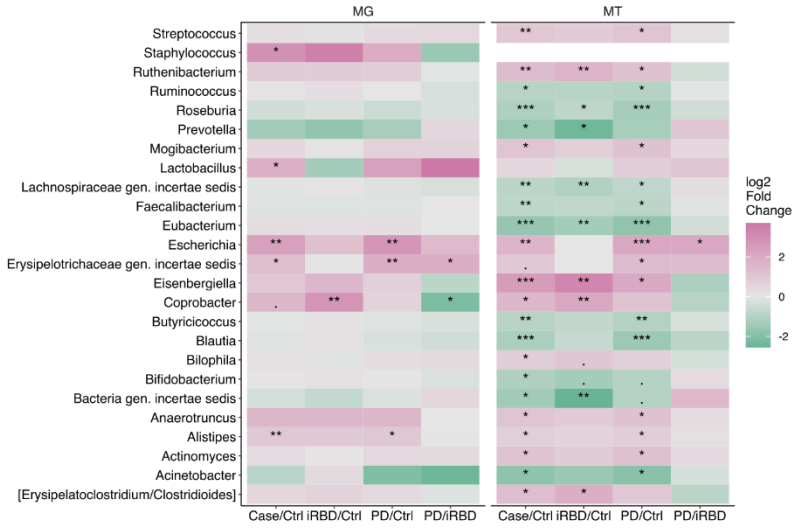

e

Data	Case/Ctrl	iRBD/Ctrl	PD/Ctrl	PD/iRBD
MG	19	7	9	2
MT	991	754	873	417
MP	3	7	0	8
MG,MT	9	1	8	2
MT,MP	0	2	0	2

f

	Decreased in cases		Increased in cases			
	MG	MT	MG	MT	MP	All
map01100 Metabolic pathways	2	156	9	173	2	342
map01110 Biosynthesis of secondary metabolites	1	61	3	61	1	127
map01120 Microbial metabolism in diverse environments	0	41	2	59	0	102
map02020 Two-component system	0	21	1	51	0	73
map01230 Biosynthesis of amino acids	0	28	1	20	0	49
map02010 ABC transporters	0	27	0	21	0	48
map01200 Carbon metabolism	0	16	1	30	0	47
map01240 Biosynthesis of cofactors	2	12	0	21	1	36
map02040 Flagellar assembly	0	25	0	1	0	26
map00620 Pyruvate metabolism	0	7	0	17	0	24

Extended Data Figure 3 | Microbial diversity and differential abundance comparisons of taxonomic and functional data. a. Alpha diversity and group in taxonomically classified metagenomic (MG) and metatranscriptomic (MT) sequence reads; box hinges: 1st and 3rd quartiles; whiskers: hinge to highest/lowest values that is within 1.5*IQR of hinge; grey cross: mean, **b.** Beta diversity and group (Non-metric Multidimensional Scaling based on Bray-Curtis dissimilarity) in MG and MT species data, with ellipses showing 95% confidence, **c.** Number of differentially abundant taxa (q (false discovery rate adjusted P) < 0.05), **d.** Genera with q < 0.05 in MG or MT data for the two-group case (either PD or iRBD) vs control contrast, **e.** Number of differentially abundant (q < 0.05) KEGG orthologs (KOs) in MG, MT, and metaproteomic (MP) data, **e.** 10 pathways most commonly represented by the differentially abundant KOs (q < 0.05) for the case vs control comparison in MG, MT and MP data. In heatmaps, . 0.1 > q > 0.05, * q < 0.05, ** q < 0.01, *** q < 0.001.

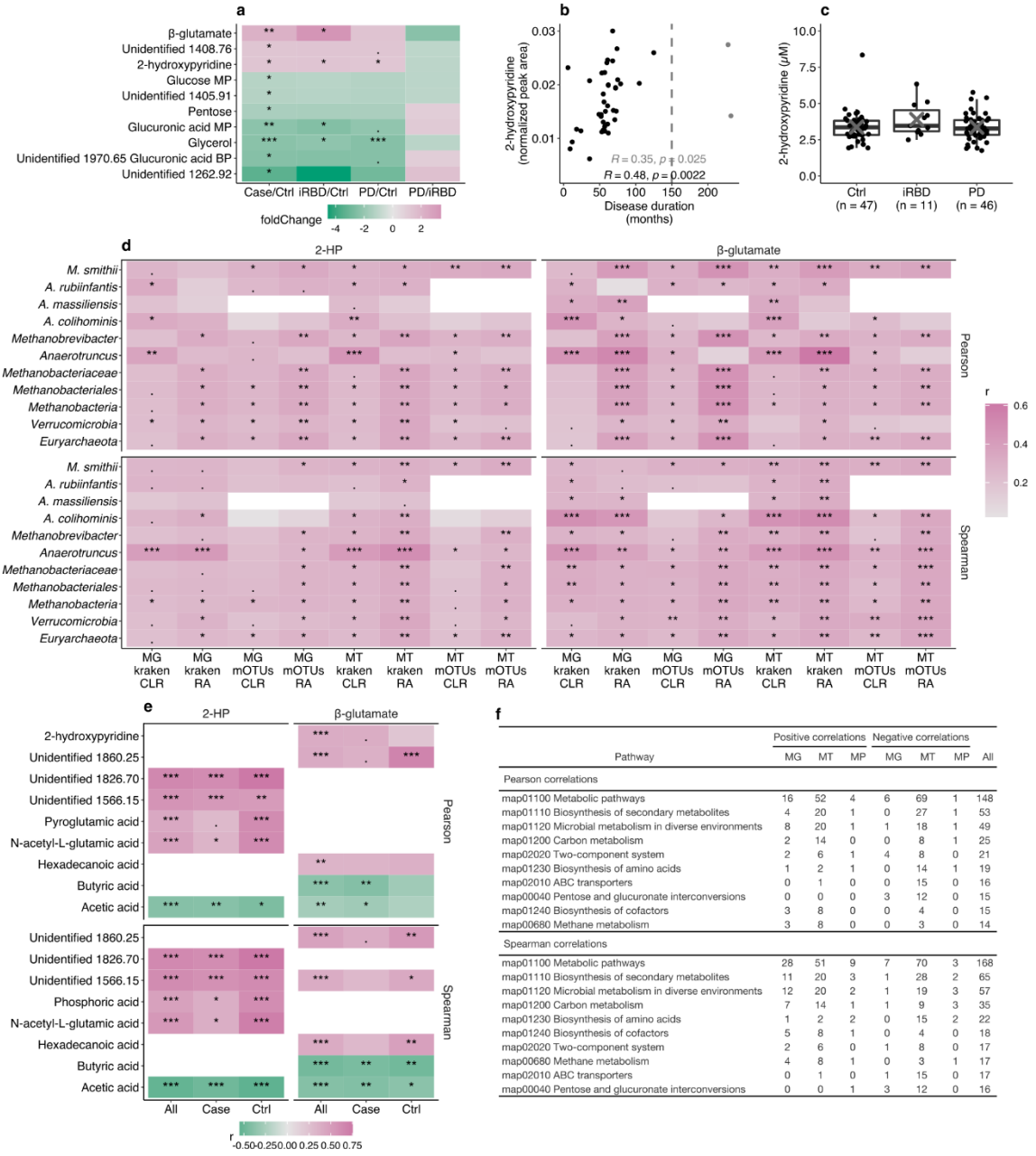

f

Pathway	Positive correlations MG	MT	MP	Negative correlations MG	MT	MP	All
Pearson correlations							
map01100 Metabolic pathways	16	52	4	6	69	1	148
map01110 Biosynthesis of secondary metabolites	4	20	1	0	27	1	53
map01120 Microbial metabolism in diverse environments	8	20	1	1	18	1	49
map01200 Carbon metabolism	2	14	0	0	8	1	25
map02020 Two-component system	2	6	1	4	8	0	21
map01230 Biosynthesis of amino acids	1	2	1	0	14	1	19
map02010 ABC transporters	0	1	0	0	15	0	16
map00040 Pentose and glucuronate interconversions	0	0	0	3	12	0	15
map01240 Biosynthesis of cofactors	3	8	0	0	4	0	15
map00680 Methane metabolism	3	8	0	0	3	0	14
Spearman correlations							
map01100 Metabolic pathways	28	51	9	7	70	3	168
map01110 Biosynthesis of secondary metabolites	11	20	3	1	28	2	65
map01120 Microbial metabolism in diverse environments	12	20	2	1	19	3	57
map01200 Carbon metabolism	7	14	1	1	9	3	35
map01230 Biosynthesis of amino acids	1	2	2	0	15	2	22
map01240 Biosynthesis of cofactors	5	8	1	0	4	0	18
map02020 Two-component system	2	6	0	1	8	0	17
map00680 Methane metabolism	4	8	1	0	3	1	17
map02010 ABC transporters	0	1	0	1	15	0	17
map00040 Pentose and glucuronate interconversions	0	0	1	3	12	0	16

Extended Data Figure 4 | Additional results for metabolomics. a. Metabolites with *q* (false discovery rate adjusted *P*) < 0.05 for the two-group case (PD or iRBD) vs control contrast and at least one pair of three-category groups, **b.** 2-HP normalized peak area and disease duration in PD patients; grey values = full data, black values = two longest-duration subjects excluded, **c.** 2-HP in plasma (targeted metabolomics); 2 extreme outliers excluded (2-HP concentration > 30 μM, both in the iRBD group); box hinges: 1st and 3rd quartiles; whiskers: hinge to highest/lowest values that is within 1.5*IQR of hinge; grey cross: mean, **d.** Correlations of metabolites and taxa, showing taxa with $q < 0.05$ in more than 20 comparisons out of a total of 32 approaches: 2 metabolites, 2 data types (MG or MT), 2 annotation methods (Kraken or mOTUs), 2 normalizations (RA = relative abundance, CLR = centered log ratio transform) and 2 correlation coefficients (Pearson or Spearman), **e.** Correlations of 2-HP and beta-glutamate and other metabolites, showing top 5 by *q* in full data for each metabolite and correlation coefficient, **f.** 10 most common pathways represented by KEGG orthologs significantly correlated with 2-HP ($q < 0.05$, and for MG and MT data, absolute value of correlation coefficient > 0.4). In all plots, MG = metagenomic data, MT = metatranscriptomic data, MP = metaproteomic data. In plots with stars, . $0.1 > q > 0.05$, * $q < 0.05$, ** $q < 0.01$, *** $q < 0.001$.

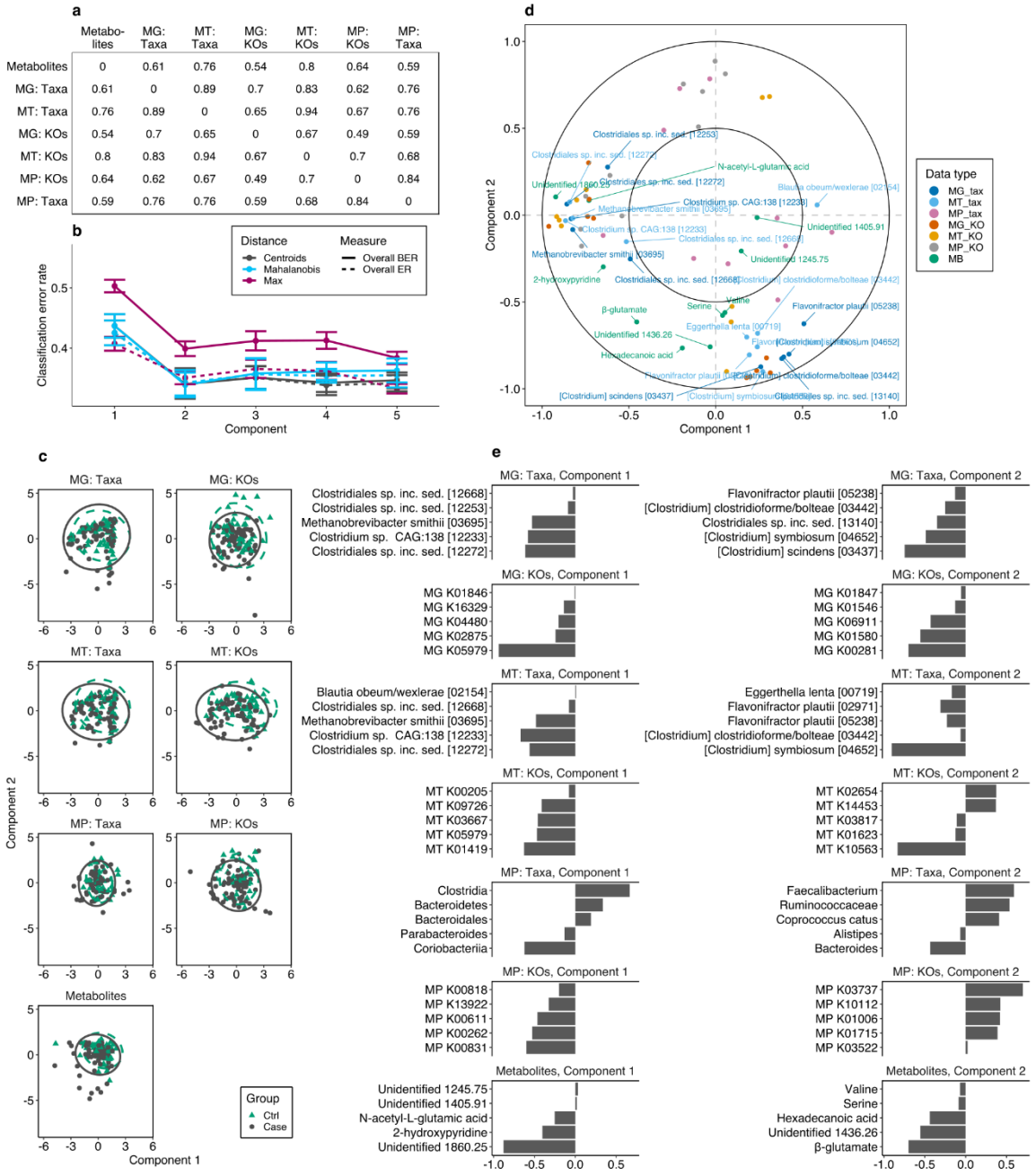

	Metabolites	MG: Taxa	MT: Taxa	MG: KOs	MT: KOs	MP: KOs	MP: Taxa
Metabolites	0	0.61	0.76	0.54	0.8	0.64	0.59
MG: Taxa	0.61	0	0.89	0.7	0.83	0.62	0.76
MT: Taxa	0.76	0.89	0	0.65	0.94	0.67	0.76
MG: KOs	0.54	0.7	0.65	0	0.67	0.49	0.59
MT: KOs	0.8	0.83	0.94	0.67	0	0.7	0.68
MP: KOs	0.64	0.62	0.67	0.49	0.7	0	0.84
MP: Taxa	0.59	0.76	0.76	0.59	0.68	0.84	0

Extended Data Figure 5 | Results of integrated multi-omics with DIABLO. The classification was run for the two-category case (iRBD or PD) vs control variable, selecting the 5 best features for differentiating between these categories on 2 axes for each of the seven data types (MG = metagenomic, MT = metatranscriptomic, MP = metaproteomic; KOs: functional annotations as represented by KEGG orthologs). **a.** Design matrix used for DIABLO, calculated based on running PLS for each pair of data blocks, **b.** Component tuning, based on which 2 was selected as the number of components to use; ER = error rate, BER = balanced error rate, error bars = standard deviations, **c.** Plots of samples and sample classes per data type; green triangles with dashed lines = controls, black circles with soldi lines = PD and iRBD patients, ellipses represent 95% confidence **d.** Correlation circle plot showing the selected features together, with labels for MG and MT taxa and metabolites, **e.** Loadings for the five selected features for each data type and component. Annotations for the selected KOs are provided in Supplementary Table 10.

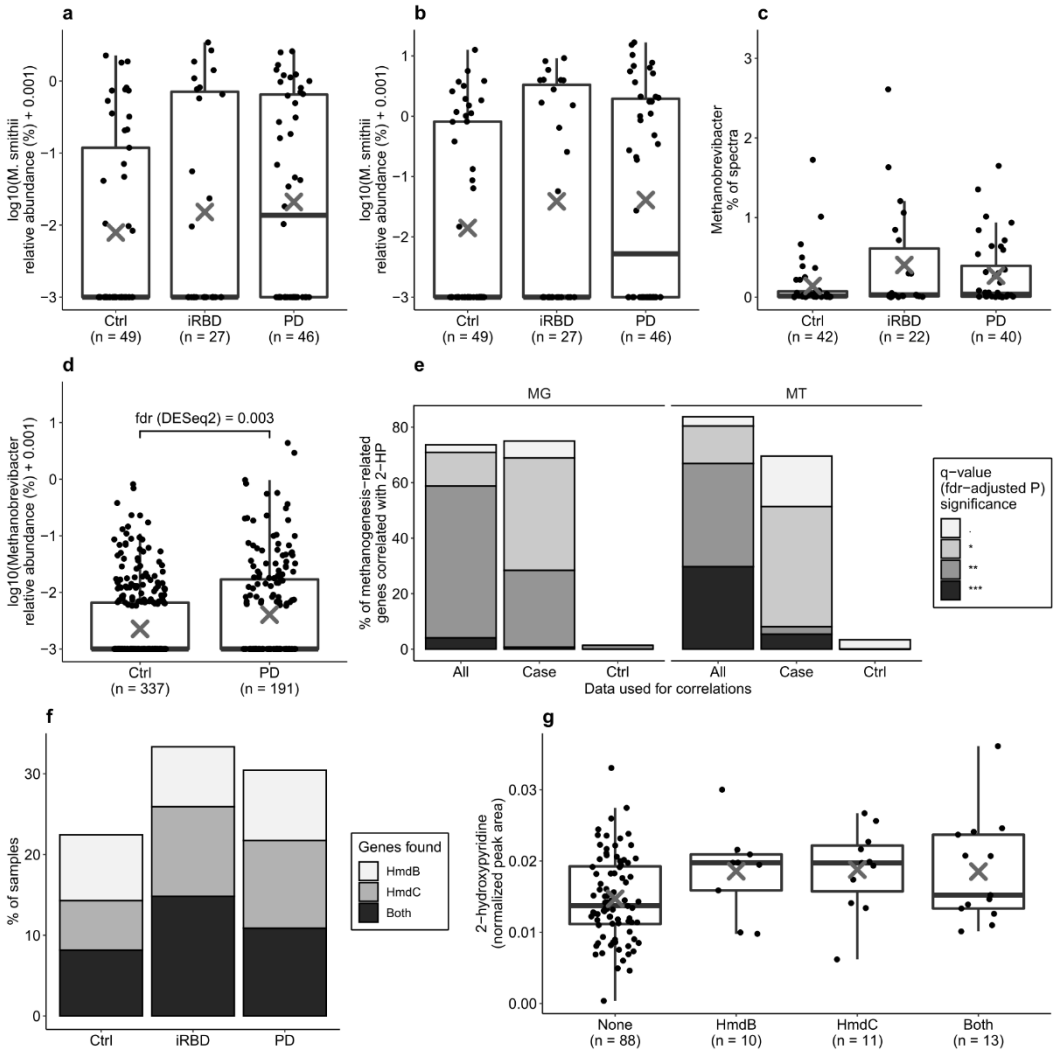

Extended Data Figure 6 | Additional results on 2-hydroxypyridine and genus *Methanobrevibacter*. **a.** log10(relative abundance) of metagenomic reads classified as *Methanobrevibacter smithii* by diagnosis group in main study cohort, **b.** log10(relative abundance) of metatranscriptomic reads classified as *Methanobrevibacter smithii* by diagnosis group in main study cohort, **c.** % of metaproteomic spectra classified as *Methanobervibacter* by diagnosis group in the main study cohort, **d.** log10(relative abundance) of 16S rRNA gene amplicons classified as *Methanobrevibacter* in the Luxembourgish NCER-PD cohort. **e.** Summaries of *q*-values (fdr-adjusted *P*-values) of correlations for 2-hydroxypyridine and 74 methanogenesis-related genes found in the sequence data (Pearson correlations, tested either in full data or with data containing samples of a specific group, as given on the x-axis). **f.** % of samples with predicted proteins containing the HmdB or HmdC genes, which code for the biosynthesis of the cofactor for Hmd. **g.** 2-hydroxypyridine normalized peak area depending on the presence of HmdB or HmdC gene in samples. MG = metagenomic data, MT = metatranscriptomic data; in boxplots, box hinges: 1st and 3rd quartiles; whiskers: hinge to highest/lowest values that is within 1.5*IQR of hinge; grey cross: mean.

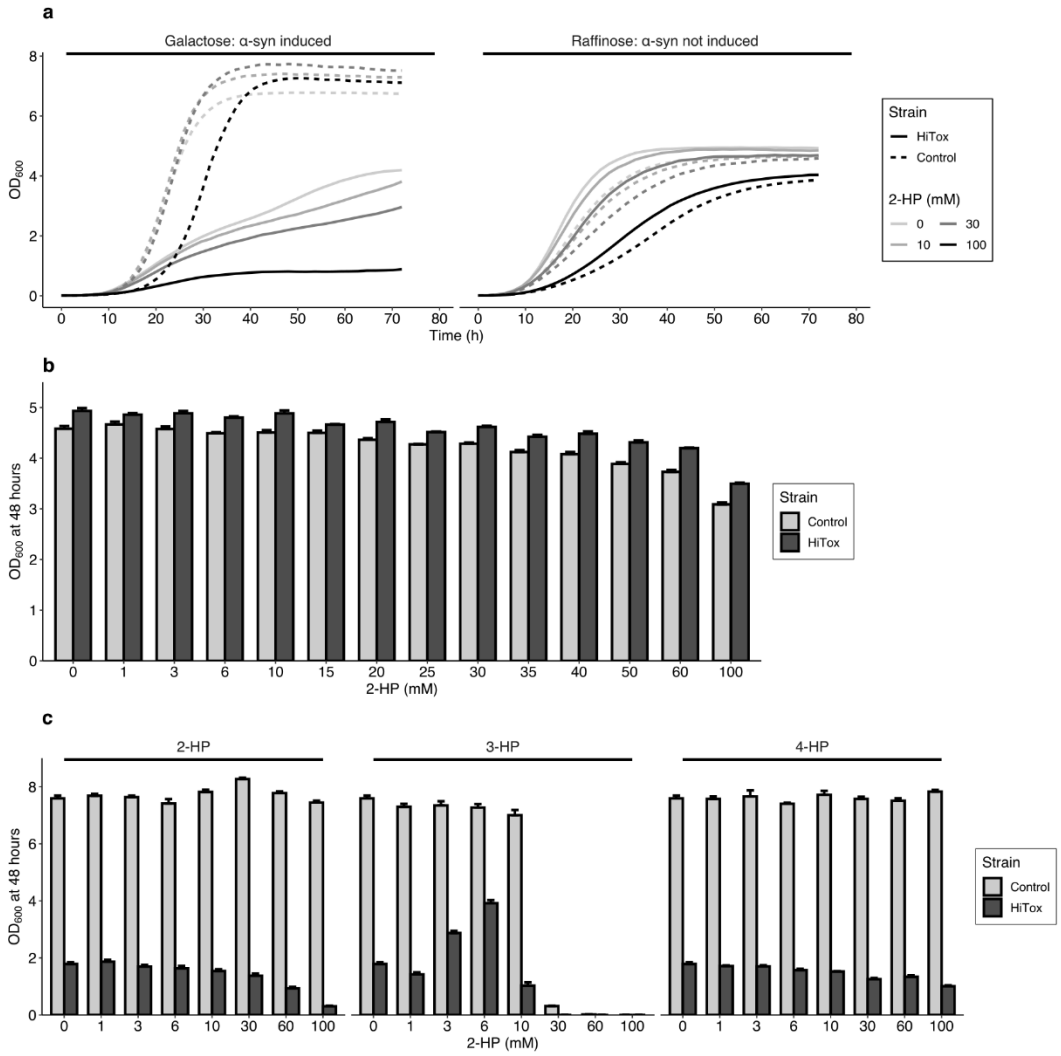

Extended Data Figure 7 | Additional results from the HiTox yeast model. a. Representative growth curves of control and HiTox strains in presence of 2-hydroxypyridine (2-HP) at the indicated concentrations. **b.** 2-HP dose-response assay in uninduced condition in HiTox and control strains. **c.** Dose-response assay in control strain and HiTox strain in aSyn-expressing condition after treatment with either 2-HP, 3-hydroxypyridine (3-HP) or 4-hydroxypyridine (4-HP). In b and c, OD_{600} was measured 48 h after inoculation and mean and SD were calculated from four biological replicates.

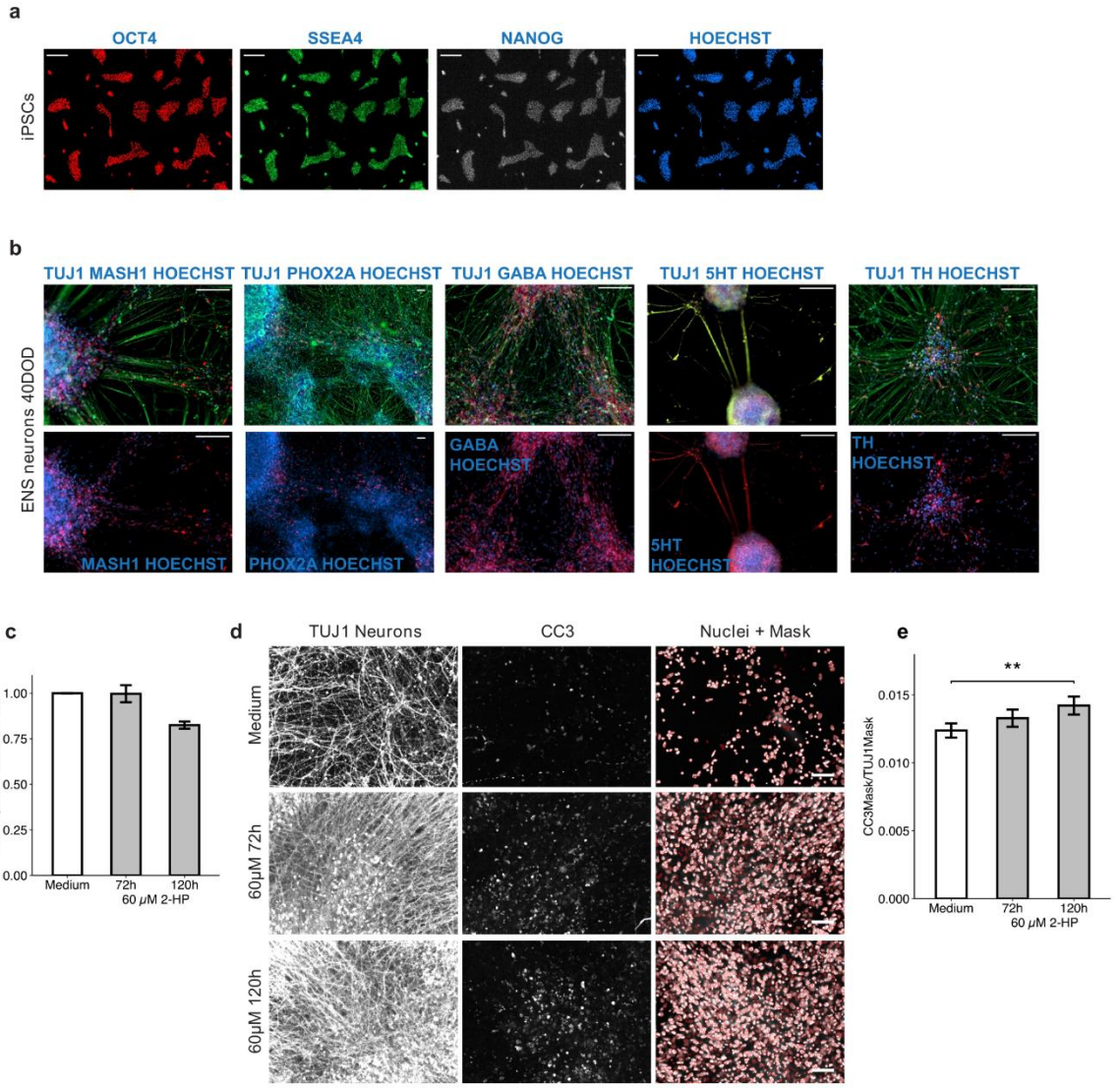

Extended Data Figure 8 | Additional results from the induced human pluripotent stem cell enteric neuron model. a. Induced human pluripotent stem cell characterization stainings show robust expression of OCT4, SEEA4 and NANOG pluripotency markers. Scale bars: 200 µm. **b.** Enteric neuron characterisation stainings at 40 days of differentiation detect presence of neural crest stem cell markers MASH1 and PHOX2A, and of different neuronal identities, such as GABAergic, serotoninergic and dopaminergic. Scale bars: 100 µm. **c.** Relative viability after 2-hydroxypyridine exposure. Comparison to untreated sample was not significant when evaluated with a Kruskal-Wallis test. **d.** High-content imaging of apoptosis marker cleaved-caspase 3 (CC3), TUJ1-positive neurons and Hoechst-positive nuclei. Nuclei images contain a representation of the mask applied to segment the nuclei; scale bar: 100 µm. **e.** Quantification of CC3-positive staining normalized to the amount of TUJ1-positive neurons. In c and d, data is represented as mean ± SEM of three independent neuronal differentiations, with 30 fields per well and 8 wells per condition quantified for each. ** $P < 0.01$.

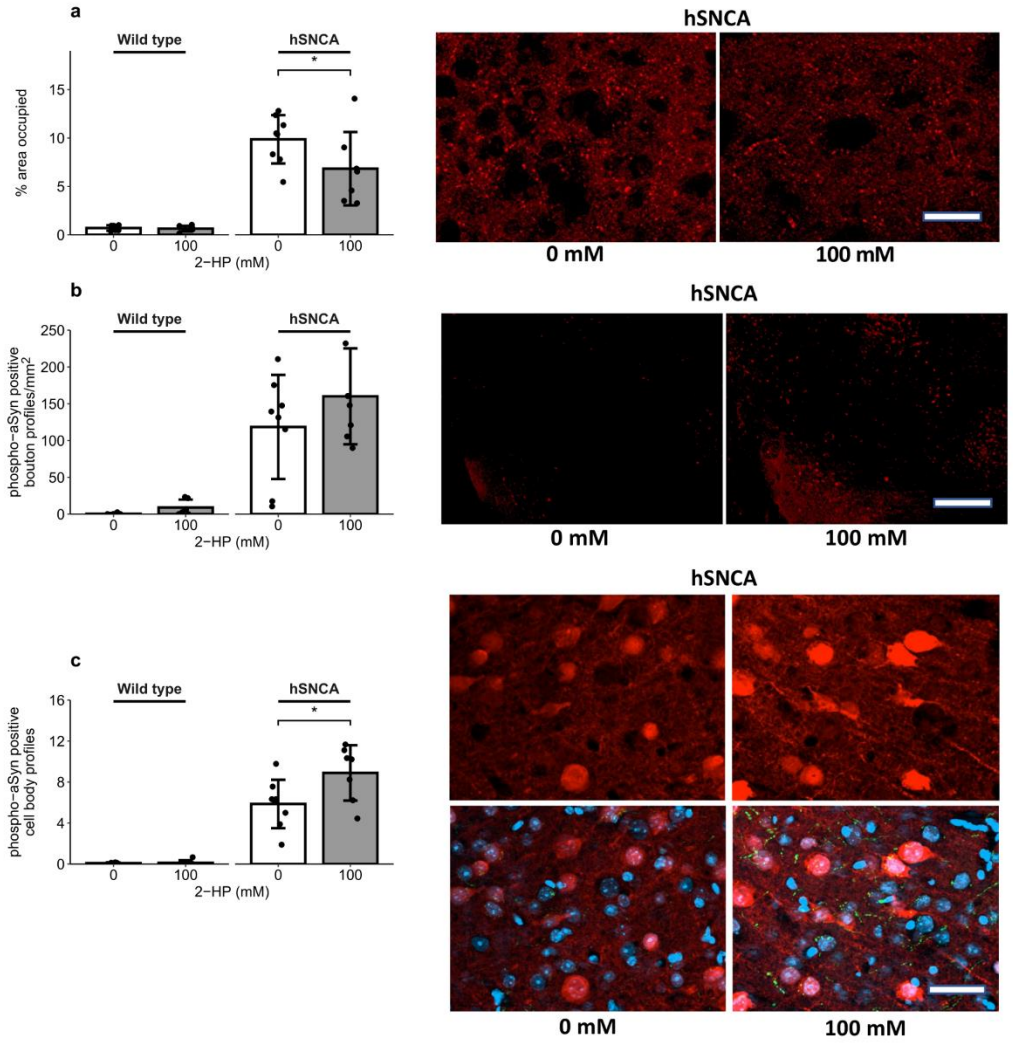

Extended Data Figure 9 | Effects of intrastriatal injections of 100 mM 2-hydroxypyridine in transgenic mouse model of PD on phospho-aSyn accumulation in different brain regions. a. Striatum: 2-HP-induced decrease of phospho-aSyn signals in synaptic boutons; scale bar: 50 µm, **b.** Substantia nigra: 2-HP-induced non-significant increase of phospho-aSyn in synaptic boutons; scale bar: 350 µm, **c.** Prefrontal cortex: 2-HP-induced significant increase of phospho-aSyn signals in cell body profiles with neuronal morphology (double-stained with DAPI, lower row of images); scale bar: 50 µm. Microphotographs show examples for 0 mM and 100 mM in hSNCA mice only. Bar plots show mean and standard deviation; n of mice = 5-8 per group. *P*-values are given between group means that are different. * $P < 0.05$.

C.2 Supplementary Tables

Extended Data Table 1 | Demographic and clinical data on study subjects

Variable	Ctrl	iRBD	PD
a. Main multi-omic analyses			
n	49	27	46
Sex (f/m/NA)	26/23/0	4/23/0	19/27/0
Constipation (no/yes/NA)	26/3/20	13/14/0	21/22/3
Antidepressant medication (no/yes/NA)	26/3/20	12/1/14	35/1/10
Metformin medication (no/yes/NA)	27/2/20	11/2/14	34/2/10
Statin medication (no/yes/NA)	27/2/20	9/4/14	31/5/10
PPI medication (no/yes/NA)	27/2/20	NA	29/7/10
Levodopa medication (no/yes/NA)	NA	NA	5/31/10
Agonist medication (no/yes/NA)	NA	NA	10/26/10
Entacapone medication (no/yes/NA)	29/0/20	13/0/14	31/5/10
Age sampling	68.14 ± 6.07	65.96 ± 7.83	65.8 ± 9.85
Disease duration months	NA	76.37 ± 56.3	63.46 ± 42.52
PD NMS sum	4.52 ± 3.05	8.31 ± 3.53	7.83 ± 3.65
UPDRS I III sum	3.31 ± 4.26	6.08 ± 4.94	31.47 ± 17
Scopa AUT sum	8.86 ± 6.22	10.17 ± 4.91	13.09 ± 6.21
Sniffin Sticks Identification	12.07 ± 2.07	7.46 ± 3.31	6.39 ± 4.15
Hoehn and Yahr	0 ± 0	0 ± 0	2.01 ± 0.77
b. 2-HP targeted validation			
n	30		30
Sex (f/m/NA)	12/18/0		8/22/0
Constipation (no/yes/NA)	27/2/1		21/9/0
Antidepressant medication (no/yes/NA)	28/2/0		24/6/0
Metformin medication (no/yes/NA)	30/0/0		29/1/0
Statin medication (no/yes/NA)	30/0/0		27/3/0
PPI medication (no/yes/NA)	30/0/0		23/7/0
Levodopa medication (no/yes/NA)	NA		2/28/0
Agonist medication (no/yes/NA)	NA		8/22/0
Entacapone medication (no/yes/NA)	30/0/0		25/5/0
Age sampling	68.63 ± 5.18		66 ± 8.25
Disease duration months	NA		94.43 ± 28.5
PD NMS sum	4.09 ± 2.11		8.55 ± 4.02
UPDRS I III sum	1.27 ± 2.39		38.27 ± 21.87
Scopa AUT sum	7.5 ± 4.09		14.74 ± 8.52
Sniffin Sticks Identification	12.93 ± 2.26		6.79 ± 3.76
Hoehn and Yahr	0 ± 0		2.05 ± 0.88
c. NCER-PD cohort (16S rRNA gene amplicons)			
n	343		194
Sex (f/m/NA)	145/198/0		63/131/0
Constipation (no/yes/NA)	325/18/0		116/78/0
Levodopa medication (no/yes/NA)	341/2/0		55/139/0
Other dopaminergic treatment (no/yes/NA)	340/3/0		45/149/0
Age sampling	60.15 ± 12.25		67.09 ± 9.69
Age at PD onset	NA		61.15 ± 10.99

NA = data not available, Ctrl = control subject, PD = Parkinson's disease patient, iRBD = patient with idiopathic REM sleep behavior disorder, PPI = proton pump inhibitor, PD NMS = Non-Motor Symptoms questionnaire, UPDRS I III = Unified Parkinson's Disease Rating Scale, Scopa AUT = Scales for Outcomes in Parkinson's Disease - Autonomic Dysfunction.

Appendix D

D.1 Supplementary Figures

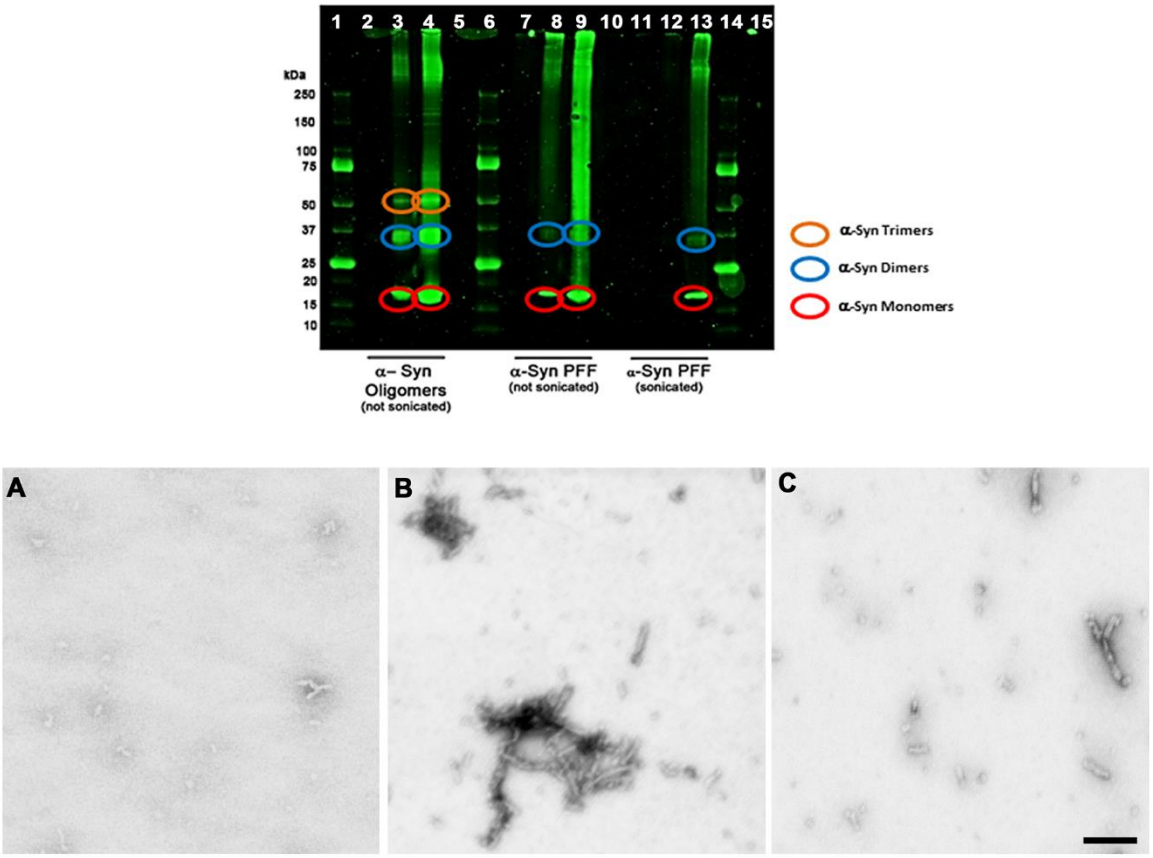

Figure S1 Upper panel: Western blot characterization of α-syn moieties used for intrastriatal injections. Loading of the gel was as follows: lanes 1, 6, 14 – ladder; lanes 5, 10,11- blank; lanes 2,3,4 – α-syn oligomer, 10, 100, and 500 ng respectively; lanes 7, 8, 9 – α-syn PFFs, not sonicated, 10,100, 500 ng respectively; lanes 11, 12, 13 – α-syn PFFs (sonicated), 10,100, 500 ng respectively. Bands from corresponding to the MW of α-syn monomers, dimers, and trimmers are circled (red, blue, orange, respectively). Note the presence of high molecular weight moieties (visible as a smear) after loading of non-sonicated PFFs. The sonication process of PFFs appears to reduce all higher molecular weight species of α-syn and the amount of dimers and monomers, since smears and monomer/dimer bands were visible after loading 100 ng of non-sonicated PFFs, but not after loading the same amount of sonicated PFFs. Lower panels: Electron microscopy of α-syn moieties. A: Oligomers; B: unsonicated α-syn PFFs; C: sonicated α-syn PFFs. Oligomers were primarily composed of small globular moieties. Unsonicated PFFs contained many large assemblies of α-syn fibrils, whereas sonicated PFFs were composed mainly of small fibrillar fragments, resulting from the sonication-induced disruption of the large assemblies. Scale bar = 152 nm.

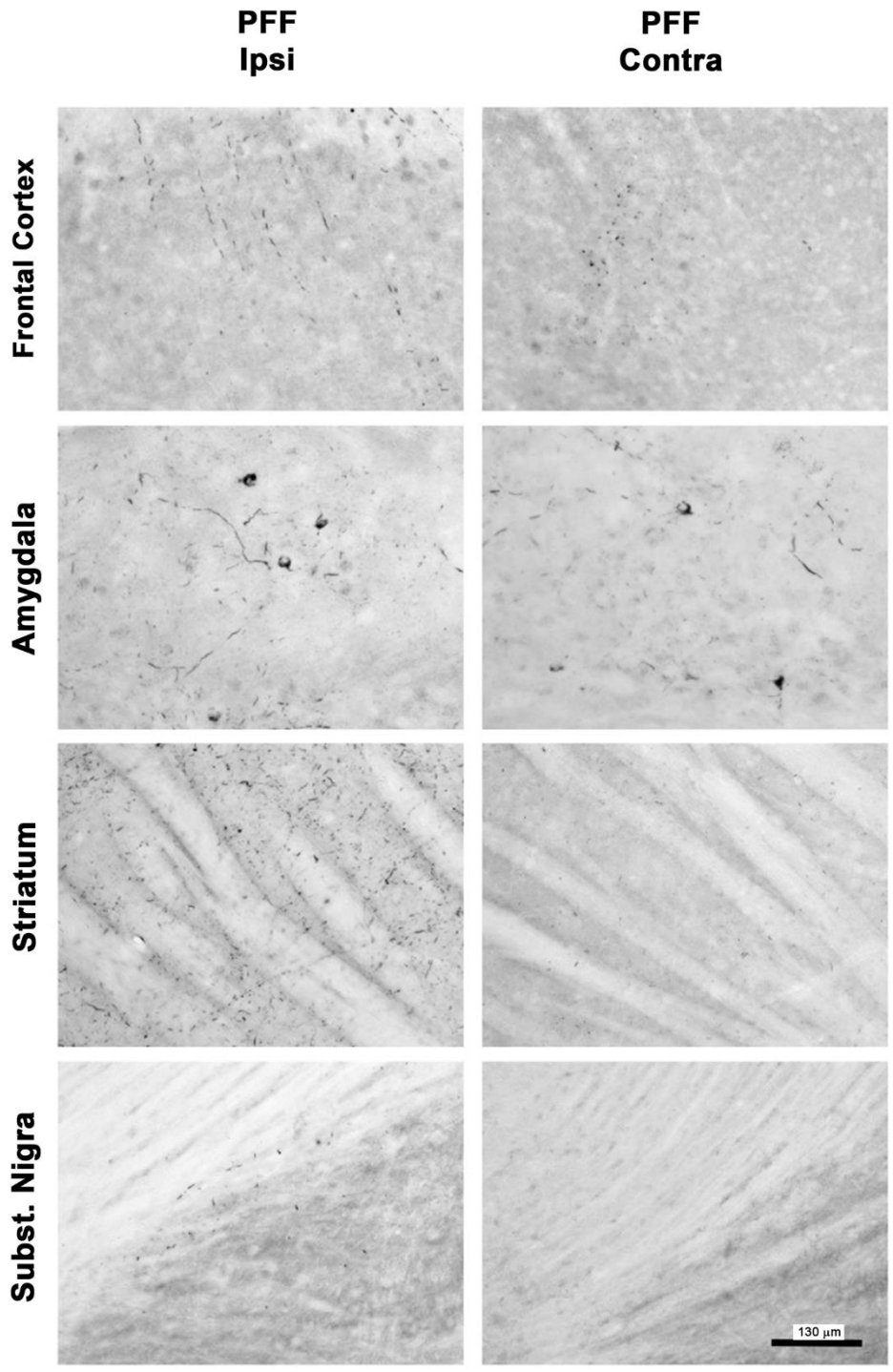

Figure S2 Minimal presence of α-syn inclusions in different brain regions 13 DPI after intrastriatal injection of α-syn PFFs. Only few α-syn inclusions were seen, ipsi- and contralaterally, in the frontal cortex, amygdala, and ipsilaterally, but not contralaterally, in the striatum and SN. Scale bar = 130 µm.

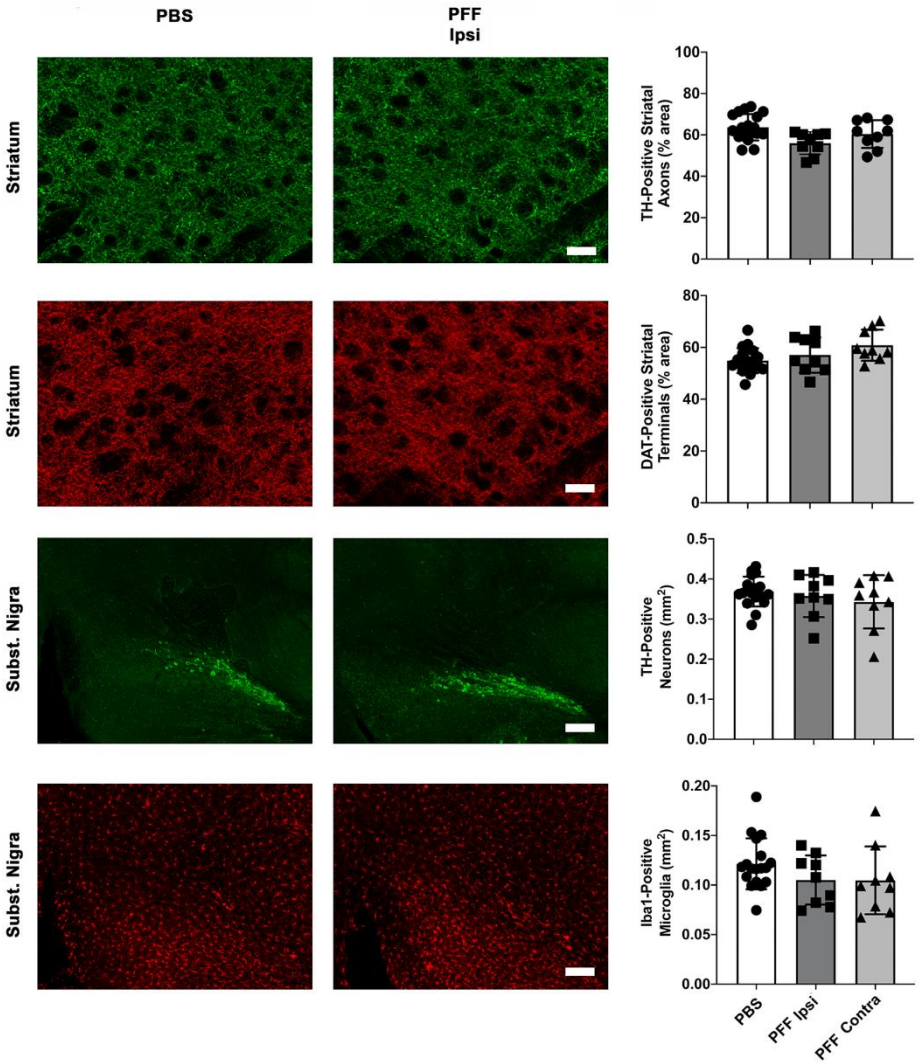

Figure S3 No nigro-striatal degeneration and microgliosis 13 dpi after intrastriatal injection of α-syn PFFs. No loss of striatal TH-positive axons (first row), striatal DAT-positive synaptic terminals (second row), nigral TH-positive neurons (third row) was observed 13 dpi after injection of PFFs. No increase of Iba1-positive microglial reaction in the SN was observed (last row). Microphotographs show examples of PBS-injected control brains (ipsilateral) and ipsilateral α-syn PFF-injected brains. Scale bars = 25 µm (striatal panels), 200 µm (Subst. Nigra panels).

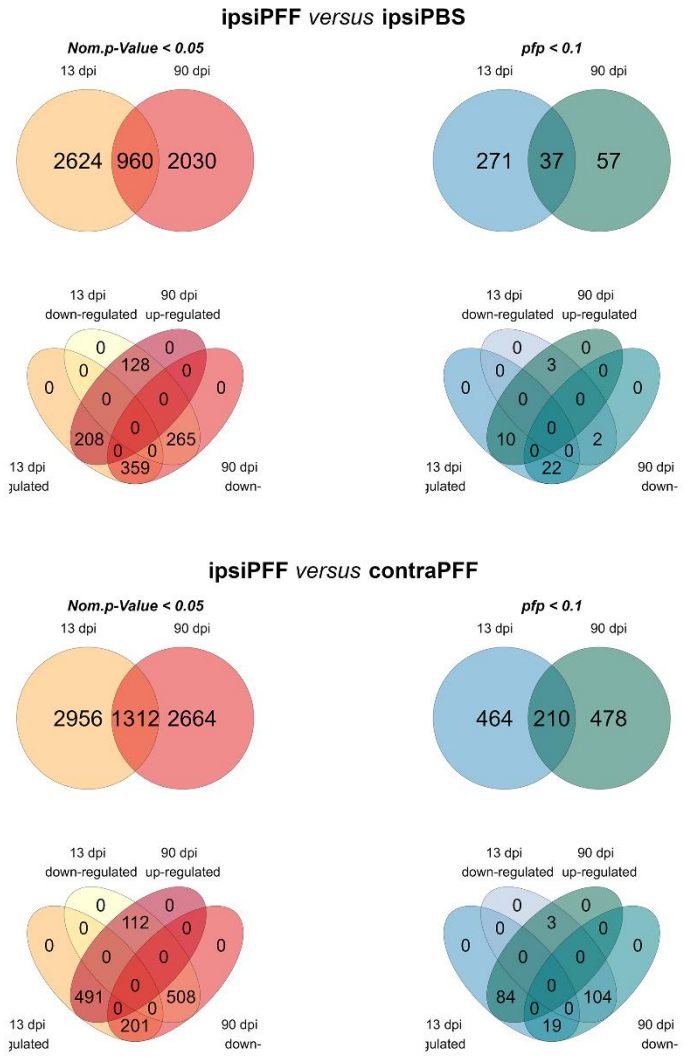

Figure S4 Venn diagrams of DEGs induced in the ventral midbrain of mice at 13 dpi and 90 dpi after striatal injections of α-syn PFFs. Comparisons for each time point were made between DEGs in ipsilateral ventral midbrain of PFF-injected mice versus those in the ipsilateral ventral midbrain for PBS-injected mice (ipsi PFF vs. ipsi PBS, *n* = 6/group; upper 4 panels), and between DEGs in ipsilateral ventral midbrain versus the contralateral ventral midbrains of PFF-injected mice (ipsi PFF vs. contra PFF, *n* = 6/group; lower 4 panels). Diagrams on the left show Venn diagrams with numbers of DEGs with a significance level of $p < .05$ (*n* = 6 mice/group). Because some gene products have an effect within biological pathways while the expression of their genes may only change minimally, we show DEGs that emerge with this low level of statistical stringency. In ipsi PFF vs. ipsi PBS, the number of DEGs was 2631 at 13 DPI, and 2584 at 90 DPI, with 985 DEGs common to both time points. In ipsi PFF vs. 3584 at 13 DPI, and 2990 at 90 DPI, with 960 DEGs common to both time points. In ipsi PFF vs. contra PFF, the number of DEGs was 4268 at 13 DPI, and 3976 at 90 DPI, with 1312 DEGs common to both time points. Panels on the right show Venn diagrams with the number of DEGs after adjusting for multiple hypothesis testing at pfp < 0.1. In ipsi PFF vs. ipsi PBS, the number of DEGs was 308 at 13 DPI, and 94 at 90 DPI, with 37 DEGs common to both time points. In ipsi PFF vs. contra PFF, the number of DEGs was 674 at 13 DPI, and 688 at 90 DPI, with 210 DEGs common to both time points. The Venn diagrams below the main ones indicate the number of DEGs that show enhanced ("up") versus decreased ("down"), as well as the overlaps, in the different comparisons.

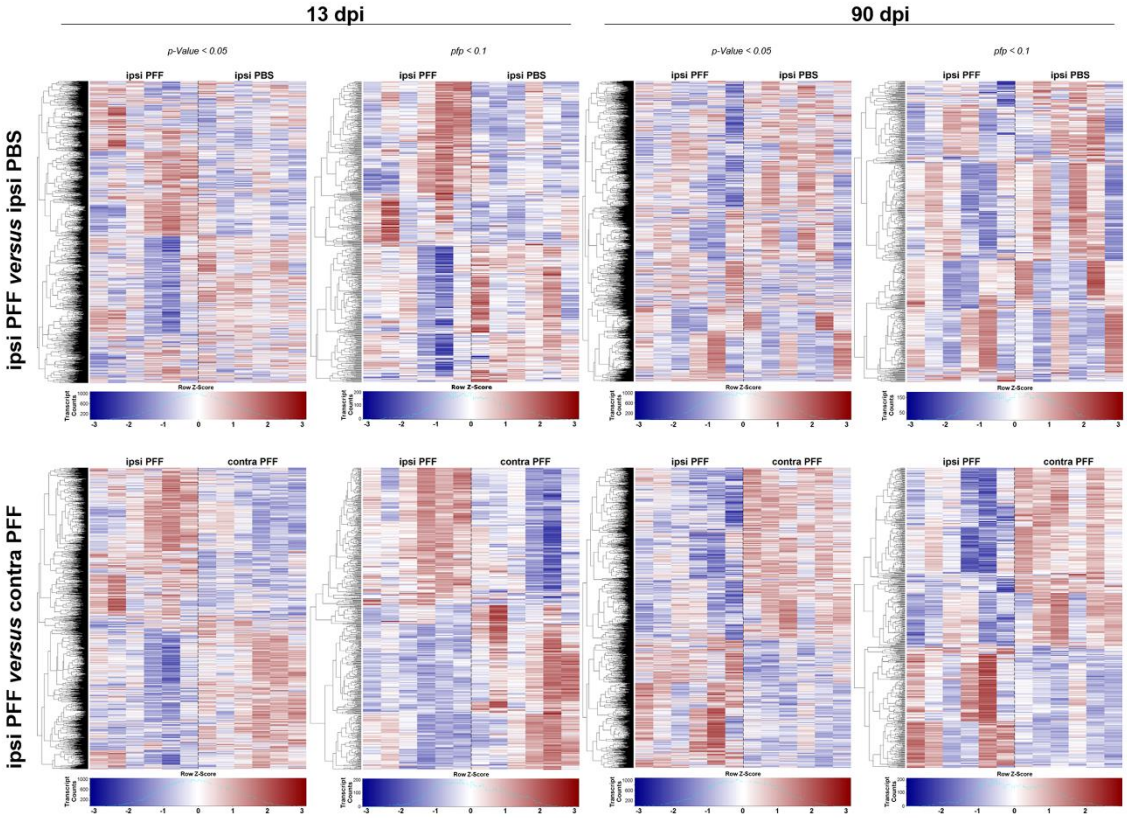

Figure S5 Heatmaps illustrating the ventral midbrain gene expression patterns at 13 dpi and 90 dpi after intrastriatal injection of α-syn PFFs. Heatmaps are shown for p-values <0.05 or pfp < 0.1. Scaled row expression values (row Z-score) in red indicate higher, in blue lower, and in white unchanged gene expression (see Materials and Methods for details). Comparisons of ipsi PFF versus ipsi PBS (upper panel row) and ipsi PBS versus contra PFF (lower panel row) reveal distinctive gene expression patterns at 13 dpi for both comparisons (whether higher, pfp < 0.1, or lower, p < 0.05, statistical stringency is used), whereas a distinctive pattern at 90 dpi only appears in the ipsi PFF versus contra PFF, but not in the ipsi PFF versus ipsi PBS, comparisons.

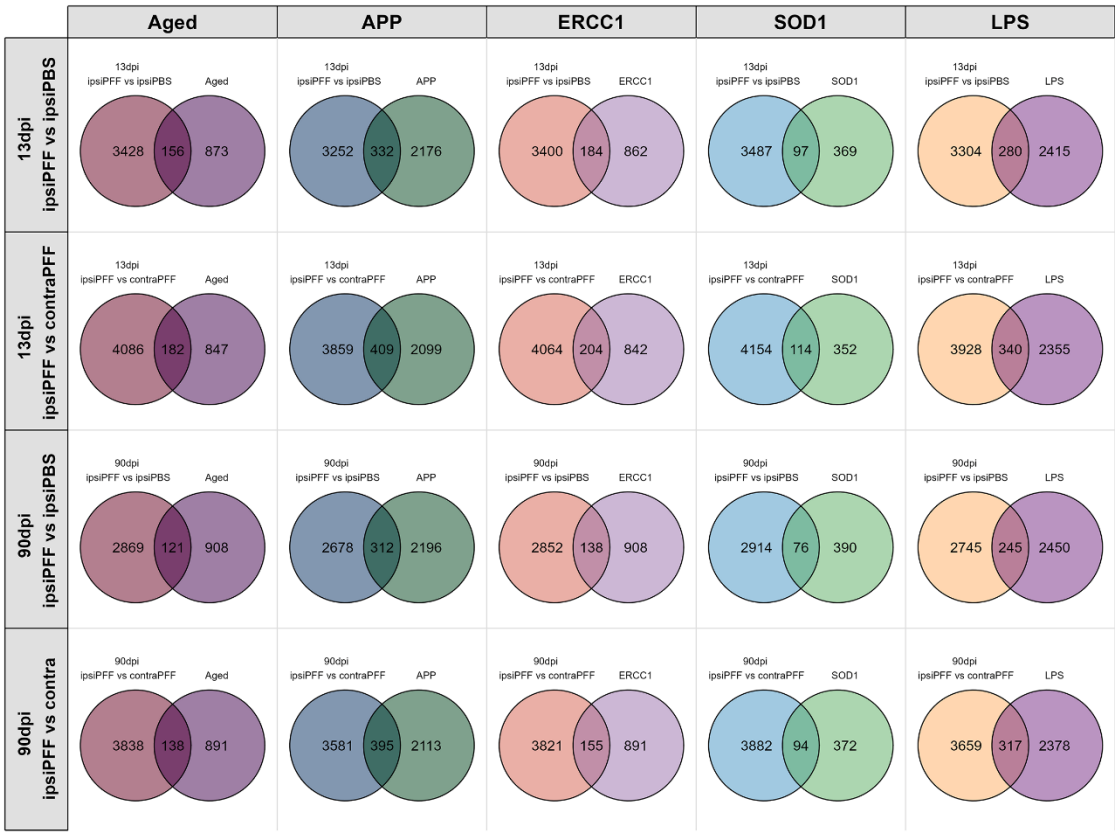

Figure S6 Venn diagrams of DEGs, induced in the ventral midbrain of mice at 13 dpi and 90 dpi after striatal injections of α-syn PFFs, overlapping with DEGs of isolated microglia from different neurological disease models. APP stands for Alzheimer model mice, ERRCC1 mice are a model of premature aging, SOP1 mice are a model for amyotrophic lateral sclerosis, and LPS are mice injected with endotoxin. See main text for details and literature reference.

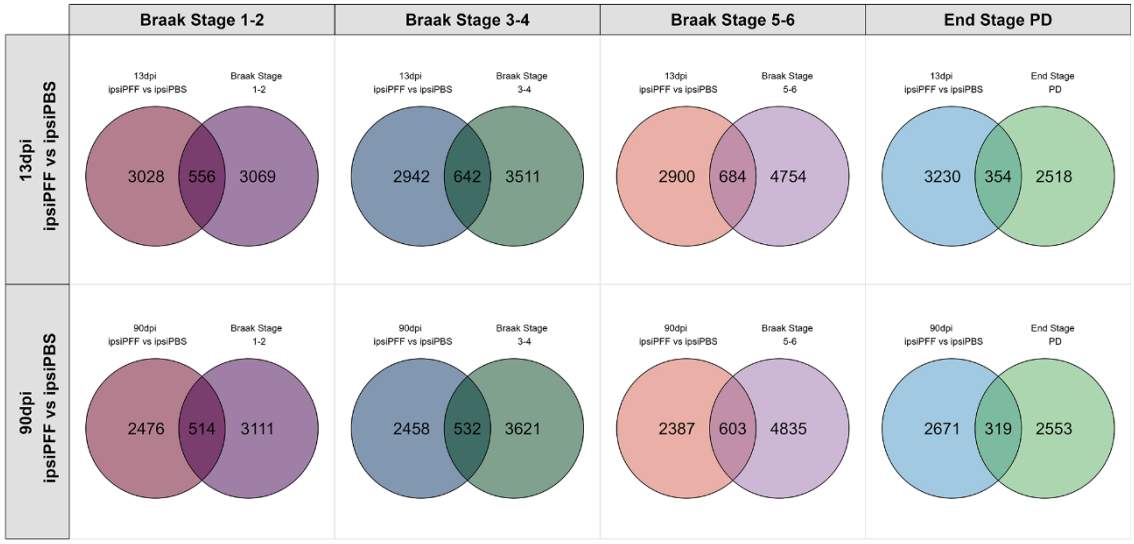

Figure S7 Venn diagrams of DEGs, induced in the ventral midbrain of mice at 13 dpi and 90 dpi after striatal injections of α-syn PFFs, overlapping with DEGs from PD databases. No clear pattern was observed at this level of analysis. See man text for details and literature references.

D.2 Supplementary Tables

antigen	species	Manu-facturer	dilution	blocking	Secondary antibody
alpha synuclein phospho S129	Rabbit polyclonal	Abcam Ab51253	1:2000	5% horse serum (immo-peroxidase) 5% BSA (immuno-fluorescence)	biotynilated goat-anti-rabbit (Vector Laboratories) Alexa 488 anti-rabbit Alexa 568 anti-rabbit
11A5 Anti SER p129 α-syn	Mouse monoclonal	Prothena	n/a	n/a	PLA assay
ionized calcium-binding adapter molecule 1 (Iba1)	Chicken polyclonal	Abcam Ab139590	1:800	5% BSA	Alexa 568 anti-chicken
Iba1	Rabbit polyclonal	Wako 019-19741	1:2000	5% BSA	Alexa 568 anti-rabbit
Tyrosine hydroxylase (TH)	Chicken polyclonal	Abcam Ab76442	1:1000	5% BSA	Alexa 488 anti-chicken
Tyrosine Hydroxylase (TH)	Rabbit polyclonal	Millipore AB152	1:1000	5% BSA	Alexa 568 anti-rabbit
Dopamine transporter (DAT)	Rat monoclonal	Millipore MAB369	1:1000	5% BSA	Alexa 594 anti-rat
Synapto-physin	Mouse monoclonal	Dakopatts Clone SY38	1:800	5% BSA	Alexa 488 anti-mouse

Table S1 Antibodies used.

Name of Software or Package	Vendor or public url	Uses
PRISM 7 (v. 7.04)	GraphPad Software Inc. (https://www.graphpad.com/)	Basic statistics (normality test, ANOVA, Kruskall-Wallis, posthoc test for multiple groups)
R (v. 3.4.3)	The R Foundation (https://www.r-project.org/)	Basic Statistical Computing and Data Manipulation
R Studio (v. 1.1.414)	https://www.rstudio.com/	User Interface for R
RankProd (v. 3.4.0)	Bioconductor (DOI: 10.18129/B9.bioc.RankProd)	Differential Gene Expression Analysis for Microarray Datasets. A non-parametric approach. FDR statistics.
VennDiagram (v. 1.6.20)	CRAN – R (https://CRAN.R-project.org/package=VennDiagram)	Generate High-Resolution Venn and Euler Plots
GSEA (v. 3.0)	Broad Institue, Inc. (http://www.gsea-msigdb.org/gsea/index.jsp)	Analyze, annotate and interpret enrichment results
Cytoscape (v. 3.6.1)	The Cytoscape Consortium (http://manual.cytoscape.org/en/3.6.0/)	Visualizing complex networks from GSEA

Table S2 Softwares used

Comparison	***Microglia Subtype***	*Gene Symbols*	*FC*	*Nom.pVal*	*Pfp*
13dpi ipsiPFF vs ipsiPBS	**Immune alerted**	Cd14	1.439	3.01E-05	1.56E-02
		H2-Ab1	1.357	1.51E-04	4.01E-02
		Rrad	-1.296	6.33E-04	1.37E-01
		Nfkbia	1.318	6.38E-04	1.01E-01
		Cdkn1a	1.309	7.28E-04	1.11E-01
		Cd74	1.282	1.65E-03	1.82E-01
		Fos	-1.193	3.72E-03	3.48E-01
		Gpr84	1.229	7.86E-03	4.10E-01
		Egr1	-1.035	1.17E-02	5.31E-01
		Btg2	1.101	1.08E-02	4.81E-01
		H2-Aa	1.135	1.52E-02	5.50E-01
		Gadd45b	1.201	1.65E-02	5.72E-01
		Ccl4	1.201	1.87E-02	5.98E-01
		Csf1	1.184	2.62E-02	6.82E-01
		Dusp1	1.067	2.84E-02	7.02E-01
		Tbca	-1.117	3.04E-02	7.47E-01
		Klf2	1.073	2.97E-02	7.10E-01
		Evi2a	1.151	3.20E-02	7.29E-01
		Atf3	1.17	3.65E-02	7.62E-01
		Mir692-1	1.158	3.72E-02	7.68E-01
	Intermediate	Fcrls	1.423	3.93E-05	1.87E-02
		Ttr	-1.188	7.10E-04	1.46E-01
		C1qa	1.372	1.04E-04	3.39E-02
	Homeostatic	Hexb	1.338	4.14E-04	7.69E-02
		Cx3cr1	1.203	1.57E-02	5.60E-01
13dpi ipsiPFF vs contraPFF	**Immune alerted**	H2-Ab1	1.607	8.31E-07	6.38E-04
		Gpr84	1.55	2.43E-06	1.26E-03
		Cd74	1.535	4.47E-06	1.94E-03
		Cd14	1.529	5.20E-06	2.19E-03
		H2-Aa	1.372	2.88E-04	3.97E-02
		Rrad	-1.333	6.65E-04	7.96E-02
		Egr1	1.238	2.16E-03	1.40E-01
		Atf3	1.294	2.54E-03	1.54E-01
		H2-K1	1.269	4.24E-03	2.07E-01
		Evi2a	1.235	7.76E-03	2.88E-01
		Ccl4	1.223	1.29E-02	3.77E-01
		Junb	1.202	1.45E-02	4.03E-01
		Mir692-1	1.217	1.56E-02	4.16E-01
		Adamts1	1.195	1.71E-02	4.34E-01
		Cd83	-1.161	2.98E-02	6.03E-01
		Gadd45b	1.192	2.87E-02	5.62E-01
		Il1a	1.172	3.09E-02	5.76E-01
		Snapc1	-1.176	3.51E-02	6.47E-01
		Cdkn1a	1.039	4.42E-02	6.70E-01
		Btg2	1.147	4.81E-02	6.95E-01
		Dusp1	1.07	4.90E-02	6.99E-01
	Intermediate	Fcrls	1.762	4.54E-08	7.31E-05
		P2ry12	1.257	5.29E-03	2.36E-01
		Ttr	1.1	2.17E-02	4.91E-01
		C1qa	1.547	1.80E-06	1.06E-03
	Homeostatic	Hexb	1.427	7.98E-05	1.66E-02
		Cx3cr1	1.338	7.29E-04	7.33E-02
90dpi ipsiPFF vs ipsiPBS	**Immune alerted**	Jun	-1.367	5.39E-04	1.41E-01
		Dusp1	-1.269	4.27E-03	3.62E-01
		Egr1	-1.206	6.94E-03	4.20E-01
		Klf2	-1.223	1.28E-02	5.12E-01
		Btg2	-1.185	1.42E-02	5.36E-01
		Adamts1	-1.222	1.50E-02	5.41E-01
		Mir692-1	-1.212	2.17E-02	6.10E-01
		Jund	-1.187	3.40E-02	6.98E-01
		H3f3b	-1.173	4.88E-02	7.66E-01
	Intermediate	Ttr	-1.303	6.95E-04	1.66E-01
90dpi ipsiPFF vs contraPFF	**Immune alerted**	Gadd45b	1.253	5.97E-03	2.74E-01
		Klf6	-1.226	1.43E-02	3.99E-01
		Cd83	-1.205	1.97E-02	4.65E-01
		Casp4	1.192	4.19E-02	6.59E-01
		Dusp1	-1.142	4.10E-02	6.18E-01
		Rrad	-1.153	4.37E-02	6.35E-01
		Jun	-1.115	4.69E-02	6.47E-01
	Intermediate	Ttr	1.439	4.87E-05	1.29E-02
	Homeostatic	Cx3cr1	1.239	9.81E-03	3.50E-01
		Hspa1a	1.149	4.76E-02	6.82E-01

Table S3 Overlapping genes of the datasets of the α-syn seeding/spreading model at 13dpi and 90 dpi with genes of microglial subtypes isolated from the nigro-striatal circuit. See main text for details.

Comparison	*Gene Symbols*	*Gene Name*	*FC*	*Nom.pVal*	*Pfp*
13dpi ipsiPFF vs ipsiPBS	Spp1	secreted phosphoprotein 1	1.921	8.25E-10	9.29E-06
	Cst7	cystatin F (leukocystatin)	1.921	1.93E-09	1.63E-05
	Ch25h	cholesterol 25-hydroxylase	1.470	1.93E-05	1.09E-02
	Cybb	cytochrome b-245, beta polypeptide	1.407	5.17E-05	2.24E-02
	Vat1	vesicle amine transport protein 1 homolog (T californica)	-1.291	1.23E-03	1.98E-01
	Gpr65	G-protein coupled receptor 65	1.287	1.90E-03	2.01E-01
	Ctsz	cathepsin Z	1.249	3.43E-03	2.68E-01
	Cxcl16	chemokine (C-X-C motif) ligand 16	1.256	3.97E-03	2.88E-01
	Rnase6	ribonuclease, RNase A family, 6	-1.268	3.15E-03	3.27E-01
	Cd9	CD9 antigen	1.208	7.46E-03	4.00E-01
	Gpr84	G protein-coupled receptor 84	1.229	7.86E-03	4.10E-01
	Egr1	early growth response 1	-1.035	1.17E-02	5.31E-01
	Kcnj2	potassium inwardly-rectifying channel, subfamily J, member 2	1.208	1.44E-02	5.36E-01
	Tlr2	toll-like receptor 2	1.199	1.51E-02	5.48E-01
	Selplg	selectin, platelet (p-selectin) ligand	1.178	1.93E-02	6.07E-01
	Ccr5	chemokine (C-C motif) receptor 5	1.185	2.07E-02	6.24E-01
	Csf1	colony stimulating factor 1 (macrophage)	1.184	2.62E-02	6.82E-01
	Cd63	CD63 antigen	1.180	3.36E-02	7.37E-01
	Npm1	NA	-1.119	4.11E-02	8.19E-01
	Slco2b1	solute carrier organic anion transporter family, member 2b1	1.170	4.63E-02	8.25E-01
	Abca1	ATP-binding cassette, sub-family A (ABC1), member 1	1.123	4.66E-02	8.27E-01
13dpi ipsiPFF vs contraPFF	Cst7	cystatin F (leukocystatin)	2.412	4.09E-13	3.46E-09
	Spp1	secreted phosphoprotein 1	2.232	2.28E-12	1.28E-08
	Ch25h	cholesterol 25-hydroxylase	1.683	2.72E-07	2.97E-04
	Gpr84	G protein-coupled receptor 84	1.550	2.43E-06	1.26E-03
	Vat1	vesicle amine transport protein 1 homolog (T californica)	-1.408	7.97E-05	1.75E-02
	Cd9	CD9 antigen	1.418	1.02E-04	1.98E-02
	Cybb	cytochrome b-245, beta polypeptide	1.413	1.09E-04	2.06E-02
	Cxcl16	chemokine (C-X-C motif) ligand 16	1.389	1.86E-04	2.99E-02
	Selplg	selectin, platelet (p-selectin) ligand	1.332	7.98E-04	7.89E-02
	Gpr65	G-protein coupled receptor 65	1.322	1.09E-03	9.44E-02
	Egr1	early growth response 1	1.238	2.16E-03	1.40E-01
	Ctsz	cathepsin Z	1.286	2.79E-03	1.62E-01
	P2ry12	purinergic receptor P2Y, G-protein coupled 12	1.257	5.29E-03	2.36E-01
	Rassf3	Ras association (RalGDS/AF-6) domain family member 3	1.167	6.00E-03	2.49E-01
	Ccr5	chemokine (C-C motif) receptor 5	1.255	6.65E-03	2.63E-01
	Upk1b	uroplakin 1B	1.250	7.16E-03	2.73E-01
	Kcnj2	potassium inwardly-rectifying channel, subfamily J, member 2	1.235	1.07E-02	3.43E-01
	Tlr2	toll-like receptor 2	1.196	2.15E-02	4.89E-01
	Id2	inhibitor of DNA binding 2	1.206	2.37E-02	5.14E-01
	P2ry13	purinergic receptor P2Y, G-protein coupled 13	1.195	2.41E-02	5.19E-01
	Lilr4b	leukocyte immunoglobulin-like receptor, subfamily B, member 4B	1.170	3.53E-02	6.14E-01
	Slco2b1	solute carrier organic anion transporter family, member 2b1	1.187	3.75E-02	6.29E-01
	Ifitm3	interferon induced transmembrane protein 3	1.163	4.09E-02	6.52E-01
90dpi ipsiPFF vs ipsiPBS	Ifitm3	interferon induced transmembrane protein 3	-1.358	8.19E-04	1.81E-01
	Spp1	secreted phosphoprotein 1	-1.235	1.48E-03	2.24E-01
	Cybb	cytochrome b-245, beta polypeptide	-1.221	5.36E-03	3.95E-01
	Cdk5r1	cyclin-dependent kinase 5, regulatory subunit 1 (p35)	-1.247	6.36E-03	4.21E-01
	Egr1	early growth response 1	-1.206	6.94E-03	4.20E-01
	Ch25h	cholesterol 25-hydroxylase	-1.234	7.48E-03	4.32E-01
	Cxcl16	chemokine (C-X-C motif) ligand 16	-1.193	7.84E-03	4.44E-01
	Vat1	vesicle amine transport protein 1 homolog (T californica)	-1.209	9.25E-03	4.65E-01
	Kcnj2	potassium inwardly-rectifying channel, subfamily J, member 2	1.021	9.55E-03	5.57E-01
	Rassf3	Ras association (RalGDS/AF-6) domain family member 3	-1.169	1.50E-02	5.41E-01
	Anxa2	annexin A2	-1.168	1.83E-02	5.76E-01
	Selplg	selectin, platelet (p-selectin) ligand	-1.185	3.49E-02	7.03E-01
	Gpr65	G-protein coupled receptor 65	-1.159	4.56E-02	7.51E-01
90dpi ipsiPFF vs contraPFF	Rassf3	Ras association (RalGDS/AF-6) domain family member 3	-1.589	7.57E-07	5.56E-04
	Spp1	secreted phosphoprotein 1	1.441	4.55E-05	1.23E-02
	Vat1	vesicle amine transport protein 1 homolog (T californica)	-1.427	4.82E-05	1.04E-02
	Cdk5r1	cyclin-dependent kinase 5, regulatory subunit 1 (p35)	-1.357	4.32E-04	4.77E-02
	Kcnj2	potassium inwardly-rectifying channel, subfamily J, member 2	1.176	7.77E-03	3.15E-01
	Cxcl16	chemokine (C-X-C motif) ligand 16	1.219	8.39E-03	3.28E-01
	Sh3pxd2b	SH3 and PX domains 2B	-1.246	8.65E-03	3.12E-01
	Capg	capping protein (actin filament), gelsolin-like	1.225	1.84E-02	4.83E-01
	Ifitm3	interferon induced transmembrane protein 3	1.155	2.49E-02	5.45E-01
	Cst7	cystatin F (leukocystatin)	1.194	3.27E-02	6.01E-01
	Cd9	CD9 antigen	1.161	3.68E-02	6.27E-01
	Anxa2	annexin A2	1.172	3.87E-02	6.42E-01
	Ch25h	cholesterol 25-hydroxylase	1.156	4.52E-02	6.74E-01
	P2ry13	purinergic receptor P2Y, G-protein coupled 13	1.183	4.98E-02	6.93E-01

Table S4 Overlapping genes of the α-syn seeding/spreading model at 13dpi and 90 dpi with genes of a disease-associated microglia core signature (see main text for details).

Gene Symbol	Protein	ipsi PFF *versus* ipsi PBS						ipsi PFF *versus* contra PFF					
		13dpi			90dpi			13dpi			90dpi		
		FC	p-Value	pfp	FC	p-Value	pfp	FC	p-Value	pfp	FC	p-Value	pfp
Cybb	**NAPDH oxidase 2**	1.407	**5.17E-05**	**2.24E-02**	-1.221	**5.36E-03**	3.95E-01	1.413	**1.09E-04**	**2.06E-02**	1.155	7.08E-02	7.60E-01
Ptgs2	**Cyclooxygenase 2**	1.285	**1.50E-03**	1.74E-01	-1.189	**1.18E-03**	2.06E-01	1.506	**1.28E-05**	**4.52E-03**	1.436	**8.06E-05**	**1.84E-02**
Cxcl10	**Chemokine (C-X-C motif) ligand 10**	1.226	**6.11E-03**	3.62E-01	-1.141	1.03E-01	9.28E-01	1.344	**7.64E-04**	**7.62E-02**	-1.003	5.15E-01	1.10E+00
Cd86	**CD86 antigen**	1.112	8.32E-02	9.65E-01	-1.139	5.96E-02	8.08E-01	1.304	**2.08E-03**	1.38E-01	1.073	1.87E-01	9.36E-01
Il1b	Interleukin 1 beta	1.131	8.25E-02	9.62E-01	1.071	3.38E-01	1.04E+00	1.085	2.54E-01	1.06E+00	1.091	2.41E-01	9.72E-01
Il6	Interleukin 6	1.030	4.26E-01	1.07E+00	-1.022	4.75E-01	1.07E+00	1.032	4.48E-01	1.09E+00	-1.050	3.33E-01	1.06E+00
Tnf	Tumor necrosis factor alpha	-1.003	6.35E-01	1.02E+00	1.002	6.81E-01	9.97E-01	1.017	4.93E-01	1.08E+00	1.082	3.04E-01	1.00E+00
Ccl2	Chemokine (C-C motif) ligand 2	-1.023	3.86E-01	1.07E+00	-1.073	1.92E-01	1.03E+00	-1.050	2.35E-01	1.06E+00	1.082	1.46E-01	9.10E-01
Nos2	Nitric oxide synthase 2, inducible	1.069	2.86E-01	1.10E+00	-1.063	3.21E-01	1.06E+00	-1.014	6.54E-01	1.05E+00	-1.003	6.12E-01	1.10E+00
Mrc1	**Mannose receptor, C type 1**	-1.029	2.09E-01	1.09E+00	-1.064	**3.72E-02**	7.06E-01	1.070	1.50E-01	9.79E-01	1.439	**5.63E-05**	**1.42E-02**
Cd68	**CD68 antigen**	1.683	**6.74E-08**	**2.07E-04**	-1.201	**1.08E-02**	4.96E-01	2.042	**3.49E-11**	**1.31E-07**	1.292	**1.49E-03**	1.28E-01
Tyrobp	**TYRO protein tyrosine kinase binding protein**	1.628	**1.75E-07**	**3.48E-04**	-1.237	**1.22E-02**	5.08E-01	1.570	**2.45E-06**	**1.26E-03**	1.129	8.70E-02	7.97E-01
Trem2	**Triggering receptor expressed on myeloid cells 2**	1.363	**8.16E-05**	**2.93E-02**	-1.183	**2.46E-02**	6.34E-01	1.582	**2.06E-06**	**1.16E-03**	1.187	**2.56E-02**	5.52E-01
Tlr2	**Toll-like receptor 2**	1.199	**1.51E-02**	5.48E-01	-1.056	2.77E-01	1.06E+00	1.196	**2.15E-02**	4.89E-01	1.057	2.35E-01	9.69E-01
P2ry6	**Pyrimidinergic receptor P2Y, 6**	1.273	**2.68E-03**	2.45E-01	-1.144	8.74E-02	8.97E-01	1.477	**1.64E-05**	**5.53E-03**	1.064	3.39E-01	1.02E+00
Aif1	**Allograft inflammatory factor 1 (Iba1)**	1.167	**2.21E-02**	6.37E-01	-1.097	1.53E-01	9.92E-01	1.225	**9.88E-03**	3.31E-01	1.147	7.10E-02	7.61E-01

Table S5 Unusual microglial gene expression signature in the α-syn seeding/spreading model at 13dpi and 90 dpi. The bold highlighted genes may be involved in inducing neurodegeneration (see main text for details).

		ipsi PFF versus ipsi PBS						ipsi PFF versus contra PFF					
		13dpi			90dpi			13dpi			90dpi		
Gene Symbols	Protein	FC	p-Value	Pfp	FC	p-Value	Pfp	FC	p-Value	Pfp	FC	p-Value	Pfp
ASTROCYTES													
Gfap	Glial fibrillary acidic protein	1.633	**7.12E-08**	**1.85E-04**	-1.123	**2.38E-02**	6.34E-01	1.736	**1.71E-08**	**3.62E-05**	1.285	**1.52E-03**	1.29E-01
Amigo2	Adhesion molecule with Ig like domain 2	-1.273	9.24E-04	1.73E-01	-1.030	9.47E-02	9.12E-01	-1.527	**6.77E-06**	**2.86E-03**	-1.400	**8.61E-05**	**1.51E-02**
Osmr	Oncostatin M receptor	1.153	**1.78E-02**	5.87E-01	-1.081	**3.66E-02**	7.10E-01	1.396	**2.21E-04**	**3.30E-02**	1.315	**1.31E-03**	1.16E-01
S1pr3	Sphingosine-1-phosphate receptor 3	-1.184	**1.71E-02**	6.07E-01	-1.054	3.00E-01	1.06E+00	-1.159	7.02E-02	8.12E-01	-1.118	1.19E-01	8.61E-01
Vim	Vimentin	1.183	**2.82E-02**	7.02E-01	-1.246	**6.29E-03**	4.18E-01	1.135	9.37E-02	8.74E-01	1.147	6.38E-02	7.42E-01
Serping1	Serine/ cysteine peptidase inhibitor, member 1	-1.031	1.05E-01	9.94E-01	-1.513	**1.35E-05**	**2.85E-02**	1.223	**6.77E-03**	2.65E-01	1.764	**1.40E-07**	**1.82E-04**
Ptx3	Pentraxin related gene	-1.028	5.39E-01	1.04E+00	1.023	6.50E-01	9.97E-01	-1.000	6.48E-01	1.06E+00	1.025	5.57E-01	1.06E+00
PERIPHERAL IMMUNE CELLS													
Ptprc	Protein tyrosine phosphatase, receptor C (CD45)	1.457	**1.69E-05**	1.02E-02	-1.063	2.00E-01	1.03E+00	1.516	**2.72E-05**	**7.71E-03**	1.193	**3.05E-02**	5.87E-01
Cd19	CD19 antigen	1.004	6.65E-01	1.02E+00	1.039	4.75E-01	1.02E+00	-1.054	4.60E-01	1.08E+00	1.024	5.14E-01	1.06E+00
Cd3e	CD3 antigen, epsilon polypeptide	1.037	4.32E-01	1.07E+00	1.045	2.82E-01	1.06E+00	-1.009	5.92E-01	1.07E+00	1.037	4.05E-01	1.03E+00
Cd4	CD4 antigen	1.172	**3.63E-02**	7.59E-01	-1.105	**1.63E-02**	5.52E-01	1.094	7.61E-02	8.15E-01	1.243	**4.32E-03**	2.30E-01
Cd8a	CD8 antigen	-1.003	4.77E-01	1.06E+00	-1.141	9.30E-02	9.07E-01	1.046	2.44E-01	1.06E+00	1.076	3.19E-01	1.01E+00

Table S6 Molecular astrocyte and peripheral immune cell genes after striatal PFF injection.